Isogeometric boundary element analysis and structural shape optimization for Helmholtz acoustic problems

(Isogeometrische Randelementanalyse und Strukturformoptimierung für akustische Helmholtz-Probleme)

Dissertation

zur Erlangung des akademischen Grades

Doktor-Ingenieur (Dr.-Ing.)

an der Fakultät Bauingenieurwesen

der Bauhaus-Universität Weimar

vorgelegt von

M.Sc. Ahmed Mostafa Shaaban Mohamed

Geboren am 24. Mai 1985 in Gizeh, Ägypten

Betreuer:

Prof. Dr.-Ing. Timon Rabczuk

Status des Doktoranden:

Intern

Weimar, Oktober 2021

Acknowledgements

Throughout the writing of this dissertation I have received a great deal of support and assistance.

I would first like to thank my supervisor, Prof. Dr. -Ing. Timon Rabczuk, whose expertise was invaluable in formulating the research questions and methodology. His insightful feedback pushed me to sharpen my thinking and brought my work to a higher level.

I would like to thank Dr. Cosmin Anitescu, who tutored me from the first day of my research at the Institute for Structural Mechanics, for his patient support and valuable guidance throughout my studies to choose the right direction and successfully complete my dissertation.

Special thanks to Dr. Elena Atroshchenko, our companion in the School of Civil and Environmental Engineering, University of New South Wales, Sydney, Australia. Although we have worked together online the most of time, she was always available to answer all my questions and pushing me to get my degree.

In addition, I would like to thank my parents and siblings for their wise counsel, sympathetic ear and unfailing emotional support. At pivotal moments, your love and care helped me fight against all odds.

I could not have completed this dissertation without the support of my friends, Mohammed Ashour, Jorge Lopez and Nam Bac Vu who provided stimulating discussions as well as happy distractions to rest my mind outside of my research.

I would also like to thank Frau. Rosemarie Mayer for readily helping me whenever needed and supporting me in numerous circumstances.

Weimar, Oktober 2021

Ahmed Mostafa Shaaban

Ehrenwörtliche Erklärung

Ich erkläre hiermit ehrenwörtlich, dass ich die vorliegende Arbeit ohne unzulässige Hilfe Dritter und ohne Benutzung anderer als der angegebenen Hilfsmittel angefertigt habe. Die aus anderen Quellen direkt oder indirekt übernommenen Daten und Konzepte sind unter Angabe der Quelle gekennzeichnet.

Insbesondere habe ich hierfür nicht die entgeltliche Hilfe von Vermittlungs-bzw. Beratungsdiensten (Promotionsberater oder anderer Personen) in Anspruch genommen. Niemand hat von mir unmittelbar oder mittelbar geldwerte Leistungen für Arbeiten erhalten, die im Zusammenhang mit dem Inhalt der vorgelegten Dissertation stehen. Die Arbeit wurde bisher weder im In-noch im Ausland in gleicher oder ähnlicher Form einer anderen Prüfungsbehörde vorgelegt. Ich versichere ehrenwörtlich, dass ich nach bestem Wissen die reine Wahrheit gesagt und nichts verschwiegen habe.

Ort, **Datum**: Weimar, Oktober 2021

Unterschrift :

Abstract

In this thesis, a new approach is developed for applications of shape optimization on the time harmonic wave propagation (Helmholtz equation) for acoustic problems. This approach is introduced for different dimensional problems: 2D, 3D axi-symmetric and fully 3D problems. The boundary element method (BEM) is coupled with the isogeometric analysis (IGA) forming the so-called (IGABEM) which speeds up meshing and gives higher accuracy in comparison with standard BEM. BEM is superior for handling unbounded domains by modeling only the inner boundaries and avoiding the truncation error, present in the finite element method (FEM) since BEM solutions satisfy the Sommerfeld radiation condition automatically. Moreover, BEM reduces the space dimension by one from a volumetric three-dimensional problem to a surface two-dimensional problem, or from a surface two-dimensional problem to a perimeter one-dimensional problem. Non-uniform rational B-splines basis functions (NURBS) are used in an isogeometric setting to describe both the CAD geometries and the physical fields.

IGABEM is coupled with one of the gradient-free optimization methods, the Particle Swarm Optimization (PSO) for structural shape optimization problems. PSO is a straightforward method since it does not require any sensitivity analysis but it has some trade-offs with regard to the computational cost. Coupling IGA with optimization problems enables the NURBS basis functions to represent the three models: shape design, analysis and optimization models, by a definition of a set of control points to be the control variables and the optimization parameters as well which enables an easy transition between the three models.

Acoustic shape optimization for various frequencies in different mediums is performed with PSO and the results are compared with the benchmark solutions from the literature for different dimensional problems

proving the efficiency of the proposed approach with the following remarks:

- In 2D problems, two BEM methods are used: the conventional isogeometric boundary element method (IGABEM) and the eXtended IGABEM (XIBEM) enriched with the partition-of-unity expansion using a set of plane waves, where the results are generally in good agreement with the linterature with some computation advantage to XIBEM which allows coarser meshes.

-In 3D axi-symmetric problems, the three-dimensional problem is simplified in BEM from a surface integral to a combination of two 1D integrals. The first is the line integral similar to a two-dimensional BEM problem. The second integral is performed over the angle of revolution. The discretization is applied only to the former integration. This leads to significant computational savings and, consequently, better treatment for higher frequencies over the full three-dimensional models.

- In fully 3D problems, a detailed comparison between two BEM methods: the conventional boundary integral equation (CBIE) and Burton-Miller (BM) is provided including the computational cost. The proposed models are enhanced with a modified collocation scheme with offsets to Greville abscissae to avoid placing collocation points at the corners. Placing collocation points on smooth surface enables accurate evaluation of normals for BM formulation in addition to straightforward prediction of jump-terms and avoids singularities in $\mathcal{O}(1/r)$ integrals eliminating the need for polar integration. Furthermore, no additional special treatment is required for the hyper-singular integral while collocating on highly distorted elements, such as those containing sphere poles. The obtained results indicate that, CBIE with PSO is a feasible alternative (except for a small number of fictitious frequencies) which is easier to implement. Furthermore, BM presents an outstanding treatment of the complicated geometry of mufflers with internal extended inlet/outlet tube as an interior 3D Helmholtz acoustic problem instead of using mixed or dual BEM.

Kurzfassung

In dieser Arbeit wird ein neuer Ansatz für Anwendungen der Formoptimierung auf die zeitliche harmonische Wellenausbreitung (Helmholtz-Gleichung) für akustische Probleme entwickelt. Dieser Ansatz wird für verschiedene dimensionale Probleme eingeführt: 2D-, 3D-axialsymmetrische und vollständig 3D-Probleme. Die Randelementemethode (Boundary-Elemente-Methode / BEM) ist mit der isogeometrischen Analyse (IGA) gekoppelt, die das sogenannte (IGABEM) bildet, was die Vernetzung beschleunigt und im Vergleich zur Standard-BEM eine höhere Genauigkeit bietet. BEM ist für den Umgang mit unbeschränkten Domänen überlegen, indem nur die inneren Grenzen modelliert und der Trunkierungsfehler vermieden wird, der in der Finite-Elemente-Methode (FEM) vorhanden ist, da BEM-Lösungen die Sommerfeld-Strahlungsbedingung automatisch erfüllen. Darüber hinaus reduziert BEM die Raumdimension um eins von einem volumetrischen dreidimensionalen Problem zu einem zweidimensionalen Oberflächenproblem oder von einem zweidimensionalen Oberflächenproblem zu einem eindimensionalen Umfangsproblem. Uneinheitliche rationale B-Splines-Basisfunktionen (NURBS) werden in einer isogeometrischen Umgebung verwendet, um sowohl die CAD-Geometrien als auch die physikalischen Felder zu beschreiben.

IGABEM ist mit einer der gradientenfreien Optimierungsmethoden, der Particle Swarm Optimization (PSO) für Strukturformoptimierungsprobleme gekoppelt. PSO ist eine unkomplizierte Methode, da sie keine Sensitivitätsanalyse erfordert, aber einige Kompromisse in Bezug auf den Rechenaufwand hat. Die Kopplung von IGA mit Optimierungsproblemen ermöglicht es den NURBS-Basisfunktionen, die drei Modelle darzustellen: Formentwurf, Analyse und Optimierungsmodelle, durch eine Definition eines Satzes von Kontrollpunkten als Kontrollvariablen und Optimierungsparameter, was einen einfachen Übergang zwischen die drei Modelle.

Mit PSO wird eine akustische Formoptimierung für verschiedene Frequenzen in verschiedenen Medien

durchgeführt und die Ergebnisse mit den Benchmark-Lösungen aus der Literatur für verschiedene Dimensionsprobleme verglichen, um die Effizienz des vorgeschlagenen Ansatzes mit den folgenden Anmerkungen zu beweisen:

- Bei 2D-Problemen werden zwei BEM-Methoden verwendet: die konventionelle isogeometrische Boundary-Elemente-Methode (IGABEM) und die eXtended IGABEM (XIBEM), angereichert mit der Partition-of-Unit-Expansion unter Verwendung eines Satzes von ebenen Wellen, wobei die Ergebnisse im Allgemeinen gut sind Übereinstimmung mit der Linteratur mit einem gewissen Rechenvorteil für XIBEM, das gröbere Netze ermöglicht.

-Bei 3D-axialsymmetrischen Problemen wird das dreidimensionale Problem in BEM von einem Oberflächenintegral zu einer Kombination von zwei 1D-Integralen vereinfacht. Das erste ist das Linienintegral ähnlich einem zweidimensionalen BEM-Problem. Das zweite Integral wird über den Drehwinkel geführt. Die Diskretisierung wird nur auf die ehemalige Integration angewendet. Dies führt zu erheblichen Recheneinsparungen und folglich zu einer besseren Behandlung höherer Frequenzen über die vollständigen dreidimensionalen Modelle.

- Bei vollständig 3D-Problemen wird ein detaillierter Vergleich zwischen zwei BEM-Methoden: der konventionellen Randintegralgleichung (CBIE) und Burton-Miller (BM) einschließlich des Rechenaufwands bereitgestellt. Die vorgeschlagenen Modelle werden durch ein modifiziertes Kollokationsschema mit Versatz zu Greville-Abszissen erweitert, um das Platzieren von Kollokationspunkten an den Ecken zu vermeiden. Das Platzieren von Kollokationspunkten auf einer glatten Oberfläche ermöglicht eine genaue Auswertung von Normalen für die BM-Formulierung zusätzlich zur direkten Vorhersage von Sprungtermen und vermeidet Singularitäten in $\mathcal{O}(1/r)$-Integralen, wodurch die Notwendigkeit von polare Integration. Darüber hinaus ist keine zusätzliche spezielle Behandlung für das hypersinguläre Integral erforderlich, während es auf stark verzerrten Elementen, wie beispielsweise solchen mit Kugelpolen, kollokiert wird. Die erhaltenen Ergebnisse weisen darauf hin, dass CBIE mit PSO eine praktikable Alternative (abgesehen von wenigen fiktiven Frequenzen) ist, die einfacher zu implementieren ist. Darüber hinaus präsentiert BM eine hervorragende Behandlung der komplizierten Geometrie des Schalldämpferproblems mit intern verlängertem Einlass-/Auslassrohr als inneres 3D-Helmholtz-Akustikproblem anstelle von gemischter oder dualer BEM.

List of Publications

The presented work in this thesis is presented in the following journal papers:

1- Ahmed Mostafa Shaaban, Cosmin Anitescu, Elena Atroshchenko, and Timon Rabczuk. 3D isogeometric boundary element analysis and structural shape optimization for Helmholtz acoustic scattering problems. Computer Methods in Applied Mechanics and Engineering, 384:113950, 2021.

2- Ahmed Mostafa Shaaban, Cosmin Anitescu, Elena Atroshchenko, and Timon Rabczuk. An isogeometric Burton-Miller method for the transmission loss optimization with application to mufflers with internal extended tubes. Applied Acoustics, 185:108410, 2022.

3- Ahmed Mostafa Shaaban, Cosmin Anitescu, Elena Atroshchenko, and Timon Rabczuk. Isogeometric boundary element analysis and shape optimization by PSO for 3D axisymmetric high frequency Helmholtz acoustic problems. Journal of Sound and Vibration, 486:115598, 2020.

4- Ahmed Mostafa Shaaban, Cosmin Anitescu, Elena Atroshchenko, and Timon Rabczuk. Shape optimization by conventional and extended isogeometric boundary element method with PSO for two-dimensional Helmholtz acoustic problems. Engineering Analysis with Boundary Elements, 113:156 - 169, 2020.

in addition to the contributions in the following conferences :

1- Ahmed Mostafa Shaaban, Cosmin Anitescu, Elena Atroshchenko, and Timon Rabczuk. Shape optimiza-

tion analysis for 3D acoustic problems using isogeometric boundary element methods. A contributed talk to Virtual International Conference on Isogeometric Analysis (VIGA) 2021, Lyon, France, September 26-29, 2021.

2- Ahmed Mostafa Shaaban, Cosmin Anitescu, Elena Atroshchenko, and Timon Rabczuk. Shape optimization for acoustic problems using boundary element method and isogeometric analysis. A contributed talk to Virtual Isogeometric Analysis (VIGA) 2020, August 11-12, 2020.

3- Ahmed Mostafa Shaaban. Two applications of isogeometric boundary eElement method for singular Helmholtz acoustic problems. Conference Proceedings of Data Driven Computing and Machine Learning in Engineering (DACOMA-19). Advances in Computational Mechanics. Volume 4, 2019. ISSN: 1940-5820 (printed). China, September 2019.

Contents

List of Figures

List of Tables

Chapter 1

Introduction

1.1 Computational models

Currently the wave propagation problem has received growing attention in the engineering and research fields of: noise control, underwater sonar, seismology, bio-acoustics, electro-acoustics and non-destructive testing. The simple forms of this type of problem can be studied using analytical or semi-analytical methods [1, 2], but these methods are not applicable to treat the practical problems and the approximate solution can be obtained using numerical methods, such as: the finite element method (FEM) [3, 4], the Galerkin/least-squares FEM [5], the generalized FEM [6], the element-free Galerkin method [7], etc. Recently, the analysis of the acoustic problem using the boundary element method (BEM) has become widely accepted due to its ease of handling infinite unbounded domains [8]. This advantage of BEM comes from its ability to model only the boundaries without any need to introduce any truncation surfaces since BEM solutions satisfy the Sommerfeld radiation condition automatically [9]. This is an advantage of BEM over domain-type approaches such as FEM, where these truncated boundaries must be modeled. Furthermore, in BEM the space dimension is reduced by one from a volumetric three-dimensional problem to a surface two-dimensional problem, or from a surface two-dimensional problem to a perimeter one-dimensional problem. In this thesis, one of the most well-known forms of the wave propagation problem which is the Helmholtz time harmonic equation is solved using BEM.

1.2 Isogeometric analysis (IGA)

In order to model exact geometries with higher order smoothness in the solution fields, different numerical methods compute higher order differential operators. Isogeometric analysis (IGA) - which was first proposed in [10] - also can be used to model complex geometries with spline basis functions. The basic idea of IGA is to connect the CAD model and the numerical analysis together using the same basis functions describing the CAD geometries and discretizing the physical variables. One of the most widely used functions are the Non-Uniform Rational B-Splines (NURBS). NURBS are capable of modelling exact conic sections using rational spline basis functions. In addition, they allow easy refinement by degree elevation or knot insertion, which corresponds to p- and h-refinements in FEM, respectively. Moreover, NURBS permit k-refinement, which can elevate the order with a knot insertion simultaneously keeping the same continuity, which cannot be implemented in FEM. This results in robust and accurate solutions, which reduce the pollution errors produced by numerical methods. The efficiency of IGA has been demonstrated not only for acoustic problem but also for different engineering applications. Many comparisons were conducted between IGA and standard FEM to establish the accuracy of the IGA models, such as those in: [10, 11, 12]. Boundary element method (BEM) can also be coupled with IGA forming the so-called IGABEM. This model was proposed previously for different engineering problems giving very accurate results. Among these problems are linear elasticity [13], fracture mechanics [14, 15], elasto-plastic inclusions [16], wave resistance [17], acoustics [18, 19, 20, 21, 22, 23, 24, 25, 26, 27, 28], etc.

1.3 Boundary Element Method (BEM) for different dimensional problems

1.3.1 BEM for two-dimensional problem

Since the solutions of the Helmholtz equation for high frequencies have a highly oscillatory behaviour, the mesh size in all numerical methods needs to be proportional to the frequency, which leads to unfeasible solution times and in some cases may surpass the available memory capacity. A number of methods were proposed to reduce this dependence and achieve higher accuracy on coarser meshes. One such approach is the so-called eXtended or enriched BEM, as was originally proposed in [29]. The main idea corresponding to the enrichment is to use the partition of unity property of the NURBS basis function together with a set of plane waves propagating in different directions to augment the approximation space. This enrichment was

first implemented in the framework of standard BEM [30] and later extended to IGABEM [22] (referred throughout this thesis as XIBEM). It has been shown in [22], that the method results in better accuracy per number of degrees of freedom in comparison with the IGABEM, and therefore can serve as an efficient tool for the numerical analysis of high frequency problems.

1.3.2 BEM for three-dimensional axi-symmetric problem

Scatterers with axi-symmetric shapes and boundary conditions can be more easily analysed with an axi-symmetric model which ends up with a much smaller system matrix. In the framework of BEM, the three-dimensional problem is simplified from a surface integral to a combination of two integrals. The first is the line integral similar to a two-dimensional BEM problem. The second integral is implemented over the angle of revolution. The discretization is applied only to the former line integration. The singularity in the Green's function is partially removed analytically using the elliptic integrals and then the normal Gauss quadrature rule is applied. This reduces the computational cost significantly, and based on that, solutions with higher frequencies can be obtained when compared to the fully three-dimensional models. These procedures were applied for acoustic radiation and scattering with the standard BEM in [31]. Several research works have studied acoustic axi-symmetric problems using different techniques for removing the singularity. A volume integral method was employed in [32], while the singularity subtraction technique was used in [33]. Some other studies use regularization methods [34, 35]. All of these studies consider the implementation of standard BEM - with the simple form of polynomial shape functions - but for low frequency problems. A semi-analytical technique for the singularity treatment was coupled with the standard BEM to analyze the axi-symmetric horn problem in [36].

1.3.3 BEM for fully three-dimensional problem

Many researchers extended the preciously discussed models to fully three-dimensional problems. An IGA-BEM model based on T-spline meshes was introduced in [37] while an extended IGABEM was proposed in [22]. IGABEM models based on NURBS are discussed in [23, 24, 25, 26, 19]. Moreover, a recent work used subdivision surfaces for modelling the boundary [27]. All the mentioned three-dimensional research works highlight the spurious eigenfrequency problem that causes non-uniqueness numerical results while using the conventional boundary integral equation (**CBIE**) for exterior acoustic problems when the wavenumber coincides with the eigenmodes. The Burton-Miller (**BM**) formulation was suggested to overcome this

problem [38]. However, another obstacle that appears in BEM models is finding the proper solution for the different types of singular integrals, such as the weakly and strongly singular integrals in **CBIE** and the weakly, strongly and hyper-singular integrals in **BM**. In order to overcome this problem, regularization schemes [39] were introduced in [37, 22] while a polar integration scheme was used for weakly and strongly singular integrals and the singularity subtraction technique (SST) [40] is applied to hyper-singular integrals in [23, 24, 25, 26, 27]. Offsets to collocation points were introduced in [41] for elasticity problems where C^0 continuity is encountered and are re-derived in this thesis for acoustic problem as well. By this method, all weakly and strongly singular integrals are transformed to regular integrals which can be evaluated using conventional Gauss quadrature, while SST is used for hyper-singular integrals. Moreover, these offsets help to define the normal directions at collocation points as required by the BM method. Consequently, the jump-term of all collocation points can be defined easily on smooth surfaces without any need for complex calculations. Collocation on highly distorted elements needs additional special treatment while performing SST for the hyper-singular integral such as the case of elements containing sphere poles. However, the proposed collocation scheme does not need any additional treatment.

1.4 The muffler problem

1.4.1 Computational models for muffler problem

The muffler problem is considered as one of the applications of noise control problem. Several works study the muffler using the simple plane wave solution or the transfer matrix method even for mufflers with extended internal inlet/outlet tubes [42, 43, 44, 45, 46, 47], mode matching method [48], eigenfunction expansion technique [49] or point collocation approach [50]. These methods can give preliminary design, however, they are not appropriate for all sizes and geometries especially for higher frequencies where the wave motion is no longer plane [51]. Thus, numerical methods are more adequate by approximating the muffler problem as an interior time-harmonic acoustic wave propagation problem modeled with the Helmholtz equation. Among these methods are the finite element method (FEM) [52, 53, 54], Galerkin-FEM (GFEM) [55], isogeometric analysis (IGA) [56] and the boundary element method (BEM) [51, 57]. BEM is capable to reduce the dimensionality of the 3D problem by modelling only the muffler surfaces/boundaries. However, conventional methods such as the conventional boundary integral equation (CBIE) is not suitable for mufflers with internal extended tubes due to the produced nearly singular integrals over these tubes. This

4

requires smaller elements and huge integration effort with higher number of Gauss quadrature points to ob-tian sufficient accuracy [58]. Many researches attempt to overcome this problem by using the dual or mixed BEM such as the works in [59, 60, 61], whilst these works are criticized due to neglecting the thin thickness of the extended tubes which leads to some discrepancies in the results compared to other numerical meth-ods and available experimental data especially for higher frequencies [52, 55]. The Burton-Miller method (BM) was originally introduced to overcome the spurious eigenfrequency problem causing instabilities due to the non-uniqueness numerical solution for exterior acoustic problems [38]. This eigenfrequency problem is not applicable for interior problems. However, BM is proposed in this thesis to properly deal with the thin thickness of the extended tubes prescribing a combination of two types of BIEs on the original thin-walled geometry getting benefit from evaluating the normal direction at the collocation points on all surfaces in the purpose of constructing the linear system of equations.

1.4.2   The transmission loss (TL)

The main factor for muffler design is the sound attenuation or the Transmission Loss (TL) which is defined as the ratio of the incident to the transmitted sound powers. TL can be computed numerically using different methods while all of them give almost the same result [60]. Among these methods is the 3-point method [59] which requires single solution for the linear system of equations but with post-processing calculations for three field points. This method is not able to couple the numerical methods with the 4-pole methods to produce the 4-pole parameters entering/exiting the inlet/outlet tubes. Therefore, the 4-pole transfer matrix is introduced [51] where the 4-pole parameters can be obtained easily by two solutions with two different boundary conditions consuming more time than the 3-point method. In order to reduce the computational time and keep getting the 4-pole parameters, the improved 4-pole transfer matrix is proposed which is considered as the fastest method from the three mentioned methods [60]. Although this method requires two solutions similarly to the 4-pole transfer matrix, different boundary conditions are assigned to speed up the solution. In this thesis, the transfer matrices and the description of the solution procedures are explained in detail showing that, the TL is computed adequately by evaluating the physical unknowns entering/exiting the muffler inlet/outlet tubes, which is convenient to the nature of boundary element methods.

5

1.5 Optimization analysis

The acoustic behaviour can be improved using optimization methods in terms of absorbing reflected waves, noise reduction or concentration of produced sound, etc. In such applications, the optimization procedures operate on either the material or the shape of the scatterer. The proposed approach addresses the shape optimization analysis. The common optimization methods are divided into two branches. The first needs to differentiate the objective function with respect to the design variables to perform the sensitivity analysis forming the so-called gradient-based optimization methods [62, 63, 64, 65]. The convergence rate obtained from these methods is faster compared to other methods. On the other hand, they require more involved treatment for the singularities appearing with the differentiation. The methods of the second branch are the gradient-free methods. Although these methods are easier to implement since they do not need any sensitivity analysis, they encounter slower convergence rates. The most popular methods from this family are the Particle Swarm Optimization (PSO) [66, 67] and the Genetic Algorithm (GA) [68]. Sun *et al.* [69] pointed out several advantages of PSO in comparison with another gradient-free algorithm; Genetic Algorithm (GA). First, PSO is faster in the searching process. Furthermore, its mathematics and parameters are easier, avoiding "crossover" and "mutation" operations, and it deals with real numbers representing its parameters in the search space, while GA converts the parameters to chromosomes or individuals in the genetic space with coding operator. These advantages lead finally to less consumption of memory capacity. Barbieri *et al.* [70] conducted a comparison between PSO and GA for the problem of the horn shape optimization and concluded that PSO had better overall results with faster convergence rate than those of GA which was only fast in the earlier stages of the optimization process.

Coupling IGABEM with shape optimization algorithms provides the advantage of employing the NURBS control points to act as control variables in the analysis model and as the optimization parameters in the optimization models. During the solution process, this allows a great deal of flexibility through the three different stages: shape design, analysis and optimization models. Several problems utilized these features in elasticity problems [69, 71, 72, 73], shells [74, 75], heat conduction problems [76], fluids [77, 78], electromagnetic scattering problems [79], potential-flow problems [80] and acoustic problems [20, 21, 63, 24, 28].

1.6   Other alternatives to NURBS in IGA

As mentioned, NURBS are the most common basis functions in IGA. However, they have some trade-offs. Among them is the special treatment of trimming surfaces [81, 82, 83]. Another trade-off is the tensor product which creates unnecessary control points in the purpose of displaying fine geometric details which subsequently leads to more computational cost. From that point, other alternatives are proposed creating unstructured surface representations, such as T-splines [11, 84, 85]. Nevertheless, the basis functions are not linearly dependent for generic T-splines and they are difficult to be enforced for 3D domains [86, 87]. This shows distinctly that, T-splines are not standard modelling tools, which led to proposing other splines called analysis suitable T-meshes [88], whilst they still suffer from implementing knot insertion refinement in complex geometries. So that, other spline functions are suggested in IGA applying adaptive local refinement using the globally C^1-continuous basis functions belonging to a class of Hermite finite elements over T-meshes where the basis function is given in terms of Bézier-Bernstein polynomials, such as: polynomials splines over hierarchical T-meshes (PHT-splines) [89, 90, 91, 92, 93, 94, 95, 96, 97, 98, 99], rational splines over hierarchical T-meshes (RHT-splines) [100, 101, 97], truncated Hierarchical B-splines (THB-splines) [102, 103], etc.

Moreover, the basic idea of local refinement in adaptive IGA can also be coupled with BEM and implemented in different applications, such as: elasticity problems, where Scott *et al.* coupled collocated IGA-BEM with unstructured analysis-suitable T-spline surfaces for linear elastostatic problems [104]. Lian *et al.* utilized the explained model for shape sensitivity analysis and gradient-based shape optimization in 3D linear elasticity [105]. The same adaptive IGA model was implemented by Simpson *et al.* to simulate acoustic phenomena [37] and by Ginnis *et al.* to solve the Neumann–Kelvin problem in the context of a ship-hydrodynamic problem or wave-resistance problem [17]. Simpson and Liu proposed a black-box fast multipole method to accelerate the computations of the adaptive IGABEM model based on T-splines for 3D problems [106].

1.7 Introduction to the present work

In this thesis, the isogeometric analysis (IGA) is coupled with the boundary element methods (BEM) forming the so-called (IGABEM) to solve the time harmonic equation of Helmholtz for acoustic applications. BEM approximates the solution of the Helmholtz equation superiorly since it models only the inner boundaries and avoids the truncation error for infinite domain problems. NURBS describe both the CAD geometries and the physical fields. IGABEM accelerates re-meshing and provides higher accuracy compared to the standard BEM.

Furthermore, Particle Swarm Optimization (PSO) is a simple gradient-free method which does not require any sensitivity analysis. It is proposed for shape optimization analysis in the framework of IGA. This model gives a great advantage in optimization models, since it utilizes the IGA feature of representing the three different models: shape design, analysis and optimization models using a single set of control points. Several numerical examples are demonstrated in this thesis to validate the proposed approach against the analytical solution and previously published numerical methods.

The organization of this thesis is as follows:

In Chapter 2, PSO in conjunction with each of IGABEM and XIBEM is used for shape optimization problems in time-harmonic acoustics for two-dimensional problem. A numerical example considering the duct problem is solved first to verify both IGABEM and XIBEM against the analytical solution. Next, two applications are studied; the vertical noise barrier and the horn problems. Then, the obtained results are compared against previously published results and the efficiency of XIBEM in comparison with IGABEM is discussed.

In Chapter 3, two directions are explored. The first direction is to verify the feasibility of IGABEM for three-dimensional axi-symmetric problems in handling higher frequencies cases. The results are compared to the analytical solution for three examples: the pulsating sphere problem, the scattering problem of spherical waves and the plane wave scattering problem by rigid spheres. The second direction demonstrates the strength of the proposed approach with PSO for shape optimization problems. The horn problem with cylin-

8

drical symmetry is presented and validated against that with standard BEM. Then, different optimization cases are studied and compared with already published optimized shapes by both BEM and FEM.

In Chapter 4, the feasibility of the two BEM models (CBIE and BM) in handling fully three-dimensional problems is discussed in the framework of isogeometric analysis for different frequency values and verified against the analytical solution. Then, the efficiency of the proposed approaches coupled with PSO algorithm is presented for different shape optimization problems and the optimized shapes are compared and validated against previously published shapes produced by BEM with sensitivity analysis.

In Chapter 5, the models of isogeometric BM (IGA-BM) are proposed to solve the muffler problem as an interior three-dimensional Helmholtz acoustic problem. The performance of IGA-BM model is discussed and compared against the previously published results using finite and boundary element methods, IGA models and the available measured data. Furthermore, optimization examples using the Particle Swarm Optimization (PSO) coupled with IGA-BM are demonstrated to maximize the TL in attenuation regions by changing the internal lengths of the extended tubes.

A summary of conclusions and future works is written in Chapter 6.

Chapter 2

Structural shape optimization with IGABEM for two-dimensional problem

based on the paper *'Shape optimization by conventional and extended isogeometric boundary element method with PSO for two-dimensional Helmholtz acoustic problems'* published in EABE, where the contribution of each author is summarized as follows:

Ahmed Mostafa Shaaban

- Research state of the art
- Investigation
- Formal analysis
- Methodology
- Software / Programming
- Data curation
- Data analysis
- Validation
- Visualization
- Writing-original draft preparation

Cosmin Anitescu

- Conceptualization

- Investigation

- Methodology

- Data analysis

- Writing-review and editing

Elena Atroshchenko

- Conceptualization

- Investigation

- Methodology

- Data analysis

- Writing-review and editing

Timon Rabczuk

- Conceptualization

- Supervision

- Mentoring the research progress

- Review of the manuscript before submission

An electronic copy of this publication is available at: `https://doi.org/10.1016/j.enganabound.2019.12.012`

2.1 General

In this chapter, a new approach is developed for applications of shape optimization on the two-dimensional time harmonic wave propagation (Helmholtz equation) in acoustic problems. The particle swarm optimization (PSO) algorithm - a gradient-free optimization method avoiding the sensitivity analysis - is coupled with two boundary element methods (BEM) and isogeometric analysis (IGA). The first method is the conventional isogeometric boundary element method (IGABEM). The second method is the eXtended IGA-BEM (XIBEM) enriched with the partition-of-unity expansion using a set of plane waves. In both methods, the computational domain is parameterized and the unknown solution is approximated using non-uniform rational B-splines basis functions (NURBS).

In the optimization models, the advantage of IGA is the feature of representing the three models; i.e. shape design/analysis/optimization, using a set of control points, which also represent control variables and optimization parameters, making communication between the three models easy and straightforward.

A numerical example is considered for the duct problem to validate the presented techniques against the analytical solution. Furthermore, two different applications for various frequencies are studied; the vertical noise barrier and the horn problems, and the obtained results are compared against previously published numerical methods using sensitivity analysis and genetic algorithms to verify the efficiency of the proposed approaches.

2.2 Boundary integral equation for time harmonic problems

The acoustic problem is formulated as follows. An infinite domain occupied by a homogeneous isotropic medium and an obstacle/scatterer with smooth boundary embedded in this unbounded domain are considered [107]. The domain is denoted by Ω, and the boundary of the obstacle is Γ. Boundary Γ in the most general case consists of Neumann Γ_v, Dirichlet Γ_p and Robin Γ_r parts, such that the intersection of the three boundaries pairwise is $\emptyset$ (see figure 2.1). The boundary value problem for the Helmholtz equation consists
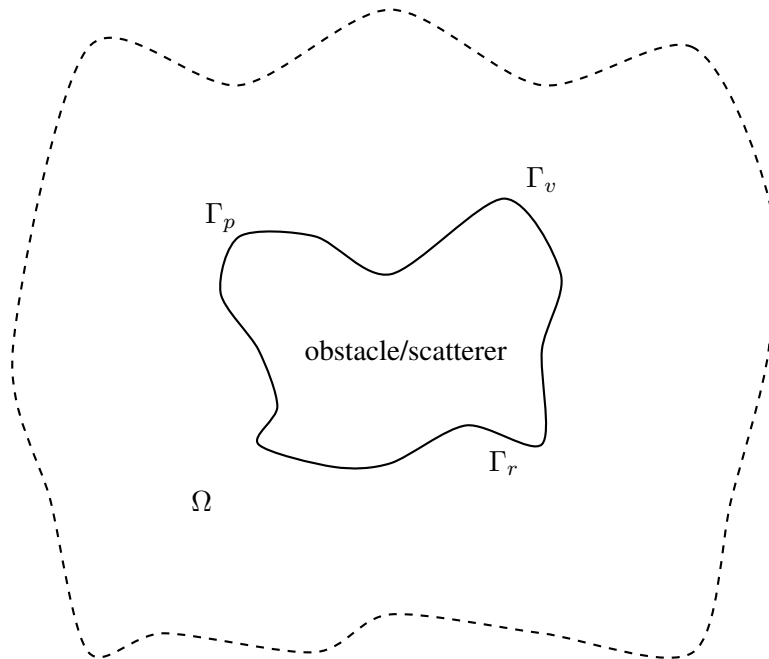
Figure 2.1: The acoustic problem.

in finding the acoustic pressure u, which satisfies the following equations:

$$\triangle u + k^2 u = f \qquad \text{in} \quad \Omega, \tag{2.1}$$

$$u = g_1 \qquad \qquad \text{on } \Gamma_p, \tag{2.2}$$

$$\frac{\partial u}{\partial n} = g_2 \qquad \qquad \text{on } \Gamma_v, \tag{2.3}$$

$$\frac{\partial u}{\partial n} - iku = g_3 \qquad \qquad \text{on } \Gamma_r, \tag{2.4}$$

where $\triangle$ is the Laplace operator, $i = \sqrt{-1}$, k is the wavenumber, related to the wavelength λ as $\lambda = 2\pi/k$, f is a function for the acoustic source term and n denotes the unit normal vector on Γ pointing outward to Ω. Functions g_1, g_2 and g_3 are prescribed on the corresponding parts of Γ. To prevent any possible reflection of spurious acoustic waves from the far-field, the Sommerfeld radiation condition is prescribed at infinity:

$$\lim_{r \to \infty} \sqrt{r} \left(\frac{\partial u}{\partial r} - iku \right) = 0, \tag{2.5}$$

where r is the distance from the origin.

Equations (2.1):(2.4) can be transformed to boundary integral equation (BIE) using Green's second identity [22]:

$$c(\mathbf{x})u(\mathbf{x}) + \int_\Gamma \frac{\partial G(\mathbf{x}, \mathbf{y})}{\partial n} u(\mathbf{y}) d\Gamma(\mathbf{y}) = \int_\Gamma G(\mathbf{x}, \mathbf{y}) \frac{\partial u(\mathbf{y})}{\partial n} d\Gamma(\mathbf{y}), \qquad \mathbf{x}, \mathbf{y} \in \Gamma, \tag{2.6}$$

where $G(\mathbf{x}, \mathbf{y})$ is the Green's function representing the field effect at $\mathbf{y}$ due to a source at $\mathbf{x}$ in free space. $c(\mathbf{x})$ is the jump-term [8].

The Green's function for 2D problems is defined as:

$$G(\mathbf{x}, \mathbf{y}) = \frac{i}{4} H_0^1(kr), \tag{2.7}$$

where H_0^1 is the Hankel function of order zero and $r = |\mathbf{x} - \mathbf{y}|$.

The integral representation of the solution, used to reduce the boundary value problem in domain Ω equations ((2.1)-(2.4)) to the boundary integral equation (BIE) on Γ eq.(2.6), automatically satisfies the Sommer-

feld radiation condition. This represents an advantage of BEM over FEM and other domain-type methods, where an additional error is introduced on the truncation boundary. Another advantage consists in reduction of the dimensionality of the problem, i.e. only the boundary of the domain needs to be discretized.

2.3 NURBS basis functions

The non-uniform rational B-spline functions (NURBS) are defined by means of the B-splines in the parametric space $\xi \in [0, 1]$ on a knot vector $\Xi = \{\xi_1 = 0, \cdots, \xi_i, \cdots, \xi_{n+p+1} = 1\}$ (a non-decreasing set of numbers from 0 to 1) where i is the knot index and n is the number of basis functions. The ith B-spline basis function of pth -degree $N_{i,p}(\xi)$ is defined recursively as follows [10, 108]:

$$N_{i,0}(\xi) = \begin{cases} 1 & \xi_i \leq \xi < \xi_{i+1}, \\ 0 & \text{otherwise}, \end{cases} \tag{2.8}$$

and for $p \geq 1$

$$N_{i,p}(\xi) = \frac{\xi - \xi_i}{\xi_{i+p} - \xi_i} N_{i,p-1}(\xi) + \frac{\xi_{i+p+1} - \xi}{\xi_{i+p+1} - \xi_{i+1}} N_{i+1,p-1}(\xi). \tag{2.9}$$

The NURBS basis function is written as:

$$R_{i,p}(\xi) = \frac{N_{i,p}(\xi) w_i}{\sum_{\bar{i}=1}^{n} N_{\bar{i},p}(\xi) w_{\bar{i}}}, \tag{2.10}$$

where w_i is the ith weight.

A NURBS curve represented by a set of control points B_i can be parametrized by:

$$C(\xi) = \sum_{i=1}^{n} R_{i,p}(\xi) B_i. \tag{2.11}$$

2.4 Conventional IGABEM for Helmholtz equation

Both known and unknown variables on the boundary (the acoustic pressure and its normal derivative) are discretized by the NURBS shape functions as follows:

$$u(\xi) = \sum_{i=1}^{n} R_{i,p}(\xi) u_i, \qquad \frac{\partial u}{\partial n}(\xi) = \sum_{i=1}^{n} R_{i,p}(\xi) q_i, \tag{2.12}$$

where u_i and q_i are the associated control variables. Eq.(2.12) is substituted into eq.(2.6), evaluated at n collocation points ξ_c yielding the following system of equations [22] :

$$c(\xi_c) \sum_{i=1}^{n} u_i R_{i,p}(\xi_c) + \sum_{i=1}^{n} \left[\int_0^1 \frac{\partial G(\xi_c, \xi)}{\partial n} R_{i,p}(\xi) |J_\xi| d\xi \right] u_i = \sum_{i=1}^{n} \left[\int_0^1 G(\xi_c, \xi) R_{i,p}(\xi) |J_\xi| d\xi \right] q_i,$$

(2.13)

where $|J_\xi|$ is the Jacobian.

Eq.(2.13) can be written in the matrix form as:

$$\mathbf{Hu} = \mathbf{Gt},$$

(2.14)

where

$$\mathbf{H}_{ci} = c(\xi_c) R_{i,p}(\xi_c) + \int_0^1 \frac{\partial G(\xi_c, \xi)}{\partial n} R_{i,p}(\xi) |J_\xi| d\xi,$$

$$\mathbf{G}_{ci} = \int_0^1 G(\xi_c, \xi) R_{i,p}(\xi) |J_\xi| d\xi,$$

(2.15)

and $\mathbf{u}$ and $\mathbf{t}$ are the vectors of the u_i and q_i components respectively. Finally, eq.(2.14) can be re-arranged into the system of linear equations:

$$\mathbf{Ax} = \mathbf{b},$$

(2.16)

where matrix $\mathbf{A}$ contains entries of matrices $\mathbf{H}$ and $\mathbf{G}$ corresponding to unknown control variables in eq.(2.13) arranged into vector $\mathbf{x}$. All known components are assembled into the right hand-side vector $\mathbf{b}$. In this study we use the collocation strategy defined by the Greville abscissae at points $\widehat{\xi}_g$ given by the formula [13]:

$$\widehat{\xi}_g = \frac{\xi_{g+1} + \xi_{g+2} + \cdots + \xi_{g+p}}{p}, \qquad g = 1, 2, \cdots, n-1.$$

(2.17)

Since the closed curves start and end with the same point, the Greville abscissae provide only $n-1$ collocation points. However, the total number of NURBS functions and control points are n. Therefore, the first and last NURBS functions are combined and the corresponding control points are considered to be one.

2.5 eXtended IGABEM (XIBEM) for the Helmholtz equation

According to the eXtended IGABEM (XIBEM), the acoustic pressure and its normal derivative are discretized using the partition of unity expansion of plane waves. Each NURBS basis is multiplied by functions representing plane waves propagating in different directions as follows [22]:

$$u(\xi) = \sum_{i=1}^{n} R_{i,p}(\xi) \sum_{m=1}^{M} A_{im} e^{ikd_{im} \cdot q(\xi)}, \tag{2.18}$$

$$\frac{\partial u}{\partial n}(\xi) = \sum_{i=1}^{n} R_{i,p}(\xi) \sum_{m=1}^{M} B_{im} e^{ikd_{im} \cdot q(\xi)}, \tag{2.19}$$

where A_{im} and B_{im} are the associated amplitude variables, $q(\xi) = (x(\xi), y(\xi))$ and M plane waves are defined by directions:

$$d_{im} = (\cos \frac{2(m-1)\pi}{M}, \sin \frac{2(m-1)\pi}{M}). \tag{2.20}$$

Then, eq.(2.13) yields the following:

$$
\begin{aligned}
c(\xi_c) \sum_{i=1}^{n} R_{i,p}(\xi_c) \sum_{m=1}^{M} A_{im} e^{ikd_{im} \cdot q(\xi_c)} + \sum_{i=1}^{n} \Big[\int_0^1 \frac{\partial G(\xi_c, \xi)}{\partial n} R_{i,p}(\xi) \sum_{m=1}^{M} e^{ikd_{im} \cdot q(\xi)} |J_\xi| d\xi \Big] A_{im} = \\
\sum_{i=1}^{n} \Big[\int_0^1 G(\xi_c, \xi) R_{i,p}(\xi) \sum_{m=1}^{M} e^{ikd_{im} \cdot q(\xi)} |J_\xi| d\xi \Big] B_{im}.
\end{aligned}
\tag{2.21}
$$

Similar to the previous section, eq.(2.21) is written in the form:

$$\mathbf{Hu} = \mathbf{Gt}, \tag{2.22}$$

with

$$
\begin{aligned}
\mathbf{H}_{ci} &= c(\xi_c) R_{i,p}(\xi_c) \sum_{m=1}^{M} e^{ikd_{im} \cdot q(\xi_c)} + \int_0^1 \frac{\partial G(\xi_c, \xi)}{\partial n} R_{i,p}(\xi) \sum_{m=1}^{M} e^{ikd_{im} \cdot q(\xi)} |J_\xi| d\xi, \\
\mathbf{G}_{ci} &= \int_0^1 G(\xi_c, \xi) R_{i,p}(\xi) \sum_{m=1}^{M} e^{ikd_{im} \cdot q(\xi)} |J_\xi| d\xi,
\end{aligned}
\tag{2.23}
$$

and subsequently re-arranged in the linear system for the unknown control variables. The number of unknowns is nM, therefore the $n-1$ collocation points defined by the Greville abscissae defined in eq.(2.17) are no longer sufficient. In this study, $(n-1)M$ collocation points are equally spaced along the parametric interval $[0,1]$. The expansion of the Hankel function of order zero includes only a weakly singular logarithmic kernel with other non-singular kernels. On the contrary, the Hankel function of order one - existing in the normal derivative of the same function of order zero - has no singular kernels [40, 63]. Further to the Gauss quadrature scheme in this chapter, 6 Gauss points with 4 uniform sub-divisions for each knot span are used for the integration of non-singular kernels, while the method of Telles is implemented to treat the weakly singular kernel with the same scheme used for application of Gauss quadrature [109]. This is the same conclusion derived in [22], where more Gauss quadrature points were proposed in order to overcome the ill-conditioning problem caused by the enrichment process.

2.6 Description of the structural shape optimization problem

2.6.1 Structural Shape Optimization Problem in BEM

The fundamental idea of any optimization problem is to minimize a defined objective function $F(x)$ of a design variable x, while satisfying certain constrains. In the proposed structural shape optimization problem in the framework of BEM, a set of NURBS control points is chosen as design optimization variables in addition to their role as control variables in both of the shape and analysis models. This permits a flexible connection between the mentioned three models during the iterations of the optimization process.

2.6.2 Particle Swarm Optimization (PSO) algorithm

Particle Swarm Optimization (PSO) as a gradient-free optimization method is a simple method which does not require any sensitivity analysis. This is considered as an advantage over gradient-based methods. However, it suffers from slower convergence. In this section, the main objective function is defined and explained. Additional two behavioural constraints; h_k and g_l are defined as follows:

$$
\begin{aligned}
&h_k(x) = 0, \ k = 1, 2, ..., n_k \text{ number of equality constraints,} \\
&g_l(x) \leq 0, \ l = 1, 2, ..., n_l \text{ number of inequality constraints.}
\end{aligned}
\tag{2.24}
$$

The upper and the lower bounds of the i-th design variable; $x_L(i)$ and $x_U(i)$ respectively, are constrained as follows:

$$x_L(i) \leq x(i) \leq x_U(i), \ i = 1, 2, ..., n_{dv} \text{ number of design variables.} \tag{2.25}$$

In order to start PSO algorithm, random initial population particles $x^{(0)}$ with population size of n_p particles and their corresponding velocities $v^{(0)}$ are generated as follows:

$$x^{(0)} = x^{(0)}(i,j) = x_L(i) + rand_j \times (x_U(i) - x_L(i)),$$
$$v^{(0)} = v^{(0)}(i,j) = rand_j \times (x_U(i) - x_L(i)), i = 1, 2, \cdots, n_{dv} \ and \ j = 1, 2, \cdots, n_p, \tag{2.26}$$

where $rand_j$ refers to a random number from 0 to 1 for each particle j [69, 70]. The updated particle $x^{(k+1)}$ and velocity $v^{(k+1)}$ are defined using their current values in the kth iteration x^k and v^k as follows:

$$v^{k+1} = v^{k+1}(i,j) = wv^k(i,j) + c_1 \times rand_j \times (pbest_j^k - x^k(i,j)) + c_2 \times rand_j \times (gbest_j^k - x^k(i,j)),$$
$$x^{k+1} = x^{k+1}(i,j) = x^k(i,j) + v^{k+1}(i,j), \tag{2.27}$$

where w is the inertia weight parameter, c_1 and c_2 are acceleration parameters. $pbest_j^k$ is the best particle location of the j-th particle in k-th iteration, and $gbest_j^k$ is the best location of the j-th particle defined by the lowest value of the fitness function until the k-th iteration. The fitness function is defined as follows:

$$\text{Fitness} = F(x) + \eta \times \max(g_l, 0) + \eta' \times |h_k|, \tag{2.28}$$

where $F(x)$ is the objective function, h_k and g_l are the equality and inequality constraints respectively and η and η' are the penalty factors. In this thesis, the PSO parameters are chosen similarly to [20, 21, 28] as follows: $w = 0.6$, $c_1 = 0.5$, and $c_2 = 0.6$. In order to initialize the parameters, the maximum number of iterations $N_1 = 100$ is defined, while the Number of Consecutive Iterations (the population size) N_2 is chosen for each problem separately depending on the number of design variables. The penalty factor η is chosen to be 10^7 while the equality constraints are not considered. The procedure of implementing the PSO is demonstrated in detail in [69].

2.7 Numerical results

Three numerical examples are presented in order to demonstrate the performance of the proposed approach. In the first example, a comparison of the conventional IGABEM and XIBEM in terms of the relative error in L_2-norm per degree of freedom is shown. Then, the shape optimization of both the vertical infinite noise barrier and the horn problems is presented. The optimized shapes obtained from both conventional IGABEM and XIBEM using PSO are compared against already published optimized shapes obtained with sensitivity analysis optimization methods and genetic algorithms.

2.7.1 The duct problem (wave propagation in a duct with rigid walls)

In order to validate the proposed algorithm for both conventional IGABEM and XIBEM that is used in the optimization process shown in the forthcoming sections, the duct problem in figure 2.2 is considered. The following boundary-value problem is solved [110]:

$$\triangle u + k^2 u = 0 \quad in \; \Omega_b = [0, 2] \times [0, 1], \tag{2.29}$$

$$\frac{\partial u}{\partial n} = \cos(m\pi y) \qquad on \; x = 0, \tag{2.30}$$

$$\frac{\partial u}{\partial n} + iku = 0 \qquad on \; x = 2, \tag{2.31}$$

$$\frac{\partial u}{\partial n} = 0 \qquad on \; y = 0, 1, \tag{2.32}$$

where m is the mode number. The lower and upper walls are perfectly rigid, i.e. the normal derivative of the acoustic pressure vanishes on these boundaries. A non-homogeneous boundary condition is applied on the inlet boundary $(x = 0)$ and an absorbing boundary condition is set on the outlet boundary $(x = 2)$. The analytical solution is defined by the following equation:

$$u^{ex}(x, y) = \cos(m\pi y)(A_1 e^{-ik_x x} + A_2 e^{ik_x x}), \tag{2.33}$$

where $k_x = \sqrt{k^2 - (m\,\pi)^2}$ and coefficients A_1 and A_2 are defined by:
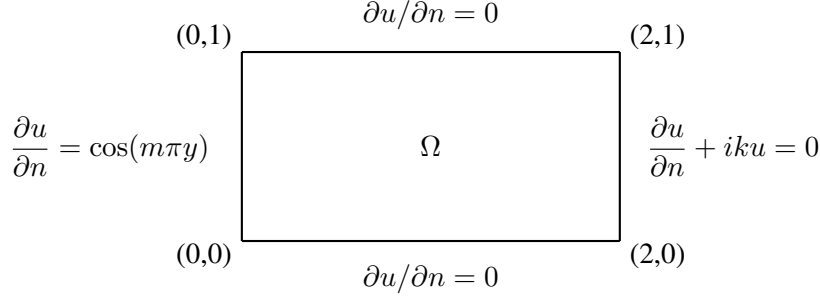
Figure 2.2: A rectangular duct domain with the boundary conditions.

$$i \begin{pmatrix} k_x & -k_x \\ (k - k_x)e^{-2ik_x} & (k + k_x)e^{2ik_x} \end{pmatrix} \begin{pmatrix} A_1 \\ A_2 \end{pmatrix} = \begin{pmatrix} 1 \\ 0 \end{pmatrix}. \tag{2.34}$$

The relative L_2 error norm of numerical solution u^{num} is defined as follows:

$$e_{L_2} \equiv \frac{||u^{ex} - u^{num}||}{||u^{ex}||} = \sqrt{\frac{\int_\Gamma (u^{num} - u^{ex})^T (u^{num} - u^{ex})d\Gamma}{\int_\Gamma u^{exT} u^{ex} d\Gamma}}. \tag{2.35}$$

Figures 2.3-2.5 show the variation of e_{L_2} as a function of degrees of freedom per wavelength. In XIBEM, 4 plane waves are used, $k = 10, 40, 80$, $m = 2$ and the polynomial degree $p = 2$.

It can be seen that, the benefit of XIBEM appears only for high wavenumber; $k = 40, 80$ with a moderate number of plane waves and the higher accuracy can be achieved with fewer DOFs/wavelength, while in low wavenumber case, $k = 10$, the conventional IGABEM results in smaller errors for the same number of DOFs. The slower convergence of XIBEM may be due to the ill-conditioning that appears when very fine meshes are used as noted also in [22], although the truncated singular value decomposition (SVD) is used to solve the linear system of equations. However, the improved accuracy of XIBEM for relatively coarser meshes make the solution of optimization problems more feasible.

2.7.2 Shape optimization analysis for an infinite vertical noise barrier

The noise barriers are built in front of noise sources to protect an area from the noise pollution. In this section, a vertical rigid noise barrier with an infinite out-of-plane length and a variable shape of the front face is modelled. The objective of the design is to minimize the acoustic pressure in the protected area behind the barrier. A line sound source is located in front of the barrier at position $(0, 1)$. The barrier is

21
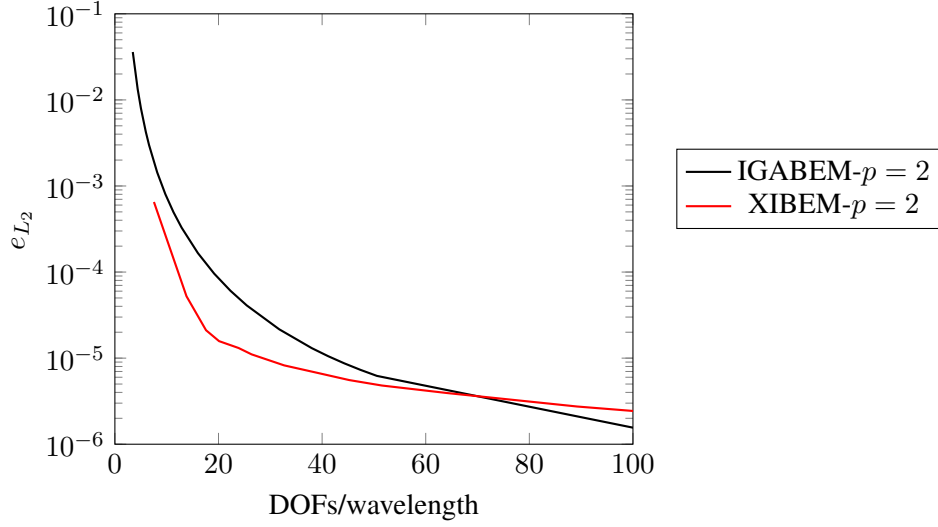
Figure 2.3: L_2 error norm of conventional IGABEM and XIBEM for k=10.
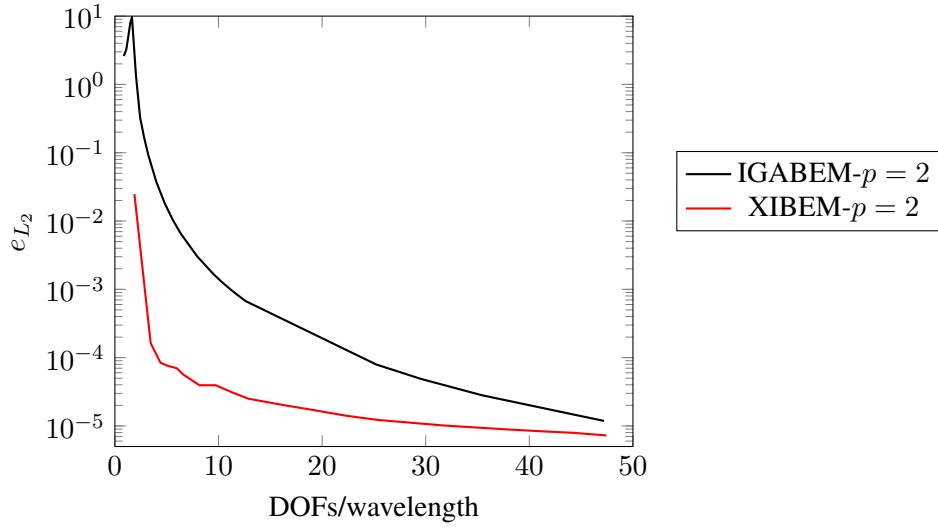
Figure 2.4: L_2 error norm of conventional IGABEM and XIBEM for k=40.

located at $(5, 0)$, the height of the barrier is 3m, the initial thickness is 0.2m (figure 2.6). For this problem, the BIE given by eq.(2.6) is modified to add the source term function as follows:

$$c(\mathbf{x})u(\mathbf{x}) + \int_\Gamma \frac{\partial G(\mathbf{x}, \mathbf{y})}{\partial n} u(\mathbf{y}) d\Gamma(\mathbf{y}) = \int_\Gamma G(\mathbf{x}, \mathbf{y}) \frac{\partial u(\mathbf{y})}{\partial n} d\Gamma(\mathbf{y}) + G(\mathbf{x}, \mathbf{x_0}), \mathbf{x}, \mathbf{y} \in \Gamma, \mathbf{x_0} \notin \Gamma, \quad (2.36)$$
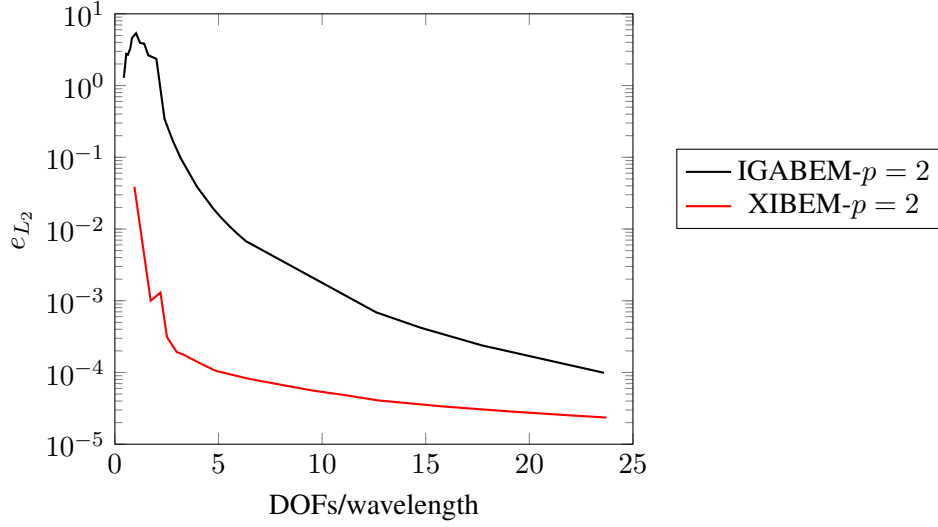
Figure 2.5: L_2 error norm of conventional IGABEM and XIBEM for k=80.
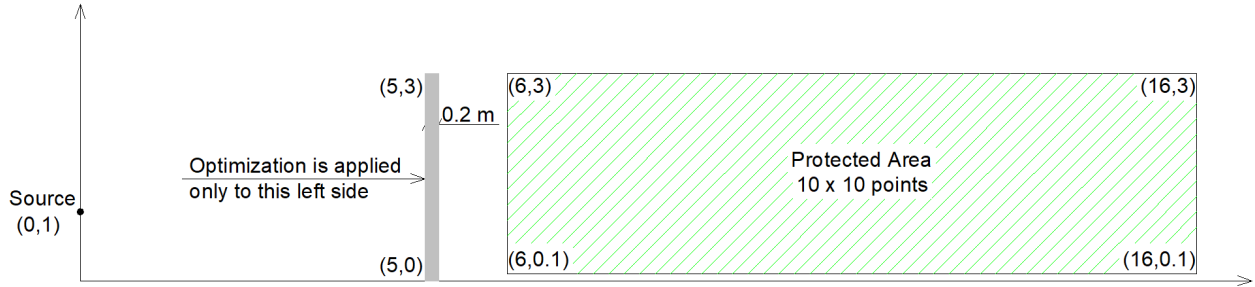
Figure 2.6: The vertical noise barrier problem.

where $\mathbf{x_0} = (0, 1)$ is the location of the sound source. The Green's function is also modified to include the symmetry effect as follows:

$$G(\mathbf{x}, \mathbf{y}) = \frac{i}{4}[H_0^1(kr) - H_0^1(kr')],\tag{2.37}$$

in which $r' = |\mathbf{x} - \overline{\mathbf{y}}|$ is the distance from point $\mathbf{x}$ to point $\overline{\mathbf{y}} = (y_1, -y_2)$ (image of $\mathbf{y} = (y_1, y_2)$) [111].

In order to minimize the sound pressure on the protected area, the shape of the left side of the barrier is optimized according to minimum objective function:

$$\Pi_\rho = \min\ \overline{u_f}u_f,\tag{2.38}$$

23

where u_f is the sound pressure vector at the 10×10 field points located in the protected area as shown in figure 2.6, $\overline{u_f}$ is the complex conjugate vector of u_f [63]. Furthermore, the area of the optimized design is restricted not to be more than the initial area $A_o = 0.6m^2$. Therefore, the fitness function is taken as:

$$\text{Fitness} = \Pi_\rho + \eta \times \max(\text{Updated Area} - 0.6, 0). \tag{2.39}$$

In the optimization problem, the design variables are x-coordinates of the control points (the top and the bottom points remain fixed). The initial value of these design variables are 5.0, while the lower and the upper limits are considered as 4.9 and 5.1 respectively. Since including y-coordinates as free design variables in this optimization case has minimal impact on both the final optimized shape and the value of the objective function, it is sufficient to optimize only the x-coordinates. The used polynomial degree is $p = 2$. The optimized shapes and objective function values obtained from conventional IGABEM and XIBEM using PSO are further compared to those obtained from the fast multipole conventional IGABEM using shape sensitivity analysis performed in [63].

Figure 2.7 demonstrates the optimized shapes for a single frequency 400 Hz (with sound speed $343m/s$ and wavenumber k=7.32733) using 5, 10, 15 and 20 design variables respectively. Figures 2.8 and 2.9 show the iteration process for the fitness function and the area respectively. It can be seen that, the optimized shapes and the objective function values obtained using 5, 10 and 15 design variables from IGABEM and XIBEM with PSO are in a good agreement with those obtained in [63], while all shapes for $N = 20$ slightly differ from each other. The results are further compared with [63] in table 2.1 in terms of the values of the objective function, area and the number of iterations. Table 2.1 also shows all parameters used in the optimization process, i.e. the number of elements per wavelength along the optimized part and kh/p where h is the maximum element size. In XIBEM, 4 plane waves are used. It can be seen that, XIBEM can usually be used with coarser meshes, however, in terms of total degrees of freedom and overall computational time, no significant advantage in using XIBEM was seen.

To demonstrate the performance of the method for different frequencies and its sensitivity to the number of consecutive iterations in PSO, figure 2.10 illustrates the optimized shapes for single frequencies; 100 Hz ($k = 1.838$) and 1000 Hz ($k = 18.3183$) respectively using 15 design variables. The results for $f = 1000$Hz show two cases: In case 1, the number of consecutive iterations $N_2 = 60$, while in case 2 $N_2 = 100$. The

24
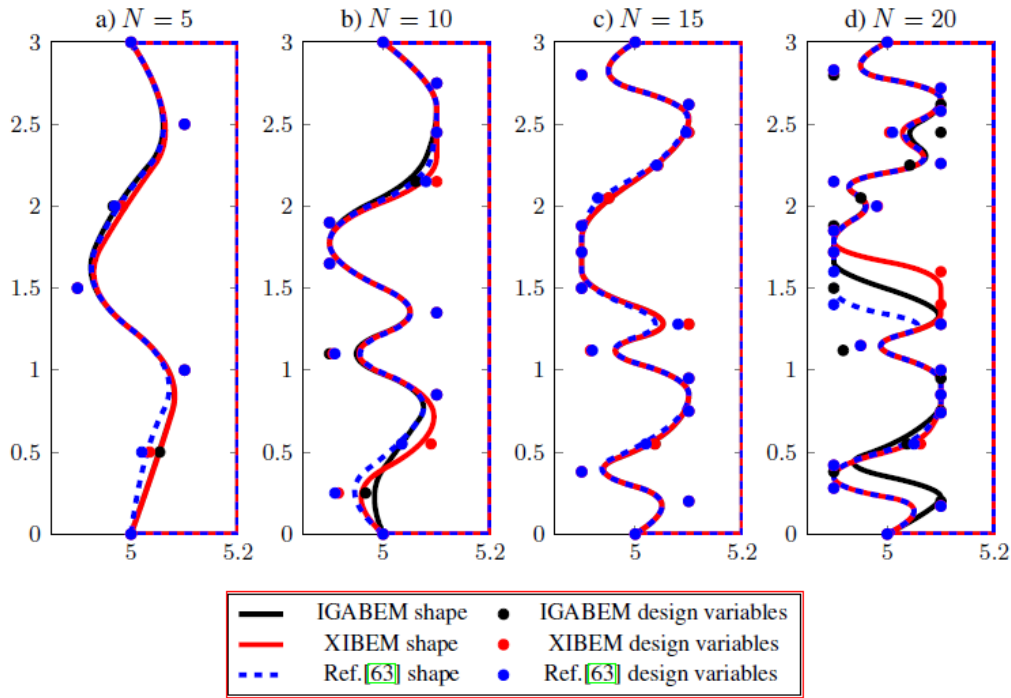
Figure 2.7: Optimized shape of the noise barrier for frequency=400 Hz.
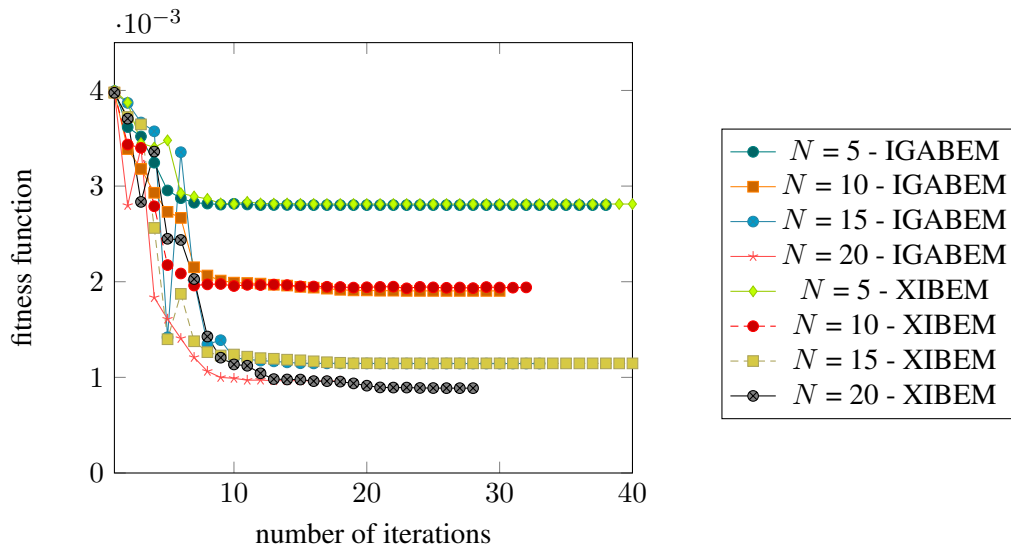
Figure 2.8: Variation of the fitness function during the optimization process, $f = 400$Hz.

corresponding convergence plots for the objective function and the area are shown in figures 2.11 and 2.12, respectively. As it can be seen from the figures and the results, shown in table 2.2, increasing N_2 leads to smaller values of the objective function, however, the total simulation time becomes unfeasible. Moreover,
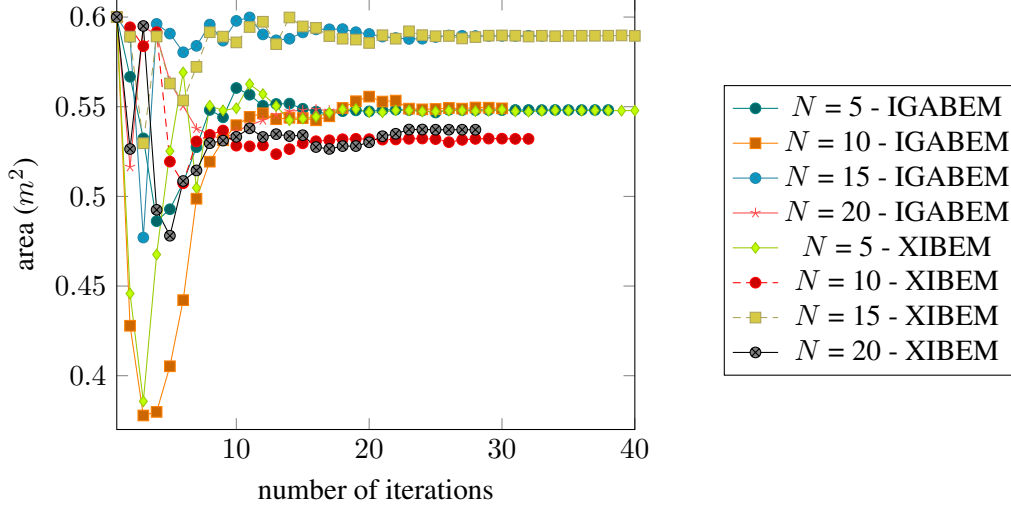
Figure 2.9: Variation of the area during the optimization process, $f = 400$Hz.

		Ref.[63]	Conventional IGABEM	XIBEM
5 Variables - Frequency=400 Hz	Objective Function	24.2x10E-4	28.01x10E-4	28.12x10E-4
	Area (m^2)	0.56	0.55	0.55
	no of Iterations	11	9	9
	N2 - Number of Consecutive Iterations for PSO	-	40	40
	kh/p along the Optimized Part	-	0.73	1.1
	no of Elements/Wavelength along the Optimized Part	-	4.3	2.9
	Total DOFs	-	40 NURBS Basis Functions	28 NURBS Basis Functions x 4 Plane Waves
10 Variables - Frequency=400 Hz	Objective Function	15.7x10E-4	19.04x10E-4	19.41x10E-4
	Area (m^2)	0.56	0.55	0.53
	no of Iterations	12	18	7
	N2 - Number of Consecutive Iterations for PSO	-	60	60
	kh/p along the Optimized Part	-	0.22	0.37
	no of Elements/Wavelength along the Optimized Part	-	14.30	8.57
	Total DOFs	-	114 NURBS Basis Functions	70 NURBS Basis Functions x 4 Plane Waves
15 Variables - Frequency=400 Hz	Objective Function	10.5x10E-4	11.45x10E-4	11.46x10E-4
	Area (m^2)	0.6	0.59	0.59
	no of Iterations	28	15	19
	N2 - Number of Consecutive Iterations for PSO	-	60	60
	kh/p along the Optimized Part	-	0.147	0.244
	no of Elements/Wavelength along the Optimized Part	-	21.44	12.86
	Total DOFs	-	164 NURBS Basis Functions	100 NURBS Basis Functions x 4 Plane Waves
20 Variables - Frequency=400 Hz	Objective Function	7x10E-4	9.63x10E-4	8.87x10E-4
	Area (m^2)	0.6	0.55	0.54
	no of Iterations	54	13	13
	N2 - Number of Consecutive Iterations for PSO	-	60	60
	kh/p along the Optimized Part	-	0.18	0.18
	no of Elements/Wavelength along the Optimized Part	-	17.15	17.15
	Total DOFs	-	130 NURBS Basis Functions	130 NURBS Basis Functions x 4 Plane Waves

Table 2.1: Comparative results for frequency=400 Hz.

optimal value of N_2 seems to grow with increasing frequency, making PSO optimization even more time-consuming.   The next study is concerned with optimization for a frequency range. In figure 2.13 the optimized shapes are shown for the range of $(\omega_1 - \omega_2)$: from 500 to 1000 Hz (wavenumber range from k=
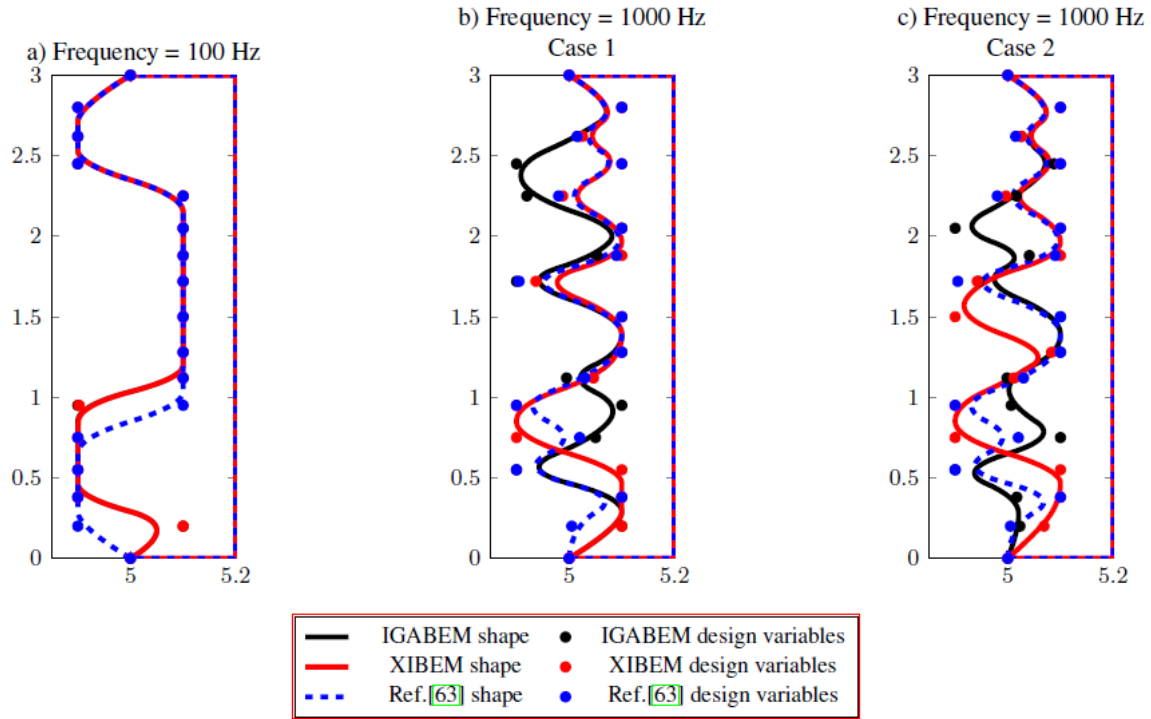
Figure 2.10: Optimized shape of the noise barrier for different frequencies.
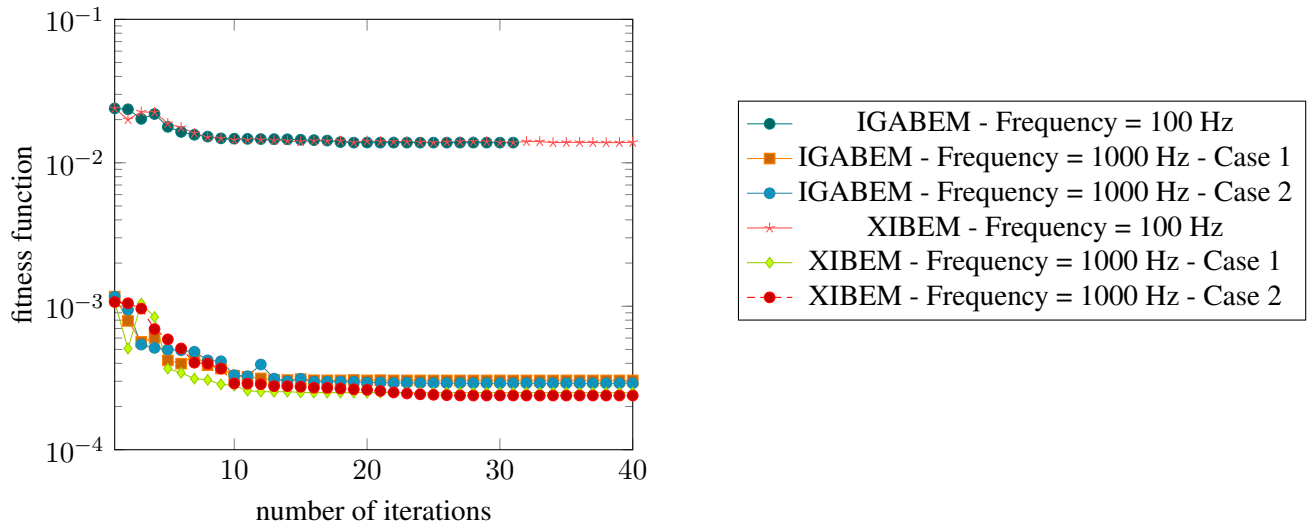
Figure 2.11: Iteration process for different frequencies; fitness function.

9.1592 to 18.3183) and from 200 to 500 Hz (wavenumber range from k= 3.6637 to 9.1592), using 15 design
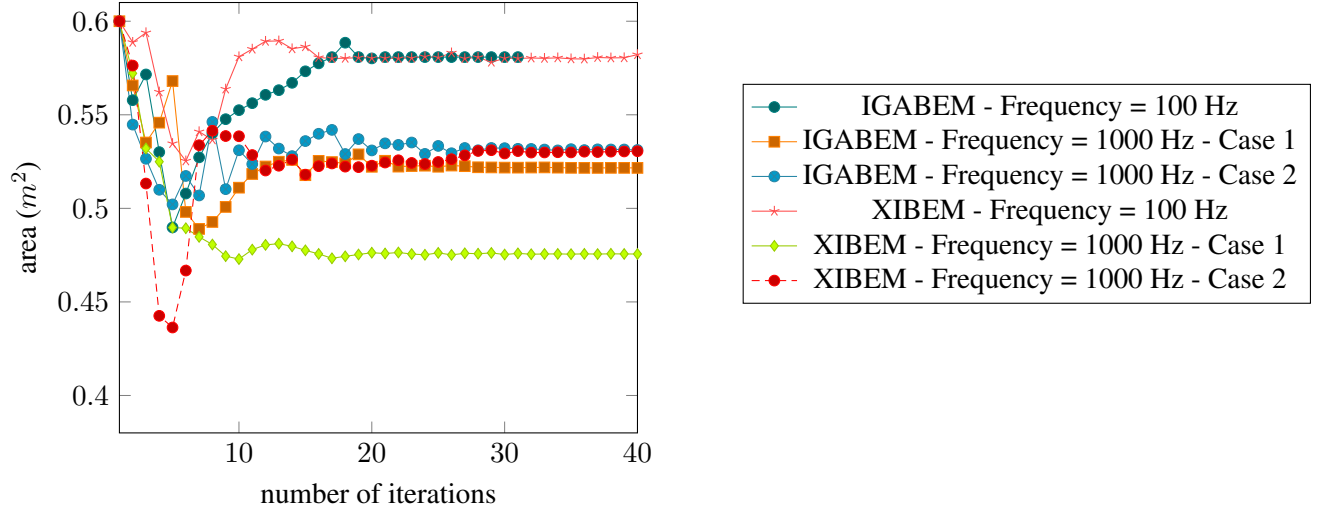
Figure 2.12: Iteration process for different frequencies; the area.

		Conventional IGABEM	XIBEM
15 Variables - Frequency=100 Hz	Objective Function	138.21x10E-4	138.23x10E-4
	Area (m^2)	0.58	0.58
	no of Iterations	19	19
	N2 - Number of Consecutive Iterations for PSO	60	60
	kh/p along the Optimized Part	0.04	0.06
	no of Elements/Wavelength along the Optimized Part	85.75	51.45
	Total DOFs	164 NURBS Basis Functions	100 NURBS Basis Functions x 4 Plane Waves
15 Variables - Frequency=1000 Hz Case 1	Objective Function	3.04x10E-4	2.50x10E-4
	Area (m^2)	0.52	0.48
	no of Iterations	16	15
	N2 - Number of Consecutive Iterations for PSO	60	60
	kh/p along the Optimized Part	0.37	0.61
	no of Elements/Wavelength along the Optimized Part	8.58	5.15
	Total DOFs	164 NURBS Basis Functions	100 NURBS Basis Functions x 4 Plane Waves
15 Variables - Frequency=1000 Hz Case 2	Objective Function	2.91x10E-4	2.39x10E-4
	Area (m^2)	0.53	0.53
	no of Iterations	28	27
	N2 - Number of Consecutive Iterations for PSO	100	100
	kh/p along the Optimized Part	0.37	0.61
	no of Elements/Wavelength along the Optimized Part	8.58	5.15
	Total DOFs	164 NURBS Basis Functions	100 NURBS Basis Functions x 4 Plane Waves

Table 2.2: Comparative results for two different frequencies with 15 design variables.

variables with an average objective function:

$$\Pi = \min \ \frac{1}{\omega_2 - \omega_1} \int_{\omega_1}^{\omega_2} \Pi_\rho d\omega. \tag{2.40}$$
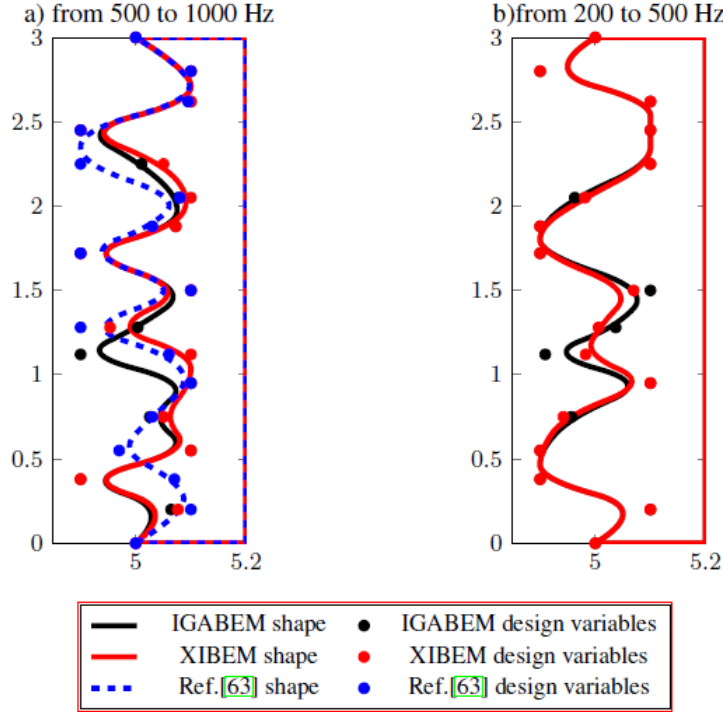
Figure 2.13: Optimized shape of the noise barrier for frequency range cases.

This function is integrated using 4 Gauss quadrature points.

Similar to previous comparisons, figure 2.14 demonstrates the iteration process of these optimization cases against the fitness function while figure 2.15 presents the same against the area. The detailed results are given in table 2.3. A conclusion that can be derived is that, the solution is not unique in many cases and different optimal geometries can be obtained. This is applicable to the presented cases for frequency of 400 Hz with $N = 20$, for frequency of 1000 Hz and for the frequency range cases. The shapes giving the minimum objective function values are presented. This conclusion was previously reached as well in [64] and [112] for the study of the horn shape optimization.

2.7.3 Shape optimization analysis for an acoustic horn problem

In order to design the acoustic horn with an effective transmission of the incoming wave energy and powerful distribution of this energy to the far field, the horn shape is optimized. The horn in an infinite domain with planar symmetry shown in figure 2.16 is considered. This problem was previously studied in [64, 113]. The computational domain is denoted by Ω (a semi-circle of radius R_Ω), with absorbing boundary conditions

29
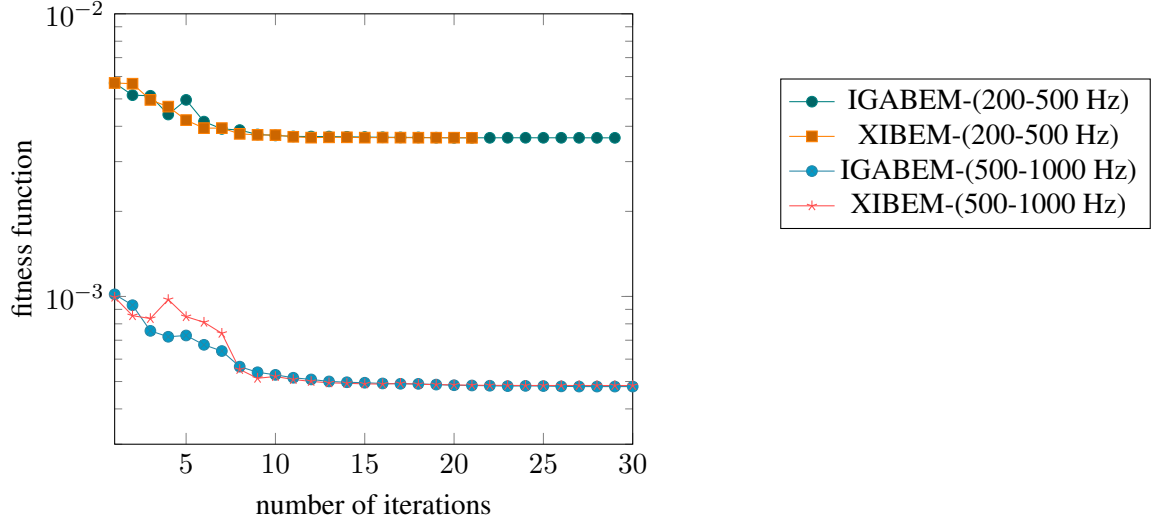
Figure 2.14: Iteration process for optimization cases of frequency range; fitness function.
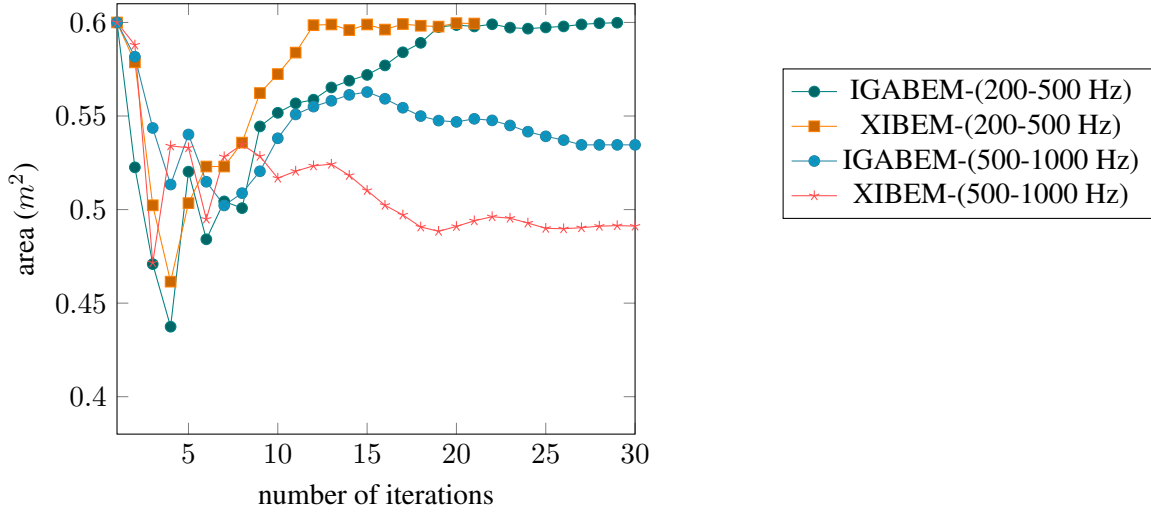
Figure 2.15: Iteration process for optimization cases of frequency range; the area.

prescribed on its outer boundary Γ_{out}. Part of the boundary, denoted by Γ_{in}, refers to the inlet for the in-going wave. The horn boundary is denoted by Γ_{rigid}. To decrease the computational effort, the symmetry of the solution is assumed along $\Gamma_{sym.}$. The boundary value problem is defined as follows:

$$\Delta u + k^2 u = 0 \qquad \qquad \text{in } \Omega, \qquad \qquad (2.41)$$

$$\frac{\partial u}{\partial n} + \left(ik + \frac{1}{2R_\Omega} \right) u = 0 \qquad \text{on } \Gamma_{out}, \qquad (2.42)$$

		Conventional IGABEM	XIBEM
15 Variables - Frequency Range of 200 to 500 Hz	Objective Function	36.41x10E-4	36.41x10E-4
	Area (m^2)	0.6	0.6
	no of Iterations	11	11
	N2 - Number of Consecutive Iterations for PSO	60	100
	kh/p along the Optimized Part for max. Frequency	0.18	0.31
	no of Elements/Wavelength along the Optimized Part for max. Frequency	17.15	10.29
	Total DOFs	164 NURBS Basis Functions	100 NURBS Basis Functions x 4 Plane Waves
15 Variables - Frequency Range of 500 to 1000 Hz	Objective Function	4.80x10E-4	4.84x10E-4
	Area (m^2)	0.53	0.49
	no of Iterations	16	13
	N2 - Number of Consecutive Iterations for PSO	100	60
	kh/p along the Optimized Part for max. Frequency	0.37	0.61
	no of Elements/Wavelength along the Optimized Part for max. Frequency	8.58	5.15
	Total DOFs	164 NURBS Basis Functions	100 NURBS Basis Functions x 4 Plane Waves

Table 2.3: Comparative results for cases of frequency range.
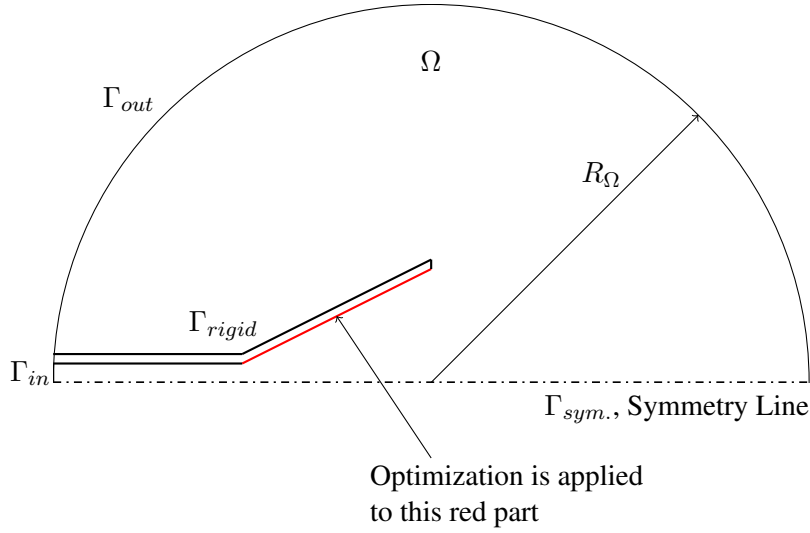
Figure 2.16: The horn problem domain.

$$\frac{\partial u}{\partial n} + iku = 2ikA_m \qquad \text{on } \Gamma_{in}, \qquad (2.43)$$

$$\frac{\partial u}{\partial n} = 0 \qquad \text{on } \Gamma_{rigid} \cup \Gamma_{sym.}, \qquad (2.44)$$

where A_m is the amplitude of the incident wave in-going on Γ_{in}.

In order to include the boundary conditions, the BIE eq.(2.6) is modified as follows:

$$c(\mathbf{x})u(\mathbf{x}) + \int_\Gamma \frac{\partial G(\mathbf{x}, \mathbf{y})}{\partial n} u(\mathbf{y}) d\Gamma(\mathbf{y}) + ik \int_{\Gamma_{in}} G(\mathbf{x}, \mathbf{y}) u(\mathbf{y}) d\Gamma(\mathbf{y}) +$$
$$(ik + \frac{1}{2R_\Omega}) \int_{\Gamma_{out}} G(\mathbf{x}, \mathbf{y}) u(\mathbf{y}) d\Gamma(\mathbf{y}) = 2ikA_m \int_{\Gamma_{in}} G(\mathbf{x}, \mathbf{y}) d\Gamma(\mathbf{y}), \mathbf{x}, \mathbf{y} \in \Gamma. \qquad (2.45)$$

The optimization problem consists in minimizing the wave reflection coefficient $R = B_m/A_m$ on Γ_{in}, in which $B_m = |u_{in} - A_m|$ is the reflected wave amplitude and u_{in} is the computed acoustic pressure along Γ_{in} defined as $u_{in} = \frac{1}{a} \int_{\Gamma_{in}} u d\Gamma$ [64, 113]. Therefore the fitness function is defined in eq.(2.46):

$$Fitness = F(x) = \min R. \tag{2.46}$$

The portion of the horn boundary being optimized is shown by the red line in figure 2.16. The design variables are x and y coordinates of the control points. In figure 2.17 the initial position of the design control points, as well as their upper and lower bounds are given.

In figure 2.18 the dimensions of the horn boundaries are shown. The horn thickness is 2.5cm. Other parameters are set as: $A_m = 1$, $R_\Omega = 1$m and the polynomial degree $p = 2$.

Figure 2.19 illustrates the reflection spectra of the initial shape shown in figure 2.18 using both IGABEM and XIBEM compared to the same spectrum presented in [113] using FEM. It can be seen that, all spectra are in good agreement except the first portion of XIBEM representing lower frequencies to 150 Hz. That can be related to the remark for the duct problem at the end of section 2.7.1. The obtained results are compared with the solutions reported in [64] and [112]. In [112], the same problem was solved using smoothing Hermite polynomials with finite element method (FEM) and genetic algorithm (GA). In [64], quasi-Newton algorithm and sensitivity analysis with FEM was performed.

Figure 2.20 demonstrates the optimized shapes for different single frequencies=280, 550, 780 and 1000 Hz with sound speed $345m/s$ and wavenumber k=5.09940, 10.01667, 14.20546 and 18.21213 respectively using one control point (i.e. 2 design variables). These shapes are further compared to those obtained in [112]. Note that, in [112] the boundary was optimized using only 1 design variable maintaining the curve smoothness along the whole length of the optimized part. Figure 2.21 shows the variation of the reflection coefficient R during the optimization process. Figure 2.22 presents the reflection spectra for the initial and optimized horn shapes. It can be seen that, both conventional IGABEM and XIBEM with PSO give similar optimized shapes, and similar reflection values in the optimization process. In XIBEM slightly coarser meshes were used along with 4 plane waves in the enrichment. The full results are shown in table 2.4.

In the next study, the optimization process using 4 design variables (i.e. 2 control points) was conducted.
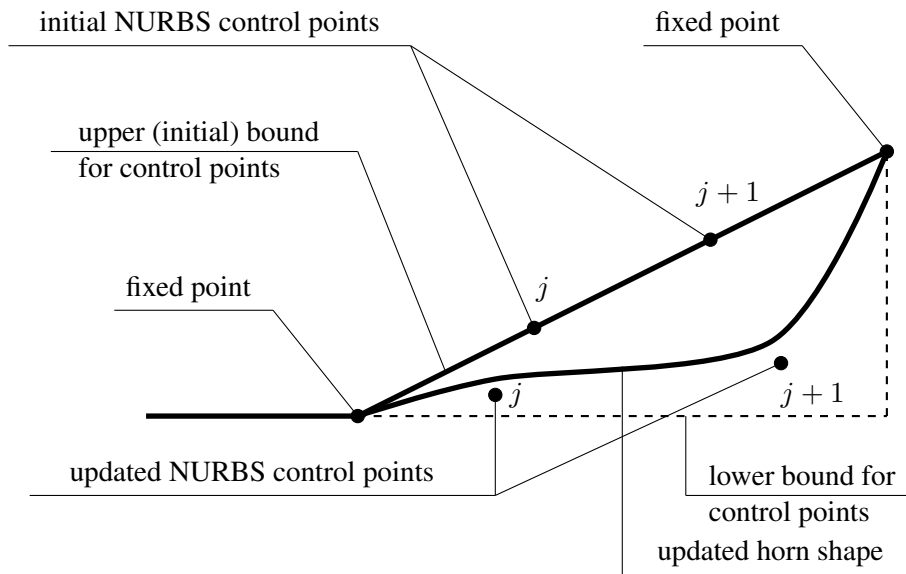
Figure 2.17: Arrangement of control points along the optimized part of the horn problem.
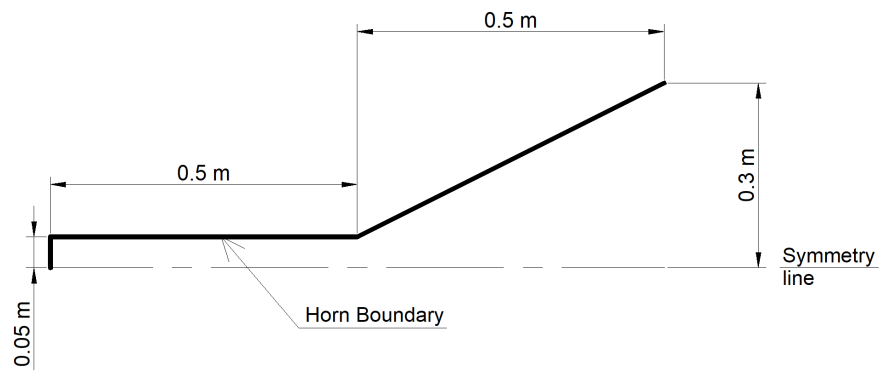
Figure 2.18: Horn dimensions.
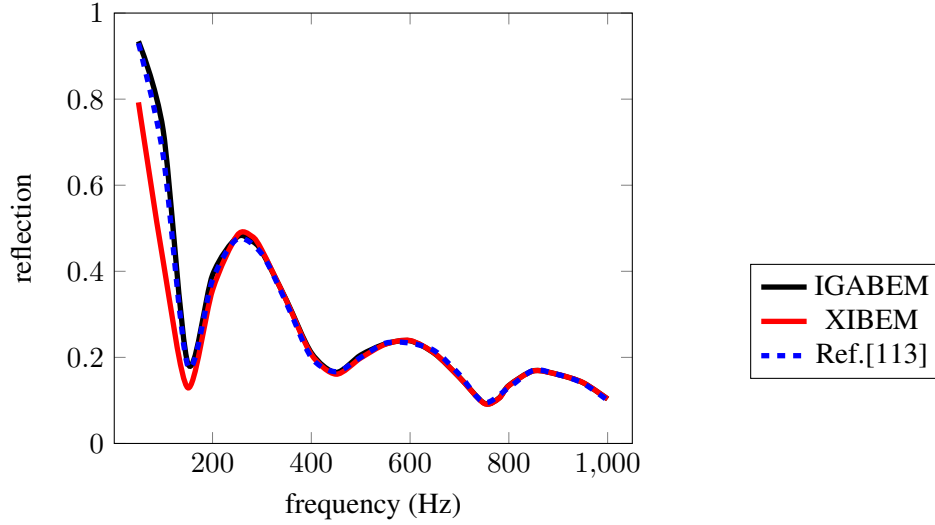
Figure 2.19: Reflection Spectra of the initial shape.

		Ref.[112]	Conventional IGABEM	XIBEM
Frequency=280 Hz	Reflection	3.0x10E-1	2.85x10E-2	2.95x10E-2
	no of Iterations	-	12	13
	N2 - Number of Consecutive Iterations for PSO	-	40	40
	kh/p along the Optimized Part	0.06	0.1	0.16
	no of Elements/Wavelength along the Optimized Part	49.3	33.1	19.8
	Total DOFs	-	144 NURBS Basis Functions	90 NURBS Basis Functions x 4 Plane Waves
Frequency=550 Hz	Reflection	2.42x10E-2	3.24x10E-2	3.47x10E-2
	no of Iterations	-	8	10
	N2 - Number of Consecutive Iterations for PSO	-	40	40
	kh/p along the Optimized Part	0.13	0.11	0.19
	no of Elements/Wavelength along the Optimized Part	25.1	28.1	16.8
	Total DOFs	-	234 NURBS Basis Functions	144 NURBS Basis Functions x 4 Plane Waves
Frequency=780 Hz	Reflection	6.71x10E-2	1.93x10E-3	3.09x10E-3
	no of Iterations	-	27	26
	N2 - Number of Consecutive Iterations for PSO	-	40	40
	kh/p along the Optimized Part	0.18	0.1	0.17
	no of Elements/Wavelength along the Optimized Part	17.7	31.6	19
	Total DOFs	-	369 NURBS Basis Functions	225 NURBS Basis Functions x 4 Plane Waves
Frequency=1000 Hz	Reflection	1.27x10E-2	3.33x10E-3	1.17x10E-3
	no of Iterations	-	14	20
	N2 - Number of Consecutive Iterations for PSO	-	40	40
	kh/p along the Optimized Part	0.23	0.09	0.15
	no of Elements/Wavelength along the Optimized Part	13.8	33.9	20.4
	Total DOFs	-	504 NURBS Basis Functions	306 NURBS Basis Functions x 4 Plane Waves

Table 2.4: Comparative results for the horn problem using 1 control point - 2 design variables.

Figure 2.23 illustrates the optimized shapes for different single frequencies=280, 400, 550 and 780 Hz with sound speed $345m/s$ and wavenumber k=5.09940, 7.28485, 10.01667 and 14.20546 respectively. These shapes are compared to those obtained from [112]. Note that, in [112] 3 design variables dividing the optimized part into 2 equal spans were used. In this study, both conventional IGABEM and XIBEM with
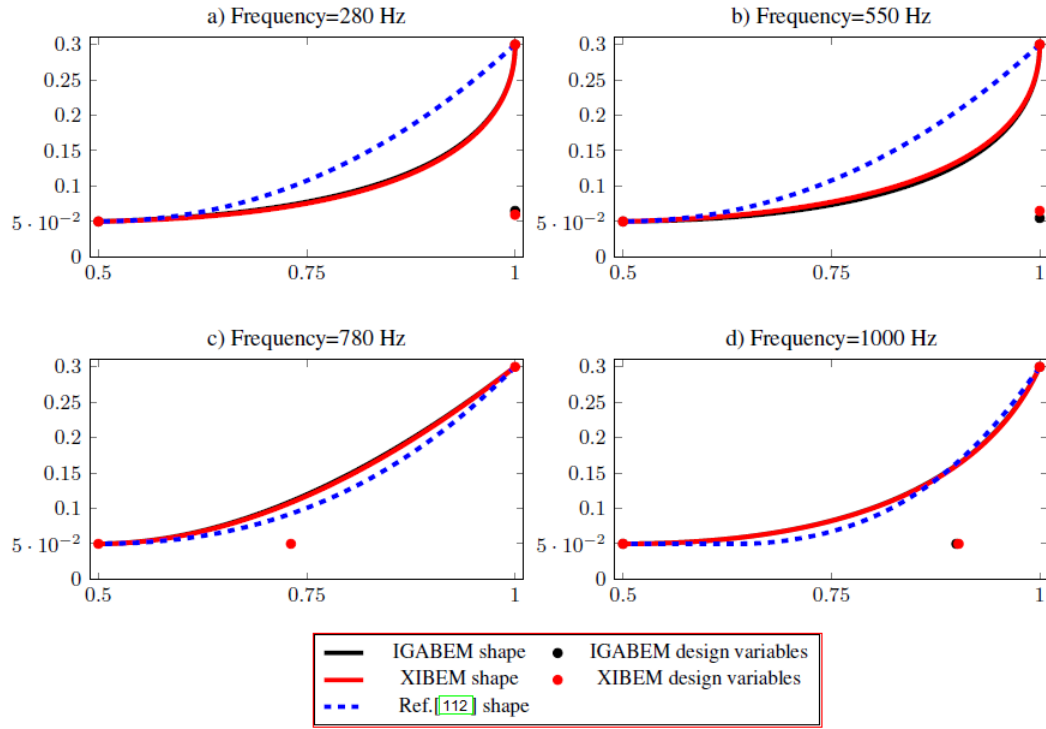
Figure 2.20: Optimized horn part using 1 control point - 2 design variables.
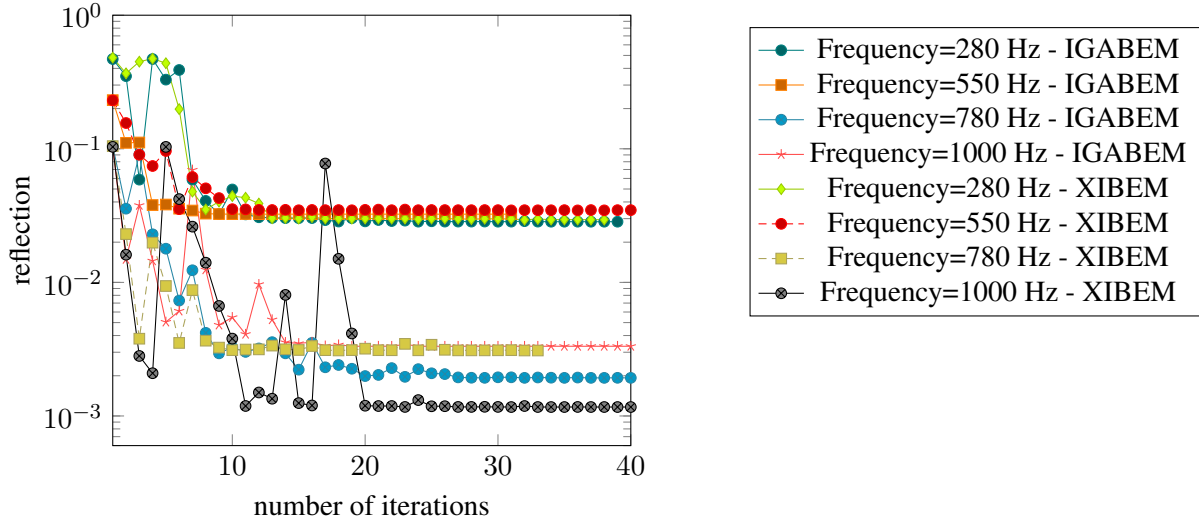
Figure 2.21: Iteration process against the reflection using 1 control point - 2 design variables.

PSO give close optimized shapes and quasi-identical reflection values as well. Slightly coarser meshes were used in XIBEM models. These curves are close to those obtained from [112] except in the case of frequency of 780 Hz. The full results are shown in table 2.5.
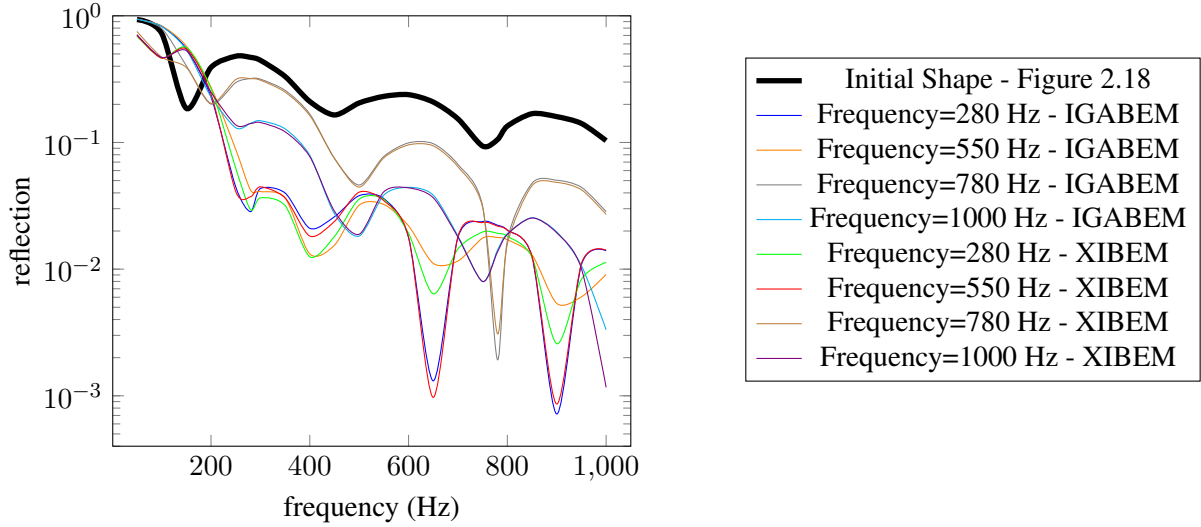
Figure 2.22: Reflection spectra for the optimized horns using 1 control point - 2 design variables.

		Ref.[64]	Ref.[112]	Conventional IGABEM	XIBEM
Frequency=280 Hz	Reflection	1.5x10E-4	2.36x10E-5	6.66x10E-4	2.61x10E-4
	N2 - Number of Consecutive Iterations for PSO	-	-	60	60
	kh/p along the Optimized Part	0.13	0.06	0.05	0.08
	no of Elements/Wavelength along the Optimized Part	24.6	49.3	66.1	39.7
	Total DOFs	-	-	159 NURBS Basis Functions	99 NURBS Basis Functions x 4 Plane Waves
Frequency=400 Hz	Reflection	3x10E-4	4.28x10E-5	5.83x10E-4	3.74x10E-4
	N2 - Number of Consecutive Iterations for PSO	-	-	60	60
	kh/p along the Optimized Part	0.18	0.09	0.05	0.08
	no of Elements/Wavelength along the Optimized Part	17.3	34.5	61.7	37
	Total DOFs	-	-	209 NURBS Basis Functions	129 NURBS Basis Functions x 4 Plane Waves
Frequency=550 Hz	Reflection	5.7x10E-4	1.35x10E-6	2.75x10E-4	1.14x10E-4
	N2 - Number of Consecutive Iterations for PSO	-	-	60	60
	kh/p along the Optimized Part	0.25	0.13	0.06	0.09
	no of Elements/Wavelength along the Optimized Part	12.5	25.1	56.1	33.7
	Total DOFs	-	-	259 NURBS Basis Functions	159 NURBS Basis Functions x 4 Plane Waves
Frequency=780 Hz	Reflection	-	3.91x10E-5	1.61x10E-4	1.34x10E-4
	N2 - Number of Consecutive Iterations for PSO	-	-	60	60
	kh/p along the Optimized Part	-	0.18	0.05	0.08
	no of Elements/Wavelength along the Optimized Part	-	17.7	63.3	38
	Total DOFs	-	-	409 NURBS Basis Functions	249 NURBS Basis Functions x 4 Plane Waves

Table 2.5: Comparative results for the horn problem using 2 control points - 4 design variables.

With reference again to figure 2.23 and table 2.5, another comparison is presented against the optimized smoothed shapes obtained from [64]. It can be seen that, all shapes are close and the reflection values are of the same order.

Another approach shown in figure 2.24 is to demonstrate the performance for frequency range of $(\omega_1 - \omega_2)$ which equal (350-450 Hz) (wavenumber range from k= 6.37425 to 8.19546) using the previous scheme of
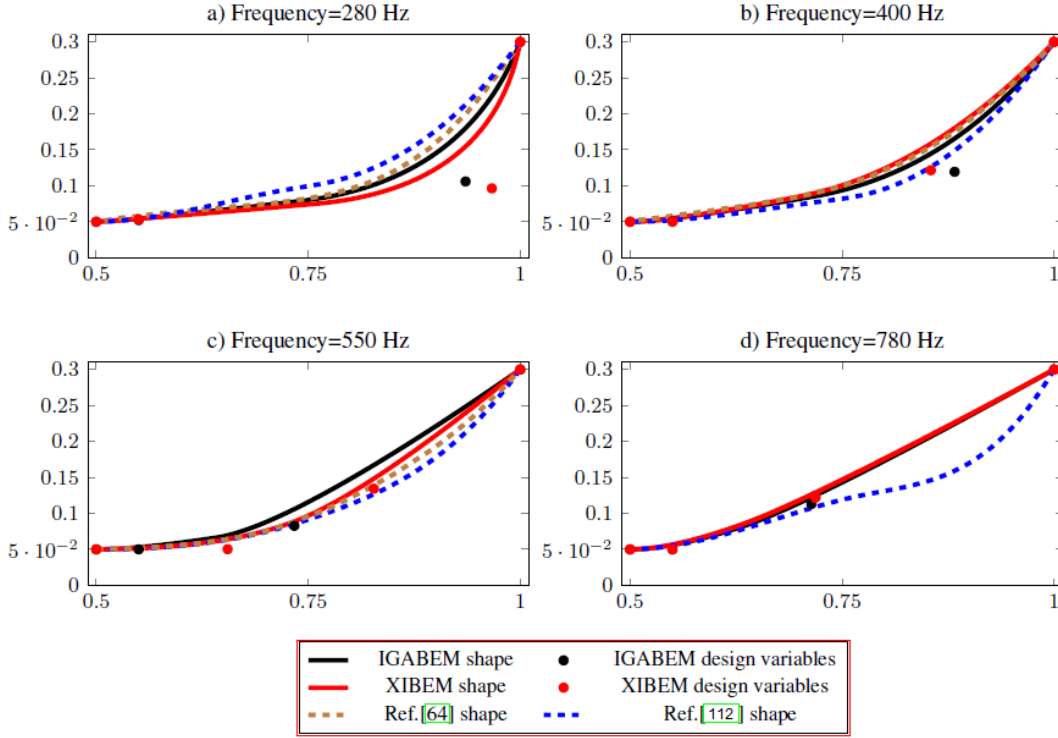
Figure 2.23: Optimized horn part using 2 control points - 4 design variables.

2 control points - 4 design variables with an average objective function:

$$\Pi = \min \frac{1}{\omega_2 - \omega_1} \int_{\omega_1}^{\omega_2} R \, d\omega. \tag{2.47}$$

This function is integrated using 4 Gauss quadrature points. Figure 2.24 shows also the smoothed and non-smoothed shapes presented in [64]. It can be seen that, the proposed shapes are similar to the smoothed shape presented in [64]. Figure 2.25 shows the variation of the reflection coefficient R during the optimization process. Figure 2.26 presents the reflection spectra for the initial and optimized horn shapes. These spectra are compared to the spectra presented in [64] for the corresponding optimization case. It can be seen from figure 2.25, XIBEM produces close spectrum to those spectra obtained from [64] with two minimum reflection values inside this frequency range. The full results are shown in table 2.6. Similar to the conclusion derived in the noise barrier example and in [64] and [112] as well, in some cases the solution may not be unique and different optimal geometries can be obtained. This is applicable to the presented cases using 4 design variables where the shapes giving the minimum objective function values are presented.
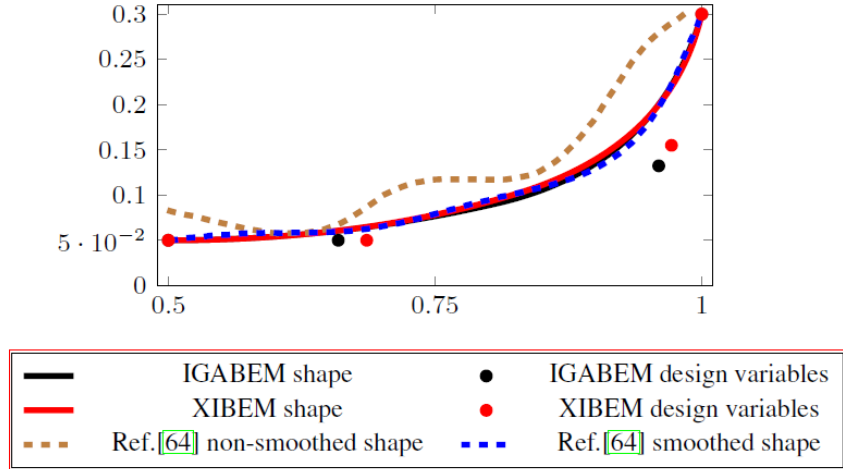
Figure 2.24: Optimized horn part for frequency range of 350 to 450 Hz.
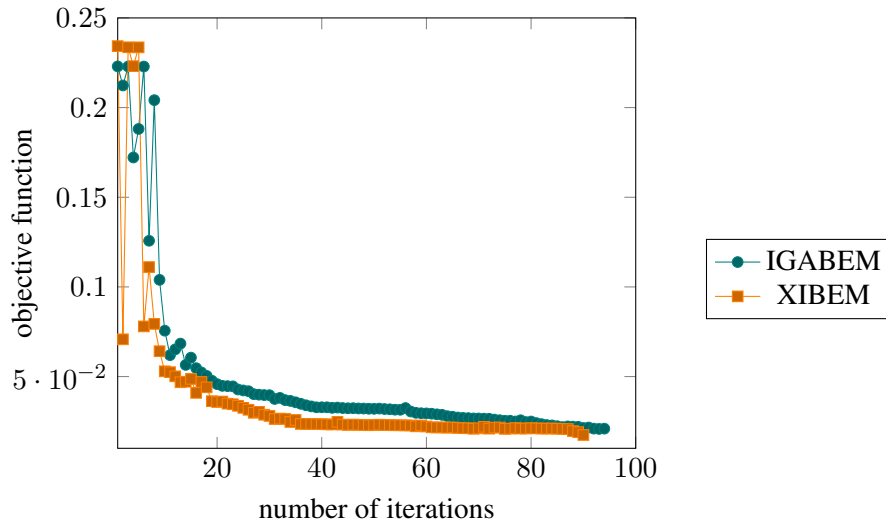
Figure 2.25: Iteration process against the reflection for frequency range of 350 to 450 Hz.

		Conventional IGABEM	XIBEM
Frequency Range of 350 to 450 Hz	Reflection	$2.07 \times 10E\text{-}2$	$1.64 \times 10E\text{-}2$
	N2 - Number of Consecutive Iterations for PSO	60	60
	kh/p along the Optimized Part for max. Frequency	0.05	0.08
	no of Elements/Wavelength along the Optimized Part for max. Frequency	65.8	38.4
	Total DOFs	249 NURBS Basis Functions	149 NURBS Basis Functions x 4 Plane Waves

Table 2.6: Comparative results for optimization case of frequency range.

2.8   Summary

In this chapter, an approach is developed for 2D Helmholtz acoustic problem by coupling one of the gradient-free optimization methods, the particle swarm method (PSO), with the isogeometric analysis (IGA) using
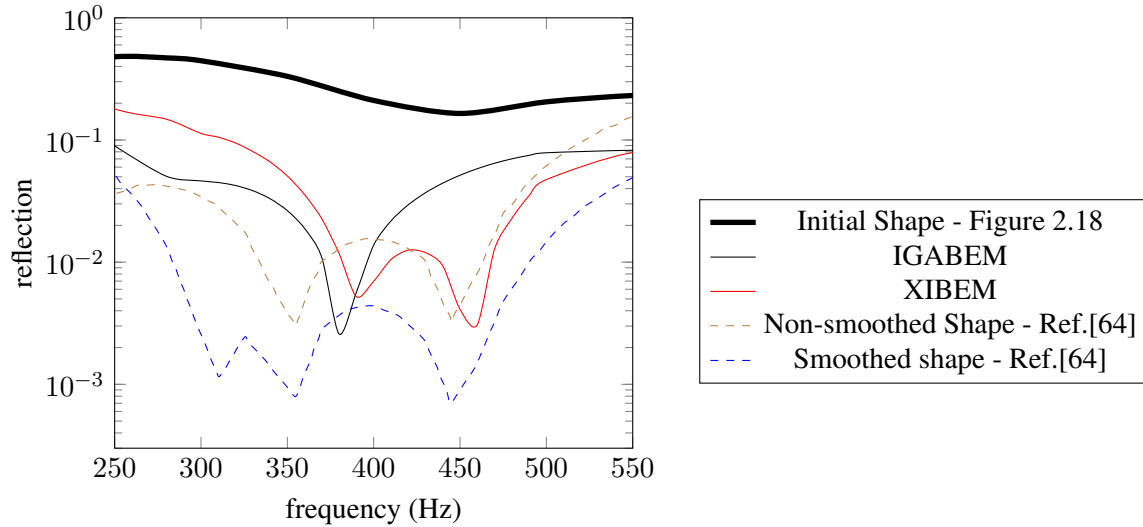
Figure 2.26: Reflection spectra for the optimized horns for frequency range of 350 to 450 Hz.

two boundary element methods avoiding an interior discretization of the domain; the conventional (IGA-BEM) and the eXtended (XIBEM).

The benefit of IGA is to employ its NURBS functions to represent all three models, i.e. shape design/-analysis/optimization, with a set of control points, which also represent control variables and optimization parameters for the three models respectively. This allows to an easy communication between the three models.

Several numerical examples considering the duct problem and different optimization cases of the noise barrier and horn problems were examined and the obtained results were compared against the analytical solution or the previously published methods. It was demonstrated that, the results of the present approach are generally in good agreement with some computation advantage to XIBEM which allows coarser meshes. In general, PSO is simpler than the gradient-based optimization methods since it does not need any sensitivity analysis, but it has some trade-offs with regard to the convergence speed. Furthermore, as the number of design variables increases, a larger number of consecutive iterations (N_2) is required. Larger N_2 helps also in higher frequency cases. In some cases the solution may not be unique and different optimal geometries can be obtained.

Chapter 3

Structural shape optimization with IGABEM for three-dimensional axi-symmetric problem

based on the paper *'Isogeometric boundary element analysis and shape optimization by PSO for 3D axi-symmetric high frequency Helmholtz acoustic problems.'* published in JSV, where the contribution of each author is summarized as follows:

Ahmed Mostafa Shaaban

- Conceptualization
- Research state of the art
- Investigation
- Formal analysis
- Methodology
- Software / Programming
- Data curation
- Data analysis
- Validation
- Visualization

- Writing-original draft preparation

Cosmin Anitescu

- Conceptualization
- Writing-review and editing

Elena Atroshchenko

- Conceptualization
- Writing-review and editing

Timon Rabczuk

- Conceptualization
- Supervision
- Mentoring the research progress
- Review of the manuscript before submission

3.1   General

In this chapter, we consider axi-symmetric domains, where the three-dimensional problem is simplified in BEM from a surface integral to a combination of two 1D integrals. The first is the line integral similar to a two-dimensional BEM problem. The second integral is performed over the angle of revolution. The discretization is applied only to the former integration. This leads to significant computational savings and, consequently, better treatment for higher frequencies over the full three-dimensional models. We first validate the capability of IGABEM for axi-symmetric problems to handle high frequencies and verify it by means of manufactured analytical solutions. Secondly, we show the performance of the proposed approach in shape optimization problems by using a particle swarm optimization (PSO) method. Coupling PSO with IGABEM in the optimization models benefits from the IGA feature of representing the three different models: shape design, analysis and optimization models using a single set of control points. The proposed method for the shape optimization of a horn is compared with reference solutions for BEM and FEM.

3.2   Boundary integral equation for time harmonic problems
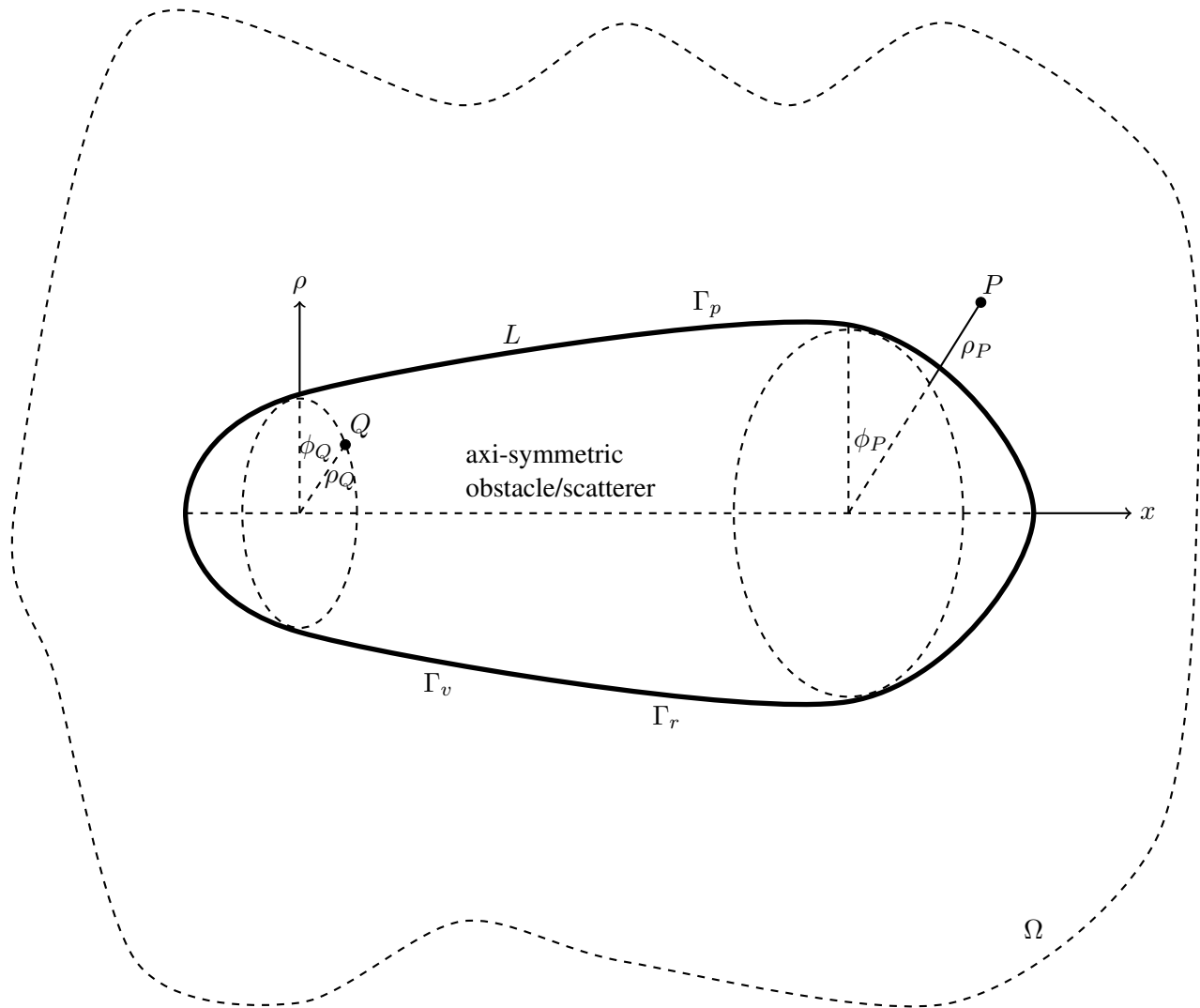
Figure 3.1: An axi-symmetric body for the acoustic problem.

The axi-symmetric acoustic problem is defined as shown in figure 3.1. The boundary value problem which fulfills the Helmholtz equation is considered similar to that of the equations (2.1)-(2.4) in the previous section 2.2. The Sommerfeld radiation condition at infinity for 3D problems is prescribed to prevent all

possible reflections of artificial acoustic waves from the far-field as follows:

$$\lim_{r \to \infty} r \left(\frac{\partial u}{\partial r} - iku \right) = 0, \tag{3.1}$$

in which r refers to the distance from the origin.

The BVP is converted to the boundary integral equation (BIE) using the Green's second identity [20]:

$$c(\mathbf{P})u(\mathbf{P}) + \int_\Gamma \frac{\partial G(\mathbf{P}, \mathbf{Q})}{\partial n} u(\mathbf{Q}) d\Gamma(\mathbf{Q}) = \int_\Gamma G(\mathbf{P}, \mathbf{Q}) \frac{\partial u(\mathbf{Q})}{\partial n} d\Gamma(\mathbf{Q}), \qquad \mathbf{P}, \mathbf{Q}, \in \Gamma, \tag{3.2}$$

where $G(\mathbf{P}, \mathbf{Q})$ is the Green's function representing the field effect at the boundary point $\mathbf{Q}$ due to a source at $\mathbf{P}$ in free space. $c(\mathbf{P})$ is the jump-term [8]. The Green's function for 3D problems is defined as [36]:

$$G(\mathbf{P}, \mathbf{Q}) = \frac{e^{-ikr}}{4\pi r}, \tag{3.3}$$

where $r = |\mathbf{P} - \mathbf{Q}|$. The reduced form of the boundary value problem in the domain Ω is represented by the boundary integral equation (BIE) on Γ (eq.(3.2)). This satisfies automatically the Sommerfeld radiation condition in eq.(3.1) which presents an advantage of BEM over FEM or other domain-type methods providing truncation errors on the far-field in such infinite domain problems. Furthermore, the problem dimensionality is reduced since only the domain boundaries are discretized. Figure 3.1 sketches the proposed three-dimensional problem solved by the surface integral of Helmholtz equation shown in eq.(3.2). We assume that surface Γ is obtained from curve L rotated about x-axis. In order to save the computational effort, the surface integral over Γ is converted to a combination of two integrals. The first is a discretized line integral over L similar to the two-dimensional BEM problems. The second integral is a simple polar integral over the angle of revolution ϕ. This is applied to a cylindrical coordinate system (x,ρ,ϕ) with axi-symmetric boundary conditions and constant boundary variables with respect to ϕ [114]. Accordingly, eq.(3.2) can be written in the following form:

$$
\begin{aligned}
c(\mathbf{P})u(\mathbf{P}) + \int_L \int_0^{2\pi} \frac{\partial G(\mathbf{P}, \mathbf{Q})}{\partial n} u(\mathbf{Q}) d\phi(\mathbf{Q}) \rho(\mathbf{Q}) dL(\mathbf{Q}) = \\
\int_L \int_0^{2\pi} G(\mathbf{P}, \mathbf{Q}) \frac{\partial u(\mathbf{Q})}{\partial n} d\phi(\mathbf{Q}) \rho(\mathbf{Q}) dL(\mathbf{Q}), \qquad \mathbf{P}, \mathbf{Q} \in \Gamma.
\end{aligned}
\tag{3.4}
$$

The integral in the left hand side is regular due to the existence of $\frac{\partial r}{\partial n(\mathbf{Q})}$ inside $\frac{\partial G(\mathbf{P},\mathbf{Q})}{\partial n}$. This term can be expressed with respect to the cylindrical coordinate system as follows:

$$\frac{\partial r}{\partial n(\mathbf{Q})} = \frac{x_Q - x_P}{r} n_x(\mathbf{Q}) + \frac{\rho_Q - \rho_P \cos \phi}{r} n_\rho(\mathbf{Q}), \tag{3.5}$$

in which $n_x(\mathbf{Q})$ and $n_\rho(\mathbf{Q})$ are the cylindrical components of the unit normal n at $\mathbf{Q}$ written as follows:

$$(n_1, n_2, n_3) = (n_x, n_\rho \cos \phi, n_\rho \sin \phi), \tag{3.6}$$

and

$$r = \sqrt{(x_Q - x_P)^2 + (\rho_Q \cos \phi_Q - \rho_P \cos \phi_P)^2 + (\rho_Q \sin \phi_Q - \rho_P \sin \phi_P)^2}$$
$$= \sqrt{(x_Q - x_P)^2 + \rho_Q^2 + \rho_P^2 - 2 \rho_Q \rho_P \cos \phi}, \tag{3.7}$$

as $\phi = \phi_Q - \phi_P$ where $\phi_P = 0$ in all examples in this chapter. The integral in the right hand side is singular when the collocation point coincides with the integrated element. This singularity needs special treatment. In this chapter, the elliptical integration is used to remove the singularity by means of the following process. Since all variables multiplied by $G(\mathbf{P}, \mathbf{Q})$ in the integral in the right hand side are constant with respect to ϕ, $G(\mathbf{P}, \mathbf{Q})$ is taken separately as follows:

$$\int_0^{2\pi} G(\mathbf{P}, \mathbf{Q})\, d\phi(\mathbf{Q}) = \int_0^{2\pi} \frac{e^{-ikr}}{4\pi r}\, d\phi(\mathbf{Q}) = \int_0^{2\pi} \frac{e^{-ikr} - 1}{4\pi r}\, d\phi(\mathbf{Q}) + \int_0^{2\pi} \frac{1}{4\pi r}\, d\phi(\mathbf{Q}), \tag{3.8}$$

in which the first integral in the right hand side is regular while the last integral is singular. Then, a new variable $\overline{R}^2$ is defined as:

$$\overline{R}^2 = (x_Q - x_P)^2 + (\rho_Q + \rho_P)^2. \tag{3.9}$$

Therefore, r is written as:

$$r = \sqrt{\overline{R}^2 - 2 \rho_Q \rho_P (1 + \cos \phi)}. \tag{3.10}$$

Furthermore, the variable $\overline{k}^2$ is introduced as:

$$\overline{k}^2 = \frac{4\,\rho_Q\,\rho_P}{\overline{R}^2}.$$

(3.11)

After that, the singular integral in the right hand side in eq.(3.8) is written in the following form:

$$\int_0^{2\pi} \frac{1}{4\pi r}\,d\phi(\mathbf{Q}) = \int_0^{2\pi} \frac{1}{4\pi\sqrt{\overline{R}^2 - 2\,\rho_Q\,\rho_P\,(1+\cos\phi)}}\,d\phi(\mathbf{Q})$$
$$= \frac{1}{4\pi\overline{R}} \int_0^{2\pi} \frac{1}{\sqrt{1 - (\overline{k}^2/2)(1+\cos\phi)}}\,d\phi(\mathbf{Q}).$$

(3.12)

Using the following definitions:

$$\eta = \phi/2,$$

(3.13)

and

$$\Psi = \pi/2 - \eta = \pi/2 - \phi/2,$$

(3.14)

yields the final regular form of this integral as:

$$\int_0^{2\pi} \frac{1}{4\pi r}\,d\phi(\mathbf{Q}) = \frac{1}{\pi\overline{R}} \int_0^{2\pi} \frac{1}{\sqrt{1 - \overline{k}^2\sin^2\Psi}}\,d\Psi = \frac{1}{\pi\overline{R}}F(\pi/2,\overline{k}),$$

(3.15)

in which $F(\pi/2,\overline{k})$ is the complete elliptic integral of the first kind with modulus $\overline{k}$. Hence, in this singularity process treatment, point P can be a corner point where the continuity of the NURBS curve is C^0.

3.3 NURBS basis functions

The description of the NURBS basis functions is considered similar to the previous section 2.3.

3.4 IGABEM for Helmholtz equation

The boundary variables are represented by the acoustic pressure and its normal derivative. The NURBS shape functions discretize these boundary variables as follows:

$$u(\xi) = \sum_{i=1}^{n} R_{i,p}(\xi)u_i, \qquad \frac{\partial u}{\partial n}(\xi) = \sum_{i=1}^{n} R_{i,p}(\xi)q_i,$$

(3.16)

46

in which u_i and q_i are the associated control variables. After substituting eq.(3.16) is into eq.(3.2), evaluating it at n collocation points ξ_c and using a non-overlapping set of N_e elements given by knot spans $[\xi_i, \xi_{i+1}]$ to discretize the boundary, the following system is obtained [20]:

$$c(\xi_c) \sum_{i=1}^{n} u_i R_{i,p}(\xi_c) + \sum_{l=1}^{Ne} \sum_{i=1}^{n} \left[\int_0^1 \left[\int_0^{2\pi} \frac{\partial G(\xi_c, \xi, \phi)}{\partial n} d\phi \right] R_{i,p}(\xi) |J_\xi^l| \rho(\xi) d\xi \right] u_i =$$
$$\sum_{l=1}^{Ne} \sum_{i=1}^{n} \left[\int_0^1 \left[\int_0^{2\pi} G(\xi_c, \xi, \phi) d\phi \right] R_{i,p}(\xi) |J_\xi^l| \rho(\xi) d\xi \right] q_i, \tag{3.17}$$

where $|J_\xi^l|$ is the Jacobian of transformation. This Jacobian is introduced at a local coordinate system $\widehat{\xi} \in [-1, 1]$ as:

$$J_\xi^l(\widehat{\xi}) = \frac{d\Gamma}{d\xi} \frac{d\xi}{d\widehat{\xi}}, \tag{3.18}$$

in which

$$\frac{d\Gamma}{d\xi} = \sqrt{\left(\frac{dx}{d\xi}\right)^2 + \left(\frac{dy}{d\xi}\right)^2}, \tag{3.19}$$

and

$$\frac{d\xi}{d\widehat{\xi}} = \frac{\xi_{i+1} - \xi_i}{2}. \tag{3.20}$$

The final matrix form of eq.(3.17) is formulated as:

$$\mathbf{H}\mathbf{u} = \mathbf{G}\mathbf{t}, \tag{3.21}$$

in which

$$\mathbf{H}_{ci} = c(\xi_c) R_{i,p}(\xi_c) + \int_0^1 \left[\int_0^{2\pi} \frac{\partial G(\xi_c, \xi, \phi)}{\partial n} d\phi \right] R_{i,p}(\xi) |J_\xi| \rho(\xi) d\xi,$$
$$\mathbf{G}_{ci} = \int_0^1 \left[\int_0^{2\pi} G(\xi_c, \xi, \phi) d\phi \right] R_{i,p}(\xi) |J_\xi| \rho(\xi) d\xi, \tag{3.22}$$

and $\mathbf{u}$ and $\mathbf{t}$ are the vectors containing the u_i and q_i components respectively. Then, eq.(3.21) is re-arranged into the linear system of equations:

$$\mathbf{A}\mathbf{x} = \mathbf{b}, \tag{3.23}$$

where matrix $\mathbf{A}$ includes the coefficients in the matrices $\mathbf{H}$ and $\mathbf{G}$ corresponding to the unknown control variables in eq.(3.17) arranged into vector $\mathbf{x}$. The right hand-side vector $\mathbf{b}$ contains all assembled known components. The collocation strategy introduced by the Greville abscissae at points $\widehat{\xi}_g$ produced by the formula [13]:

$$\widehat{\xi}_g = \frac{\xi_{g+1} + \xi_{g+2} + \cdots + \xi_{g+p}}{p}, \qquad g = 1, 2, \cdots, n-1, \qquad (3.24)$$

is used. The total number of NURBS functions and control points are n, whilst the closed curves share both the start and end points and consequently the Greville abscissae give only $n-1$ collocation points. Thus, the first and last NURBS functions are summed together to unite the corresponding control points as one control point. In relation to the used integration scheme by Gauss quadrature, 6 Gauss points with 4 uniform sub-divisions for each knot span are used for each discretized line integral. The polar integration over the angle of revolution is defined for each problem separately relative to the used frequency.

3.5 Description of the structural shape optimization problem

The coupled structural shape optimization problem with BEM using the Particle Swarm Optimization (PSO) algorithm is considered as same as the previous section 2.6

3.6 Numerical results

Different numerical examples are discussed in order to illustrate the performance of the proposed approach of IGABEM for axi-symmetric problems. The examples are divided into two parts. In the first part, three problems including the pulsating sphere problem, the scattering problem of spherical waves by a rigid sphere and the plane wave scattering problem by a rigid sphere are analyzed with IGABEM against the analytical solutions to verify the capability of the proposed approach. Then, the horn problem is presented and the optimized shapes obtained using IGABEM with PSO are compared against already published optimized shapes obtained from BEM and FEM using sensitivity analysis optimization methods and PSO.

3.6.1 Verification examples

In order to verify the proposed IGABEM algorithm that is used in the optimization process shown in the next horn problem, the forthcoming three problems are studied.

48
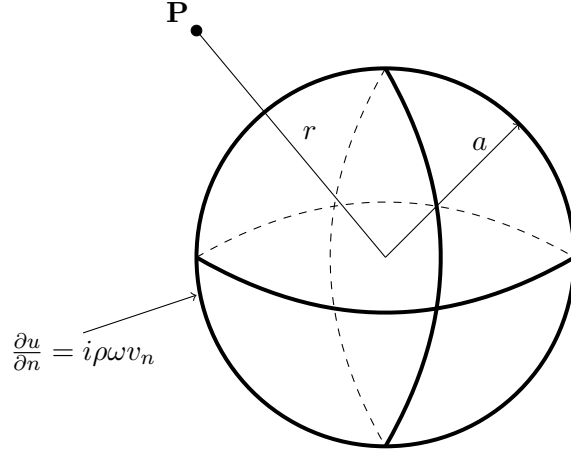
Figure 3.2: The pulsating sphere Problem.

3.6.1.1 The pulsating sphere problem

A sphere with a radius $a = 0.5$ m centered at the origin is considered. The sphere is subject to a constant acoustic radial velocity $v_n = -1$ m/s prescribed over its entire surface as shown in figure 3.2. The problem is solved by the application of the BIE eq.(3.17) with reference to eq.(2.3) in which the Neumann boundary condition is defined as follows:

$$\frac{\partial u}{\partial n} = i\rho\omega v_n. \tag{3.25}$$

Here, the angular frequency ω is related to the wavenumber k and the sound speed c by $\omega = kc$. In this chapter, the sphere is embedded in the air of density $\rho = 1.2$ kg/m^3 where the sound speed is $c = 343$ m/s. The analytical solution is defined by the following equation [37, 24]:

$$u^{ex}(r) = \frac{a}{r}v_n\rho c\frac{-ika}{1 - ika}e^{ik(r-a)}, \tag{3.26}$$

where r is the distance from the origin to the concerned point **P**.

Since the boundary condition is homogeneous along the boundary of the sphere, it is possible to investigate the model performance for extremely high frequencies. Figure 3.3 explains the NURBS description with polynomial degree $p = 2$ and the corresponding control points in terms of x- and y-coordinates with the weight w in the form (x, y, w) used in the axi-symmetric model. As shown, only the upper half is modeled
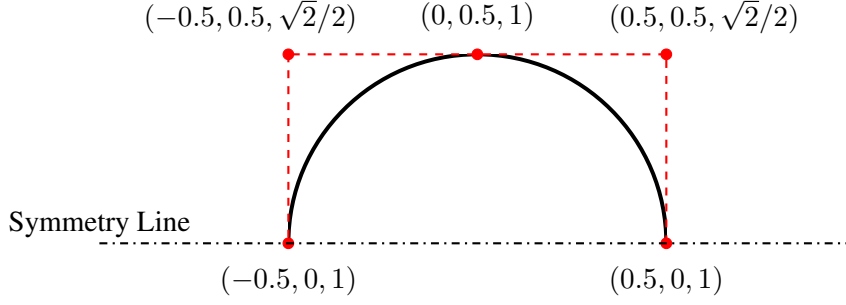
Figure 3.3: NURBS model for an axi-symmetric sphere.

with a symmetry line. The relative L_2 error norm of numerical solution u^{num} is written as follows:

$$e_{L_2} \equiv \frac{||u^{ex} - u^{num}||}{||u^{ex}||}. \tag{3.27}$$

Figure 3.4 shows the variation of e_{L_2} as a function of degrees of freedom (DOFs) per wavelength along 200 equally spaced points on a circle outside the sphere with a radius of 0.75m for frequencies 100Hz, 10kHz and 22kHz with wavenumbers k=1.83, 183.2 and 403 respectively. 50, 100 and 200 Gauss points are used in the purpose of the polar integration over the angle of revolution for the three selected frequencies respectively.

It can be shown the capability of IGABEM with an axi-symmetric model using moderate DOFs per wavelength to handle such spherical problems especially for cases of very high frequencies. This supports the proposed approach over the full 3D models with T-splines presented in [37] or with NURBS studied in [24] which could analyze only much lower frequencies (maximum frequency was 1100Hz in [37] and 300Hz in [24]). For further clarification to the performance of the proposed model, figures 3.5,3.6,3.7 present the contours of the acoustic pressure field values in terms of the real and imaginary parts for IGABEM and the analytical solution respectively with the corresponding absolute error. The models which employ only 3 DOFs/wavelength are used for the cases of higher frequencies of 10 and 22 kHz. In the case of the lowest frequency of 100Hz, the coarse model containing only 2 refined points inside each knot span (13 DOFs/wavelength) is used. The acoustic pressure fields are calculated at points placed inside a circle domain with a radius of 3m with a step size equals one-fifth of the wavelength for the higher frequency cases while a larger step size is used only due to smooth visualization reasons in the lowest frequency case. It can be seen
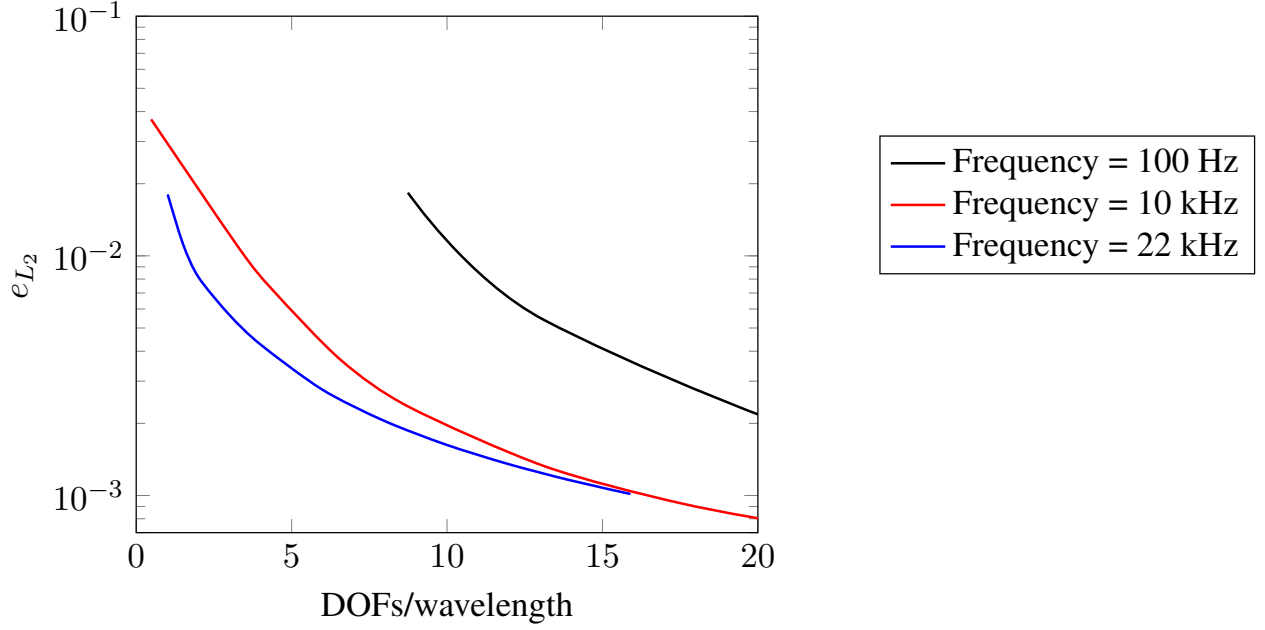
Figure 3.4: L_2 error norm for the pulsating sphere problem for different frequencies.

that, the analytical and numerical solutions are in excellent agreement except some errors at the horizontal symmetry line next to the sphere sides.

3.6.1.2   The scattering problem of spherical waves by a rigid sphere

The similar sphere with a radius $a = 0.5$ m centered at the origin - discussed in the previous section - is considered in this example again. This sphere is rigid ($\frac{\partial u}{\partial n} = 0$). The boundary conditions are defined by an incident spherical wave produced from a sound source located outside the sphere at a point on the symmetry axis as shown in figure 3.8. The coordinate of this point is $\mathbf{S} = (1.50, 0, 0)$. The incident wave is written as follows:

$$u_{inc} = \frac{e^{-ik|\mathbf{S}-\mathbf{P}|}}{4\pi|\mathbf{S}-\mathbf{P}|}, \tag{3.28}$$

in which $|\mathbf{S} - \mathbf{P}|$ denotes the distance between the points $\mathbf{S}$ and $\mathbf{P}$. The total acoustic pressure fulfills $u = u_{sc} + u_{inc}$ where u_{sc} is the solution of the BIE eq.(3.17). This yields the following form:

$$c(\xi_c)\sum_{i=1}^{n} u_i R_{i,p}(\xi_c) + \sum_{l=1}^{Ne}\sum_{i=1}^{n}\left[\int_0^1\left[\int_0^{2\pi}\frac{\partial G(\xi_c,\xi,\phi)}{\partial n}d\phi\right]R_{i,p}(\xi)|J_\xi^l|\rho(\xi)d\xi\right]u_i = \frac{e^{-ik|\mathbf{S}-\mathbf{P}|}}{4\pi|\mathbf{S}-\mathbf{P}|}. \tag{3.29}$$

The analytical solution of the total acoustic pressure is defined by the following equation [115, 116, 117]:

51

(a) IGABEM - Real part

(b) Analytical solution - Real part

(c) IGABEM - Imaginary part

(d) Analytical solution - Imaginary part

(e) Absolute error
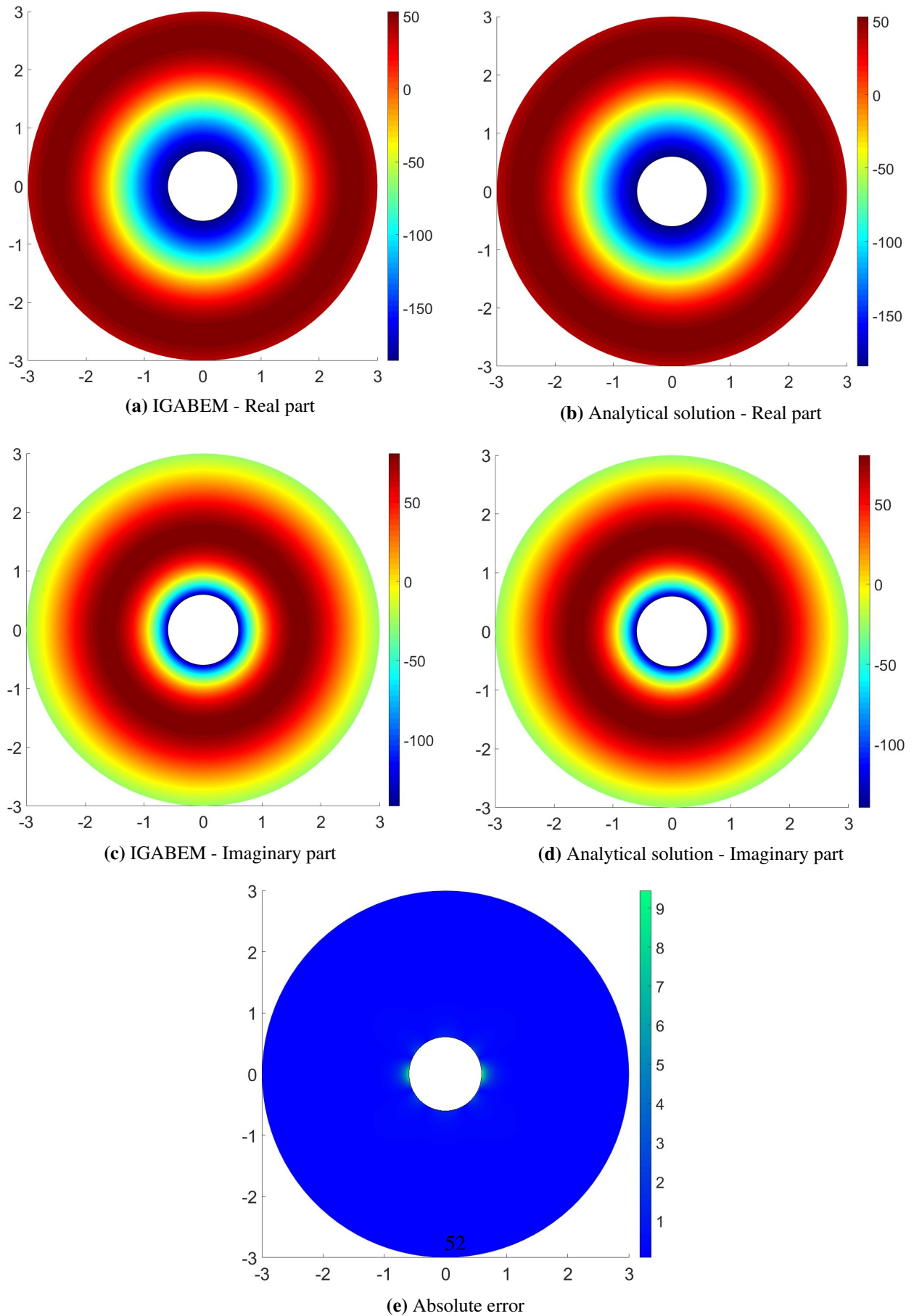
Figure 3.5: Acoustic pressure field values for the pulsating sphere problem for frequency of 100Hz.

52

(a) IGABEM - Real part

(b) Analytical solution - Real part

(c) IGABEM - Imaginary part

(d) Analytical solution - Imaginary part

(e) Absolute error
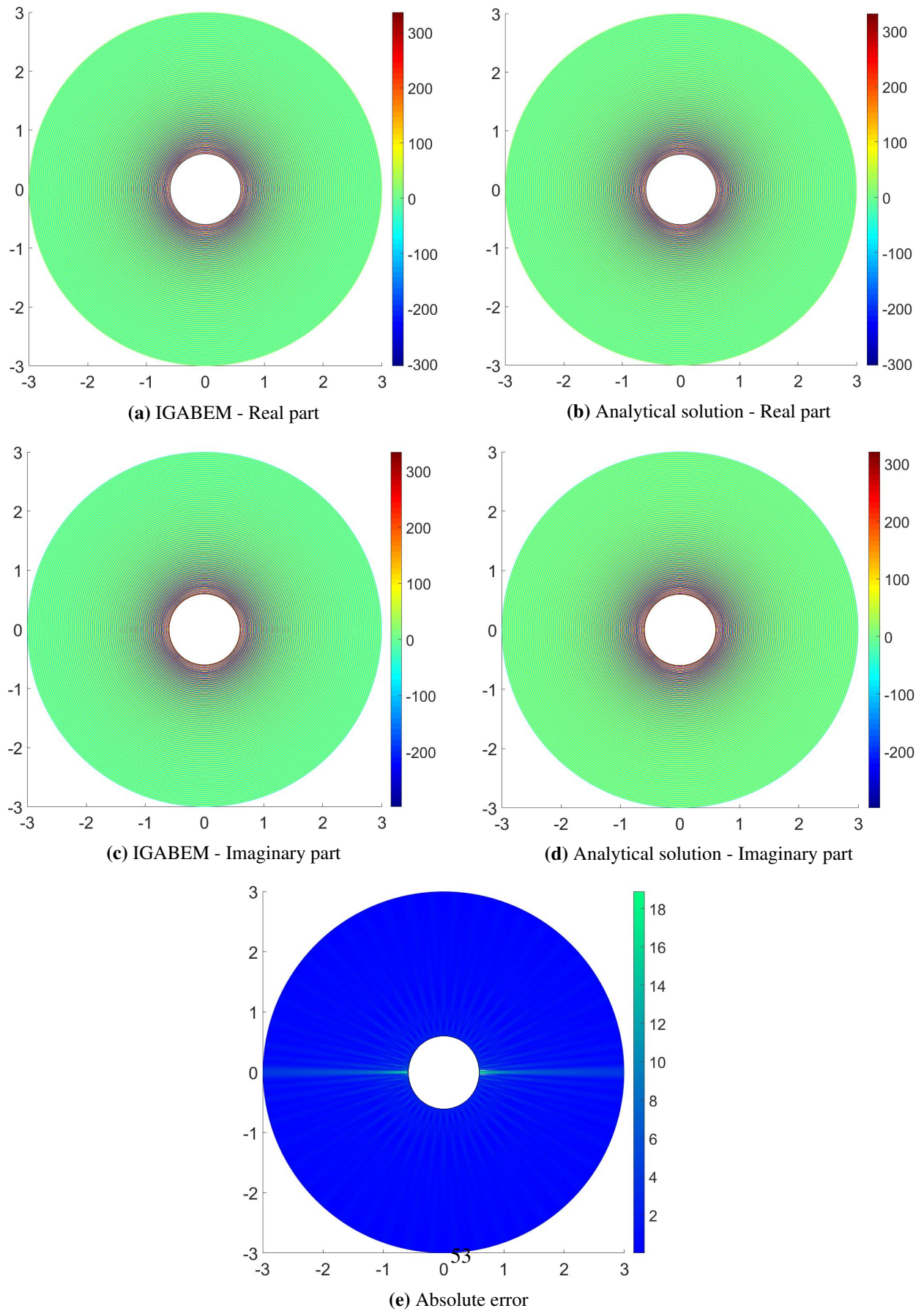
Figure 3.6: Acoustic pressure field values for the pulsating sphere problem for frequency of 10kHz.

(a) IGABEM - Real part

(b) Analytical solution - Real part

(c) IGABEM - Imaginary part

(d) Analytical solution - Imaginary part

(e) Absolute error
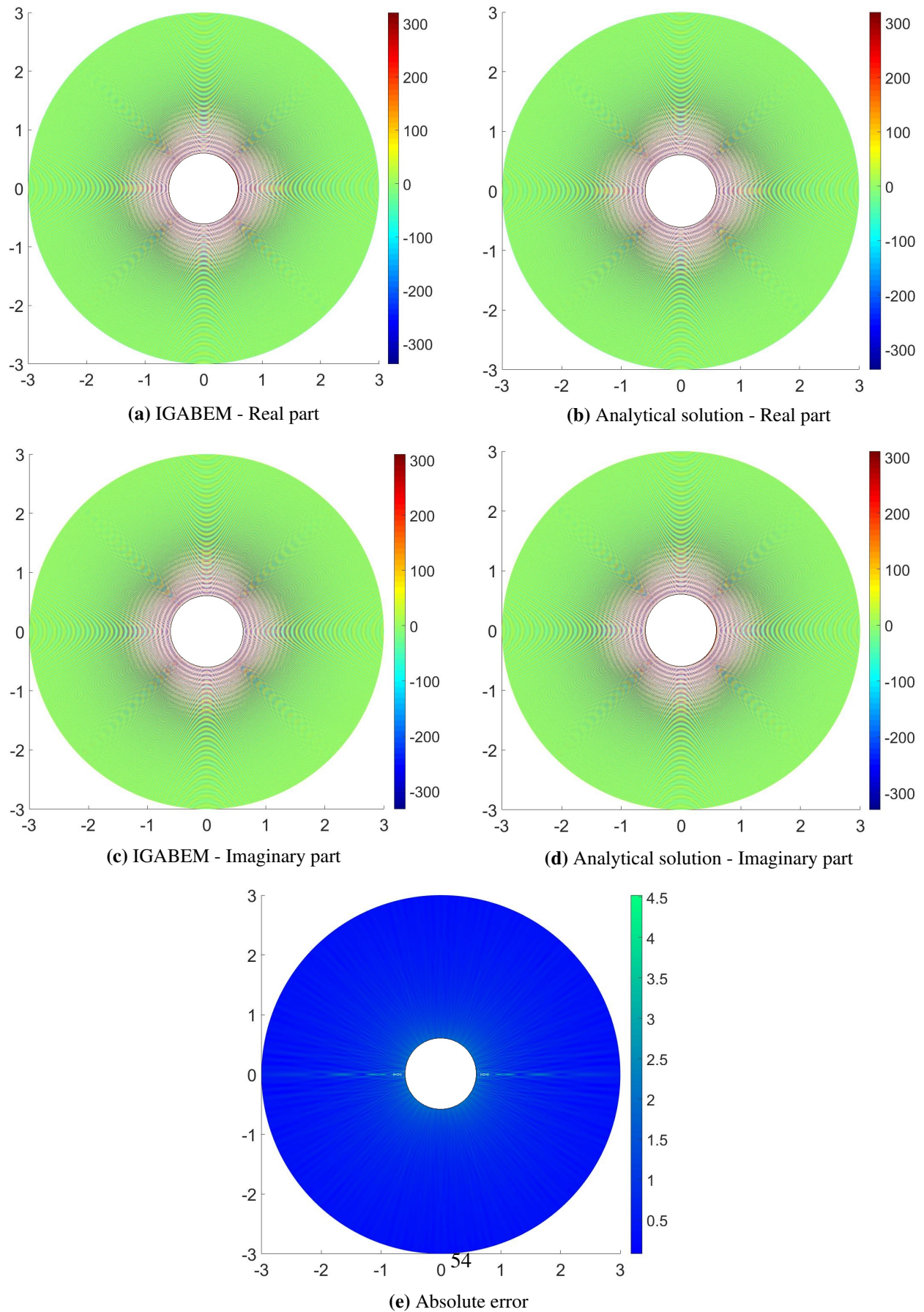
Figure 3.7: Acoustic pressure field values for the pulsating sphere problem for frequency of 22kHz.
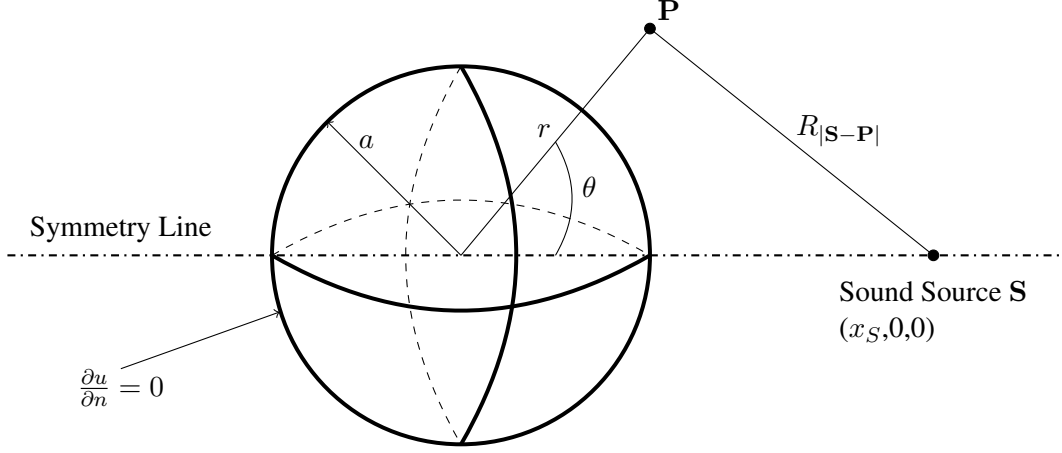
Figure 3.8: The scattering problem of spherical waves by a rigid sphere.

$$u^{ex}(r,\theta) = \frac{e^{ik|\mathbf{S}-\mathbf{P}|}}{4\pi|\mathbf{S}-\mathbf{P}|} - \frac{ik}{4\pi}\sum_{m=0}^{\infty}(2m+1)\frac{j'_m(ka)}{h'_m(ka)}h_m(kR_s)h_m(kr)P_m(cos\theta), r \geq a, \qquad (3.30)$$

where r is the distance from the origin to the concerned point $\mathbf{P}$, R_s denotes the distance from the origin to the source point $\mathbf{S}$ and θ is the angle between the axes of two points $\mathbf{S}$ and $\mathbf{P}$ as shown in figure 3.8. P_m is is the Legendre polynomial of order m. h_m and j_m are the spherical Hankel and Bessel functions of the first kind, respectively of order m. $(')$ refers to the derivative with respect to its argument.

We refer again to figure 3.3 for the proposed axi-symmetric model with NURBS using polynomial degree $p = 2$. The sphere is embedded in the air of density $\rho = 1.2$ kg/m^3 where the sound speed is $c = 343$ m/s. The relative L_2 error norm is similar to eq.(3.27).

Similar to the analysis performed in the previous section, figure 3.9 shows the variation of e_{L_2} as a function of DOFs per wavelength along 200 equally spaced points on a circle outside the sphere with a radius of 0.75m. Due to heterogeneity of the boundary conditions, finer meshes are required for the cases of extremely high frequencies. Therefore, the maximum frequency of 22kHz - used in the previous example - is slightly reduced to 20kHz with wavenumber $k = 366.4$ to get acceptable results with the already prescribed discretization. For the numerical evaluation of the polar integrals over the angle of revolution for the three selected frequencies, 50, 100 and 200 Gauss points are used, respectively. The order m of the Legendre polynomial and its corresponding spherical Hankel and Bessel functions in eq.(3.30) is sensitive to the frequency (wavenumber). Therefore, for the purpose of convergence, orders of 10, 100 and 200 are chosen for

the three studied frequencies respectively.

As concluded in the previous section, the proposed approach is feasible for treating much higher frequencies
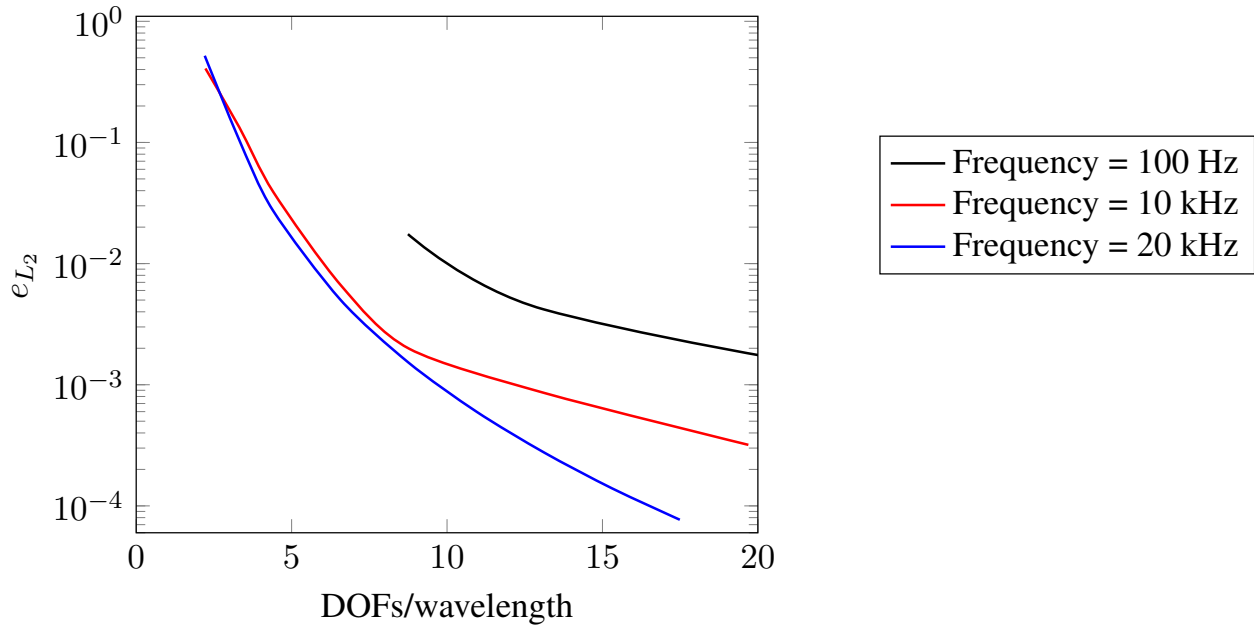
Figure 3.9: L_2 error norm for scattering problem of spherical waves by a rigid sphere.

using a reasonable number of DOFs per wavelength. The contours of acoustic pressure field values in terms of the real and imaginary parts for IGABEM and the analytical solution respectively with the corresponding absolute error for this problem are similar to the previous example and presented in figures 3.10,3.11,3.12. 4.5 DOFs/wavelength are used for the higher frequency cases of 10 and 20 kHz. In the case of the lowest frequency of 100Hz, the coarse model containing only 2 refined points inside each knot span (13 DOFs/wavelength) is used. The previous scheme of the points - placed inside a circle domain with a radius of 3m to calculate the acoustic variables - is preserved. The previous conclusion also holds here as IGABEM is in excellent agreement with the analytical solution. Some errors are noticeable at the horizontal symmetry line next to the sphere sides. The location of the sound source point can be noticed from the figures where the maximum sound is produced around it and increases directly with relative to higher frequencies.

3.6.1.3 Plane wave scattering by a rigid sphere

Consider again the rigid sphere of the previous section with a radius $a = 0.5$ m centered at the origin and embedded in the air of density $\rho = 1.2$ kg/m^3 where the sound speed is $c = 343$ m/s. The boundary

(a) IGABEM - Real part

(b) Analytical solution - Real part

(c) IGABEM - Imaginary part

(d) Analytical solution - Imaginary part

(e) Absolute error
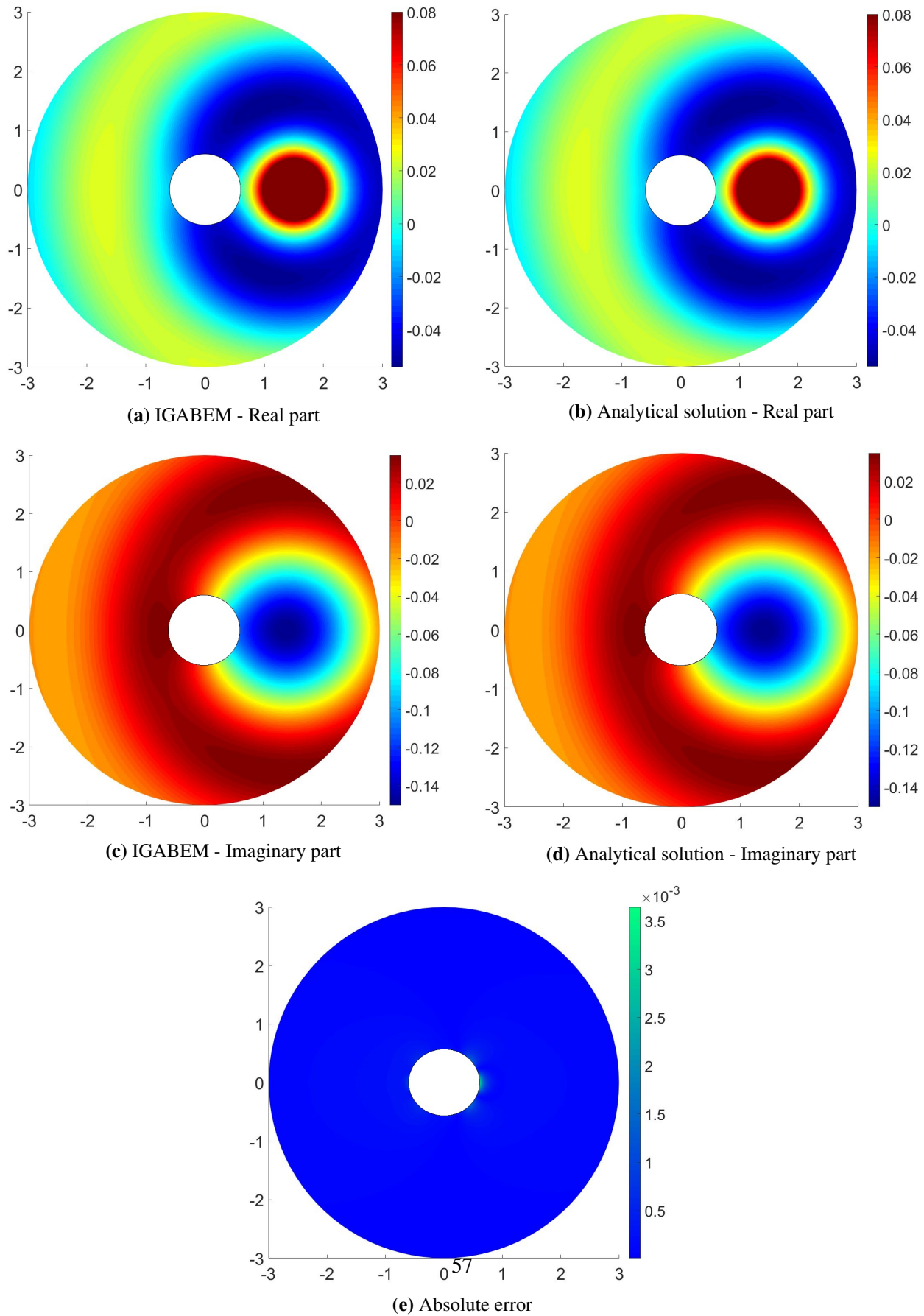
Figure 3.10: Acoustic pressure field values for the scattering problem of spherical waves by a rigid sphere for frequency of 100Hz.

(a) IGABEM - Real part

(b) Analytical solution - Real part

(c) IGABEM - Imaginary part

(d) Analytical solution - Imaginary part

58

(e) Absolute error
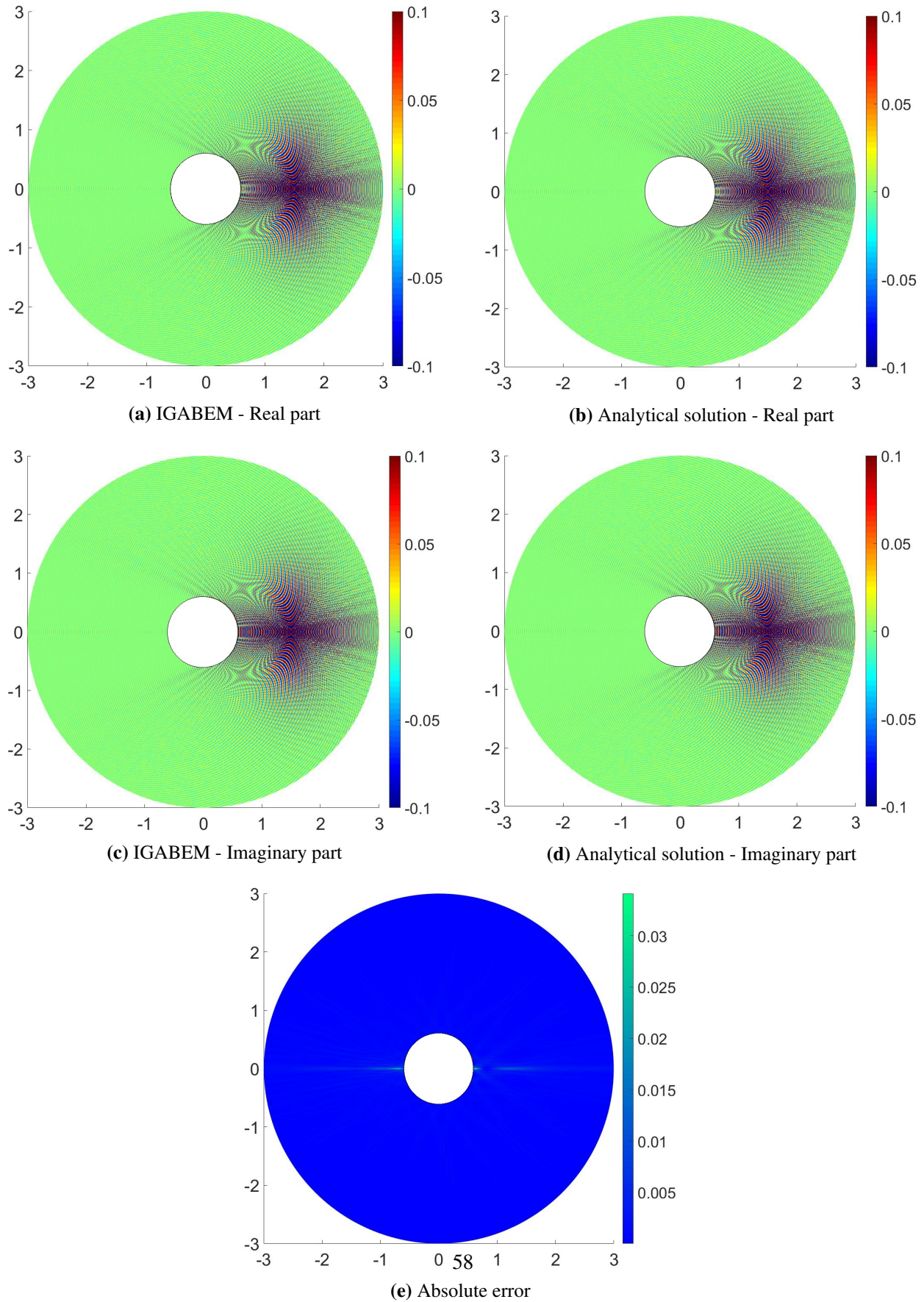
Figure 3.11: Acoustic pressure field values for the scattering problem of spherical waves by a rigid sphere for frequency of 10kHz.

(a) IGABEM - Real part

(b) Analytical solution - Real part

(c) IGABEM - Imaginary part

(d) Analytical solution - Imaginary part

(e) Absolute error
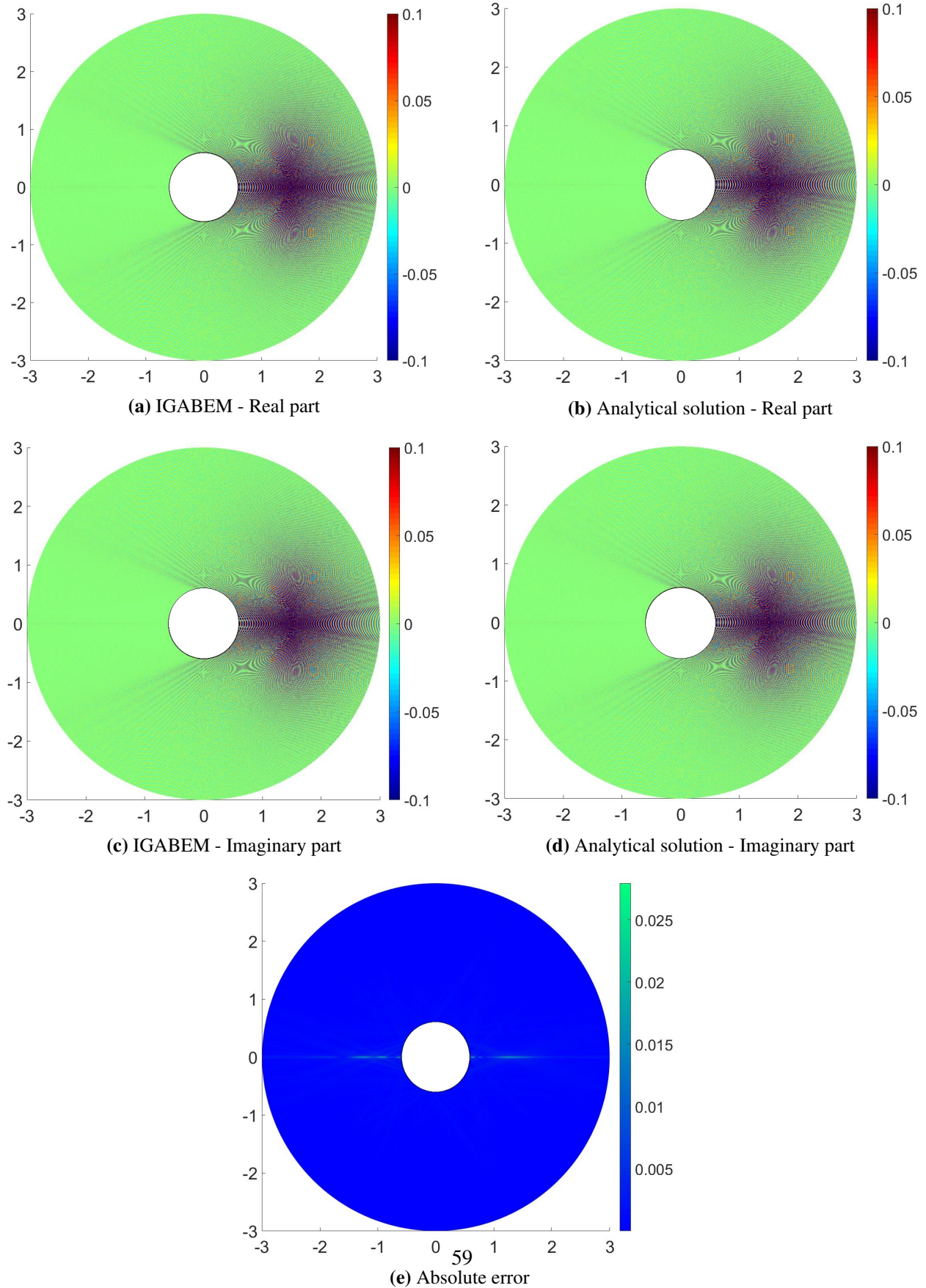
Figure 3.12: Acoustic pressure field values for the scattering problem of spherical waves by a rigid sphere for frequency of 20kHz.
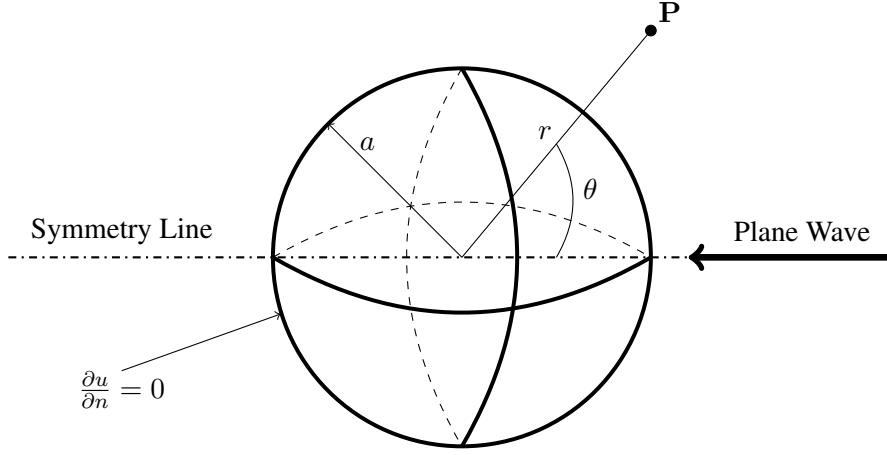
Figure 3.13: Plane wave scattering problem by a rigid sphere.

conditions are defined by an incident plane wave written as follows:

$$u_{inc} = Ae^{-ik\mathbf{d}\cdot\mathbf{q}}, \tag{3.31}$$

in which A denotes the wave amplitude, $|\mathbf{d}| = 1$ is the wavevector in the direction $\mathbf{d}$ and $\mathbf{q} = \{\mathbf{X_P}, \mathbf{Y_P}, \mathbf{Z_P}\}$ is the coordinates of the concerned point $\mathbf{P}$. In this example, the incident wave moves from the positive side of the symmetry axis as $\mathbf{d} = \{1, 0, 0\}$ with a unit amplitude $A = 1$ (see figure 3.13). With reference to the total acoustic pressure discussed in eq.(3.29) and with introducing the incident plane wave in eq.(3.31) to eq.(3.17), this yields:

$$c(\xi_c) \sum_{i=1}^{n} u_i R_{i,p}(\xi_c) + \sum_{l=1}^{Ne} \sum_{i=1}^{n} \left[\int_0^1 \left[\int_0^{2\pi} \frac{\partial G(\xi_c, \xi, \phi)}{\partial n} d\phi \right] R_{i,p}(\xi) |J_\xi^l| \rho(\xi) d\xi \right] u_i = Ae^{-ik\mathbf{d}\cdot\mathbf{q}}. \tag{3.32}$$

The analytical solution of the total acoustic pressure - presented in [118, 119, 31] - is defined by the following equation including the functions and polynomials defined previously in eq.(3.30):

$$u^{ex}(r, \theta) = Ae^{ik\mathbf{d}\cdot\mathbf{q}} - \sum_{m=0}^{\infty} i^m (2m+1) \frac{j_m'(ka)}{h_m'(ka)} h_m(kr) P_m(cos\theta) \quad , r \geq a, \tag{3.33}$$

in which θ in this equation denotes the angle between the axis of the incident wave (symmetry axis) and the axis containing the point $\mathbf{P}$ from the origin as shown in figure 3.13. The description of the isogeometric model is similar to figure 3.3. The relative L_2 error norm follows eq.(3.27). The procedures of studying the

60

the variation of e_{L_2} as a function of DOFs per wavelength is performed here in figure 3.14 following the previous section. The obtained accuracy from this problem coincides with the previous example studying the spherical wave problem. This is considered as another validation of the proposed method to address extremely higher frequencies over the full 3D models in [37] or [24]. The contours of acoustic pressure
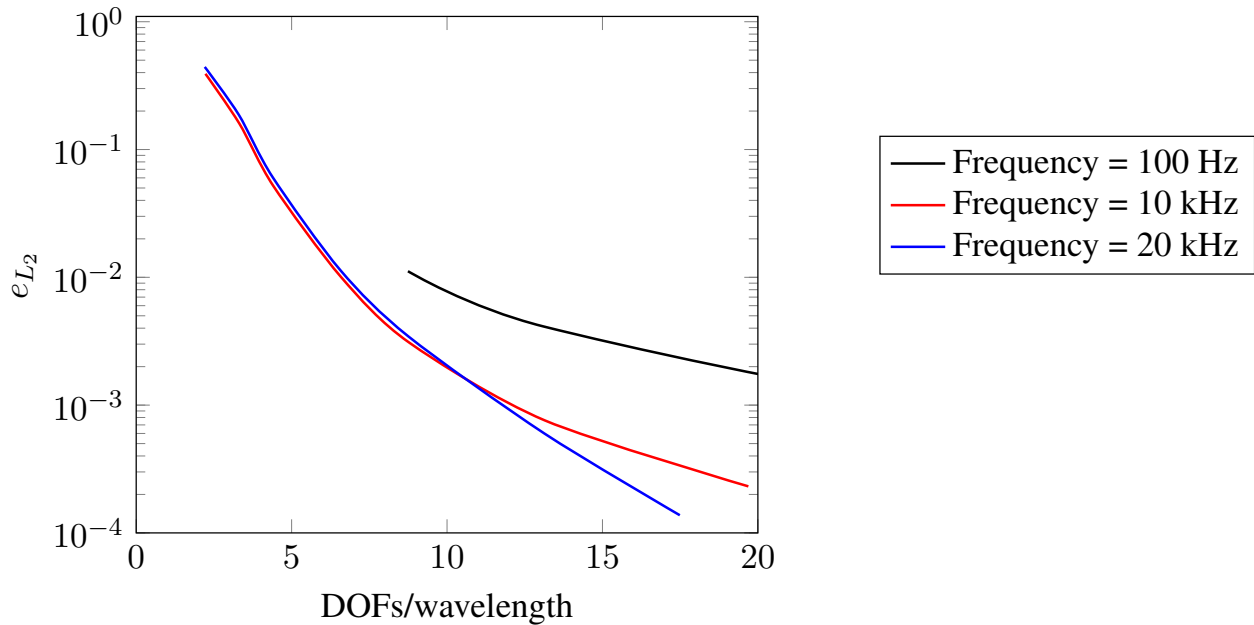
Figure 3.14: L_2 error norm for the plane wave scattering problem by a rigid sphere.

field values are demonstrated in figures 3.15, 3.16, 3.17 following the previous section. Since the behaviour of the plane wave is different than those of the previous sections, the acoustic pressure fields are calculated at points placed inside a square domain of 6m length centered in the origin. The step size between these points is one-fifth of the wavelength for the higher frequency cases. For the case of the lowest frequency, larger step size is used due to smooth visualization reasons. It can be concluded that, IGABEM gives excellent values verified by the analytical solution except some errors at the horizontal symmetry line next to the sphere sides. It can also be noticed clearly the direction of the incident plane waves - that moves from the positive side of the symmetry line - for the cases of higher frequencies where the produced sound fades in this side.

(a) IGABEM - Real part

(b) Analytical solution - Real part

(c) IGABEM - Imaginary part

(d) Analytical solution - Imaginary part

(e) Absolute error
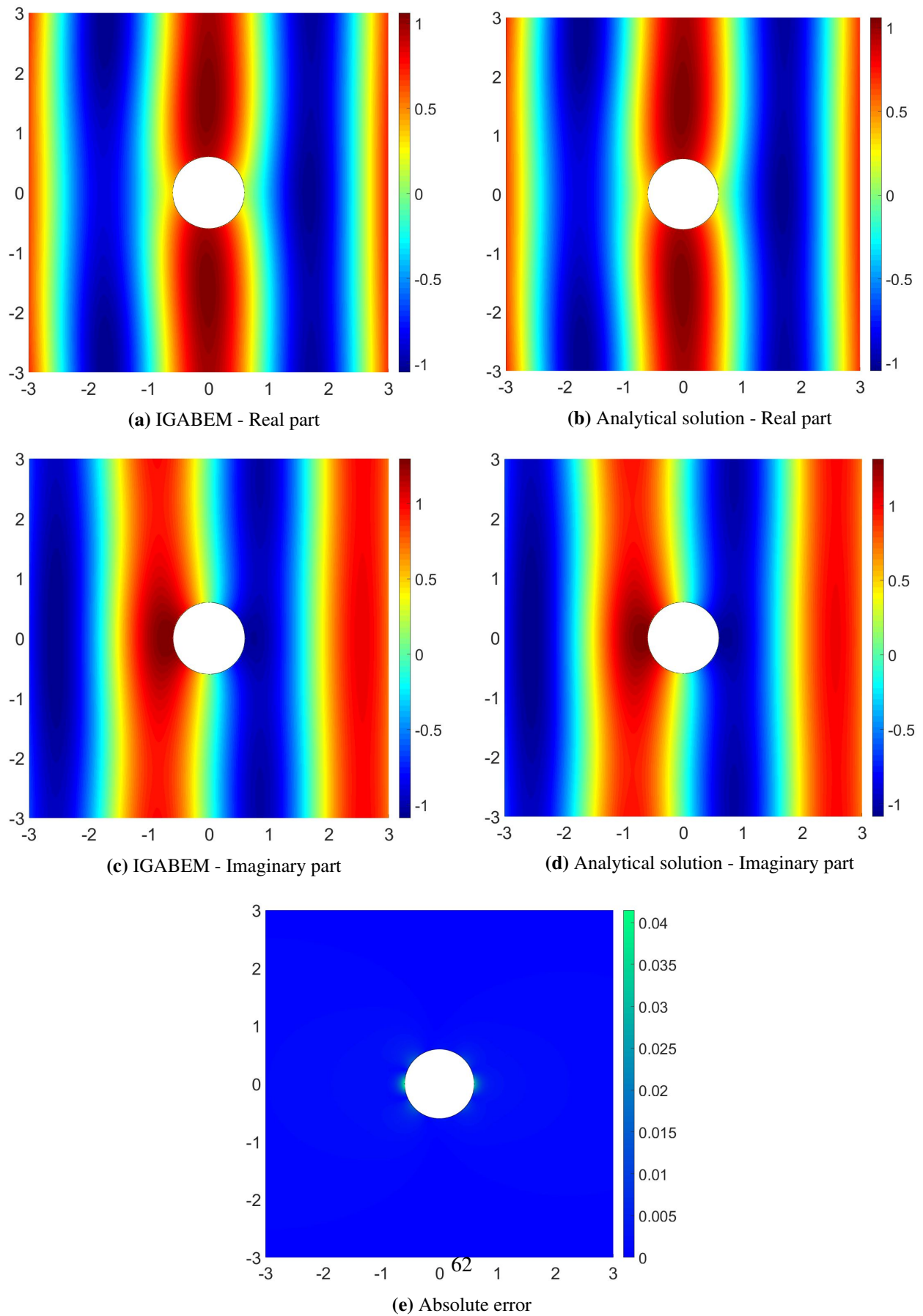
Figure 3.15: Acoustic pressure field values for the plane wave scattering problem by a rigid sphere for frequency of 100Hz.

(a) IGABEM - Real part

(b) Analytical solution - Real part

(c) IGABEM - Imaginary part

(d) Analytical solution - Imaginary part

(e) Absolute error
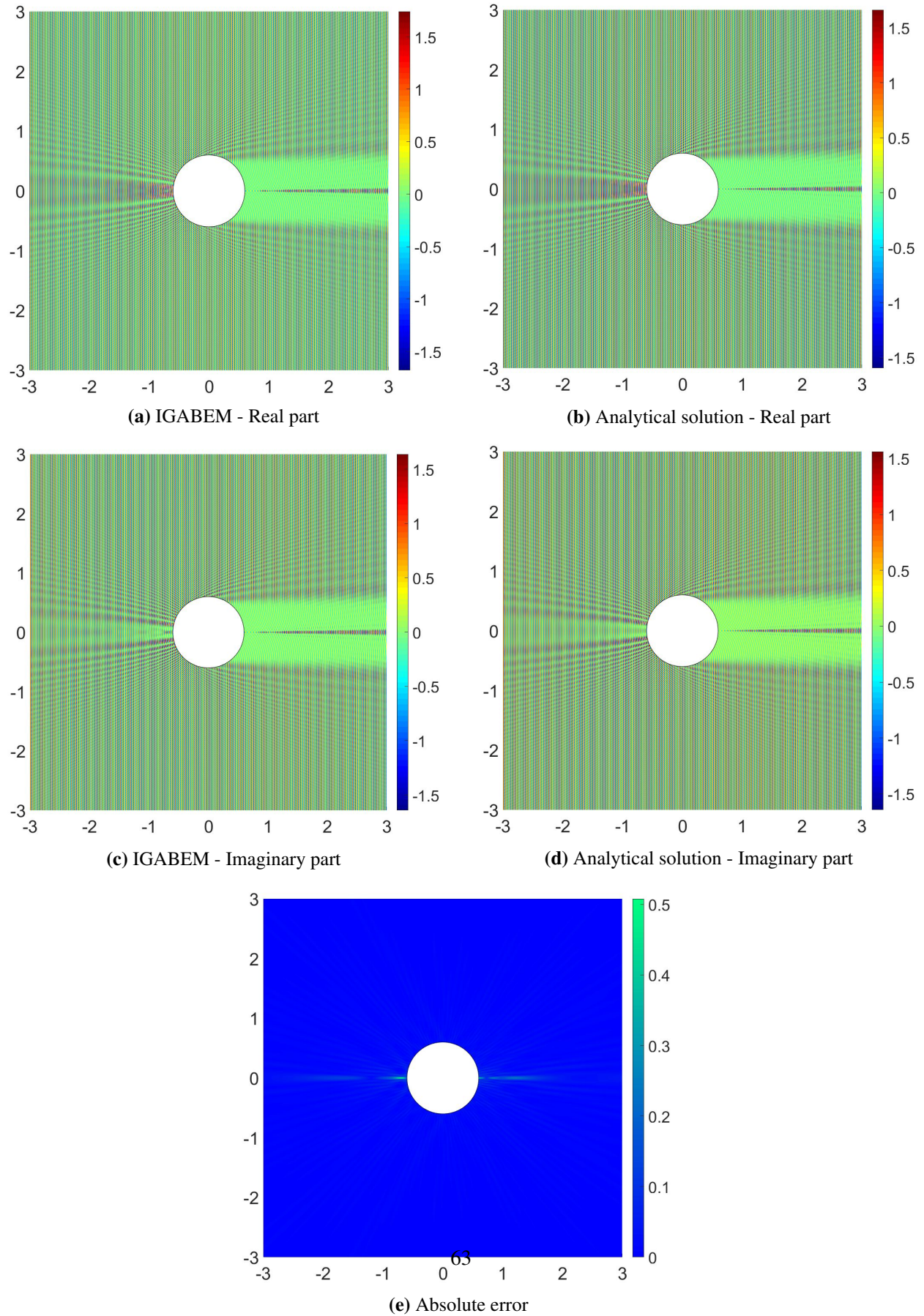
Figure 3.16: Acoustic pressure field values for the plane wave scattering problem by a rigid sphere for frequency of 10kHz.

(a) IGABEM - Real part

(b) Analytical solution - Real part

(c) IGABEM - Imaginary part

(d) Analytical solution - Imaginary part

(e) Absolute error
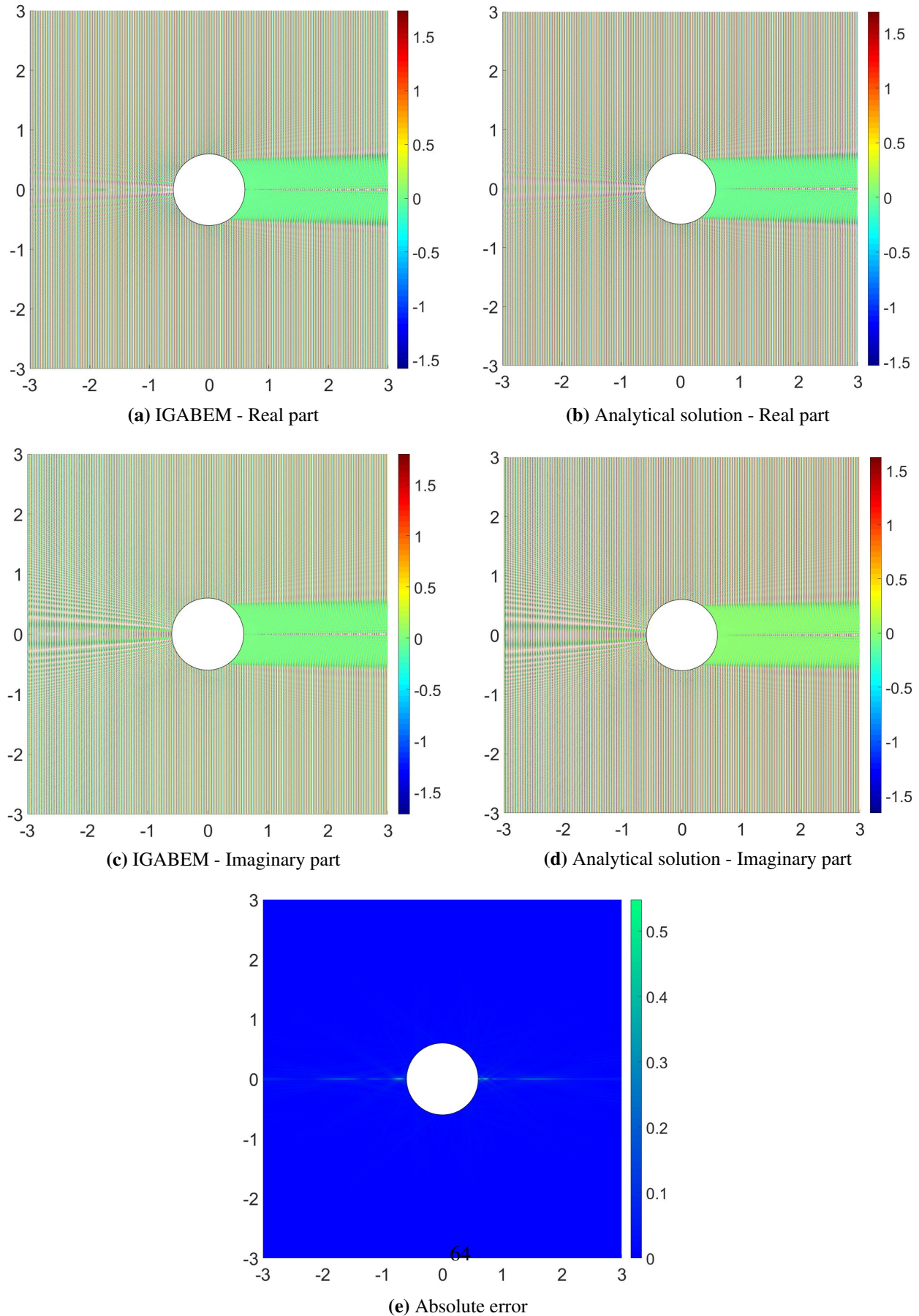
Figure 3.17: Acoustic pressure field values for the plane wave scattering problem by a rigid sphere for frequency of 20kHz.
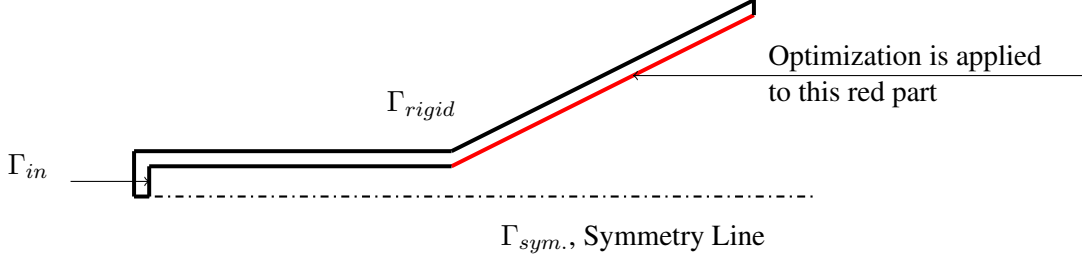
Figure 3.18: The horn problem domain.

3.6.2 Shape optimization analysis for the acoustic horn problem

The main objective of this shape optimization problem is to design the acoustic horn providing an efficient transmission of the incoming wave energy and robust distribution of this energy to the far field. The horn problem was previously studied in planar symmetry as a 2D problem in many researches using FEM with the topology optimization [120, 121], and the sensitivity analysis [64, 113]. Sensitivity analysis was also employed with cut-FEM in [122]. Gradient-free optimization methods were implemented for such problems using FEM with genetic algorithm [112] and using BEM with PSO [20]. The concerned study in this section is the horn problem with cylindrical symmetry in an infinite domain as a 3D axi-symmetric model for practical frequency values. In this chapter, the axi-symmetric model is coupled with PSO. This problem was previously studied by FEM with PSO [70]. Sensitivity analysis was coupled with FEM in [113], with discontinuous Galerkin method in [123] and with standard BEM in [36].

Consider the horn shown in figure 3.18, the horn inlet for the in-going wave is denoted by Γ_{in}. Γ_{rigid} refers to the rest of the horn rigid boundary. Due to the axial-symmetry of the problem along $\Gamma_{sym.}$, only the part shown in the figure is modelled.

The boundary value problem is written as follows:

$$\Delta u + k^2 u = 0 \qquad \text{in } \Omega, \tag{3.34}$$

$$\frac{\partial u}{\partial n} + iku = 2ikA_m \qquad \text{on } \Gamma_{in}, \tag{3.35}$$

$$\frac{\partial u}{\partial n} = 0 \qquad \text{on } \Gamma_{rigid} \cup \Gamma_{sym.}, \tag{3.36}$$

65

in which A_m refers to the amplitude of the incident wave in-going on Γ_{in}. The BIE eq.(3.2) is re-written to match the prescribed boundary conditions as follows:

$$c(\mathbf{P})u(\mathbf{P}) + \int_\Gamma \frac{\partial G(\mathbf{P}, \mathbf{Q})}{\partial n} u(\mathbf{Q}) d\Gamma(\mathbf{Q}) + ik \int_{\Gamma_{in}} G(\mathbf{P}, \mathbf{Q})u(\mathbf{Q}) d\Gamma(\mathbf{Q}) +$$
$$= 2ikA_m \int_{\Gamma_{in}} G(\mathbf{P}, \mathbf{Q}) d\Gamma(\mathbf{Q}), \mathbf{P}, \mathbf{Q} \in \Gamma. \tag{3.37}$$

With reference to the discretization using the NURBS shape functions, eq.(3.17) and eq.(3.37) can be rewritten as the following:

$$c(\xi_c) \sum_{i=1}^n u_i R_{i,p}(\xi_c) + \sum_{l=1}^{Ne} \sum_{i=1}^n \Big[\int_0^1 \Big[\int_0^{2\pi} \frac{\partial G(\xi_c, \xi, \phi)}{\partial n} d\phi \Big] R_{i,p}(\xi) |J_\xi^l| \rho(\xi) d\xi \Big] u_i +$$
$$ik \sum_{k=1}^{Ne_{in}} \sum_{j=1}^{nj} \Big[\int_0^1 \Big[\int_0^{2\pi} G(\xi_c, \xi, \phi) d\phi \Big] R_{j,p}(\xi) |J_\xi^k| \rho(\xi) d\xi \Big] u_j \tag{3.38}$$
$$= 2ikA_m \sum_{k=1}^{Ne_{in}} \Big[\int_0^1 \Big[\int_0^{2\pi} G(\xi_c, \xi, \phi) d\phi \Big] (\xi) |J_\xi^k| \rho(\xi) d\xi \Big],$$

in which Ne_{in} is the number of knot spans along the horn inlet Γ_{in} and nj is the number of NURBS basis functions inside the horn inlet Γ_{in}.

The wave reflection coefficient $R = B_m/A_m$ on Γ_{in} is minimized to fulfill the optimization problem, where $B_m = |u_{in} - A_m|$ is the reflected wave amplitude and u_{in} is the computed acoustic pressure along Γ_{in}. Since there is no constraint function in this optimization case, the fitness function defined in eq.(2.28) can be written in the form in eq.(3.39):

$$Fitness = F(x) = \min R. \tag{3.39}$$

The optimization is applied to the red portion of the horn boundary shown in figure 3.18. The x and y coordinates of the control points are considered as the design variables. The initial position of the design control points in addition to their upper and lower bounds are presented in figure 3.19.

The dimensions of the horn boundaries are chosen as follows: the inlet radius is 5cm. This radius is constant for a length of 50cm. Then, a flaring of length 50cm is introduced as shown in figure 3.18 with a varying radius from 5cm to 30cm. 2.5cm are set as the horn thickness with an amplitude $A_m = 1$ and the polynomial

66
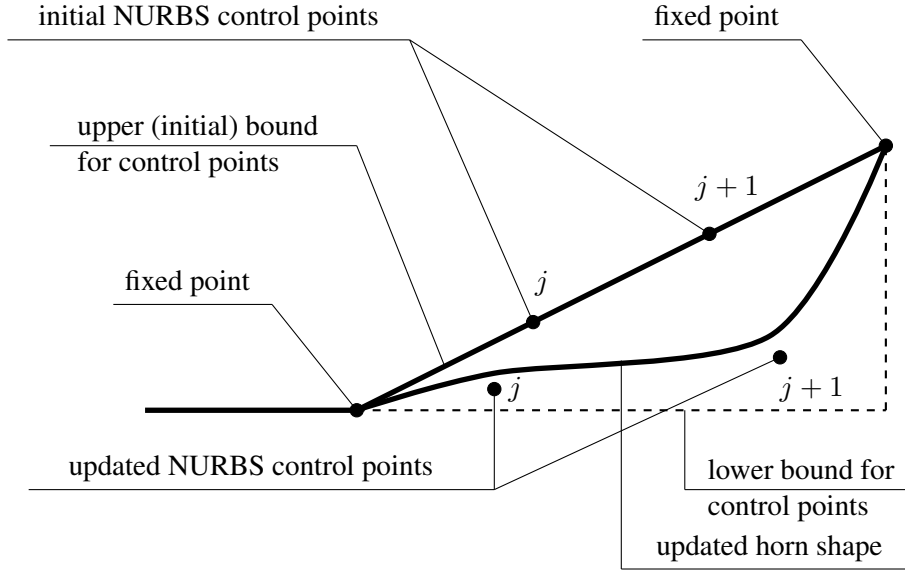
Figure 3.19: Arrangement of control points along the optimized part of the horn problem.

degree $p = 2$. 20 Gauss points are used in the purpose of the polar integration over the angle of revolution.

The differences between the proposed approach and the previous analysis performed in chapter 2 analyzing the horn problem with planar symmetry are summarized as follows:

1. In the current study, only the boundary of horn is modelled without the need to define any absorbing boundary conditions at infinity. This automatically satisfies the Sommerfeld radiation condition in eq.(3.1) and reduces the total degrees of freedom of the problem.

2. The presented model is simplified to an axi-symmetric three-dimensional problem with the 3D Green's function [36].

3. Singularities appear in eq.(3.38) in all integrals containing $G(\mathbf{P}, \mathbf{Q})$ along the the horn inlet Γ_{in} when the collocation points belong to the integrated element. These singularities are removed using the elliptical integration described in section 3.2.

4. The computed acoustic pressure along Γ_{in} in the current problem is defined as $u_{in} = \frac{2}{a^2} \int_{\Gamma_{in}} \rho u d\Gamma$ in which ρ is the distance from the cylindrical axis of symmetry [113, 36, 70].

3.6.2.1 Validation example using the initial shape of the horn

In order to illustrate the validity of the proposed technique, figure 3.20 presents the reflection spectrum of the initial shape shown in figure 3.18 using IGABEM compared to the same spectrum presented in [36]
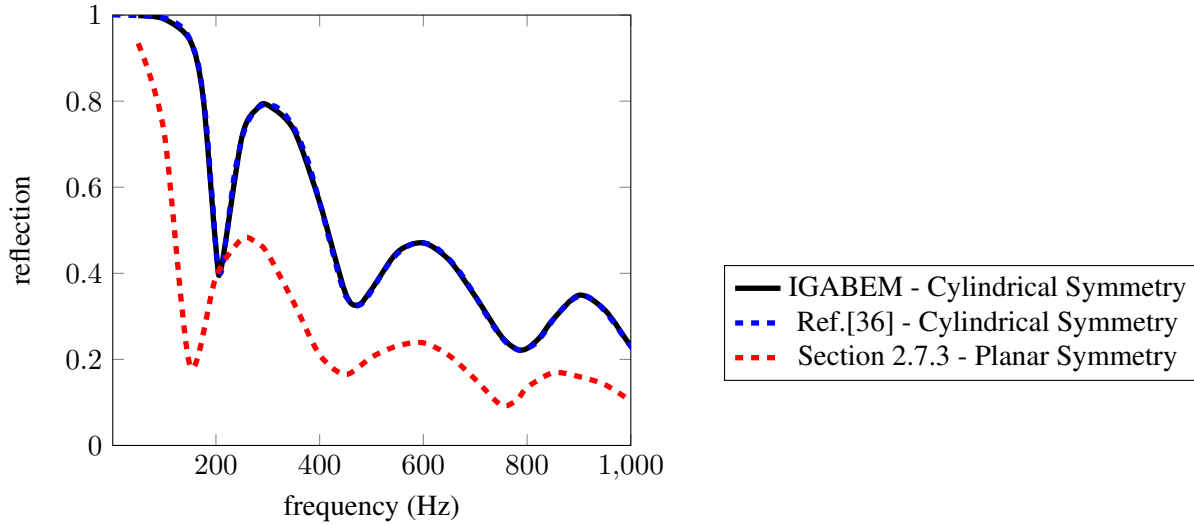
Figure 3.20: Reflection Spectra of the initial shape.

using BEM with the simple form of polynomial shape functions. Both spectra consider the horn problem with cylindrical symmetry. In addition, the spectrum considering the horn problem with planar symmetry presented in section 2.7.3 is included in the comparison. It can be seen that, the obtained spectrum from the proposed technique using only 128 NURBS Basis Functions is in excellent agreement with that obtained from [36] using 452 elements.

Furthermore, it is clear that, the reflection values obtained from the cylindrical horn are higher than those obtained from the planar horn. However, these higher values are more realistic since the actual/practical body of the horn is modelled in the axi-symmetric problem and no assumptions/approximations are considered in contrast to what is performed in the planar symmetry problem. This consequently prevents any misleading results in the optimization process.

In the following optimization cases, the obtained results from the proposed approach are presented in comparison with those reported in [113, 36, 70] which studied the cylindrical horn problem with axi-symmetric modeling as well. Sensitivity analysis with standard BEM using the simple form of polynomial shape functions was implemented in [36]. In [70], the same problem was solved using smoothing Hermite polynomials with finite element method (FEM) and PSO, while in [113], sensitivity analysis with FEM was performed. Both [70] and [113] used FEM with truncated boundaries in the far-field so that they required exaggerated degrees of freedom to model the infinite domain.

68
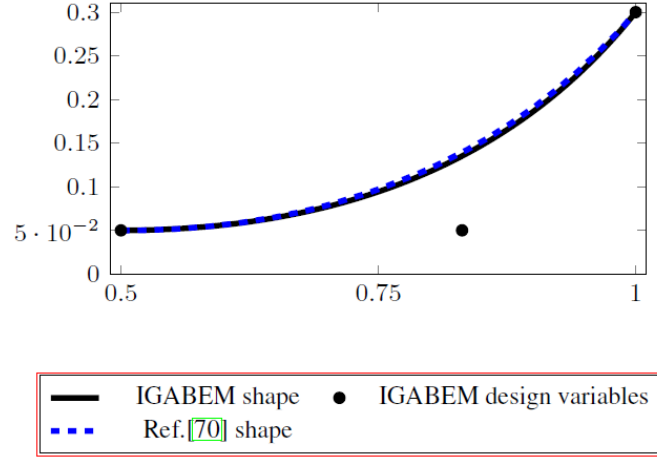
Figure 3.21: Optimized horn parts for frequency of 550 Hz.

3.6.2.2 Optimization for different single frequencies

Figure 3.21 demonstrates the optimized shape for a single frequency of 550 Hz with sound speed 345 m/s and wavenumber k=10.01667 using one control point (i.e. 2 design variables). This shape is compared to that obtained from [70]. Note that, in [70] the boundary was optimized using 3 design variables dividing the optimized part into 2 equal spans.

With reference again to figure 3.22, another comparison is presented against the optimized shapes obtained from [113] for single frequencies of 400, 600, 800 and 1000 Hz with wavenumber k=7.28485, 10.92728, 14.56971 and 18.21213, respectively using 59 design variables.

Figure 3.23 shows the variation of the reflection coefficient R during the optimization process. Figure 3.24 presents the reflection spectra for the initial and optimized horn shapes. The full description of the comparative models are shown in table 3.1.

3.6.2.3 Optimization for frequency band from 350 to 450 Hz

Another approach is presented in the following study to illustrate the performance of the proposed approach using 4 design variables (i.e. 2 control points) for different frequency bands from ω_1 to ω_2. Three schemes are used to compute the objective function values:

Scheme 1 is to minimize the average objective function of the reflection R:

$$\Pi = \min \frac{1}{\omega_2 - \omega_1} \int_{\omega_1}^{\omega_2} R \, d\omega. \tag{3.40}$$

69
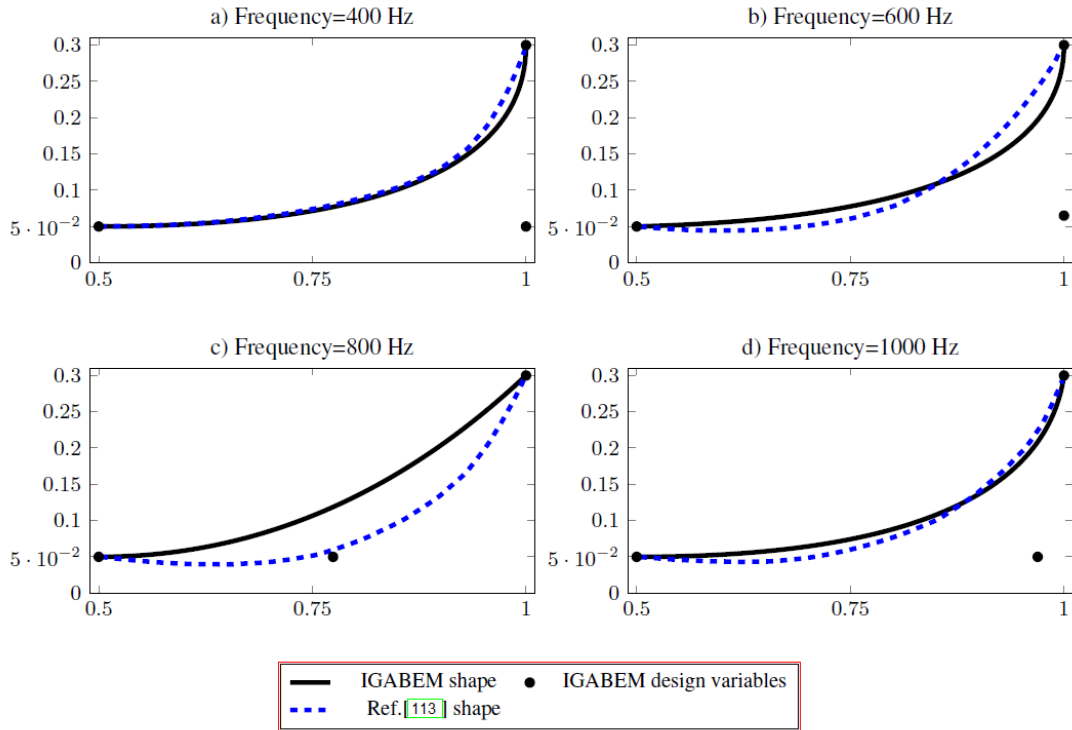
Figure 3.22: Optimized horn parts for different single frequencies.
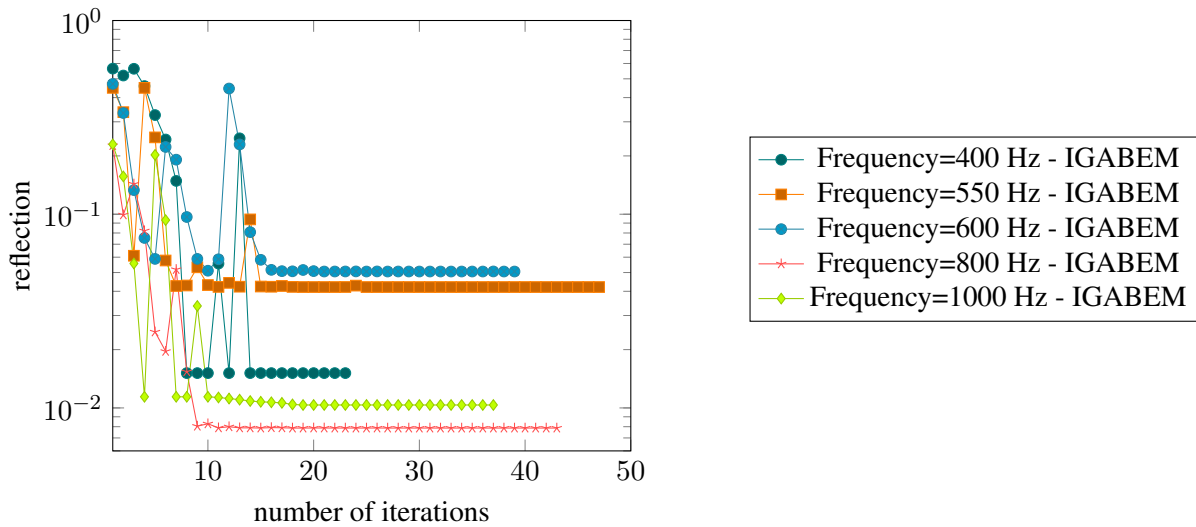
Figure 3.23: The reflection values vs the number of iterations for different single frequencies.

This function is integrated using only 4 Gauss quadrature points.

Scheme 2 is to compute the summation objective function of the reflection R for each frequency f:

$$\Pi = \min c \sum_{f \in F} |R_f|^2, \tag{3.41}$$

70
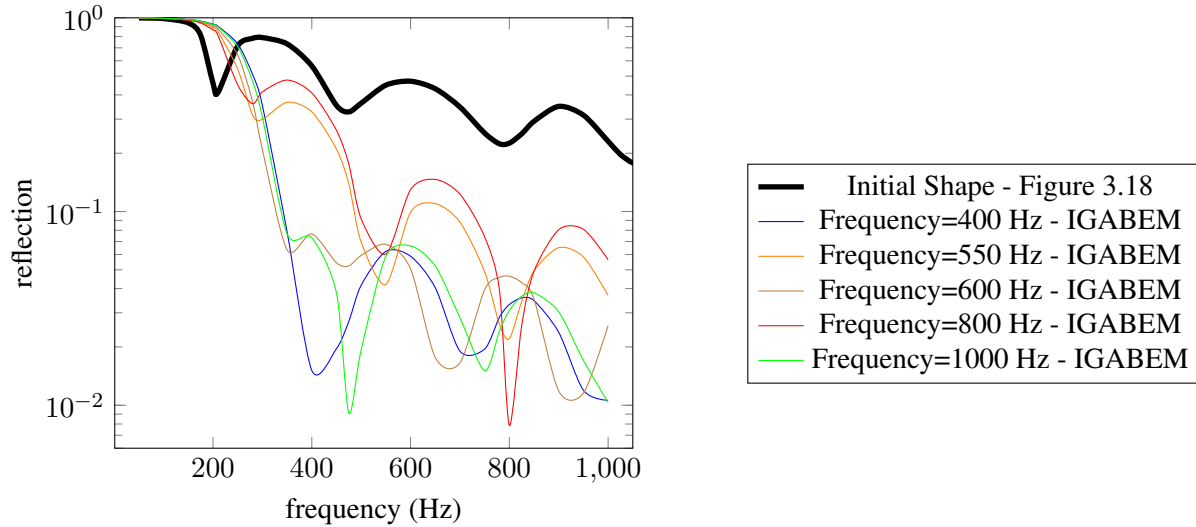
Figure 3.24: Reflection spectra for the optimized horns for different single frequencies.

		Ref.[70]	Ref.[113]	IGABEM
Frequency=400 Hz	Number of Design Variables	-	59	2
	N2 - Number of Consecutive Iterations for PSO	-	-	20
	kh/p along the Optimized Part	-	0.09	0.14
	Number of Elements/Wavelength along the Optimized Part	-	34.5	23.14
	Max. Element Size along the Optimized Part (m)	-	0.025	0.037
	Total DOFs	-	24304	128 NURBS Basis Functions
Frequency=550 Hz	Number of Design Variables	3	-	2
	N2 - Number of Consecutive Iterations for PSO	20	-	20
	kh/p along the Optimized Part	0.13	-	0.19
	Number of Elements/Wavelength along the Optimized Part	25.1	-	16.8
	Max. Element Size along the Optimized Part (m)	0.025	-	0.037
	Total DOFs	-	-	128 NURBS Basis Functions
Frequency=600 Hz	Number of Design Variables	-	59	2
	N2 - Number of Consecutive Iterations for PSO	-	-	20
	kh/p along the Optimized Part	-	0.14	0.20
	Number of Elements/Wavelength along the Optimized Part	-	23	15.40
	Max. Element Size along the Optimized Part (m)	-	0.025	0.037
	Total DOFs	-	24304	128 NURBS Basis Functions
Frequency=800 Hz	Number of Design Variables	-	59	2
	N2 - Number of Consecutive Iterations for PSO	-	-	20
	kh/p along the Optimized Part	-	0.18	0.20
	Number of Elements/Wavelength along the Optimized Part	-	17.25	15.40
	Max. Element Size along the Optimized Part (m)	-	0.025	0.028
	Total DOFs	-	24304	168 NURBS Basis Functions
Frequency=1000 Hz	Number of Design Variables	-	59	2
	N2 - Number of Consecutive Iterations for PSO	-	-	20
	kh/p along the Optimized Part	-	0.23	0.25
	Number of Elements/Wavelength along the Optimized Part	-	13.8	12.3
	Max. Element Size along the Optimized Part (m)	-	0.025	0.028
	Total DOFs	-	24304	168 NURBS Basis Functions

Table 3.1: Comparative models for the horn problem for different single frequencies.
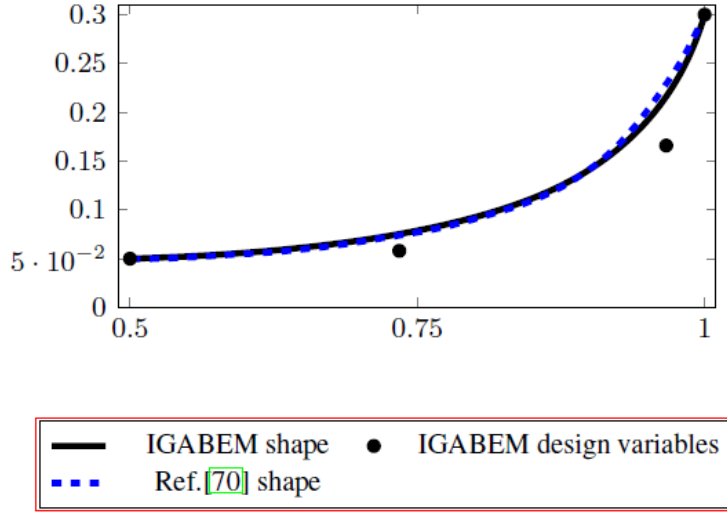
Figure 3.25: Optimized horn parts for frequency band from 350 to 450 Hz.

in which c is a chosen constant and $\mathbf{F}$ is the set of frequency band from ω_1 to ω_2 divided to 4 frequencies.

Scheme 3 is similar to Scheme 2, but the frequency band is divided to 10 frequencies.

Figure 3.25 demonstrates the optimized shape for a frequency band from 350 to 450 Hz compared to that obtained from [70] optimized using 15 design variables. The proposed shape is optimized using scheme 1 with 4 frequencies inside the frequency band while 11 frequencies are used in [70] with the same objective function scheme. It can be seen that, both shapes are in excellent agreement.

Figure 3.26 presents the variation of the objective function during the optimization process while figure

	Ref.[70]	IGABEM
Average Objective Function	1.37x10E-2	1.19x10E-2
Number of Design Variables	15	4
Number of frequencies inside the the frequency band	11	4
Number of Iterations	200	100
N2 - Number of Consecutive Iterations for PSO	10	20
kh/p along the Optimized Part	0.1	0.076
Number of Elements/Wavelength along the Optimized Part	30.7	41.14
Max. Element Size along the Optimized Part (m)	0.025	0.0186
Total DOFs	-	143 NURBS Basis Functions

Table 3.2: Comparative models for the horn problem for frequency band from 350 to 450 Hz.

3.27 shows the reflection spectra for the initial and optimized horn shapes. The full description of the comparative models are shown in table 3.2.

Figure 3.26: Convergence of the objective function in terms of the number of iterations for frequency band from 350 to 450 Hz.
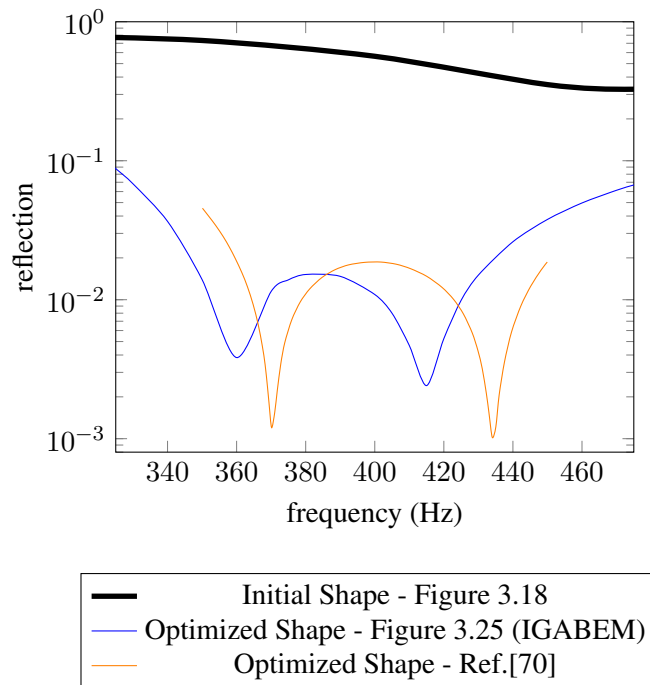
Figure 3.27: Reflection spectra for the initial and optimized horns for frequency band from 350 to 450 Hz.

3.6.2.4 Optimization for frequency band from 350 to 1150 Hz

In this case, the optimized shapes for a frequency band from 350 to 1150 Hz are compared to that obtained from [113] as shown in figure 3.28. In the proposed approach, the three prescribed schemes for computing
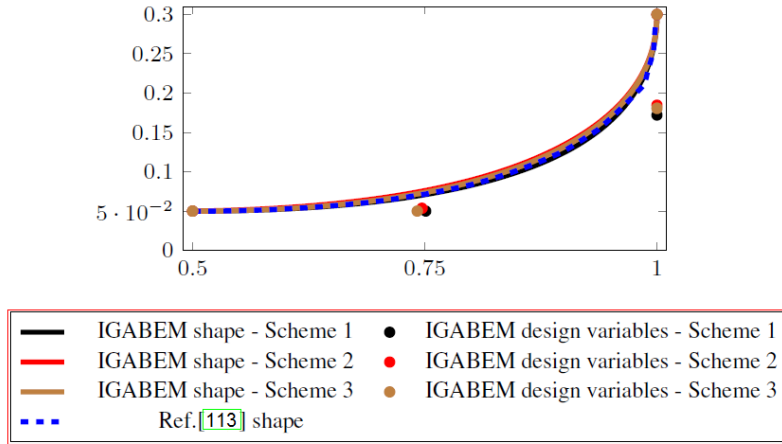
Figure 3.28: Optimized horn parts for frequency band from 350 to 1150 Hz.

the minimum objective function are used while Scheme 2 is used in [113] but with 31 frequencies inside the frequency band. The constant c in schemes 2 and 3 is chosen as 0.5 similarly to [113]. It can be seen that, all shapes are in excellent agreement which validates using only 4 frequencies inside the frequency band in schemes 1 and 2.
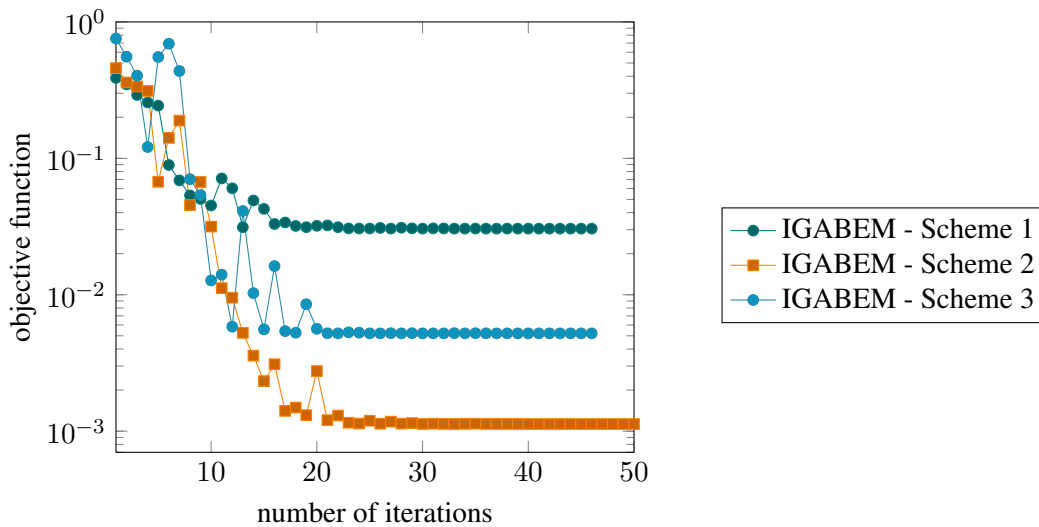
Figure 3.29: Convergence of the objective function in terms of the number of iterations for frequency band from 350 to 1150 Hz.

Figure 3.29 shows the variation of the objective function during the optimization processes while figure
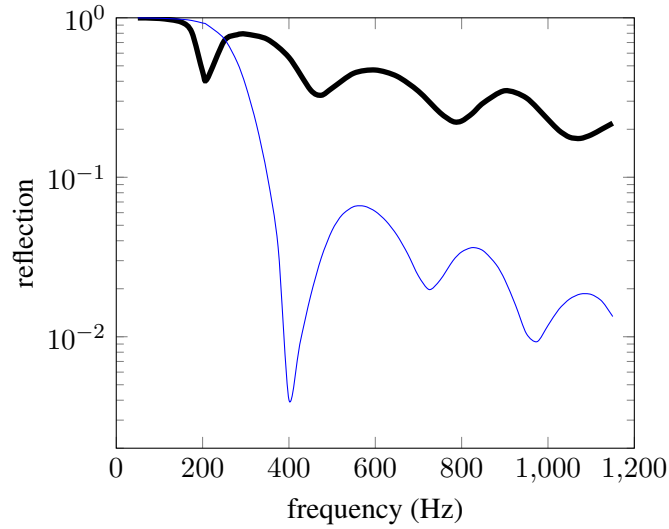
Figure 3.30: Reflection spectra for the initial and optimized horn for frequency band from 350 to 1150 Hz.

	Ref.[113]	IGABEM
Number of Design Variables	59	4
N2 - Number of Consecutive Iterations for PSO	-	20
kh/p along the Optimized Part for max. Frequency	0.26	0.2
Number of Elements/Wavelength along the Optimized Part for max. Frequency	12	16.1
Max. Element Size along the Optimized Part (m)	0.025	0.0186
Total DOFs	24304	143 NURBS Basis Functions

Table 3.3: Comparative models for the horn problem for frequency band from 350 to 1150 Hz.

3.30 illustrates the reflection spectra for the initial and optimized horn shapes. The full description of the comparative models are shown in table 3.3.

3.6.2.5 Optimization for frequency band from 523 to 880 Hz

The optimized shapes for a frequency band from 523 to 880 Hz are studied in this case and compared to that obtained from [36] using BEM with 452 degrees of freedom of the simple form of polynomial shape functions as shown in figure 3.31. Similar to the previous section, the three prescribed schemes for computing the minimum objective function are used while Scheme 2 is used in [36] using 10 frequencies inside the frequency band. The constant c in schemes 2 and 3 is chosen as $c=1$, similarly to [36]. In this optimization case, the solution is not unique and different optimal geometries can be obtained. The
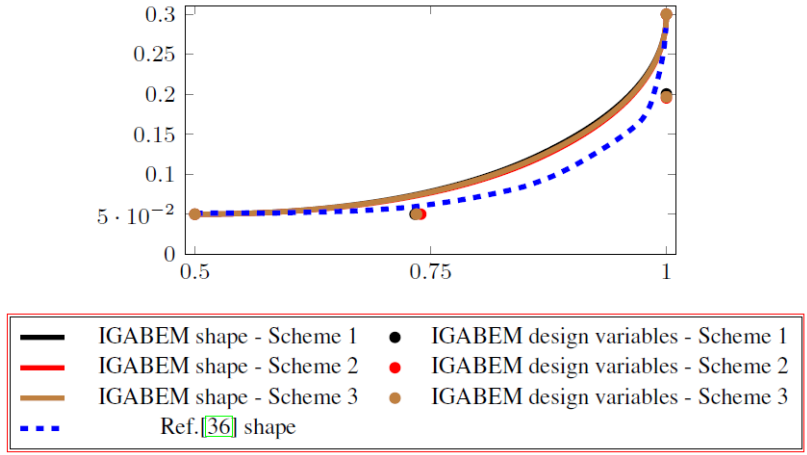
Figure 3.31: Optimized horn parts for frequency band from 523 to 880 Hz.

presented shapes are those giving minimum values of objective function. This conclusion is similar to what obtained from [113, 36, 70]. From figure 3.31 it can be seen that, the three proposed schemes give the same shapes. This validates both of schemes 1 and 2 which use only 4 frequencies inside the frequency band. The proposed shapes are in a good agreement with that obtained from the reference. The variation of the
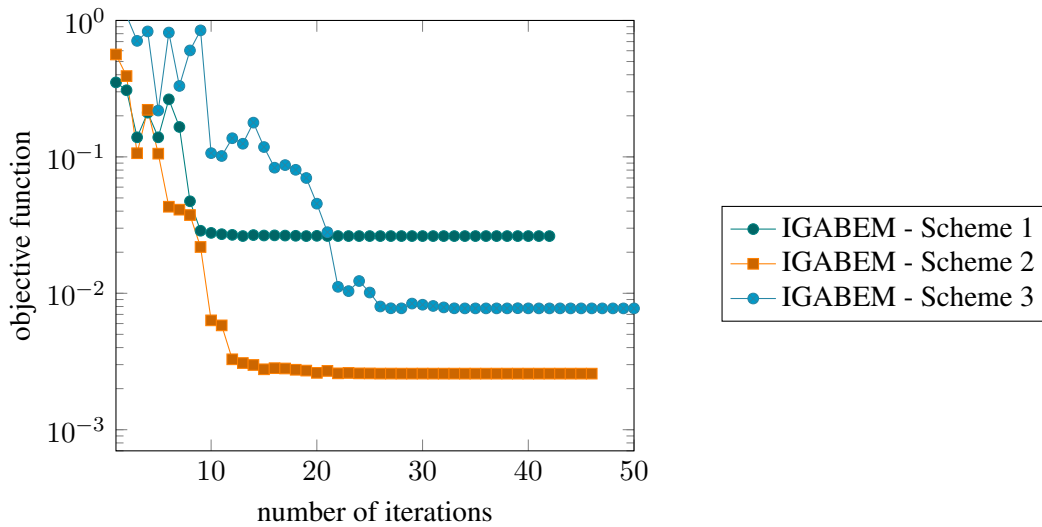
Figure 3.32: Convergence of the objective function in terms of the number of iterations for frequency band from 523 to 880 Hz.

objective function during the optimization processes is presented in figure 3.32 and the reflection spectra for the initial and optimized horn shapes are shown in figure 3.33. The full description of the model is shown in table 3.4.
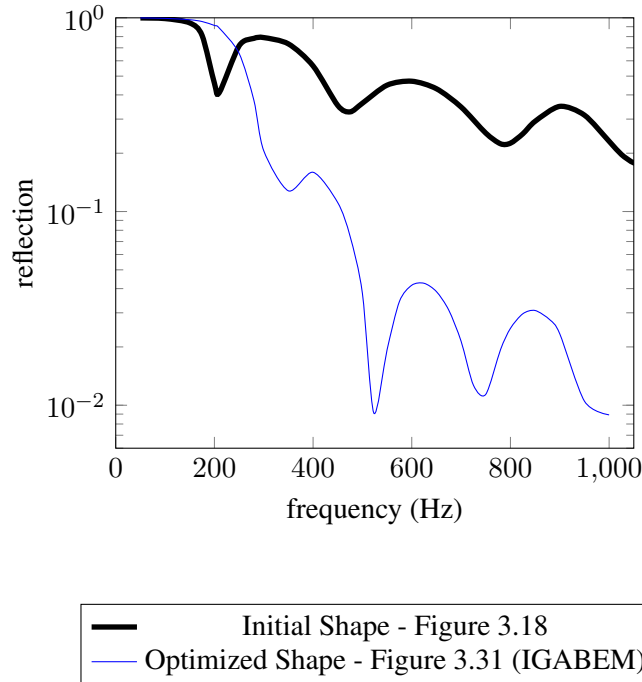
Figure 3.33: Reflection spectra for the initial and optimized horn for frequency band from 523 to 880 Hz.

	IGABEM
Number of Design Variables	4
N2 - Number of Consecutive Iterations for PSO	20
kh/p along the Optimized Part for max. Frequency	0.15
Number of Elements/Wavelength along the Optimized Part for max. Frequency	21
Max. Element Size along the Optimized Part (m)	0.0186
Total DOFs	143 NURBS Basis Functions

Table 3.4: Model description for the horn problem for frequency band from 523 to 880 Hz.

3.6.2.6 Optimization for frequency band from 622 to 1046 Hz

Similar to the optimization case discussed in section 3.6.2.5 compared to that obtained from [36], the frequency band from 622 to 1046 Hz is studied in this section as shown in figure 3.34. The proposed approach minimizes the objective function with the previous three prescribed schemes while Scheme 2 is used in [36] using 10 frequencies inside the frequency band. The constant c in schemes 2 and 3 is set equal to 1. Since the solution is not unique in this case as well and different optimal geometries can be obtained, only the shapes giving minimum values of objective function are presented. These shapes are typical as shown in figure 3.34 and are close to that obtained from the reference. Figure 3.35 presents the variation of the objective function during the optimization processes and the reflection spectra for the initial and optimized
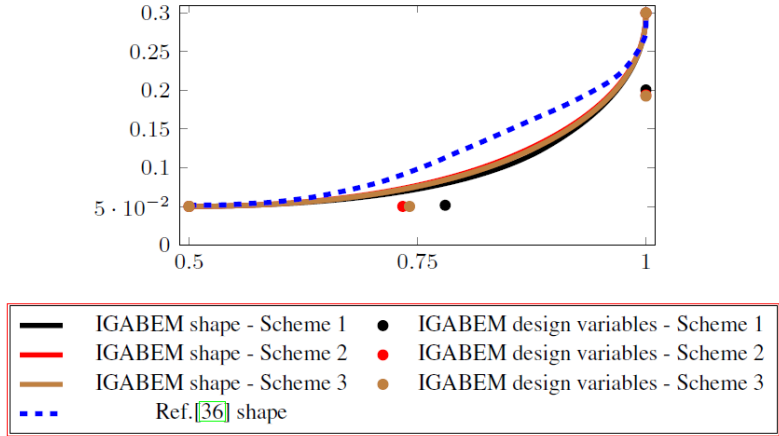
Figure 3.34: Optimized horn parts for frequency band from 622 to 1046 Hz.

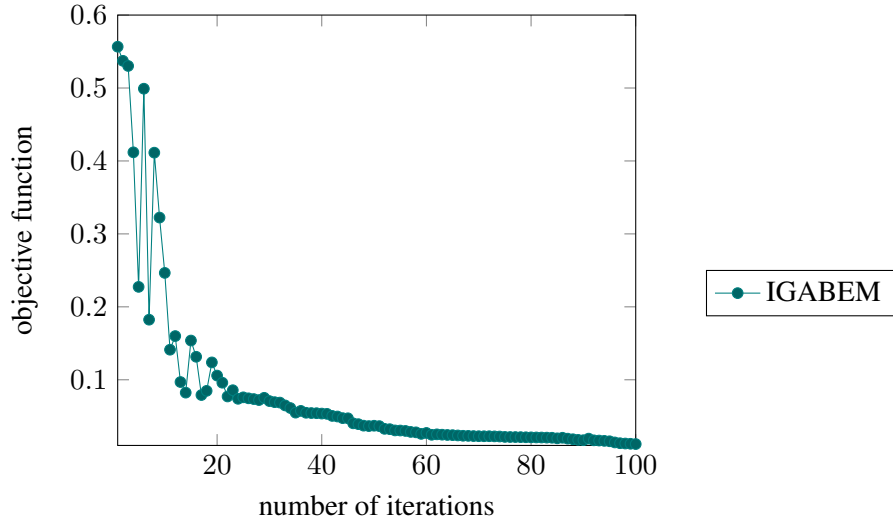horn shapes are shown in figure 3.36. The full description of the model is shown in table 3.5.
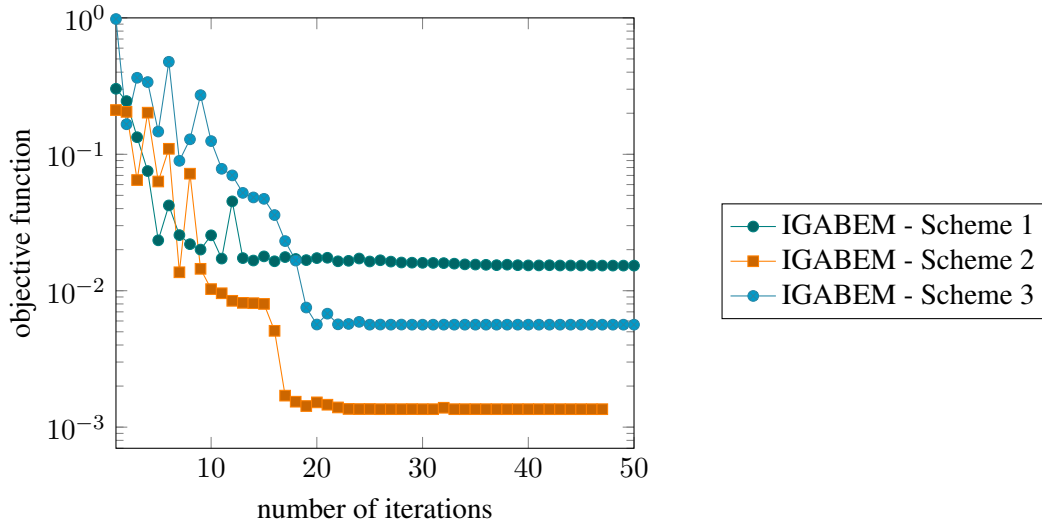
Figure 3.35: Convergence of the objective function in terms of the number of iterations for frequency band from 622 to 1046 Hz.

	IGABEM
Number of Design Variables	4
N2 - Number of Consecutive Iterations for PSO	40
kh/p along the Optimized Part for max. Frequency	0.18
Number of Elements/Wavelength along the Optimized Part for max. Frequency	17.7
Max. Element Size along the Optimized Part (m)	0.0186
Total DOFs	143 NURBS Basis Functions

Table 3.5: Model description for the horn problem for frequency band from 622 to 1046 Hz.
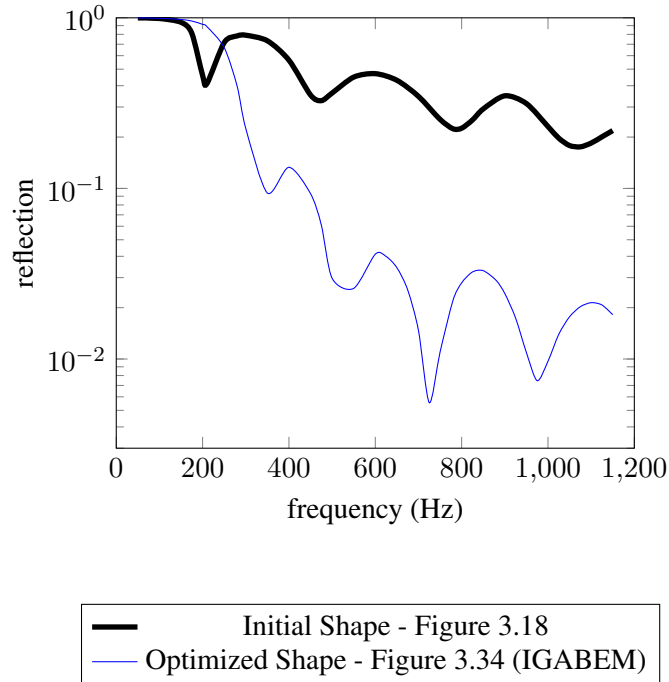
Figure 3.36: Reflection spectra for the initial and optimized horn for frequency band from 622 to 1046 Hz.

3.7 Summary

A 3D axi-symmetric Helmholtz acoustic problem is solved in this chapter by coupling the isogeometric analysis (IGA) and the boundary element method (IGABEM). Due to the axial symmetry, surface integration in the boundary integral equation (BIE) can be split into the line integral and reduced integration in the angular direction. This enables us to reduce dimensionality of the BIE to 1D (i.e. only the line BIE is descretised), resulting in significant computational savings and therefore, for the same computational capabilities, the proposed approach can be applied to much higher frequencies in comparison to a full 3D IGABEM.

Three numerical examples with a variety of frequencies were analysed for the spherical problems. The performance of IGABEM for axi-symmetric models was verified with the analytical solutions showing better capabilities for handling extremely high frequencies compared to the already published 3D models.

Axi-symmetric IGABEM was subsequently paired with the PSO for shape optimization. The advantage of using IGA in the optimization problem is to utilize the NURBS functions to represent the three different models: shape design, analysis and optimization models, using a set of control points representing also control variables and optimization parameters for the three models respectively making the transition through

the three models easy and straightforward.

Generally, since PSO does not require any sensitivity analysis, it is considered simpler to implement than the gradient-based optimization methods, but has a higher computational cost.

Then, different numerical examples considering several optimization cases of the horn problem with cylindrical symmetry were studied and the obtained results were compared with previously published methods. It was demonstrated that, the results of the present approach using fewer degrees of freedoms were in very good agreement with the previously published results. Minimization of the objective function regarding the frequency band cases using either summation or averaging methods with only 4 frequencies showed superior efficiency.

Chapter 4

Structural shape optimization with IGABEM for fully three-dimensional problem

based on the paper *'3D isogeometric boundary element analysis and structural shape optimization for Helmholtz acoustic scattering problems'* published in CMAME, where the contribution of each author is summarized as follows:

Ahmed Mostafa Shaaban

- Conceptualization
- Research state of the art
- Investigation
- Formal analysis
- Methodology
- Software / Programming
- Data curation
- Data analysis
- Validation
- Visualization

- Writing-original draft preparation

Cosmin Anitescu

- Conceptualization
- Writing-review and editing

Elena Atroshchenko

- Conceptualization
- Writing-review and editing

Timon Rabczuk

- Conceptualization
- Supervision
- Mentoring the research progress
- Review of the manuscript before submission

An electronic copy of this publication is available at: `https://doi.org/10.1016/j.cma.2021.113950`

4.1 General

The capability of boundary element methods (BEM) for solving three-dimensional time harmonic Helmholtz acoustic scattering problems is presented in the framework of the isogeometric analysis (IGA). Both the CAD geometry and the physical boundary variables are approximated using Non-uniform Rational B-splines basis functions (NURBS) in an isogeometric setting. A detailed comparison between two BEM methods: the conventional boundary integral equation (CBIE) and Burton-Miller (BM) is provided including the computational cost. The proposed models are enhanced with a modified collocation scheme with offsets to Greville abscissae to avoid placing collocation points at the corners. Placing collocation points on smooth surface enables accurate evaluation of normals for BM formulation in addition to straightforward prediction of jump-terms and avoids singularities in $\mathcal{O}(1/r)$ integrals eliminating the need for polar integration. Furthermore, no additional special treatment is required for the hyper-singular integral while collocating on highly distorted elements, such as those containing sphere poles.

Acoustic shape optimization in different mediums (air and water) is performed with Particle Swarm Optimization (PSO) and the results are compared with the benchmark solutions from the literature. The reference solutions are obtained with BM which deals with higher order singularities and gradient-based optimization, and requires more complicated sensitivity analysis. The obtained results indicate that, CBIE with PSO is a feasible alternative (except for a small number of fictitious frequencies) which is easier to implement.

4.2 Formulation of BEM for Helmholtz time harmonic equation
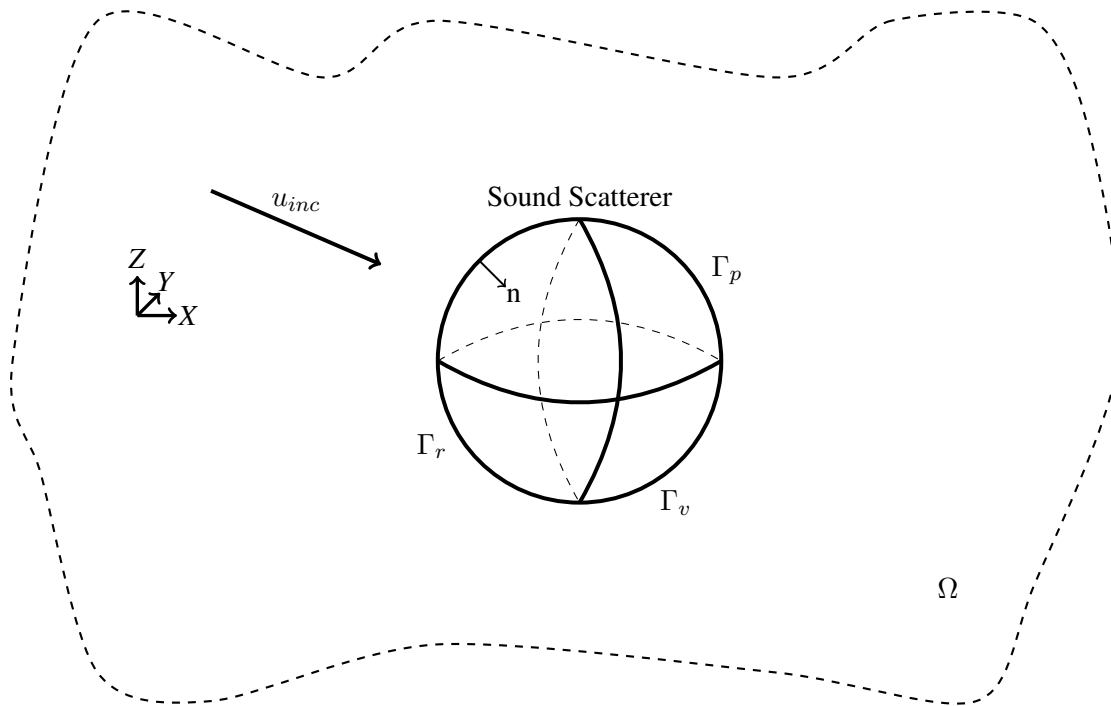
Figure 4.1: The exterior infinite 3D acoustic problem.

The exterior infinite three dimensional domain Ω for an acoustic problem is occupied by an isotropic homogeneous medium as shown in figure 4.1. The boundary value problem which fulfills the Helmholtz equation is considered similar to that of the equations (2.1)-(2.4) in the previous section 2.2. On the scatterer boundary Γ, a unit normal vector $\mathbf{n}$ is defined pointing outward of Ω. Since this chapter concerns exterior problems, the direction of the vector n is pointing inside the scatterer.

Further to studying such cases of infinite domains, all potential reflections of spurious acoustic waves from the far-field at infinity must be truncated by the Sommerfeld radiation condition according to the formula:

$$\lim_{r \to \infty} r \left(\frac{\partial u}{\partial r} - iku \right) = 0, \tag{4.1}$$

where the distance from the origin is denoted by r.

The BVP with the application of the Green's second identity is transformed into the reduced form of the conventional boundary integral equation (CBIE) giving the final form [20, 21]:

$$c(\mathbf{p})u(\mathbf{p}) + \int_\Gamma \frac{\partial G(\mathbf{p}, \mathbf{q})}{\partial \mathbf{n}(\mathbf{q})} u(\mathbf{q}) d\Gamma(\mathbf{q}) = \int_\Gamma G(\mathbf{p}, \mathbf{q}) \frac{\partial u(\mathbf{q})}{\partial \mathbf{n}(\mathbf{q})} d\Gamma(\mathbf{q}) + u_{inc}(\mathbf{p}), \qquad \mathbf{p}, \mathbf{q} \in \Gamma, \tag{4.2}$$

in which $G(\mathbf{p}, \mathbf{q})$ refers to the Green's second identity representing the effect of a boundary point $\mathbf{q}$ on a free space source point $\mathbf{p}$. $u_{inc}(\mathbf{p})$ denotes the incident acoustic pressure. $c(\mathbf{p})$ indicates the jump-term which depends on the location of the source point $\mathbf{p}$. $c(\mathbf{p})$ equals 0.5 when the source point lies on a smooth surface, 0 when it is located outside the domain or 1 for any point inside the domain [8].

In some cases of exterior acoustic problems, fictitious eigenfrequencies appear due to the non-uniqueness of the numerical solution when using CBIE alone. Therefore, the Burton-Miller (BM) formulation is employed to overcome this problem, in which two boundary integral equations are merged together forming the following equation [38]:

$$\mathbf{CBIE} + \beta \mathbf{HBIE} = 0, \tag{4.3}$$

where CBIE denotes the conventional boundary integral equation. β is the coupling parameter which is chosen as $\beta = \frac{i}{k}$ according to [124]. HBIE refers to the hyper-singular boundary integral equation which is formulated by the differentiation of CBIE with respect to the normal $\mathbf{n}(\mathbf{p})$ at the source point $\mathbf{p}$ giving the following equation:

$$c(\mathbf{p}) \frac{\partial u(\mathbf{p})}{\partial \mathbf{n}(\mathbf{p})} + \int_\Gamma \frac{\partial^2 G(\mathbf{p}, \mathbf{q})}{\partial \mathbf{n}(\mathbf{q}) \partial \mathbf{n}(\mathbf{p})} u(\mathbf{q}) d\Gamma(\mathbf{q}) = \int_\Gamma \frac{\partial G(\mathbf{p}, \mathbf{q})}{\partial \mathbf{n}(\mathbf{p})} \frac{\partial u(\mathbf{q})}{\partial \mathbf{n}(\mathbf{q})} d\Gamma(\mathbf{q}) + \frac{\partial u_{inc}(\mathbf{p})}{\partial \mathbf{n}(\mathbf{p})}, \quad \mathbf{p}, \mathbf{q} \in \Gamma. \tag{4.4}$$

The Green's second identity corresponding to the Helmholtz equation for 3D problems is formulated as [124]:

84

$$G(\mathbf{p}, \mathbf{q}) = \frac{e^{ikr}}{4\pi r}, \tag{4.5}$$

in which $r = |\mathbf{p} - \mathbf{q}|$. The derivatives of the Green's second identity can be written as follows:

$$\frac{\partial G(\mathbf{p}, \mathbf{q})}{\partial \mathbf{n}(\mathbf{q})} = -\frac{e^{ikr}}{4\pi r^2}(1 - ikr)\frac{\partial r}{\partial \mathbf{n}(\mathbf{q})}, \tag{4.6}$$

$$\frac{\partial G(\mathbf{p}, \mathbf{q})}{\partial \mathbf{n}(\mathbf{p})} = -\frac{e^{ikr}}{4\pi r^2}(1 - ikr)\frac{\partial r}{\partial \mathbf{n}(\mathbf{p})}, \tag{4.7}$$

$$\frac{\partial^2 G(\mathbf{p}, \mathbf{q})}{\partial \mathbf{n}(\mathbf{q})\partial \mathbf{n}(\mathbf{p})} = \frac{e^{ikr}}{4\pi r^3}\left[(3 - 3ikr - k^2 r^2)\frac{\partial r}{\partial \mathbf{n}(\mathbf{q})}\frac{\partial r}{\partial \mathbf{n}(\mathbf{p})} + (1 - ikr)\mathbf{n}(\mathbf{p}) \cdot \mathbf{n}(\mathbf{q})\right], \tag{4.8}$$

in which

$$\frac{\partial r}{\partial n(\mathbf{q})} = \frac{\mathbf{x}(\mathbf{q}) - \mathbf{x}(\mathbf{p})}{r}\mathbf{n}(\mathbf{q}), \tag{4.9}$$

$$\frac{\partial r}{\partial n(\mathbf{p})} = -\frac{\mathbf{x}(\mathbf{q}) - \mathbf{x}(\mathbf{p})}{r}\mathbf{n}(\mathbf{p}), \tag{4.10}$$

where $\mathbf{x} = \{x, y, z\}$ is the coordinates of the concerned point either $\mathbf{p}$ or $\mathbf{q}$. The kernel in eq.(4.5) has a singularity of order $\mathcal{O}(1/r)$. The kernels in both equations (4.6) and (4.7) involve a singularity of order $\mathcal{O}(1/r^2)$. However, due to the existence of $\frac{\partial r}{\partial \mathbf{n}}$, the singularity order is reduced to $\mathcal{O}(1/r)$. A method for treating this singularity is presented in section 4.3. Due to the presence of the hyper-singular term $\frac{\mathbf{n}(\mathbf{p}) \cdot \mathbf{n}(\mathbf{q})}{4\pi r^3}$ after expanding the kernel in eq.(4.8) into series while $r \to 0$, a hyper-singularity of order $\mathcal{O}(1/r^3)$ appears under the integral and requires special treatment when the collocation point is in the integrated element. The hyper-singularity in this case is removed using the singularity subtraction technique (SST) following [40]. Due to the existence of $\frac{\partial r}{\partial \mathbf{n}(\mathbf{q})}\frac{\partial r}{\partial \mathbf{n}(\mathbf{p})}$, the rest of kernels in eq.(4.8) are either regular or singular of order $\mathcal{O}(1/r)$ similar to the kernels in equations (4.6) and (4.7).

The incident acoustic pressure considered in this chapter is written as:

$$u_{inc}(\mathbf{p}) = Ae^{ik\,\mathbf{d}\cdot\mathbf{x}(\mathbf{p})}, \tag{4.11}$$

where A denotes the wave amplitude which is taken as 1.0. $|\mathbf{d}| = 1$ refers to the wavevector in the direction $\mathbf{d}$. $\mathbf{x}(\mathbf{p}) = \{x, y, z\}$ is the coordinates of point $\mathbf{p}$. The normal derivative of the incident acoustic pressure is formulated as follows:

$$\frac{\partial u_{inc}(\mathbf{p})}{\partial \mathbf{n}(\mathbf{p})} = ik\,\mathbf{d}\cdot\mathbf{n}(\mathbf{p})\,u_{inc}(\mathbf{p}). \tag{4.12}$$

Domain-type numerical methods (such as FEM) have to define another truncation surface on the far-field to fulfill the Sommerfeld radiation condition in eq.(4.1). However, both CBIE and BM automatically satisfy this condition without any need to define such surfaces.

4.3 NURBS basis functions and collocation

In one-dimensional parametric space $\xi \in [0, 1]$, the non-uniform rational B-spline functions (NURBS) can be written by means of the B-splines on a knot vector with a non-decreasing set of real numbers as follows: $\Xi = \{\xi_1 = 0, \cdots, \xi_i, \cdots, \xi_{n+p+1} = 1\}$, in which i refers to the knot index and n indicates the number of basis functions. As described in [10, 108], the ith B-spline basis function of pth -degree $N_{i,p}(\xi)$ in a recursive form is introduced as follows:

$$N_{i,0}(\xi) = \begin{cases} 1 & \xi_i \leq \xi < \xi_{i+1}, \\ 0 & \text{otherwise}, \end{cases} \tag{4.13}$$

and for $p \geq 1$

$$N_{i,p}(\xi) = \frac{\xi - \xi_i}{\xi_{i+p} - \xi_i} N_{i,p-1}(\xi) + \frac{\xi_{i+p+1} - \xi}{\xi_{i+p+1} - \xi_{i+1}} N_{i+1,p-1}(\xi). \tag{4.14}$$

The continuity of the B-spline basis function at ξ_i is C^{p-k} where k is the multiplicity. The continuity can be decreased by repeating the knot until it reaches C^0 when $k = p$. Discontinuity C^{-1} is obtained when the knots have multiplicity of $k = p + 1$.

The previous definitions can be extended into two-dimensional parametric space$(\xi, \eta) \in [0, 1] \times [0, 1]$.

Thus, two knot vectors are defined as follows: $\Xi = \{\xi_1 = 0, \cdots, \xi_i, \cdots, \xi_{n+p+1} = 1\}$ and $\Upsilon = \{\eta_1 = 0, \cdots, \eta_j, \cdots, \eta_{m+q+1} = 1\}$. The corresponding NURBS basis can be written in terms of the tensor product of 2D B-spline basis functions $N_{i,p}(\xi)$ and $N_{j,q}(\eta)$ as:

$$R_{ij}(\xi, \eta) = \frac{N_{i,p}(\xi)N_{j,q}(\eta)w_{ij}}{\sum\limits_{\bar{i}=1}^{n}\sum\limits_{\bar{j}=1}^{m} N_{\bar{i},p}(\xi)N_{\bar{j},q}(\eta)w_{\bar{i}\bar{j}}}, \tag{4.15}$$

where w_{ij} is the weight associated with the control point P_{ij}. The parameterization of the NURBS surface is then:

$$S(\xi, \eta) = \sum_{i=1}^{n}\sum_{j=1}^{m} R_{ij}(\xi, \eta)P_{ij}. \tag{4.16}$$

Thus, the physical boundary variables are defined as the acoustic pressure $u(\xi, \eta)$ and its normal derivative $\frac{\partial u}{\partial n}(\xi, \eta)$. These variables are approximated with NURBS basis functions as follows:

$$u(\xi, \eta) = \sum_{i=1}^{n}\sum_{j=1}^{m} R_{ij}(\xi, \eta)u_{ij}, \qquad \frac{\partial u}{\partial n}(\xi, \eta) = \sum_{i=1}^{n}\sum_{j=1}^{m} R_{ij}(\xi, \eta)q_{ij}, \tag{4.17}$$

in which u_{ij} and q_{ij} are the associated control variables.

The collocation strategy of the Greville abscissae presented in [13] is introduced here as well to generate the collocation points $\widehat{\xi}_a$ and $\widehat{\eta}_b$ for the two parametric spaces according to the formulas:

$$\begin{aligned}
\widehat{\xi}_a &= \frac{\xi_{a+1} + \xi_{a+2} + \cdots + \xi_{a+p}}{p}, & a &= 1, 2, \cdots, n, \\
\widehat{\eta}_b &= \frac{\eta_{b+1} + \eta_{b+2} + \cdots + \eta_{b+q}}{q}, & b &= 1, 2, \cdots, m,
\end{aligned} \tag{4.18}$$

producing $n \times m$ total collocation points which is equal to the total number of unknown control variables. In this chapter, the discontinuous basis functions with corresponding discontinuous physical boundary variables are implemented, wherever C^0 is encountered, by increasing the multiplicity of the corresponding knot in the knot vector and repeating the control point as well [41]. Thus, a discontinuity C^{-1} is obtained. With reference to the Greville abscissae in eq.(4.18) repeating the knot vector introduces repeated collocation point and this leads to a repeated equation in the linear system. In order to separate the two overlaid points and introduce another equation, an offset α between the original and shifted points is defined following the
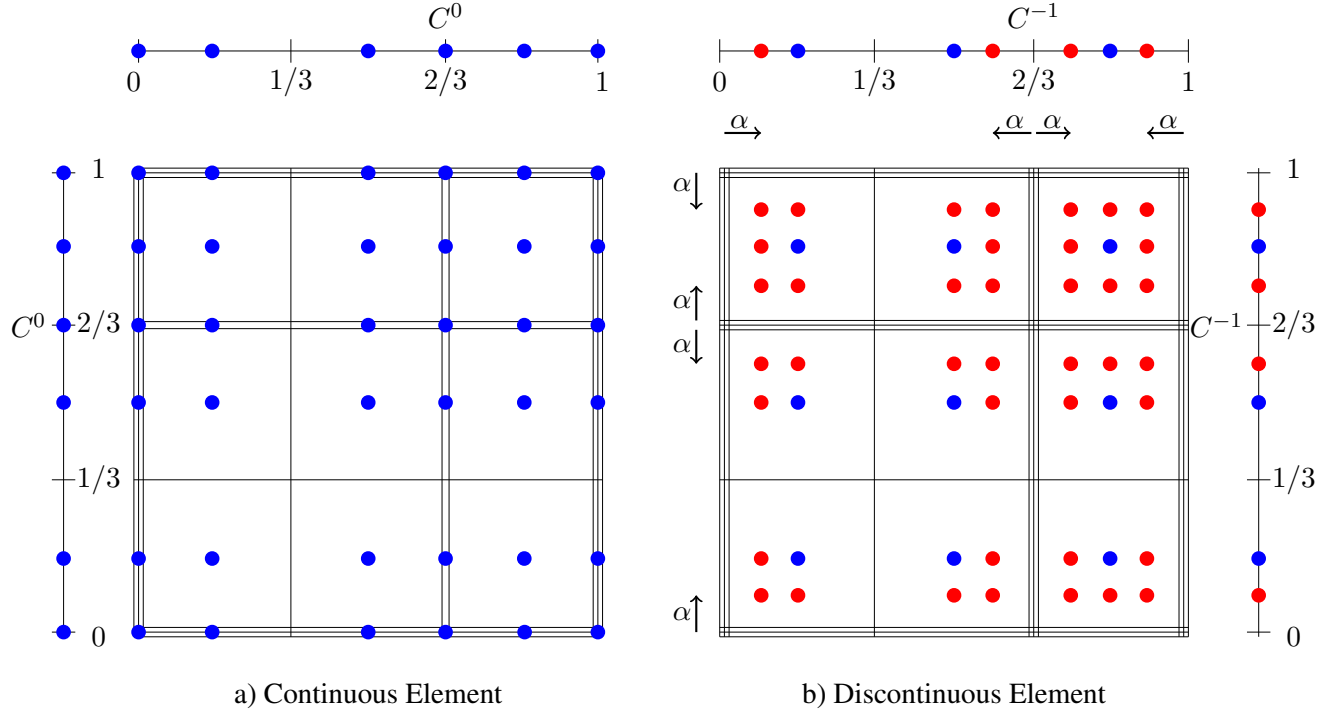
Figure 4.2: The offsets α between the original points in blue and the shifted points in red.

formulas:

$$\widehat{\widehat{\xi}}_a = \widehat{\xi}_a + \alpha(\widehat{\xi}_{a+1} - \widehat{\xi}_a), \qquad \text{and}$$

$$\widehat{\widehat{\xi}}_a = \widehat{\xi}_a - \alpha(\widehat{\xi}_a - \widehat{\xi}_{a-1}), \qquad 0 < \alpha < 1. \tag{4.19}$$

These offsets are applied to the first and last collocation points in the knot vector as well. Figure 4.2 explains the offsets between the original and shifted collocation points with the corresponding transition from C^0 to C^{-1} for an example with two knot vectors: $\Xi = \{0,0,0,1/3,2/3,2/3,1,1,1\}$ and $\Upsilon = \{0,0,0,1/3,2/3,2/3,1,1,1\}$ for the continuous element converted to $\Xi = \{0,0,0,1/3,2/3,2/3,2/3,1,1,1\}$ and $\Upsilon = \{0,0,0,1/3,2/3,2/3,2/3,1,1,1\}$ for the discontinuous element. The two NURBS polynomials are of degree 2.

As discussed in the previous section, HBIE requires the normal $\mathbf{n}(\mathbf{p})$ at the collocation/source point $\mathbf{p}$. But at sharp corners the normals are discontinuous. Moreover, when a collocation/source point is laid on either ξ_i or ξ_{i+1} sharing more than one element, that causes integration problem for the hyper-singular kernel since an integrated term appears that cannot be cancelled unlike the Cauchy Principle Value in the treatment of

the singular integral of order $\mathcal{O}(1/r)$ [125]. The offset α is considered as a key solution for this dilemma and the discontinuous basis functions allow the total DOFs to be equal to the total number of equations in the linear system without any loss of accuracy. These discontinuous basis functions can handle properly the discontinuous normal derivative of the acoustic pressure defined on the scatterers. Another advantage of the proposed offsets appears in the integration of the singular kernels of order $\mathcal{O}(1/r)$ in equations ((4.5)-(4.8)) as they can be treated as regular integrals since the collocation point $\widehat{\xi}_a$ is laid neither on ξ_i nor ξ_{i+1}. In addition, all collocation points are located on smooth surfaces, so that the jump-term $c(\mathbf{p})$ would equal 0.5 without any need for complex angle calculations at sharp corners. However, this offset has a drawback as it produces nearly singular integration for the kernel in eq.(4.8) over the neighbor element to the collocation point in BM. This could be overcome by an adaptive integration with more Gauss quadrature points only for the neighbor elements.

As a conclusion, the offset α should be chosen not to be so large so the accuracy would be reduced, nor so small so a nearly singular integral would occur over the neighbor element to the collocation point. In this thesis, the offset α is taken as 0.5 giving the best accuracy in the discussed examples. It is worth noting that, BM with the proposed discontinuous basis functions could produce satisfactory results using only NURBS polynomial of degree 2. The parameterization of the NURBS surface, the physical boundary variables and its normal derivative in eq.(4.17) and (4.16) can be re-written for each element as follows [15]:

$$
\begin{aligned}
S(\xi, \eta) &= \sum_{A=1}^{N} R_A(\xi, \eta) P_A, \\
u(\xi, \eta) &= \sum_{A=1}^{N} R_A(\xi, \eta) u_A, \\
\frac{\partial u}{\partial n}(\xi, \eta) &= \sum_{A=1}^{N} R_A(\xi, \eta) q_A,
\end{aligned}
\tag{4.20}
$$

where $N = (p+1) \times (q+1)$ is the total number of NURBS basis functions for an element, P_A, u_A and q_A are the associated control variables after mapping the local indices ij to the global index A.

Both CBIE and HBIE can be re-written after substituting eq.(4.20) into eq.(4.2) and eq.(4.4) at $n \times m$ collocation points (ξ_c, η_c) over a set of non-overlapping elements N_e discretizing the scatterer boundary to

give the following system of equations respectively:

$$c(\xi_c, \eta_c) \sum_{A=1}^{N} R_A(\xi_c, \eta_c) u_A + \sum_{e=1}^{Ne} \sum_{A=1}^{N} \left[\int_{\xi_{e_1}}^{\xi_{e_1+1}} \int_{\eta_{e_2}}^{\eta_{e_2+1}} \frac{\partial G(\mathbf{p}(\xi_c, \eta_c), \mathbf{q}(\xi, \eta))}{\partial \mathbf{n}(\xi, \eta)} R_A(\xi, \eta) |J^e(\xi, \eta)| d\xi d\eta \right] u_A =$$

$$\sum_{e=1}^{Ne} \sum_{A=1}^{N} \left[\int_{\xi_{e_1}}^{\xi_{e_1+1}} \int_{\eta_{e_2}}^{\eta_{e_2+1}} G(\mathbf{p}(\xi_c, \eta_c), \mathbf{q}(\xi, \eta)) R_A(\xi, \eta) |J^e(\xi, \eta)| d\xi d\eta \right] q_A + u_{inc}(\xi_c, \eta_c),$$

$$(4.21)$$

and

$$c(\xi_c, \eta_c) \sum_{A=1}^{N} R_A(\xi_c, \eta_c) q_A + \sum_{e=1}^{Ne} \sum_{A=1}^{N} \left[\int_{\xi_{e_1}}^{\xi_{e_1+1}} \int_{\eta_{e_2}}^{\eta_{e_2+1}} \frac{\partial^2 G(\mathbf{p}(\xi_c, \eta_c), \mathbf{q}(\xi, \eta))}{\partial \mathbf{n}(\xi, \eta) \partial \mathbf{n}(\xi_c, \eta_c)} R_A(\xi, \eta) |J^e(\xi, \eta)| d\xi d\eta \right] u_A =$$

$$\sum_{e=1}^{Ne} \sum_{A=1}^{N} \left[\int_{\xi_{e_1}}^{\xi_{e_1+1}} \int_{\eta_{e_2}}^{\eta_{e_2+1}} \frac{\partial G(\mathbf{p}(\xi_c, \eta_c), \mathbf{q}(\xi, \eta))}{\partial \mathbf{n}(\xi_c, \eta_c)} R_A(\xi, \eta) |J^e(\xi, \eta)| d\xi d\eta \right] q_A + \frac{\partial u_{inc}(\xi_c, \eta_c)}{\partial \mathbf{n}(\xi_c, \eta_c)},$$

$$(4.22)$$

where $[\xi_{e_1}, \xi_{e_1+1}] \times [\eta_{e_2}, \eta_{e_2+1}]$ is the eth NURBS element in the parametric space and $|J^e(\xi, \eta)|$ is the Jacobian from the physical to parametric space. e_1 and e_2 refer to the knot indices corresponding to the eth NURBS element for the first and second knot vectors, respectively. However, the numerical integration is implemented in the parent space $[-1, 1] \times [-1, 1]$. Thus, the Jacobian can be written at a local point $(\overline{\xi}, \overline{\eta})$ in the parent space as follows:

$$J_{\xi}^e(\overline{\xi}, \overline{\eta}) = \frac{dS}{d\xi} \frac{d\xi}{d\overline{\xi}} + \frac{dS}{d\eta} \frac{d\eta}{d\overline{\eta}}, \tag{4.23}$$

in which $\frac{dS}{d\xi}$ and $\frac{dS}{d\eta}$ are obtained from eq.(4.20), and

$$\frac{d\xi}{d\overline{\xi}} = \frac{\xi_{e_1+1} - \xi_{e_1}}{2},$$
$$\frac{d\eta}{d\overline{\eta}} = \frac{\eta_{e_2+1} - \eta_{e_2}}{2}. \tag{4.24}$$

The NURBS transformation for an integration point $(\overline{\xi}, \overline{\eta})$ in the parent space $[-1, 1] \times [-1, 1]$ to a global point (ξ, η) in the parametric space is introduced as follows:

$$\xi = \frac{(\xi_{e_1+1} - \xi_{e_1})\overline{\xi} + (\xi_{e_1+1} + \xi_{e_1})}{2},$$
$$\eta = \frac{(\eta_{e_2+1} - \eta_{e_2})\overline{\eta} + (\eta_{e_2+1} + \eta_{e_2})}{2}. \tag{4.25}$$

With reference to eq. (4.21), CBIE has the matrix form:

$$\mathbf{Hu} = \mathbf{Gt} + \mathbf{u}_{inc}, \tag{4.26}$$

where

$$\mathbf{H}_{ci} = c(\xi_c, \eta_c)R_A(\xi_c, \eta_c) + \int_{\xi_{e_1}}^{\xi_{e_1+1}} \int_{\eta_{e_2}}^{\eta_{e_2+1}} \frac{\partial G(\mathbf{p}(\xi_c, \eta_c), \mathbf{q}(\xi, \eta))}{\partial \mathbf{n}(\xi, \eta)} R_A(\xi, \eta)|J^e(\xi, \eta)|d\xi d\eta, \tag{4.27}$$

and

$$\mathbf{G}_{ci} = \int_{\xi_{e_1}}^{\xi_{e_1+1}} \int_{\eta_{e_2}}^{\eta_{e_2+1}} G(\mathbf{p}(\xi_c, \eta_c), \mathbf{q}(\xi, \eta))R_A(\xi, \eta)|J^e(\xi, \eta)|d\xi d\eta. \tag{4.28}$$

The previous matrix form can be written for BM using both equations (4.21) and (4.22) with the coupling parameter $\beta = \frac{i}{k}$ as follows:

$$\tilde{\mathbf{H}}\mathbf{u} = \tilde{\mathbf{G}}\mathbf{t} + \mathbf{u}_{inc} + \beta\frac{\partial \mathbf{u}_{inc}}{\partial \mathbf{n}}, \tag{4.29}$$

where

$$\tilde{\mathbf{H}}_{ci} = c(\xi_c, \eta_c)R_A(\xi_c, \eta_c) + \int_{\xi_{e_1}}^{\xi_{e_1+1}} \int_{\eta_{e_2}}^{\eta_{e_2+1}} \left[\frac{\partial G(\mathbf{p}(\xi_c, \eta_c), \mathbf{q}(\xi, \eta))}{\partial \mathbf{n}(\xi, \eta)} + \right.$$
$$\left. \beta\frac{\partial^2 G(\mathbf{p}(\xi_c, \eta_c), \mathbf{q}(\xi, \eta))}{\partial \mathbf{n}(\xi, \eta)\partial \mathbf{n}(\xi_c, \eta_c)} \right] R_A(\xi, \eta)|J^e(\xi, \eta)|d\xi d\eta, \tag{4.30}$$

and

$$\tilde{\mathbf{G}}_{ci} = \int_{\xi_{e_1}}^{\xi_{e_1+1}} \int_{\eta_{e_2}}^{\eta_{e_2+1}} \left[G(\mathbf{p}(\xi_c, \eta_c), \mathbf{q}(\xi, \eta)) + \right.$$
$$\left. \beta\frac{\partial G(\mathbf{p}(\xi_c, \eta_c), \mathbf{q}(\xi, \eta))}{\partial \mathbf{n}(\xi_c, \eta_c)} \right] R_A(\xi, \eta)|J^e(\xi, \eta)|d\xi d\eta - \beta c(\xi_c, \eta_c)R_A(\xi_c, \eta_c), \tag{4.31}$$

where $\mathbf{u}$, $\mathbf{t}$, $\mathbf{u}_{inc}$ and $\frac{\partial \mathbf{u}_{inc}}{\partial \mathbf{n}}$ refer to the vectors including the u_A, q_A, u_{inc} and $\frac{\partial u_{inc}}{\partial \mathbf{n}}$ components respectively.

Conclusively, eq.(4.26) or eq.(4.29) can be re-ordered into the linear system of equations:

$$\mathbf{Ax} = \mathbf{b}, \tag{4.32}$$

in which matrix $\mathbf{A}$ includes all entries of matrices $\mathbf{H}$ (or $\tilde{\mathbf{H}}$) and $\mathbf{G}$ (or $\tilde{\mathbf{G}}$) corresponding to the unknown control variables in CBIE or BM arranged in the vector $\mathbf{x}$, while the known components are placed in vector $\mathbf{b}$.

4.4 Numerical integration

4.4.1 Regular and Nearly Singular Integration

The integration schemes performed for each proposed boundary element method in this chapter are described as follows:

a) For CBIE models: Each knot span/interval $[\xi_{e_1}, \xi_{e_1+1}]$ or $[\eta_{e_2}, \eta_{e_2+1}]$ is divided into 4 uniform subdivisions resulting in 16 sub-divisions for $[\xi_{e_1}, \xi_{e_1+1}] \times [\eta_{e_2}, \eta_{e_2+1}]$. Since CBIE contains only regular integrals as discussed in sections 4.2 and 4.3, the integration is performed over each sub-division using 6 $\times$ 6 Gauss quadrature points. No adaptive integration is performed for the integration over the neighbor elements to the collocation point.

b) For BM models: The uniform sub-divisions are implemented here as well similar to the previous integration. 6 $\times$ 6 Gauss quadrature points are implemented for all regular integrals over each sub-division. Where the collocation point is subject to the transition procedures from C^0 to C^{-1} explained in section 4.3, a nearly singular integral appears over the neighbor elements to the collocation point. In order to overcome it, the singular part in the kernel of eq.(4.8) is extracted. Then, an adaptive integration using 20×20 Gauss quadrature points over each sub-division is implemented only for the integration of this part. The extraction of the singular part is explained in detail in the next subsection. Finally, the rest of the kernel is integrated using the regular integration scheme similar to regular integrals.

It is worth noting that, the numerical accuracy has been extensively investigated with relative to the integration Gauss quadrature points in both [24] and [26] where it was found out that, the relative error first decreased dramatically before it converged as the quadrature points increased, leading to a similar conclu-

sion suggesting using the proposed number of quadrature points.

4.4.2 Singularity Subtraction Technique for Hyper-singular Integration

In this section, the singularity subtraction technique (SST) proposed in [40] is discussed in detail with the associated integration scheme to overcome the hyper-singular integral of order $\mathcal{O}(1/r^3)$ for the kernel in eq.(4.8) when the collocation points are inside the integrated elements in BM models.

By expanding the kernel in eq.(4.8) into series for $r \to 0$, it can be found that, the whole kernel is regular except the hyper-singular term $\frac{\mathbf{n}(\mathbf{p}) \cdot \mathbf{n}(\mathbf{q})}{4\pi r^3}$. Thus, the following integral extracted from eq.(4.30):

$$I = \int_{\xi_{e_1}}^{\xi_{e_1}+1} \int_{\eta_{e_2}}^{\eta_{e_2}+1} \beta \frac{\partial^2 G(\mathbf{p}(\xi_c, \eta_c), \mathbf{q}(\xi, \eta))}{\partial \mathbf{n}(\xi, \eta) \partial \mathbf{n}(\xi_c, \eta_c)} R_A(\xi, \eta) |J^e(\xi, \eta)| d\xi d\eta, \tag{4.33}$$

can be re-written in the form:

$$I = \beta \int_{\xi_{e_1}}^{\xi_{e_1}+1} \int_{\eta_{e_2}}^{\eta_{e_2}+1} \left[\frac{\partial^2 G(\mathbf{p}(\xi_c, \eta_c), \mathbf{q}(\xi, \eta))}{\partial \mathbf{n}(\xi, \eta) \partial \mathbf{n}(\xi_c, \eta_c)} - \frac{\mathbf{n}(\mathbf{p}) \cdot \mathbf{n}(\mathbf{q})}{4\pi r^3} \right] R_A(\xi, \eta) |J^e(\xi, \eta)| d\xi d\eta +$$
$$\beta \int_{\xi_{e_1}}^{\xi_{e_1}+1} \int_{\eta_{e_2}}^{\eta_{e_2}+1} \frac{\mathbf{n}(\mathbf{p}) \cdot \mathbf{n}(\mathbf{q})}{4\pi r^3} R_A(\xi, \eta) |J^e(\xi, \eta)| d\xi d\eta = I_1 + I_2, \tag{4.34}$$

in which I_1 is a regular integral and can be obtained by the ordinary Gauss quadrature integration scheme explained in the previous subsection for regular integrals, while I_2 is a hyper-singular integral of order $\mathcal{O}(1/r^3)$. In order to remove this hyper-singularity, the integration is implemented in a polar coordinate system (ρ, θ) centered at the collocation/source point $(\bar{\xi}_c, \bar{\eta}_c)$ introduced in the parent space $[-1, 1] \times [-1, 1]$. For quadrature, the parent domain is divided into four triangles sharing the collocation/source point $(\bar{\xi}_c, \bar{\eta}_c)$ as shown in figure 4.3. Each field point $(\bar{\xi}, \bar{\eta})$ in the sub-triangles can be written in the parent space as follows:

$$\bar{\xi} = \bar{\xi}_c + \rho \cos \theta,$$
$$\bar{\eta} = \bar{\eta}_c + \rho \sin \theta, \tag{4.35}$$

and the transformation from the polar domain to the parent domain is:

$$d\bar{\xi} d\bar{\eta} = \rho d\rho d\theta, \tag{4.36}$$

93
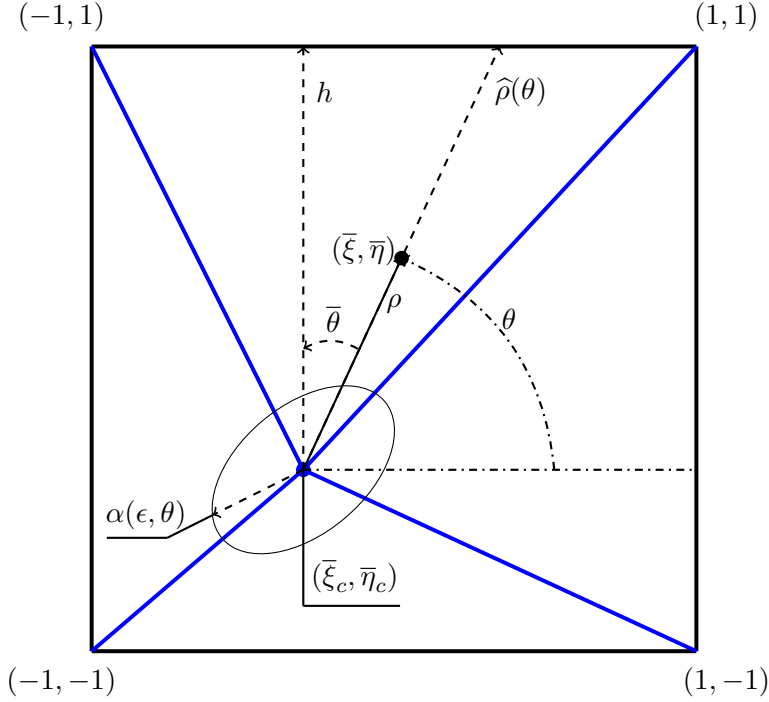
Figure 4.3: Polar coordinate systems in the parent space for SST.

so that, the integral I_2 is re-written as follows:

$$I_2 = \beta \lim_{\epsilon \to 0} \int_0^{2\pi} \int_{\alpha(\epsilon,\theta)}^{\widehat{\rho}(\theta)} \frac{\mathbf{n}(\mathbf{p}) \cdot \mathbf{n}(\mathbf{q})}{4\pi r^3} R_A(\rho, \theta) |J^e(\rho, \theta)| \frac{\partial \xi}{\partial \bar{\xi}} \frac{\partial \eta}{\partial \bar{\eta}} \rho d\rho d\theta. \tag{4.37}$$

Hence, $\widehat{\rho}(\theta) = h/\cos\bar{\theta}$ where h is the shortest perpendicular length from the collocation/source point to the element edge and $\bar{\theta}$ is the angle from the perpendicular direction to the field point. A small hemisphere of radius ϵ is built around the source point. When $\rho \to 0$, $\alpha(\epsilon, \theta)$ can be written with respect to ϵ by Taylor series expansion as follows:

$$\rho = \alpha(\epsilon, \theta) = \epsilon\beta(\theta) + \epsilon^2\gamma(\theta) + \mathcal{O}(\epsilon^3), \tag{4.38}$$

as $\epsilon\beta(\theta)$ is an ellipse equation. The definitions of $\gamma(\theta)$ and $\beta(\theta)$ will be introduced later. The components of the integral I_2 are expanded separately as follows:

$$\frac{1}{r^3} = \frac{1}{A^3(\theta)\rho^3} - \frac{3C(\theta)}{A^5(\theta)\rho^2} + \mathcal{O}(\frac{1}{\rho}), \tag{4.39}$$

94

in which

$$A(\theta) = [A_1^2(\theta) + A_2^2(\theta) + A_3^2(\theta)]^{1/2},$$

$$B(\theta) = [B_1^2(\theta) + B_2^2(\theta) + B_3^2(\theta)]^{1/2},$$

$$C(\theta) = A_1(\theta)B_1(\theta) + A_2(\theta)B_2(\theta) + A_3(\theta)B_3(\theta). \tag{4.40}$$

Moreover,

$$A_i(\theta) = \frac{\partial x_i}{\partial \bar{\xi}}\bigg|_{\substack{\bar{\xi}=\bar{\xi}_c \\ \bar{\eta}=\bar{\eta}_c}} \cos(\theta) + \frac{\partial x_i}{\partial \bar{\eta}}\bigg|_{\substack{\bar{\xi}=\bar{\xi}_c \\ \bar{\eta}=\bar{\eta}_c}} \sin(\theta),$$

$$B_i(\theta) = \frac{\partial^2 x_i}{\partial \bar{\xi}^2}\bigg|_{\substack{\bar{\xi}=\bar{\xi}_c \\ \bar{\eta}=\bar{\eta}_c}} \frac{\cos^2(\theta)}{2} + \frac{\partial^2 x_i}{\partial \bar{\xi} \partial \bar{\eta}}\bigg|_{\substack{\bar{\xi}=\bar{\xi}_c \\ \bar{\eta}=\bar{\eta}_c}} \cos(\theta)\sin(\theta) + \frac{\partial^2 x_i}{\partial \bar{\eta}^2}\bigg|_{\substack{\bar{\xi}=\bar{\xi}_c \\ \bar{\eta}=\bar{\eta}_c}} \frac{\sin^2(\theta)}{2}, \tag{4.41}$$

where

$$\frac{\partial x_i}{\partial \bar{\xi}} = \frac{\partial x_i}{\partial \xi} \frac{\partial \xi}{\partial \bar{\xi}},$$

$$\frac{\partial x_i}{\partial \bar{\eta}} = \frac{\partial x_i}{\partial \eta} \frac{\partial \eta}{\partial \bar{\eta}},$$

$$\frac{\partial^2 x_i}{\partial \bar{\xi}^2} = \frac{\partial^2 x_i}{\partial \xi^2} \left(\frac{\partial \xi}{\partial \bar{\xi}}\right)^2,$$

$$\frac{\partial^2 x_i}{\partial \bar{\eta}^2} = \frac{\partial^2 x_i}{\partial \eta^2} \left(\frac{\partial \eta}{\partial \bar{\eta}}\right)^2,$$

$$\frac{\partial^2 x_i}{\partial \bar{\xi} \partial \bar{\eta}} = \frac{\partial^2 x_i}{\partial \xi \partial \eta} \frac{\partial \xi}{\partial \bar{\xi}} \frac{\partial \eta}{\partial \bar{\eta}}, \tag{4.42}$$

95

and

$$x_i = \sum_{A=1}^{N} R_A(\xi, \eta) x_i^A,$$

$$\frac{\partial x_i}{\partial \xi} = \sum_{A=1}^{N} \frac{\partial R_A(\xi, \eta)}{\partial \xi} x_i^A,$$

$$\frac{\partial x_i}{\partial \eta} = \sum_{A=1}^{N} \frac{\partial R_A(\xi, \eta)}{\partial \eta} x_i^A,$$

$$\frac{\partial^2 x_i}{\partial \xi^2} = \sum_{A=1}^{N} \frac{\partial^2 R_A(\xi, \eta)}{\partial \xi^2} x_i^A,$$

$$\frac{\partial^2 x_i}{\partial \eta^2} = \sum_{A=1}^{N} \frac{\partial^2 R_A(\xi, \eta)}{\partial \eta^2} x_i^A,$$

$$\frac{\partial^2 x_i}{\partial \xi \partial \eta} = \sum_{A=1}^{N} \frac{\partial^2 R_A(\xi, \eta)}{\partial \xi \partial \eta} x_i^A, \tag{4.43}$$

in which x_i^A is the associated control variables.

The NURBS basis functions are expanded as follows:

$$R_A(\xi, \eta) = R_A(\xi_c, \eta_c) + \rho \left[\cos(\theta) \frac{\partial R_A}{\partial \bar{\xi}} \Big|_{\substack{\bar{\xi} = \bar{\xi}_c \\ \bar{\eta} = \bar{\eta}_c}} + \sin(\theta) \frac{\partial R_A}{\partial \bar{\eta}} \Big|_{\substack{\bar{\xi} = \bar{\xi}_c \\ \bar{\eta} = \bar{\eta}_c}} \right] + \mathcal{O}(\rho^2) = R_A^0 + \rho R_A^1(\theta) + \mathcal{O}(\rho^2), \tag{4.44}$$

in which

$$\frac{\partial R_A}{\partial \bar{\xi}} = \frac{\partial R_A}{\partial \xi} \frac{\partial \xi}{\partial \bar{\xi}},$$
$$\frac{\partial R_A}{\partial \bar{\eta}} = \frac{\partial R_A}{\partial \eta} \frac{\partial \eta}{\partial \bar{\eta}}. \tag{4.45}$$

The normal vector at a field point $\mathbf{q}(\xi, \eta)$ can be expressed as:

$$\mathbf{n}(\xi, \eta) = \frac{J_i(\xi, \eta)}{|J^e(\xi, \eta)|}, \tag{4.46}$$

96

where $J_i(\xi, \eta)$ are the components of the vector

$$
\begin{aligned}
J(\xi, \eta) = m_1 \times m_2 &= \left[\frac{\partial x_1}{\partial \xi}, \frac{\partial x_2}{\partial \xi}, \frac{\partial x_3}{\partial \xi} \right] \times \left[\frac{\partial x_1}{\partial \eta}, \frac{\partial x_2}{\partial \eta}, \frac{\partial x_3}{\partial \eta} \right] = \\
&\left[\frac{\partial x_2}{\partial \xi} \frac{\partial x_3}{\partial \eta} - \frac{\partial x_3}{\partial \xi} \frac{\partial x_2}{\partial \eta}, \frac{\partial x_3}{\partial \xi} \frac{\partial x_1}{\partial \eta} - \frac{\partial x_1}{\partial \xi} \frac{\partial x_3}{\partial \eta}, \frac{\partial x_1}{\partial \xi} \frac{\partial x_2}{\partial \eta} - \frac{\partial x_2}{\partial \xi} \frac{\partial x_1}{\partial \eta} \right],
\end{aligned}
\tag{4.47}
$$

in which m_1 and m_2 are the two tangential vectors along ξ and η directions respectively. The expansion of the kernel $\mathbf{n}(\mathbf{p}) \cdot \mathbf{n}(\mathbf{q})|J^e(\xi, \eta)|$ can be written as:

$$
\mathbf{n}(\mathbf{p}) \cdot \mathbf{n}(\mathbf{q})|J^e(\xi, \eta)| = \mathbf{n}(\xi_\mathbf{c}, \eta_\mathbf{c}) \cdot \mathbf{n}(\xi, \eta)|J^e(\xi, \eta)| = \mathbf{n}(\xi_\mathbf{c}, \eta_\mathbf{c}) \cdot J_i(\xi, \eta) =
$$

$$
\mathbf{n}(\xi_\mathbf{c}, \eta_\mathbf{c}) \cdot J_i(\xi_c, \eta_c) + \rho \mathbf{n}(\xi_\mathbf{c}, \eta_\mathbf{c}) \cdot \left[\cos(\theta) \frac{\partial J_i}{\partial \overline{\xi}} \bigg|_{\substack{\overline{\xi}=\overline{\xi}_c \\ \overline{\eta}=\overline{\eta}_c}} + \sin(\theta) \frac{\partial J_i}{\partial \overline{\eta}} \bigg|_{\substack{\overline{\xi}=\overline{\xi}_c \\ \overline{\eta}=\overline{\eta}_c}} \right] + \mathcal{O}(\rho^2)
$$

$$
= J_i^0 + \rho J_i^1(\theta) + \mathcal{O}(\rho^2),
\tag{4.48}
$$

in which

$$
\begin{aligned}
\frac{\partial J_i}{\partial \overline{\xi}} &= \frac{\partial J_i}{\partial \xi} \frac{\partial \xi}{\partial \overline{\xi}}, \\
\frac{\partial J_i}{\partial \overline{\eta}} &= \frac{\partial J_i}{\partial \eta} \frac{\partial \eta}{\partial \overline{\eta}}.
\end{aligned}
\tag{4.49}
$$

The integral I_2 in eq.(4.37) can be re-written after the explained expansions as follows:

$$
I_2 = \frac{\beta}{4\pi} \lim_{\epsilon \to 0} \int_0^{2\pi} \int_{\alpha(\epsilon,\theta)}^{\widehat{\rho}(\theta)} \left[\frac{1}{A^3(\theta)\rho^3} - \frac{3C(\theta)}{A^5(\theta)\rho^2} + \mathcal{O}(\frac{1}{\rho}) \right] \left[R_A^0 + \rho R_A^1(\theta) + \mathcal{O}(\rho^2) \right]
$$

$$
\left[J_i^0 + \rho J_i^1(\theta) + \mathcal{O}(\rho^2) \right] \frac{\partial \xi}{\partial \overline{\xi}} \frac{\partial \eta}{\partial \overline{\eta}} \rho d\rho d\theta =
$$

$$
\frac{\beta}{4\pi} \lim_{\epsilon \to 0} \int_0^{2\pi} \int_{\alpha(\epsilon,\theta)}^{\widehat{\rho}(\theta)} \left[\frac{R_A^0 J_i^0}{A^3(\theta)\rho^2} + \frac{R_A^0 J_i^1 + R_A^1 J_i^0}{A^3(\theta)\rho} - \frac{3C R_A^0 J_i^0}{A^5(\theta)\rho} + \mathcal{O}(1) \right] \frac{\partial \xi}{\partial \overline{\xi}} \frac{\partial \eta}{\partial \overline{\eta}} d\rho d\theta =
$$

$$
\frac{\beta}{4\pi} \lim_{\epsilon \to 0} \int_0^{2\pi} \int_{\alpha(\epsilon,\theta)}^{\widehat{\rho}(\theta)} \left[\frac{F_{-2}(\theta)}{\rho^2} + \frac{F_{-1}(\theta)}{\rho} + \mathcal{O}(1) \right] \frac{\partial \xi}{\partial \overline{\xi}} \frac{\partial \eta}{\partial \overline{\eta}} d\rho d\theta,
\tag{4.50}
$$

where

$$F_{-1}(\theta) = \frac{R_A^0 J_i^1 + R_A^1 J_i^0}{A^3(\theta)} - \frac{3C R_A^0 J_i^0}{A^5(\theta)}, \tag{4.51}$$

$$F_{-2}(\theta) = \frac{R_A^0 J_i^0}{A^3(\theta)}. \tag{4.52}$$

After that, the singular two terms are subtracted from the original integral I_2 in eq.(4.37) giving the regular integral I_{reg}:

$$I_{reg} = \frac{\beta}{4\pi} \int_0^{2\pi} \int_0^{\widehat{\rho}(\theta)} \left[\frac{\mathbf{n}(\mathbf{p}) \cdot \mathbf{n}(\mathbf{q})}{r^3} R_A(\rho,\theta) |J^e(\rho,\theta)| \rho - \frac{F_{-2}(\theta)}{\rho^2} - \frac{F_{-1}(\theta)}{\rho} \right] \frac{\partial \xi}{\partial \overline{\overline{\xi}}} \frac{\partial \eta}{\partial \overline{\eta}} d\rho d\theta, \tag{4.53}$$

which is integrated numerically using ordinary Gauss quadrature. Then, the two subtracted terms are summed again after an analytical integration with respect to ρ giving the following final forms:

$$I_{analytical_1} = \frac{\beta}{4\pi} \lim_{\epsilon \to 0} \int_0^{2\pi} \int_{\alpha(\epsilon,\theta)}^{\widehat{\rho}(\theta)} \frac{F_{-2}(\theta)}{\rho^2} \frac{\partial \xi}{\partial \overline{\overline{\xi}}} \frac{\partial \eta}{\partial \overline{\eta}} d\rho d\theta = \frac{\beta}{4\pi} \int_0^{2\pi} F_{-2}(\theta) \left[-\frac{\gamma(\theta)}{\beta^2(\theta)} - \frac{1}{\widehat{\rho}(\theta)} \right] \frac{\partial \xi}{\partial \overline{\overline{\xi}}} \frac{\partial \eta}{\partial \overline{\eta}} d\theta, \tag{4.54}$$

and

$$I_{analytical_2} = \frac{\beta}{4\pi} \lim_{\epsilon \to 0} \int_0^{2\pi} \int_{\alpha(\epsilon,\theta)}^{\widehat{\rho}(\theta)} \frac{F_{-1}(\theta)}{\rho} \frac{\partial \xi}{\partial \overline{\overline{\xi}}} \frac{\partial \eta}{\partial \overline{\eta}} d\rho d\theta = \frac{\beta}{4\pi} \int_0^{2\pi} F_{-1}(\theta) \ln \left| \frac{\widehat{\rho}(\theta)}{\beta(\theta)} \right| \frac{\partial \xi}{\partial \overline{\overline{\xi}}} \frac{\partial \eta}{\partial \overline{\eta}} d\theta, \tag{4.55}$$

where

$$\beta(\theta) = \frac{1}{A(\theta)},$$

$$\gamma(\theta) = \frac{-C(\theta)}{A^4(\theta)}, \tag{4.56}$$

so that,

$$I_2 = I_{reg} + I_{analytical_1} + I_{analytical_2}. \tag{4.57}$$

The integration with respect to θ is performed numerically for both $I_{analytical_1}$ and $I_{analytical_2}$. We refer to [40] for the evaluation of the analytical solution and any further details. The numerical integration with respect to θ is performed using 20 Gauss quadrature points for each sub-triangle while 40 points are used for the integration with respect to ρ.

4.5   Description of the structural shape optimization problem

The coupled structural shape optimization problem with BEM using the Particle Swarm Optimization (PSO) algorithm is considered as same as the previous section 2.6. In this chapter, the sound pressure in selected locations inside the problem domain is minimized relative to the minimum objective function:

$$F(x) = \min \, \overline{u_f} u_f, \tag{4.58}$$

in which u_f refers to the sound pressure vector at the defined locations, $\overline{u_f}$ indicates the complex conjugate vector of u_f. Moreover, the volume of the optimized scatterer is restricted not to exceed a constraint volume defined in each problem separately and is calculated as follows:

$$\text{Volume} = \int_\Omega d\Omega = \frac{1}{3} \sum_{e=1}^{ne} \int_0^1 \int_0^1 \mathbf{x} \cdot \mathbf{n} J_e(\xi, \eta) d\xi d\eta. \tag{4.59}$$

Thus, the fitness function can be re-written as follows:

$$\text{Fitness} = F(x) + \eta \times \max[(\text{Updated Volume} - \text{Constraint Volume}), 0]. \tag{4.60}$$

A flowchart explaining the different steps of the optimization algorithm with references to the corresponding equations is presented in figure 4.4.

4.6   Numerical results

In order to examine the performance of the proposed techniques for 3D problems, several numerical examples are solved. The first example presents an isogeometric analysis with both CBIE and BM against the analytical solution using the plane wave scattering problem by a rigid sphere showing the potential of the proposed approach. Then, different optimization problems are studied and the optimized shapes obtained from both CBIE and BM coupled with PSO are compared against the already published optimized shapes
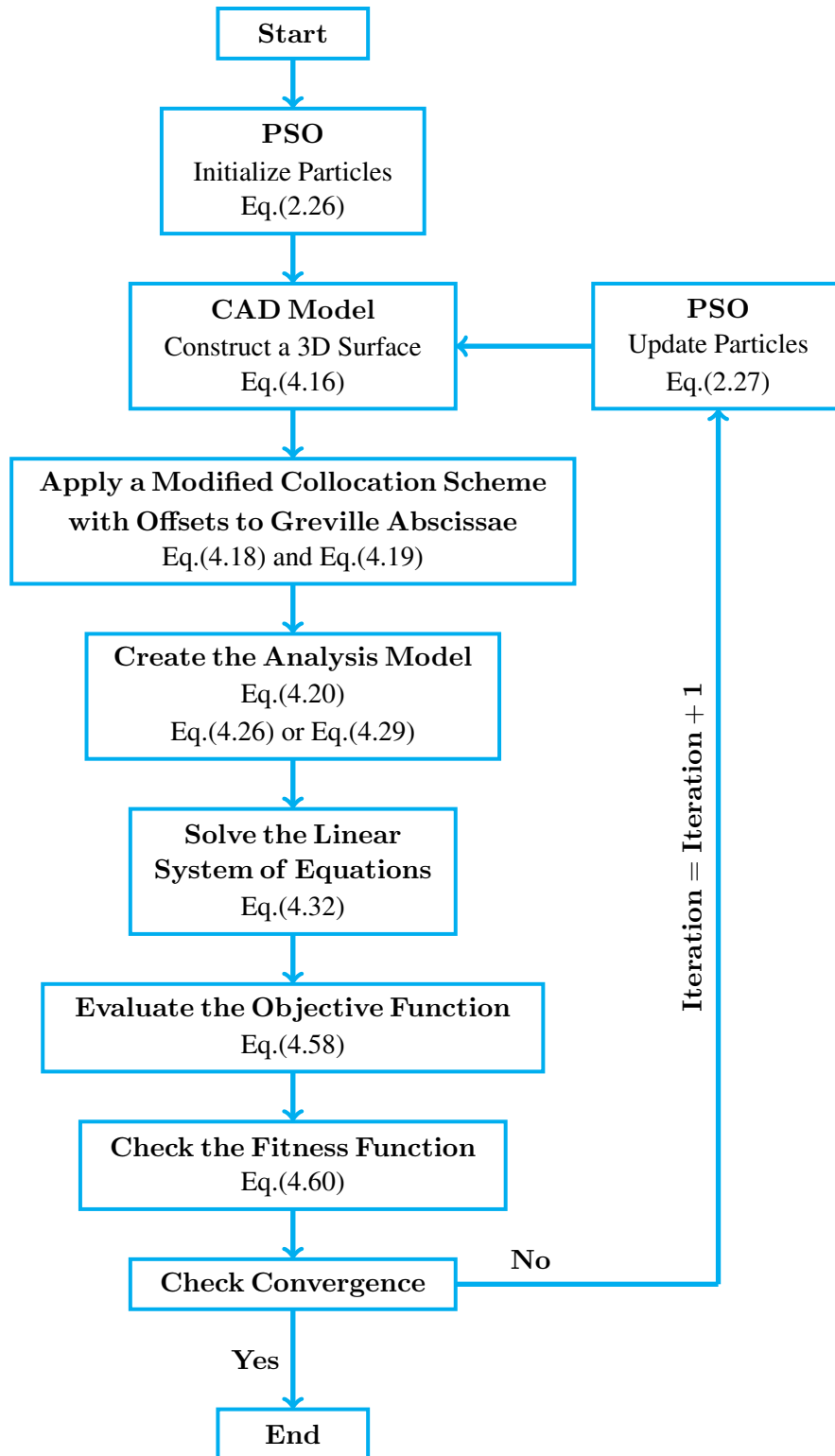
Figure 4.4: Flowchart showing the different steps of the optimization algorithm.
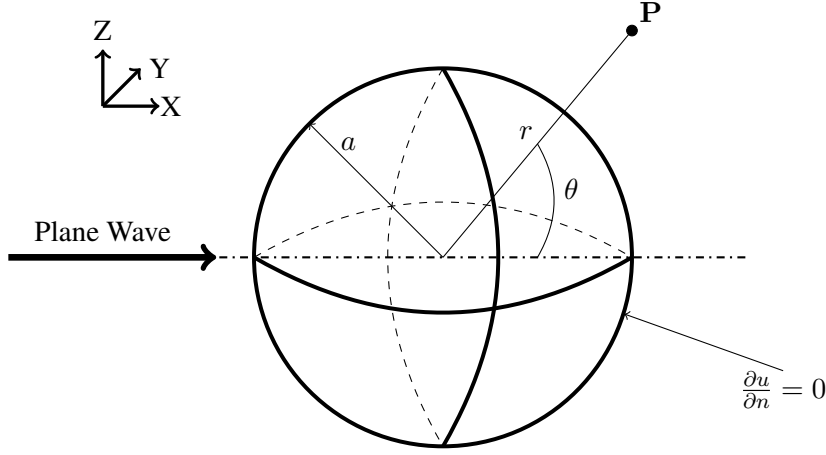
Figure 4.5: Plane wave scattering problem by a rigid sphere.

produced by BEM with shape sensitivity analysis.

4.6.1 Isogeometric analysis with CBIE and BM

In this section the plane wave scattering problem by a rigid sphere is discussed and validated by comparison with the analytical solution in order to verify the proposed techniques utilized in the optimization problems. Consider a rigid sphere ($\frac{\partial u}{\partial n} = 0$) centered at the origin with a radius $a = 1.0$ m embedded in air with density $\rho = 1.2$ kg/m^3 and sound speed $c = 343$ m/s.

With reference to the incident acoustic pressure mentioned in eq.(4.11), the incident wave transfers from the positive side of x-axis as $\mathbf{d} = \{1, 0, 0\}$. Then, the analytical solution of the total acoustic pressure [118, 119, 31] can be written as follows:

$$u^{ex}(r, \theta) = Ae^{ik\, d \cdot \mathbf{x}(\mathbf{p})} - \sum_{m=0}^{\infty} i^m (2m + 1) \frac{j'_m(ka)}{h'_m(ka)} h_m(kr) P_m(cos\theta) \quad , r \geq a, \tag{4.61}$$

in which r refers to the distance from the origin to the concerned point $\mathbf{P}$ and θ indicates the angle between the direction of the incident wave and the axis linking the point $\mathbf{P}$ with the origin as shown in figure 4.5. h_m and j_m are the spherical Hankel and Bessel functions of the first kind, respectively of order m. P_m is the Legendre polynomial of order m. The derivative with respect to its argument is denoted by $(')$. m is taken as 10 in this example which is sufficient for the purpose of studying the convergence for the used frequencies in this chapter.

The NURBS polynomial degree is considered as 2 for each knot direction to model the sphere with the cor-
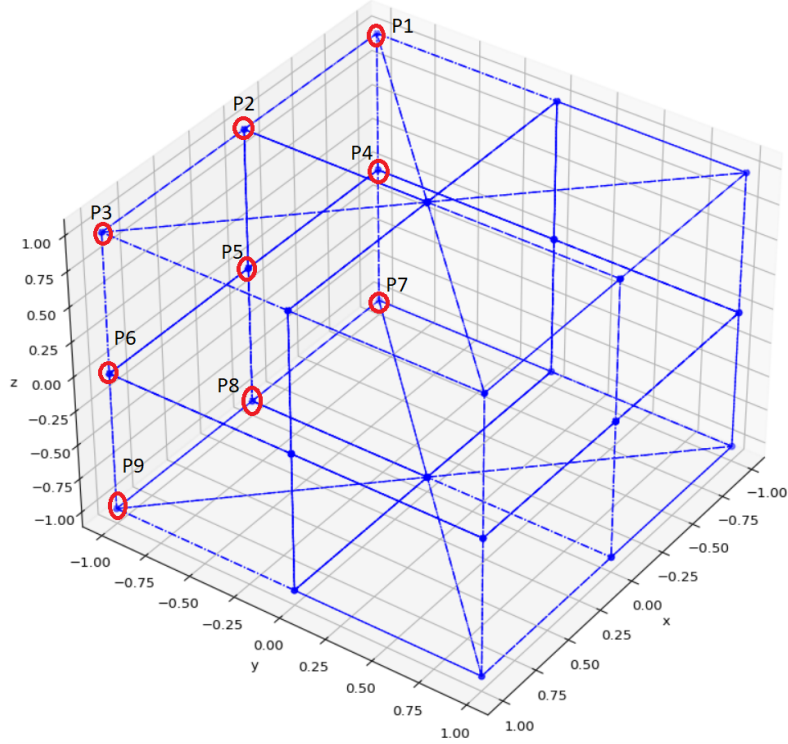
Figure 4.6: NURBS model and control points grid for the 3D sphere.

responding control points explained in figure 4.6. The two knot vectors in the two dimensions are defined as follows: $\Xi = \{0,0,0,0.5,0.5,1,1,1\}$ and $\Upsilon = \{0,0,0,0.25,0.25,0.5,0.5,0.75,0.75,1,1,1\}$. To verify the proposed numerical solution against the exact analytical solution, two schemes are studied:

1- On-Surface Relative L_2 Error Norm (e_{L_2})

Since the main objective of the boundary element methods is to find the accurate solution first on the surface/boundary of the domain (which is the spherical scatterer in this case), the relative L_2 error norm of numerical solution u^{num} is checked on the surface of the sphere using the following formula:

$$e_{L_2} \equiv \frac{||u^{ex} - u^{num}||}{||u^{ex}||} = \sqrt{\frac{\int_\Gamma (u^{num} - u^{ex})^T (u^{num} - u^{ex})d\Gamma}{\int_\Gamma u^{exT} u^{ex} d\Gamma}}, \tag{4.62}$$

in which the integration is performed using 6 Gauss quadrature points for each knot span.

2- Off-Surface Relative Error (e_D)

With respect to the optimization problem where the sound pressure values inside the domain and away from the scatterer have more attention, the relative error e_D is examined along $N = 200$ uniformly spaced points

on a circle in the X-Y plane at Z=0 inside the domain with a radius of 1.50m centered in the sphere origin according to the following:

$$e_D \equiv \frac{||u^{ex} - u^{num}||}{||u^{ex}||} = \sqrt{\frac{\sum\limits_{i=1}^{N} \left(u_i^{num} - u_i^{ex}\right)^T \left(u_i^{num} - u_i^{ex}\right)}{\sum\limits_{i=1}^{N} u_i^{exT} u_i^{ex}}}. \tag{4.63}$$

In the BEM solution, it is found that usually the produced errors from the Off-Surface scheme are less than those got from the On-Surface scheme due to the smooth integration away from the collocation point in the case of the Off-Surface scheme.

It is worth noting that, the elements containing the sphere poles are highly distorted triangle elements which are modelled by NURBS quadrangular elements with a collapsed edge. Special treatments are performed in [15, 23] to overcome the produced nearly singularity in the θ direction when using SST for the hyper-singular integral while collocating on the pole. However, in this thesis the application of the offsets to the collocation points with the integration scheme - explained in sections 4.3 and 4.4 - is sufficient and gives more accurate results.

Figure 4.7 illustrates the variation of the relative errors (e_{L_2} and e_D) as a function of the total degrees of freedom (DOFs) for both On- and Off-Surface schemes for some different frequencies: 50, 100, 150, 200, 250 and 300 Hz with wavenumbers k=0.92, 1.83, 2.75, 3.66, 4.58 and 5.50 respectively. These values are chosen since the same range of frequencies is used in the forthcoming optimization problems as well. Figure 4.8 demonstrates the compiled On-Surface plots showing the accuracy variation with higher frequencies using the same total DOFs while the compiled Off-Surface plots are presented in figure 4.9. As a function of moderate DOFs per wavelength in each coordinate direction (for each knot vector), the variation of the relative error is re-plotted in figure 4.10 where it can be concluded that, almost the same accuracy can be obtained using the same DOFs/wavelength for all frequency cases. This can be seen as well in figure 4.11 where the relative error is plotted in terms of different frequencies using 16 DOFs/wavelength for each coordinate direction. Figure 4.11 also demonstrates the fictitious eigenfrequency problem in which using CBIE at frequencies of 171.5 and 343 Hz with wavenumbers $k=\pi$ and 2π respectively shows clear instabilities. In contrast, BM is stable for all frequencies.
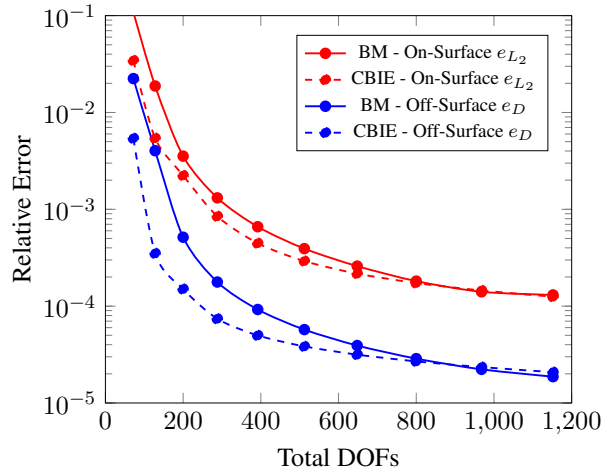
(a) Frequency = 50 Hz
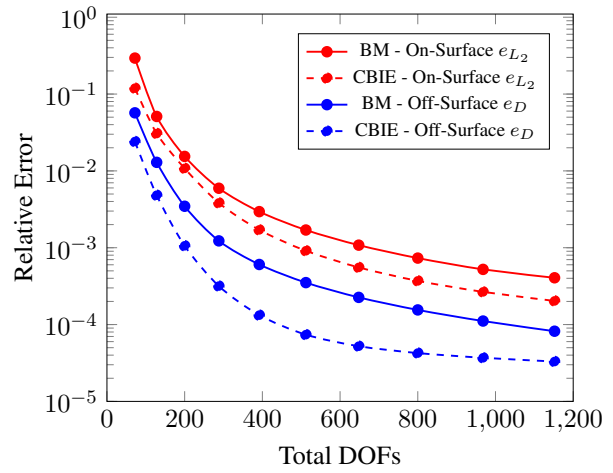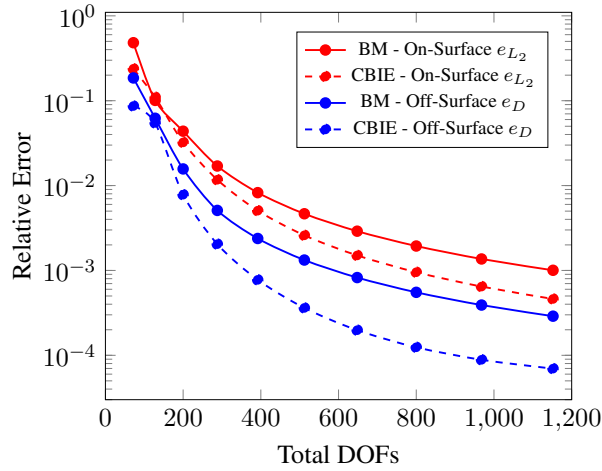
(b) Frequency = 100 Hz

(c) Frequency = 150 Hz
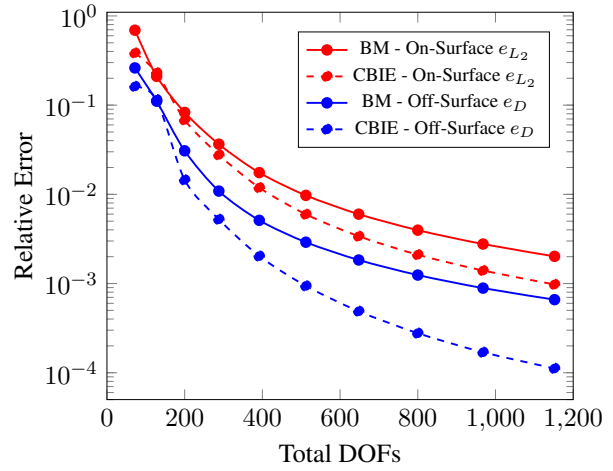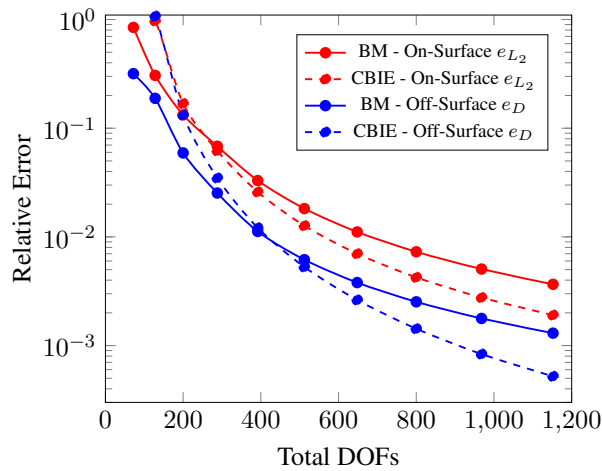
(d) Frequency = 200 Hz

(e) Frequency = 250 Hz
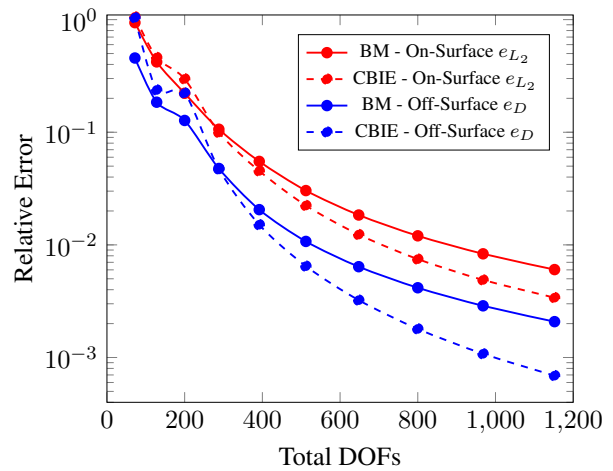
(f) Frequency = 300 Hz

Figure 4.7: Relative error for different frequencies in terms of total DOFs.
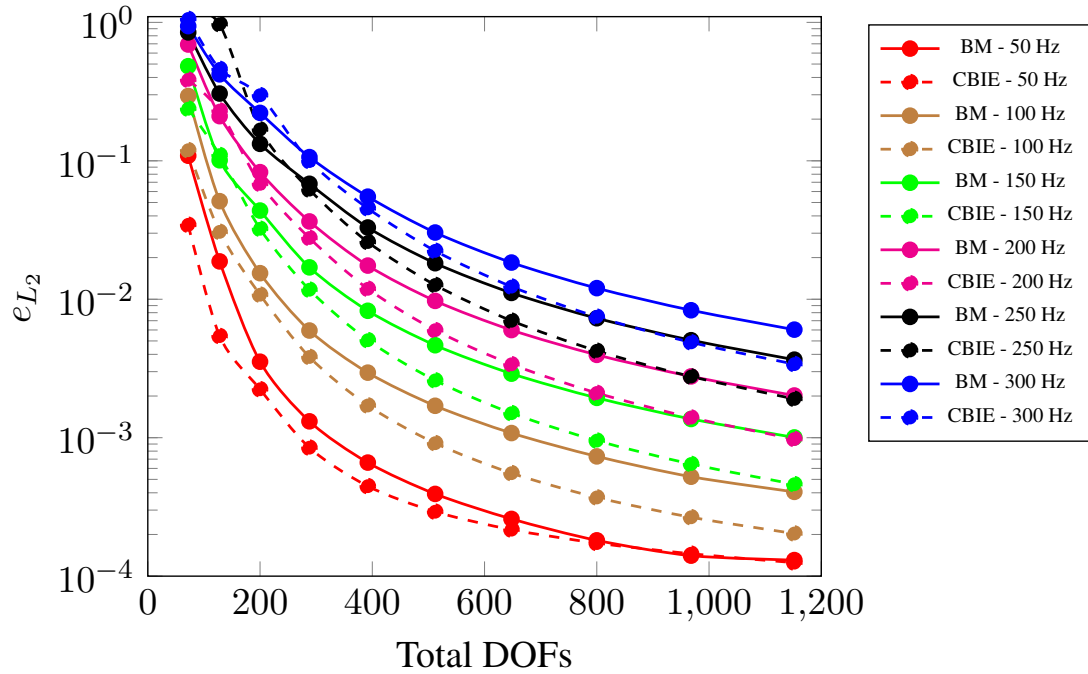
Figure 4.8: Compiled On-Surface plots for L_2 error norm (e_{L_2}) for different frequencies.
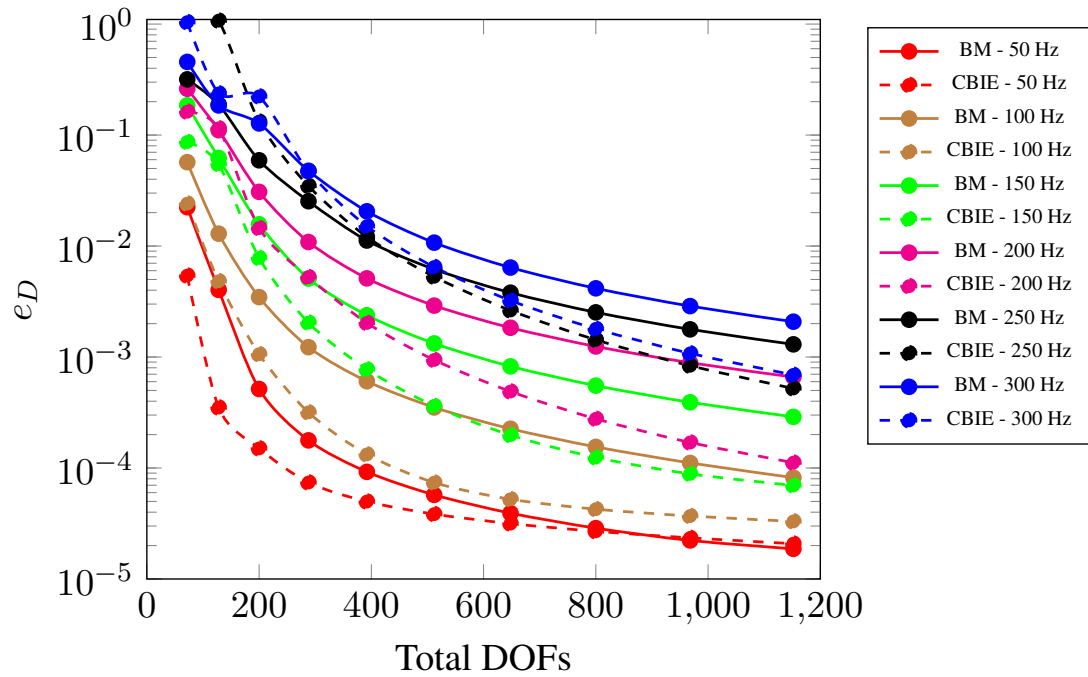
Figure 4.9: Compiled Off-Surface plots for relative error (e_D) for different frequencies.

(a) Frequency = 50 Hz

(b) Frequency = 100 Hz

(c) Frequency = 150 Hz

(d) Frequency = 200 Hz

(e) Frequency = 250 Hz

106
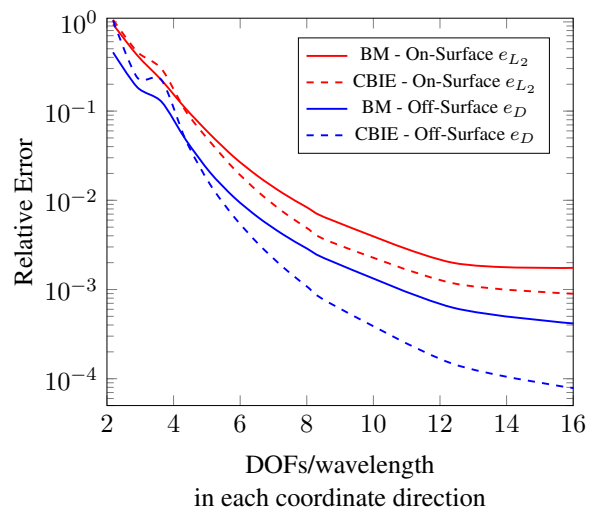
(f) Frequency = 300 Hz

Figure 4.10: Relative error for different frequencies in terms of DOFs per wavelength in each coordinate direction.
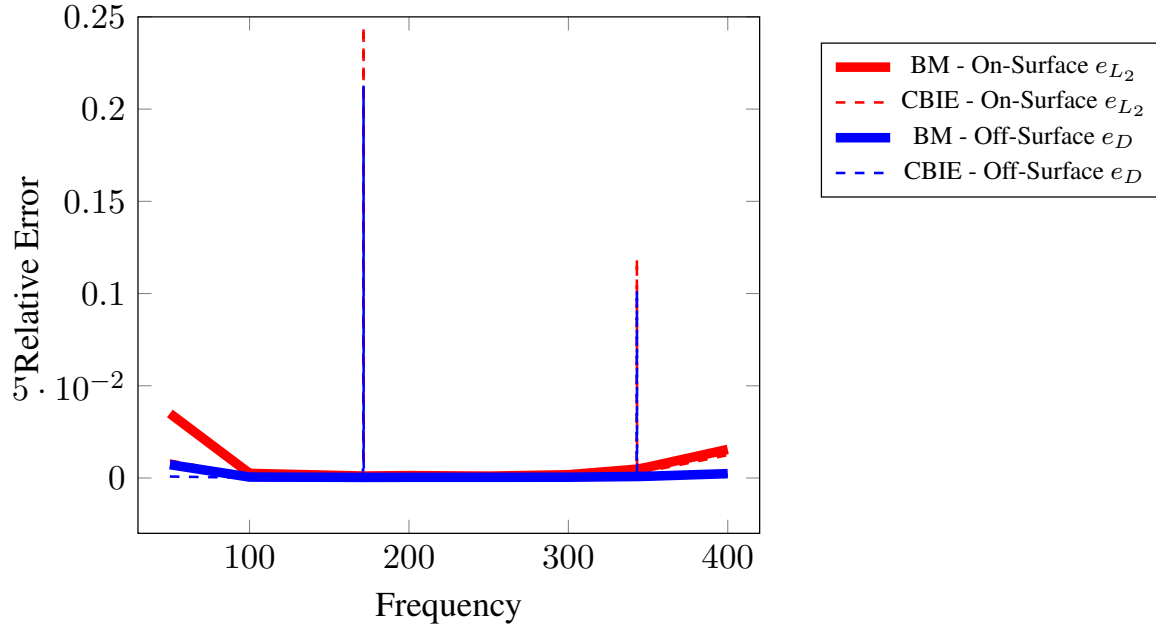
Figure 4.11: Relative error for different frequencies using 16 DOFs/wavelength for each coordinate direction.

These results show the efficiency of the proposed techniques for handling such acoustic problems with satisfactory accuracy using relatively few DOFs and Gauss quadrature points. Several research works have solved the same sphere problem either using T-splines with regularization integration scheme in [37] or using NURBS with different integration schemes in [24, 22, 25] giving almost the same accuracy which supports the proposed approach. In the absence of fictitious eigenfrequencies as this example, it is worth noting that, although BM gives satisfactory results, CBIE using the same DOFs gives more accurate results since it does not include any singular integral. This conclusion was derived as well in [26] using more NURBS with an adaptive integration scheme.

To further verify the effectiveness of the proposed techniques, surface and domain values in the X-Y plane at Z=0 in terms of the real and imaginary parts in addition to the absolute error for both CBIE and BM methods with relative to the analytical solution of eq.(4.61) are presented in figures 4.12-4.23 for the same frequencies: 50, 100, 150, 200, 250, 300 Hz. The total DOFs utilized to model the spherical scatterer for the prescribed frequencies are chosen as 128, 200, 288, 392, 512 and 648 respectively for each proposed method. Since both CBIE and BM produce almost the same values, the real and imaginary parts are presented once for simplicity in addition to the absolute error for each method. It can be concluded that, both CBIE and

(a) Real Part   **(b)** Imaginary Part   **(c) CBIE** - Absolute Error   **(d) BM** - Absolute Error
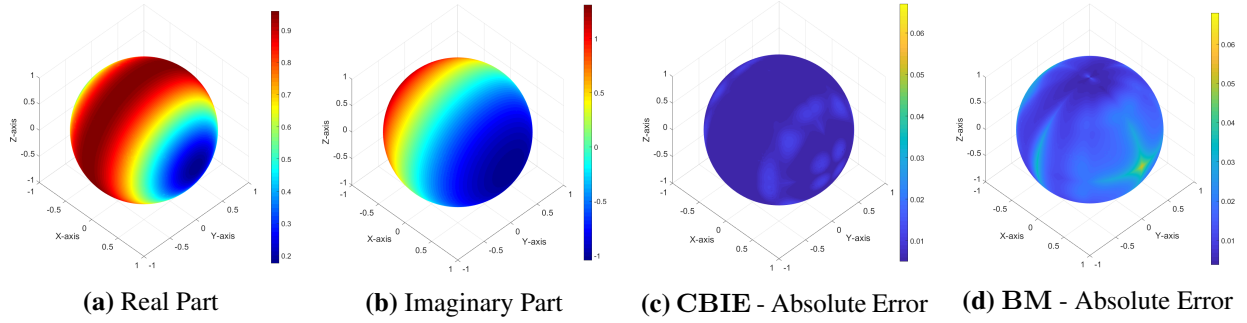
Figure 4.12: Surface values for frequency of 50Hz.

(a) Real Part   **(b)** Imaginary Part   **(c) CBIE** - Absolute Error   **(d) BM** - Absolute Error
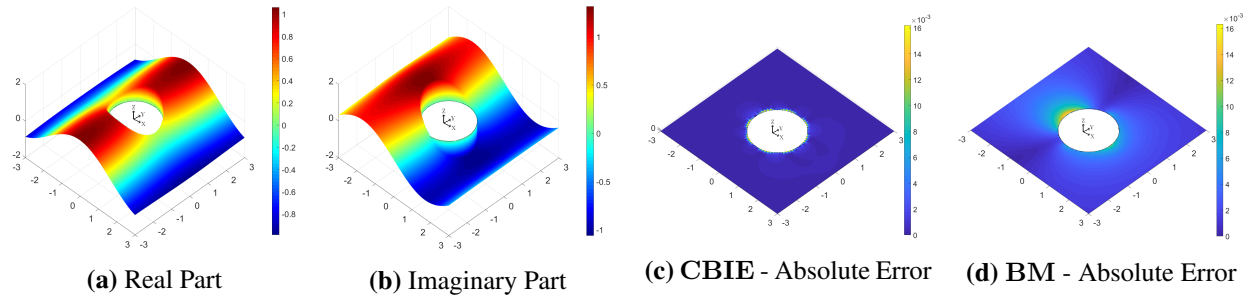
Figure 4.13: Domain values in the x-y plane at z=0 for frequency of 50Hz.

BM are in excellent agreement with the analytical solution avoiding the few errors appearing in the axi-symmetric model of [21] along the symmetry line in the direction of the incident wave. The advantage of CBIE over BM to produce less errors is applicable in these examples as well.

Another comparison between CBIE and BM is presented in figure 4.24 in terms of the total DOFs versus the CPU time used to calculate the relative error e_{L_2}. The numerical analysis is implemented using Intel Fortran Compiler (Beta) supporting Fortran 95 and the parallelization features of OpenMP 4.5. It can be seen that, CBIE models are faster than those of BM. This is due to less integration effort in CBIE rather than BM. It is mentioned in [24] that, due to the recursion functions which are employed to predict NURBS basis functions, IGA BEM models consume more time than the conventional BEM. Nevertheless, IGA models are capable to produce higher accuracy using the same DOFs.

4.6.2 Shape optimization analysis for the plane wave scattering problem by a rigid sphere

In this section, the PSO algorithm is checked on the plane wave scattering problem by a rigid sphere to minimize the sound pressure on some chosen field points. The same rigid sphere studied in section 4.6.1 with its properties and the embedding medium is considered in this analysis as well. Only the direction of

(a) Real Part   **(b)** Imaginary Part   **(c) CBIE** - Absolute Error   **(d) BM** - Absolute Error
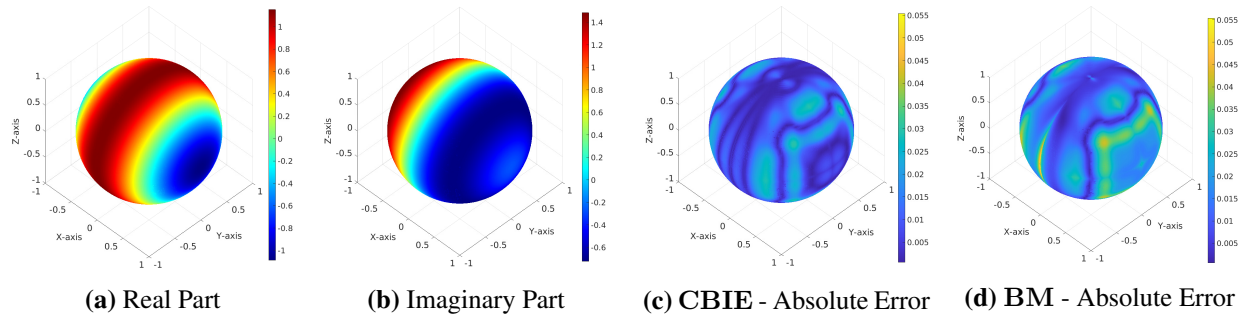
Figure 4.14: Surface values for frequency of 100Hz.

(a) Real Part   **(b)** Imaginary Part   **(c) CBIE** - Absolute Error   **(d) BM** - Absolute Error
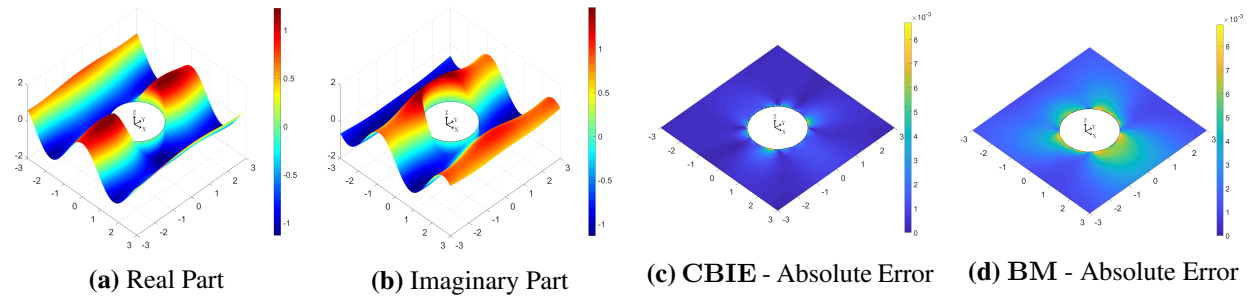
Figure 4.15: Domain values in the x-y plane at z=0 for frequency of 100Hz.

(a) Real Part   **(b)** Imaginary Part   **(c) CBIE** - Absolute Error   **(d) BM** - Absolute Error
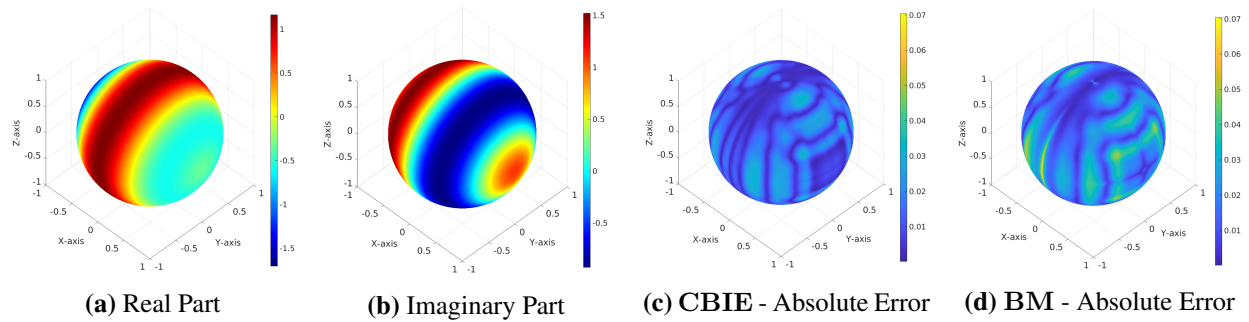
Figure 4.16: Surface values for frequency of 150Hz.

(a) Real Part   **(b)** Imaginary Part   **(c) CBIE** - Absolute Error   **(d) BM** - Absolute Error
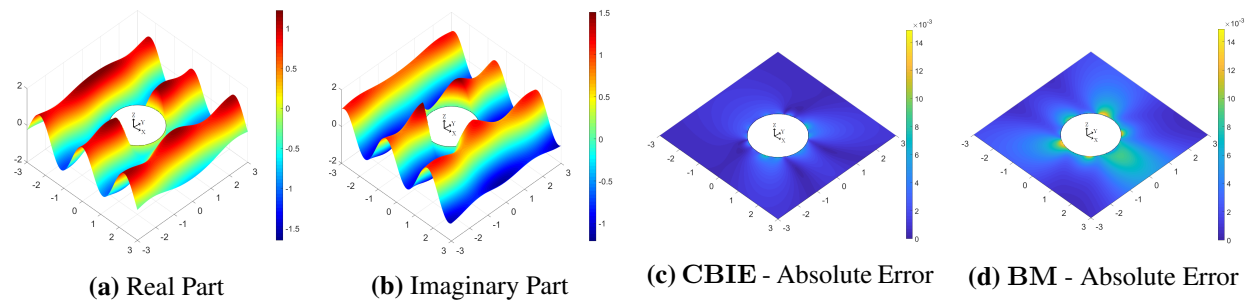
Figure 4.17: Domain values in the x-y plane at z=0 for frequency of 150Hz.

(a) Real Part **(b)** Imaginary Part **(c) CBIE** - Absolute Error **(d) BM** - Absolute Error
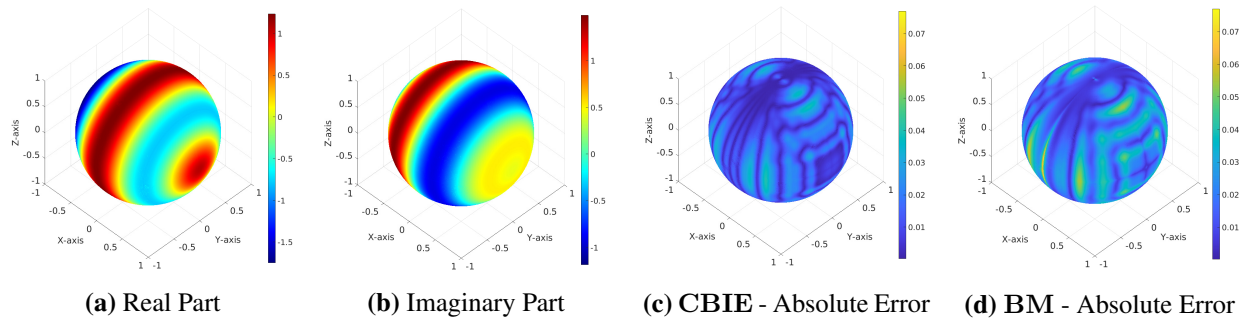
Figure 4.18: Surface values for frequency of 200Hz.

(a) Real Part **(b)** Imaginary Part **(c) CBIE** - Absolute Error **(d) BM** - Absolute Error
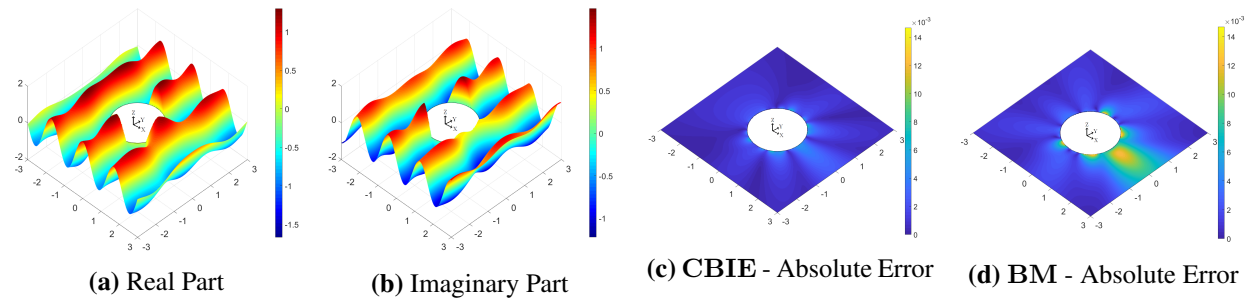
Figure 4.19: Domain values in the x-y plane at z=0 for frequency of 200Hz.

(a) Real Part **(b)** Imaginary Part **(c) CBIE** - Absolute Error **(d) BM** - Absolute Error
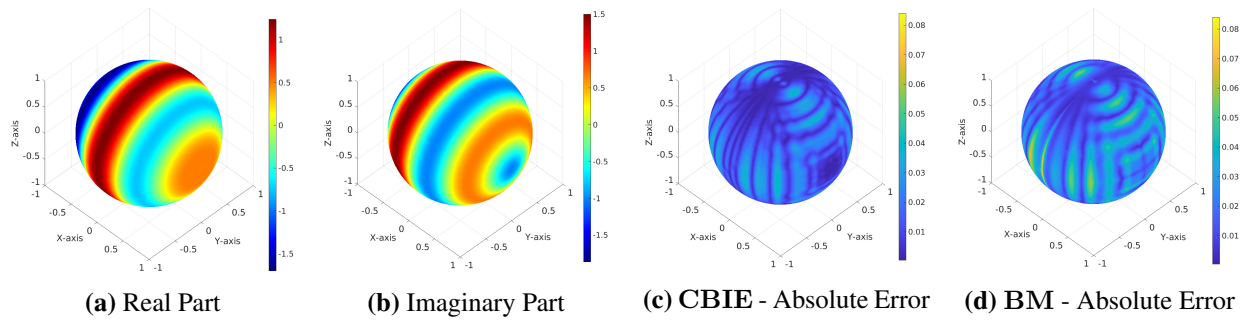
Figure 4.20: Surface values for frequency of 250Hz.

(a) Real Part **(b)** Imaginary Part **(c) CBIE** - Absolute Error **(d) BM** - Absolute Error
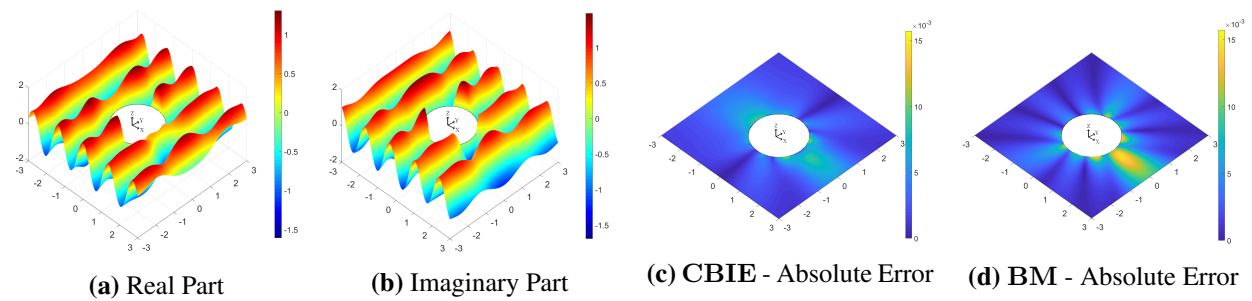
Figure 4.21: Domain values in the x-y plane at z=0 for frequency of 250Hz.

(a) Real Part   **(b)** Imaginary Part   **(c) CBIE** - Absolute Error   **(d) BM** - Absolute Error
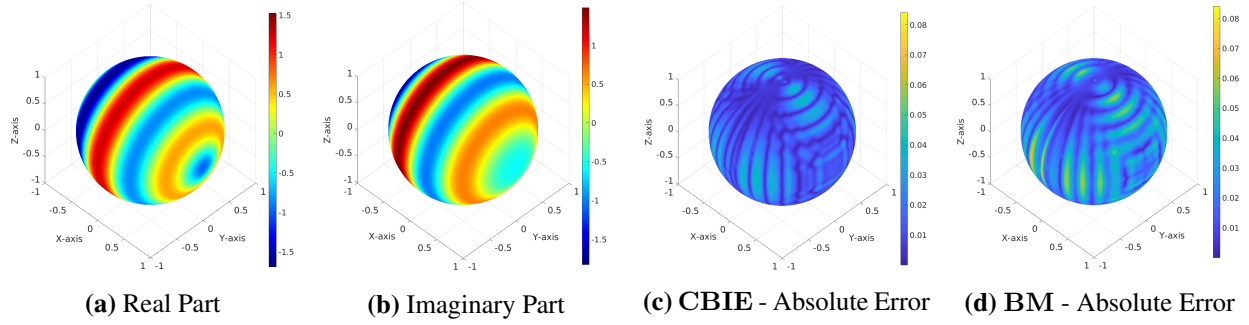
Figure 4.22: Surface values for frequency of 300Hz.

(a) Real Part   **(b)** Imaginary Part   **(c) CBIE** - Absolute Error   **(d) BM** - Absolute Error
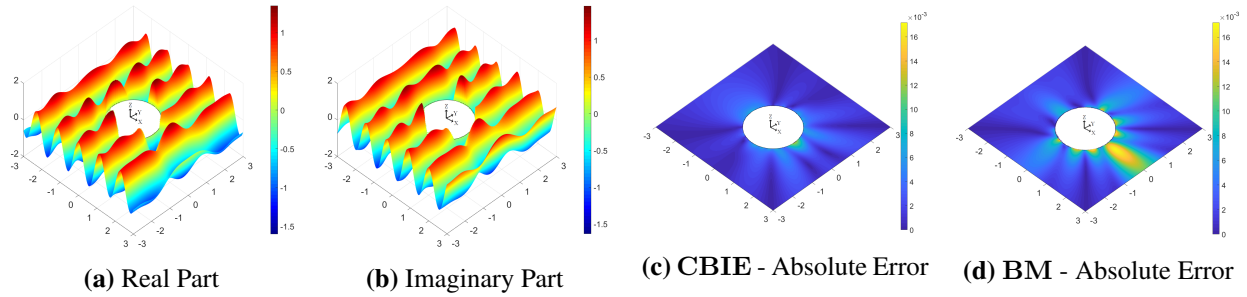
Figure 4.23: Domain values in the x-y plane at z=0 for frequency of 300Hz.
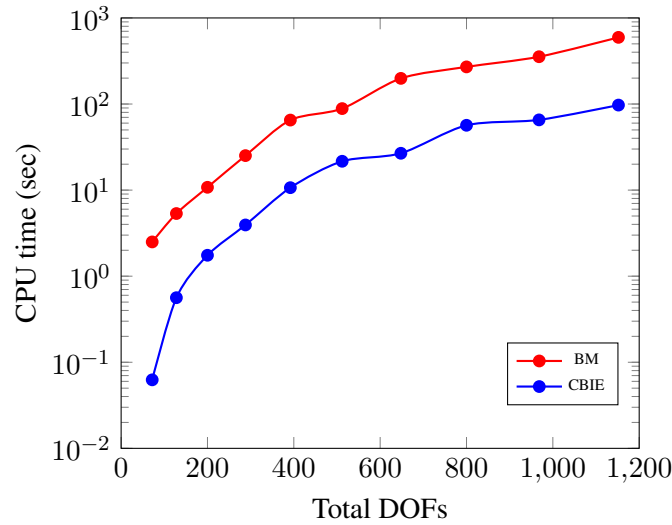
Figure 4.24: CPU time used to calculate the relative error e_{L_2}.

the incident wave following eq.(4.11) has been changed, so that the incident wave would transfer from the positive side of y-axis as $\mathbf{d} = \{0, 1, 0\}$. The nine control points defining the NURBS model of the sphere in the x-y plane with y= -1m (Points P1-P9 shown in figure 4.6) are set as design variables for the optimization

111

process. Only the y-coordinate of these nine control points / design variables is free to change during the optimization process between the range of -0.5m to -1.5m with an initial value of -1m. The the spherical scatterer has a constraint volume during the optimization iterations not to exceed the $4.22m^3$. The objective function in eq.(4.58) is calculated along equally spaced 21 points located inside the line connecting the two points $\{0, 2, -1\}$ and $\{0, 2, 1\}$.

Figure 4.25 presents the initial shape in addition to the optimized shapes obtained by both CBIE and BM with PSO for a frequency of 100 Hz (k=1.83) compared to the optimized shape produced by [24] using BM with sensitivity analysis. It can be shown that, all shapes are almost the same. For all comparative data, we refer to table 4.1 where BM requires more DOFs than CBIE for convergence purpose. The BM model in [24] required almost the same DOFs similar to the proposed approach. Although the isogeometric analysis discussed in the previous section for the same rigid sphere problem shows satisfactory accuracy using BM with 200 DOFs for the same case of frequency, 288 DOFs are used in the optimization problem. The reason of this difference is that, PSO algorithm initiates random non-smooth shapes and these shapes are enhanced until the minimum fitness function is obtained. The integration over the non-smooth surfaces of these initial shapes needs more refined meshes.

Figures 4.26 and 4.27 clarify the convergences of both the fitness function (eq.(4.60)) and the volume (eq.(4.59)) during the optimization process respectively.

	CBIE	BM	Ref.[24]
Number of Design Variables	9	9	9
Total DOFs (NURBS Basis Functions)	200	288	266
N_2 - Number of Consecutive Iterations for PSO	60	60	-
Optimized Design Variables - y-coordinates for points:			
P1	-0.50	-0.50	-0.50
P2	-0.50	-0.50	-0.50
P3	-0.50	-0.50	-0.50
P4	-0.84	-0.89	-0.83
P5	-1.50	-1.50	-1.50
P6	-0.82	-0.76	-0.83
P7	-0.50	-0.50	-0.50
P8	-0.50	-0.50	-0.50
P9	-0.50	-0.50	-0.50

Table 4.1: Comparative data of the rigid sphere problem for a frequency of 100 Hz.
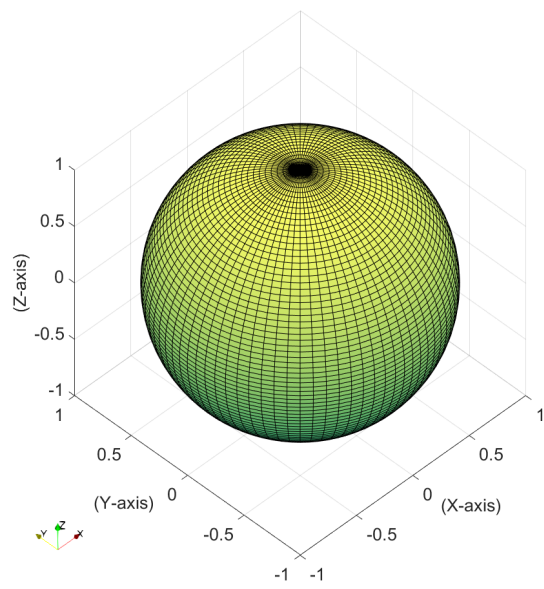
(a) Initial Shape
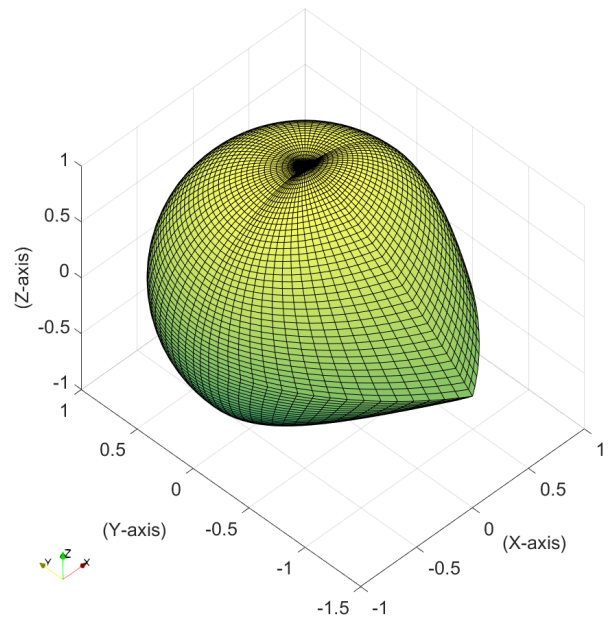
(b) Optimized Shape - CBIE
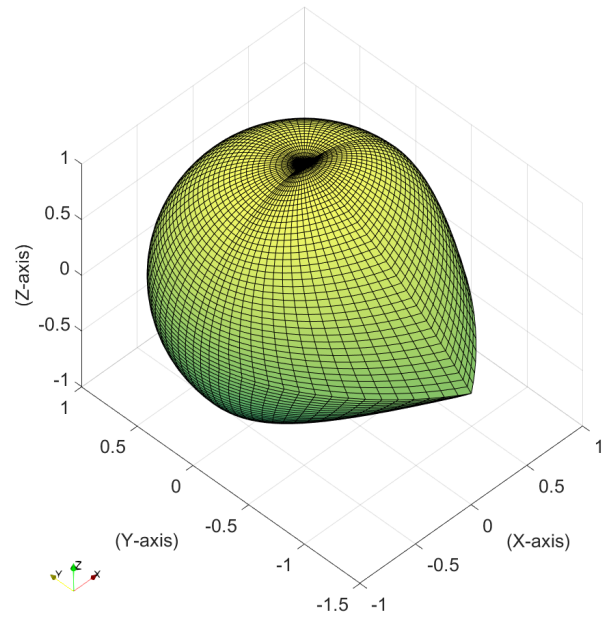
(c) Optimized Shape - BM
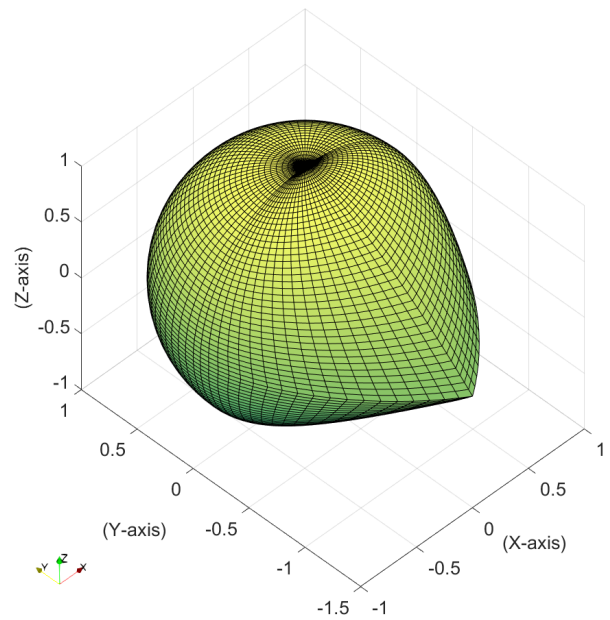
(d) Optimized Shape - Ref. [24]

Figure 4.25: Initial and optimized shapes of the rigid sphere for a frequency of 100 Hz.
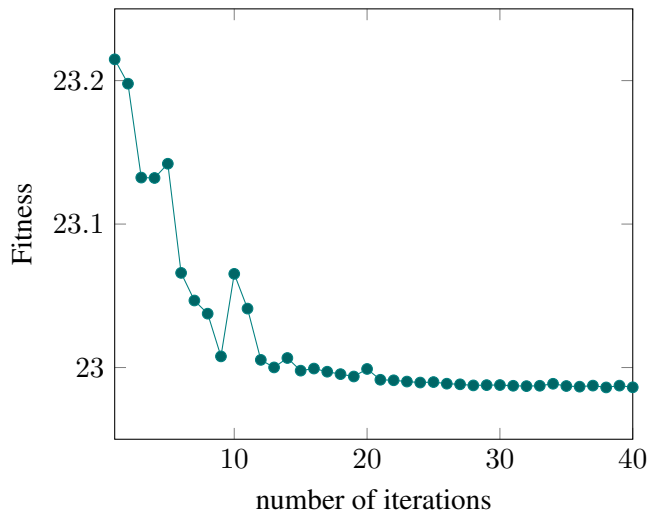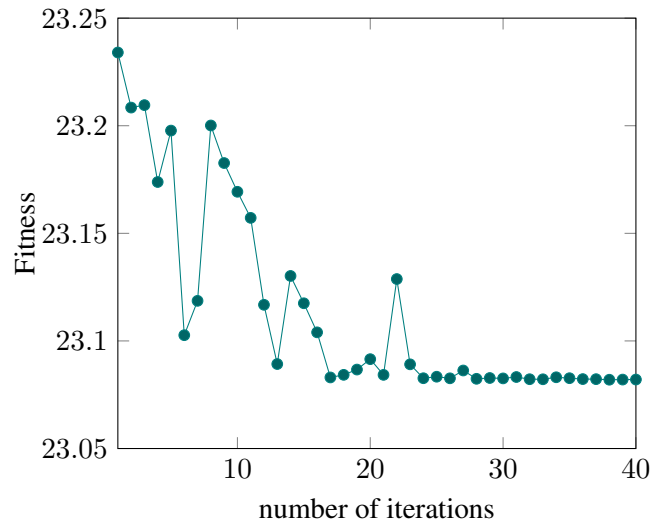
(a) CBIE

(b) BM

Figure 4.26: Convergence of the fitness function in terms of the number of iterations for the rigid sphere problem for a frequency of 100 Hz.
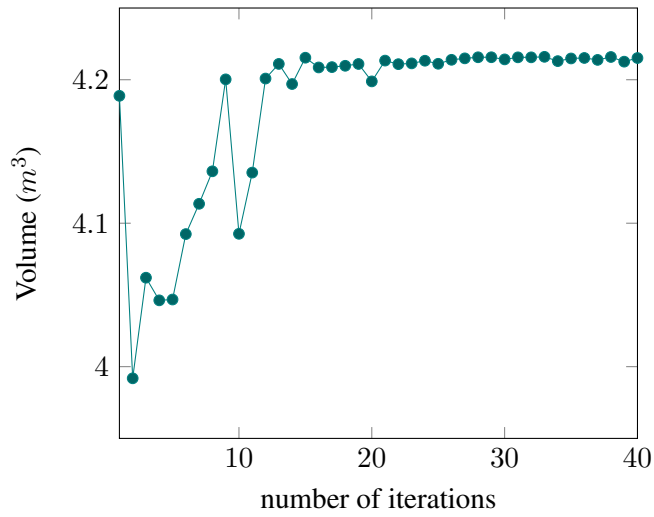
(a) CBIE
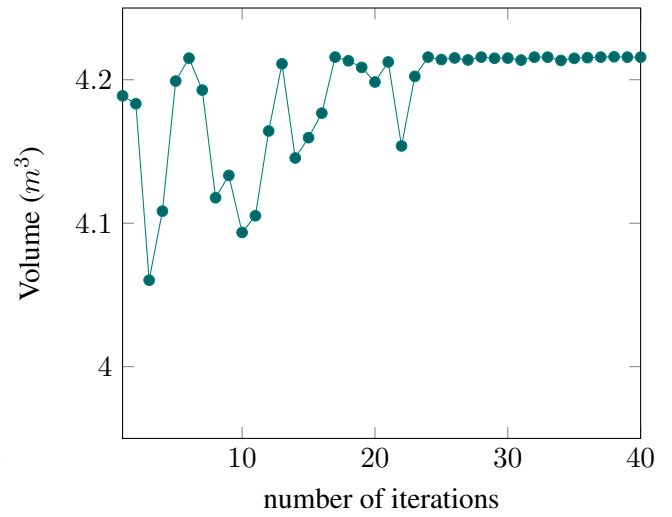
(b) BM

Figure 4.27: Convergence of the volume in terms of the number of iterations for the rigid sphere problem for a frequency of 100 Hz.

4.6.3 Shape optimization analysis for the plane wave scattering problem by a rigid vase

Another example is presented in this section discussing the validity of the PSO algorithm for shape optimization analysis. The initial configuration is a rigid vase shown in figure 4.28, which was previously studied in [24]. The vase is embedded in the air medium with density $\rho = 1.2$ kg/m^3 and sound speed $c = 343$ m/s. Further to the isogeometric model for the initial vase shape, a NURBS polynomial of degree 2 is considered for each knot direction with the control points explained in figure 4.29 and the following corresponding two knot vectors: $\Xi = \{0, 0, 0, 1/12, 2/12, 3/12, 4/12, 5/12, 6/12, 7/12, 8/12, 9/12, 10/12, 11/12, 1, 1, 1\}$ and $\Upsilon = \{0, 0, 0, 0.25, 0.25, 0.5, 0.5, 0.75, 0.75, 1, 1, 1\}$.

The direction of the incident wave of eq.(4.11) is given by $\mathbf{d} = \{0, 1, 0\}$. Moreover, figure 4.29 illustrates the seven control points (P1-P7) which are set as design variables for the optimization analysis. The z-coordinate only of the seven control points / design variables is allowed for a free transition during the optimization analysis between the range of 3.7m to 4.4m with an initial value of 4.0m. The constraint volume is adjusted not to exceed the original volume $32.58m^3$ through the iterations. The objective function in this example is set to minimize the sound pressure at the point located at $\{10, 10, 0\}$.

Figure 4.30 displays the optimized shapes obtained by both CBIE and BM with PSO for a frequency of 200 Hz (k=3.66) in addition to the optimized shape produced by [24] using BM with sensitivity analysis. It can be shown that, both proposed methods validate each other as they give the same optimized shapes. However, there is a difference between those two optimized shapes and the reference shape in one control point as shown in table 4.2 and in figure 4.30. Table 4.2 includes also all comparative data.

Convergences of both the fitness function (eq.(4.60)) and the volume (eq.(4.59)) during the optimization process are shown in figures 4.31 and 4.32 respectively.

4.6.4 Shape optimization analysis for the plane wave scattering problem by a rigid underwater submarine

The shape optimization analysis of the plane wave scattering problem by a rigid underwater submarine is studied in this section. Figure 4.33 shows the initial shape of the Benchmark Target Strength Simulation Submarine (BeTSSi-Sub), previously used in [24]. The NURBS polynomial model of degree 2 for each knot direction and the corresponding control points are presented in figure 4.34. The two knot vectors defining the submarine model are written as follows: $\Xi = \{0, 0, 0, 0.2, 0.2, 0.4, 0.6, 0.8, 0.8, 1, 1, 1\}$ and
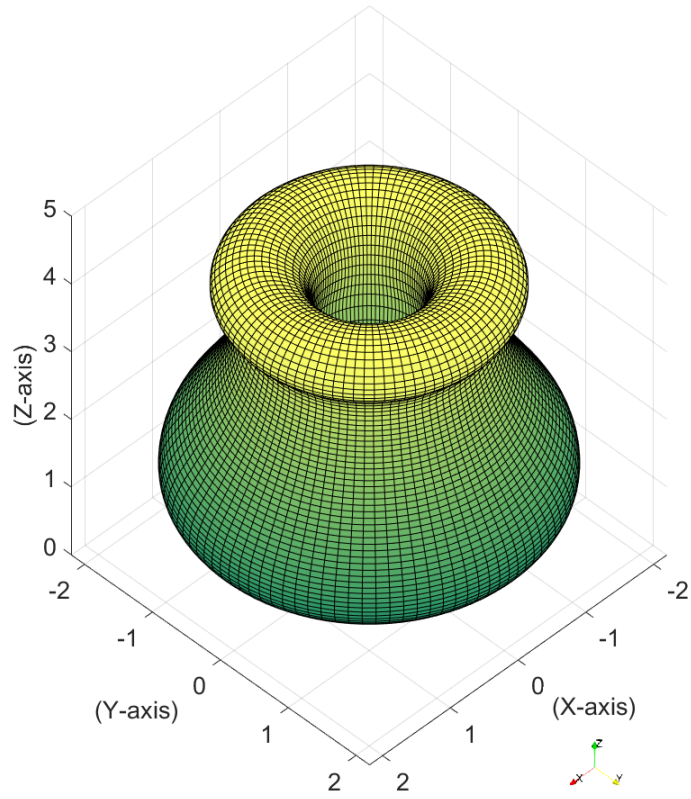
Figure 4.28: Initial shape of the rigid vase.
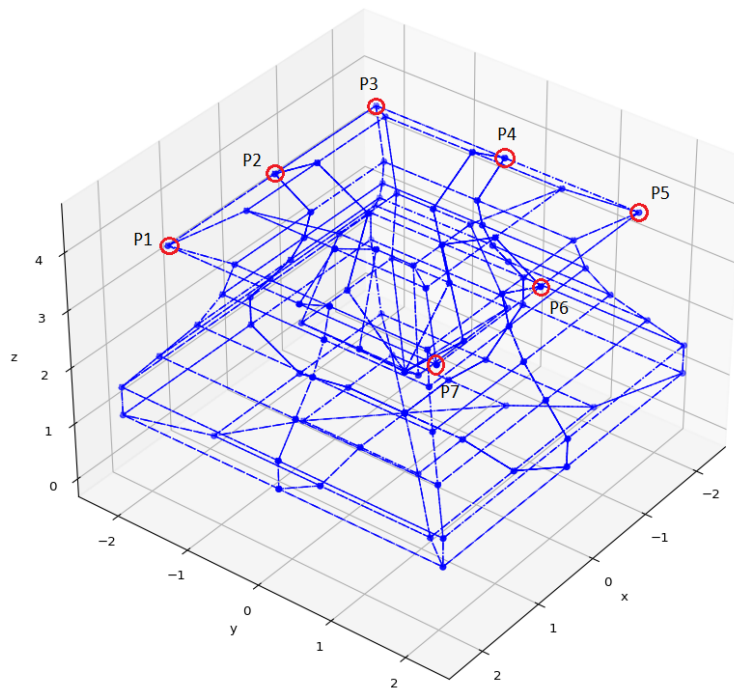
Figure 4.29: NURBS model and control points grid for the initial vase shape.

(a) CBIE & BM

(b) Ref. [24]
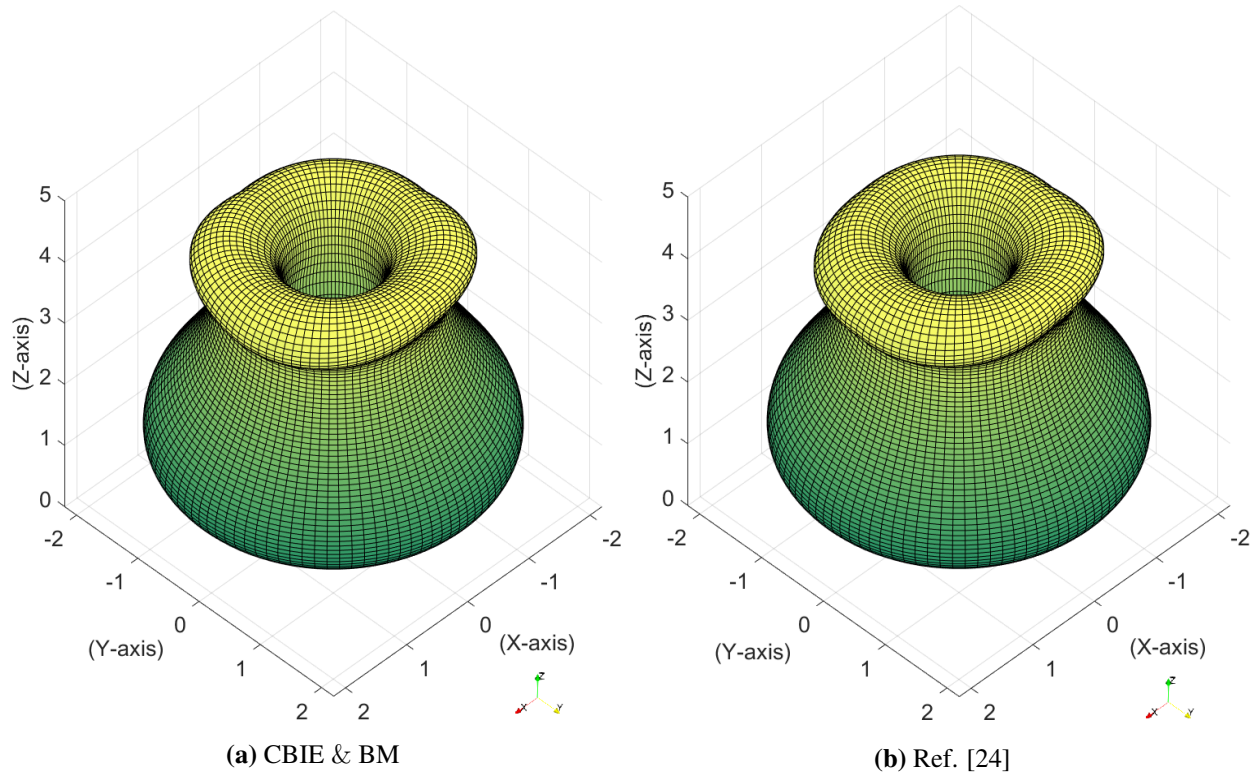
Figure 4.30: Optimized shapes of the rigid vase for a frequency of 200 Hz.

(a) CBIE

(b) BM

Figure 4.31: Convergence of the fitness function in terms of the number of iterations for the rigid vase problem for a frequency of 200 Hz.

(a) CBIE

(b) BM

Figure 4.32: Convergence of the volume in terms of the number of iterations for the rigid vase problem for a frequency of 200 Hz.

		CBIE	BM	Ref.[24]
Number of Design Variables		7	7	7
Total DOFs (NURBS Basis Functions)		1200	760	-
N_2 - Number of Consecutive Iterations for PSO		20	40	-
Optimized Design Variables - z-coordinates for points:				
	P1	4.40	4.38	3.80
	P2	3.70	3.70	3.70
	P3	4.14	4.15	4.09
	P4	3.70	3.70	3.70
	P5	4.40	4.40	4.40
	P6	4.40	4.40	4.40
	P7	3.70	3.70	3.70

Table 4.2: Comparative data of the rigid vase problem for a frequency of 200 Hz.

$\Upsilon = \{0, 0, 0, 0.25, 0.25, 0.5, 0.5, 0.75, 0.75, 1, 1, 1\}$. The submarine is embedded in a lower depth of a salt seawater where the sound speed is $c = 1509$ m/s.

The direction of the incident wave - mentioned in eq.(4.11) - is given by $\mathbf{d} = \{0, 1, 0\}$. Figure 4.34 highlights also the six control points (P1-P6) which are set as design variables for the optimization analysis. The pair of points (P2 with P3) and (P5 with P6) share the same initial coordinates. For the six control points / design
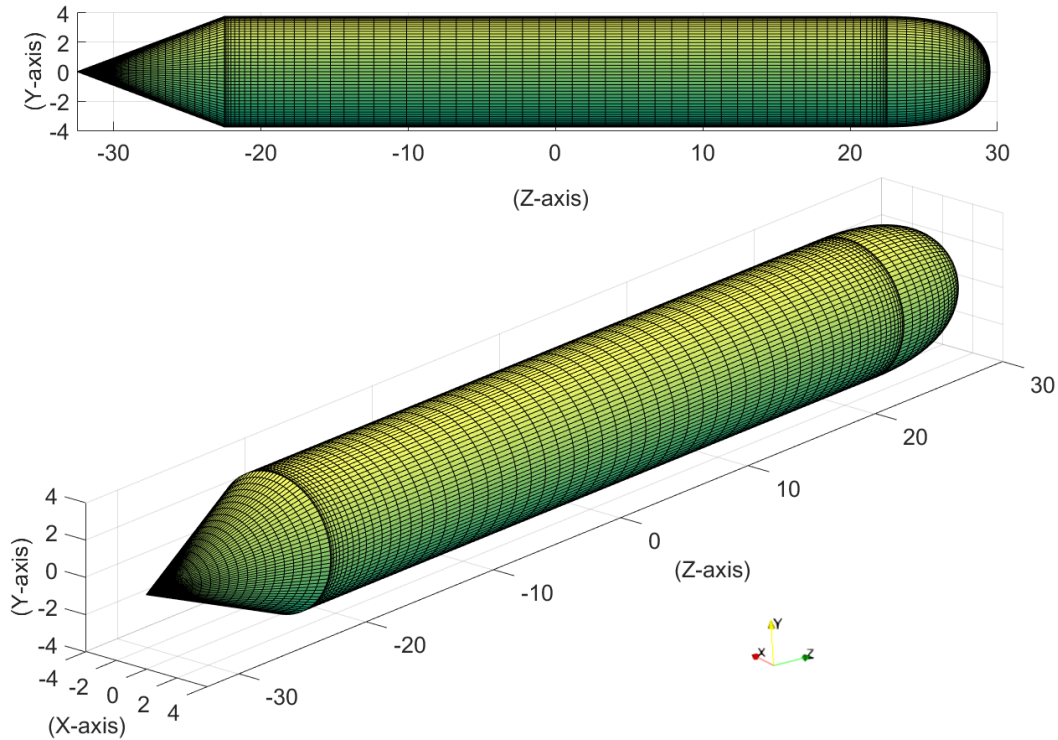
Figure 4.33: Initial shape of the rigid underwater submarine.

variables, only the y-coordinate is permitted for a free movement during the optimization analysis in the range from 1m to 6m with an initial value of 3.75m. The original volume $2362.085m^3$ is set as a constraint volume not to be exceeded through the iterations. The objective function is chosen to minimize the sound pressure at the point located at $\{10, 10, 0\}$.

Both shapes produced by CBIE and BM with PSO in addition to the optimized shape produced by [24] using BM with sensitivity analysis for a frequency of 220 Hz (k=0.916) are presented in figure 4.35. Although the optimized shapes are not close, they share almost the point (P4) which is the nearest point to the field point where the sound pressure is minimized. Since the submarine body is quite big, the further points - which have less effect on the concerned field point - can be differed as shown in table 4.3. Figures 4.36 and 4.37 show the convergence of the fitness function (eq.(4.60)) and the volume (eq.(4.59)) during the optimization process respectively.
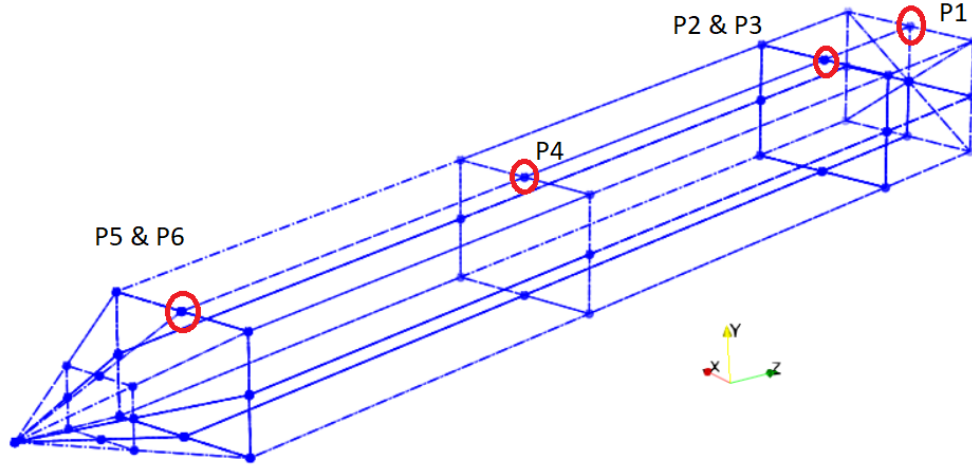
Figure 4.34: NURBS model and control points grid for the initial submarine shape.

		CBIE	BM	Ref.[24]
Number of Design Variables		6	6	6
Total DOFs (NURBS Basis Functions)		1344	1344	-
N_2 - Number of Consecutive Iterations for PSO		20	20	-
Optimized Design Variables - y-coordinates for points:				
	P1	2.53	1.39	1.85
	P2	4.52	3.59	3.82
	P3	1.00	1.00	1.41
	P4	5.22	5.34	5.05
	P5	2.81	2.12	4.81
	P6	4.91	3.94	1.00

Table 4.3: Comparative data of the rigid underwater submarine problem for a frequency of 220 Hz.

4.7 Summary

In the framework of the isogeometric analysis (IGA), two boundary element methods (BEM): the conventional boundary integral equation (CBIE) and Burton-Miller (BM), are employed to solve three dimensional Helmholtz acoustic scattering problems forming IGABEM. BEM is superior in simulating infinite-domain scattering problems as they model only the scatterer boundary without any need to discretize the exterior domain nor to define any truncation boundary fulfilling the Sommerfeld radiation condition. BEM reduces also the dimensionality of the problem.

Generally, BM is employed to overcome the fictitious eigenfrequencies problem caused by the non-uniqueness

(a) CBIE

(b) BM

(c) Ref. [24]
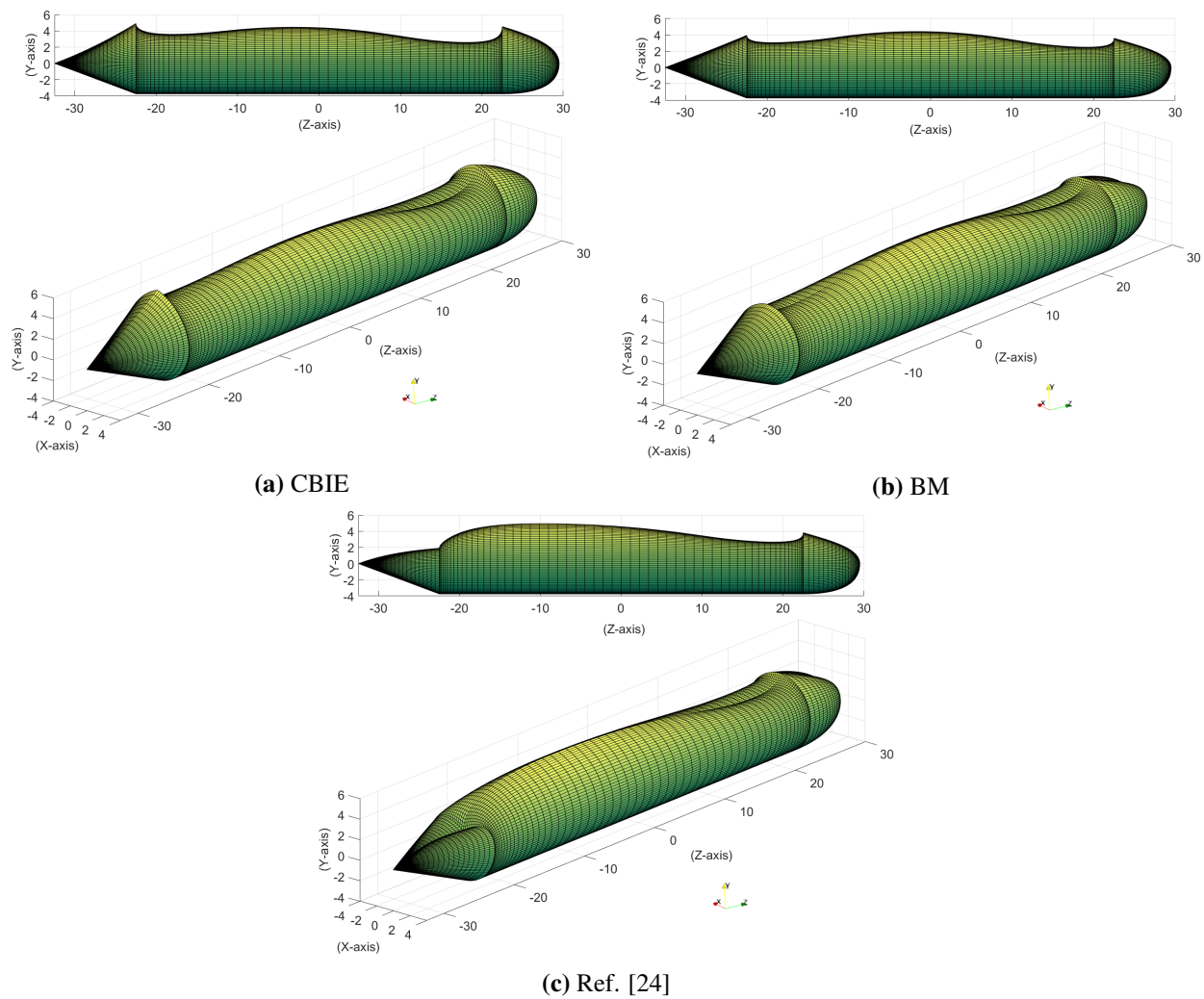
Figure 4.35: Optimized shapes of the rigid underwater submarine for a frequency of 220 Hz.
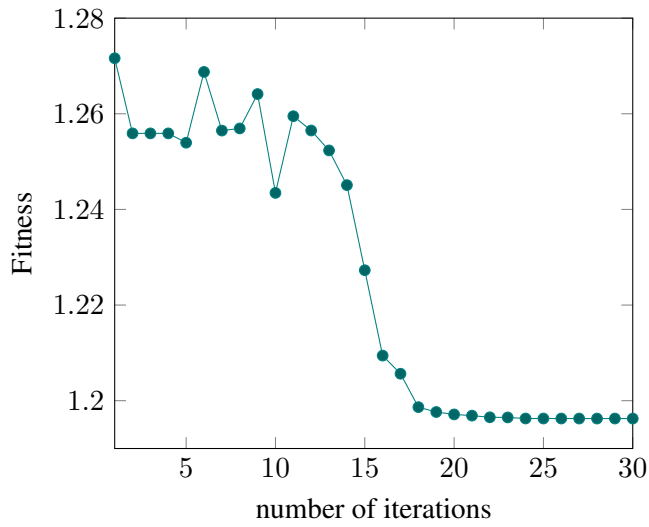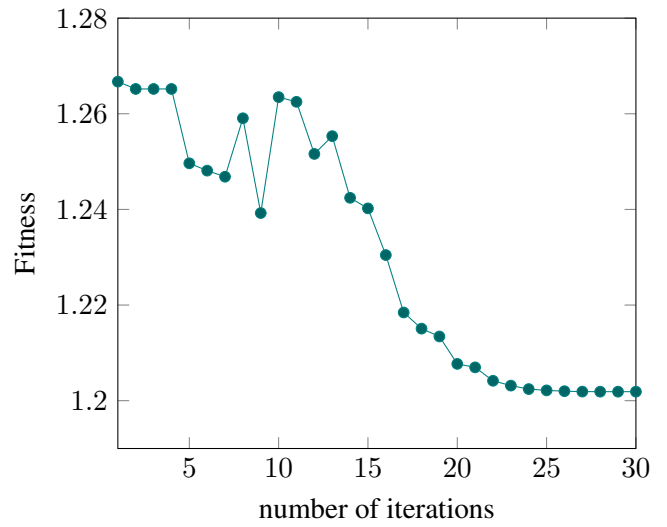
(a) CBIE

(b) BM

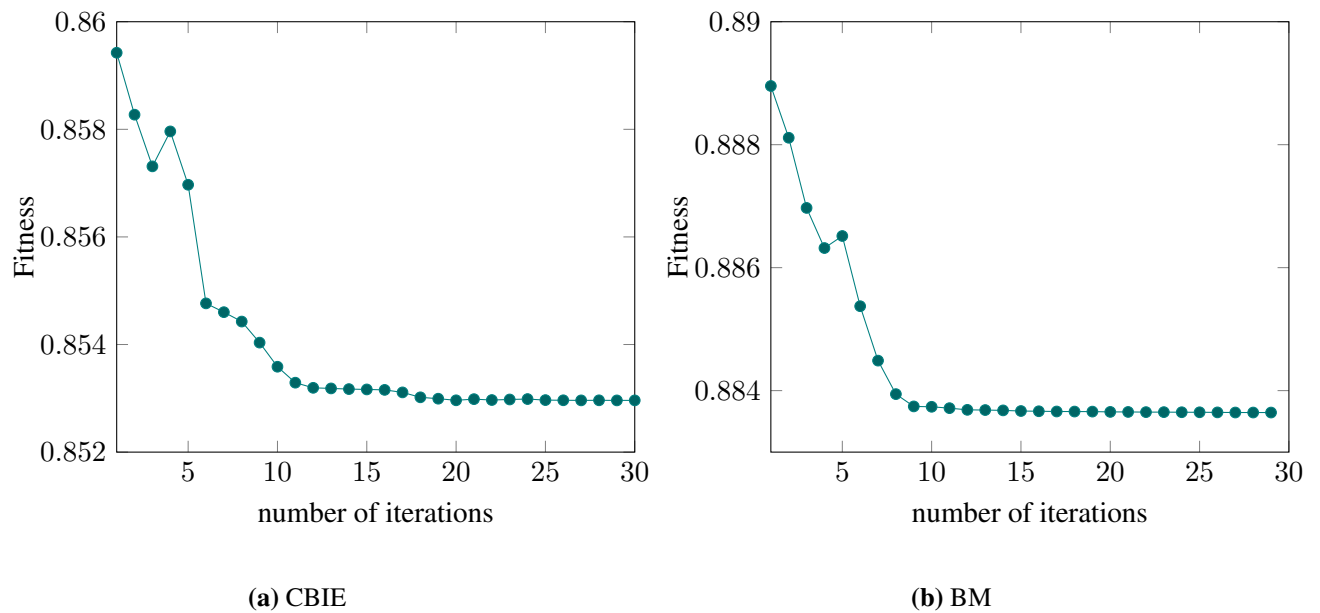**Figure 4.36:** Convergence of the fitness function in terms of the number of iterations for the rigid underwater submarine problem for a frequency of 220 Hz.
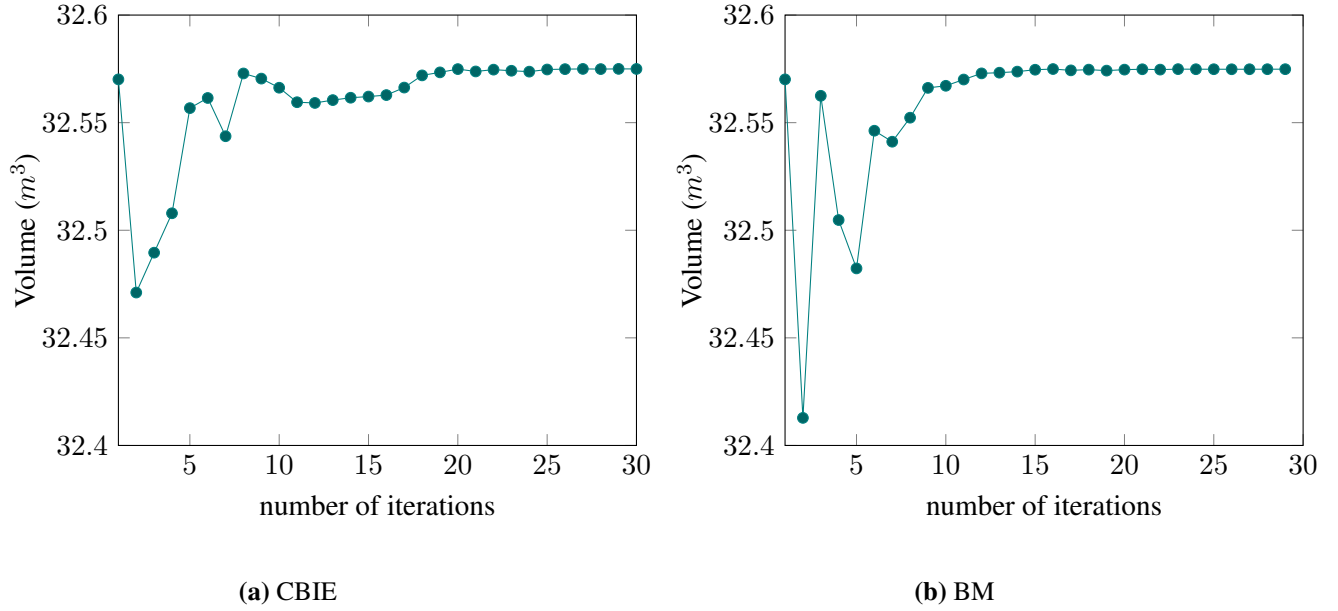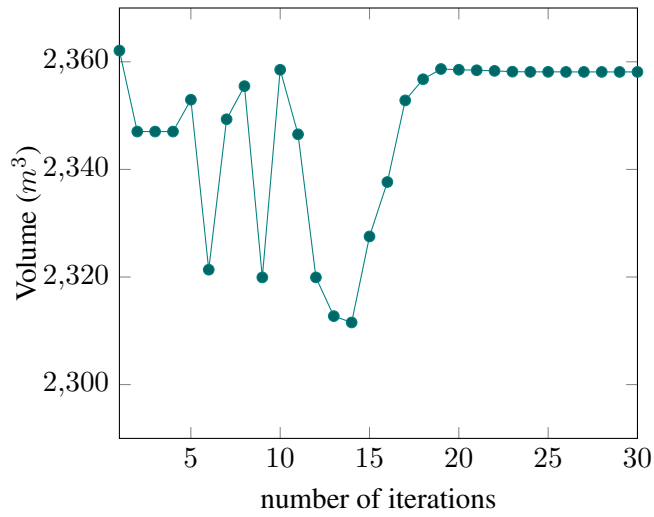

(a) CBIE
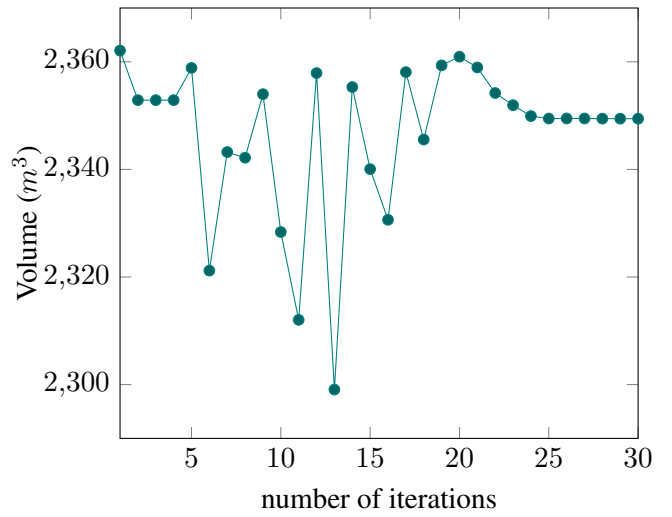
(b) BM

Figure 4.37: Convergence of the volume in terms of the number of iterations for the rigid underwater submarine problem for a frequency of 220 Hz.

of the numerical solution when using CBIE alone. However, in the absence of the eigenfrequencies problem CBIE produces competitive results since it contains only regular integrals. We have applied the NURBS basis functions with an offset to the collocation points wherever C^0 is encountered, so that the normal directions at collocation points required by BM can be defined distinctly and the total DOFs would equal the total number of linear system of equations. The jump-term is defined also easily on smooth surfaces without any need for complex calculations. It can also prevent any singularity of order $\mathcal{O}(1/r)$ and convert it into regular integrals. Singularity subtraction technique (SST) is employed to overcome the hyper-singular integral of order $\mathcal{O}(1/r^3)$ that appears in BM when the collocation point coincides with the integrated element, while an adaptive integration is implemented for neighbor elements to the collocation point. Both CBIE and BM show satisfactory results using only NURBS polynomial of degree 2. Nearly singularity treatment corresponding to collocation on sphere poles when using SST for the hyper-singular integral due to highly distorted elements is avoided using the offset scheme.

IGABEM is coupled with one of the gradient-free optimization methods, the Particle Swarm Optimization (PSO) for structural shape optimization problems. Coupling IGA with optimization problems enables the NURBS basis functions to represent the three models: shape design, analysis and optimization models, by a definition of a set of control points to be the control variables and the optimization parameters as well which enables an easy transition between the three models.

Different numerical examples are discussed to present the validity of the proposed approach w.r.t. the analytical solution and against already published numerical results showing the agreement between the results.

Chapter 5

The muffler problem

based on the paper *'An isogeometric Burton-Miller method for the transmission loss optimization with application to mufflers with internal extended tubes'* published in Applied Acoustics, where the contribution of each author is summarized as follows:

<u>**Ahmed Mostafa Shaaban**</u>

- Conceptualization
- Research state of the art
- Investigation
- Formal analysis
- Methodology
- Software / Programming
- Data curation
- Data analysis
- Validation
- Visualization
- Writing-original draft preparation

<u>**Cosmin Anitescu**</u>

- Conceptualization
- Writing-review and editing

Elena Atroshchenko

- Conceptualization

- Writing-review and editing

Timon Rabczuk

- Conceptualization

- Supervision

- Mentoring the research progress

- Review of the manuscript before submission

5.1 General

The problem of a muffler with internal extended inlet/outlet tubes is studied with the aim to optimize its geometric design as a practical application to the Helmholtz acoustic problem. When boundary element method (BEM) based on the conventional boundary integral equation (CBIE) is used for structures with thin walls (internal extended tubes of small thickness), it produces nearly singular integrals which require smaller elements and higher number of Gauss quadrature points to maintain sufficient accuracy of the overall solution. An alternative approach, known as mixed or dual BEM, which consists of neglecting the tube thickness, models the wall as a single surface and prescribes BIEs of different types on each side. However, this alternative leads to some discrepancies in the obtained results compared to other numerical or experimental data especially at higher frequencies. Another approach in this chapter is to utilize Burton-Miller method (BM) prescribing a combination of two types of BIEs on the original thin-walled geometry. BM is introduced in the framework of isogeometric analysis (IGA) to solve the muffler problem as an interior 3D Helmholtz acoustic problem producing more accurate results. In addition, the isogeometric BM (IGA-BM) model benefits from the BEM philosophy of reducing the dimensionality of a 3D problem to consider only its surfaces/boundaries. Moreover, producing the 4-pole parameters of the transmission loss (TL) entering/exiting the inlet/outlet tubes is convenient to the nature of BEM of predicting the physical variables on the problem boundary.

The performance of IGA-BM model is discussed and compared with the previously published results using finite and boundary element methods, IGA models and the available experimental data. Furthermore, optimization examples using the Particle Swarm Optimization (PSO) coupled with IGA-BM are demonstrated to maximize the TL in attenuation regions by changing the internal lengths of the extended tubes.

5.2 The Mathematical model of muffler with BM

The muffler problem considered in this chapter is illustrated in figure 5.1. The in-going wave enters an interior acoustic domain Ω from a muffler inlet Γ_{in} while it exits from a muffler outlet Γ_{out}. The rest of the muffler body Γ_{rigid} is defined with rigid boundary conditions. The main muffler chamber has a diameter D and length L. In order to enhance the muffler performance, the inlet/outlet tubes are extended internally with lengths L_1 & L_2 and diameters D_1 & D_2 respectively. The tubes have a small thickness t as clarified by the detail in figure 5.2. The unit normal vector $\mathbf{n}$ is pointing out outside the muffler domain.

The solution to the interior Helmholtz time harmonic wave propagation equation is the acoustic pressure u,
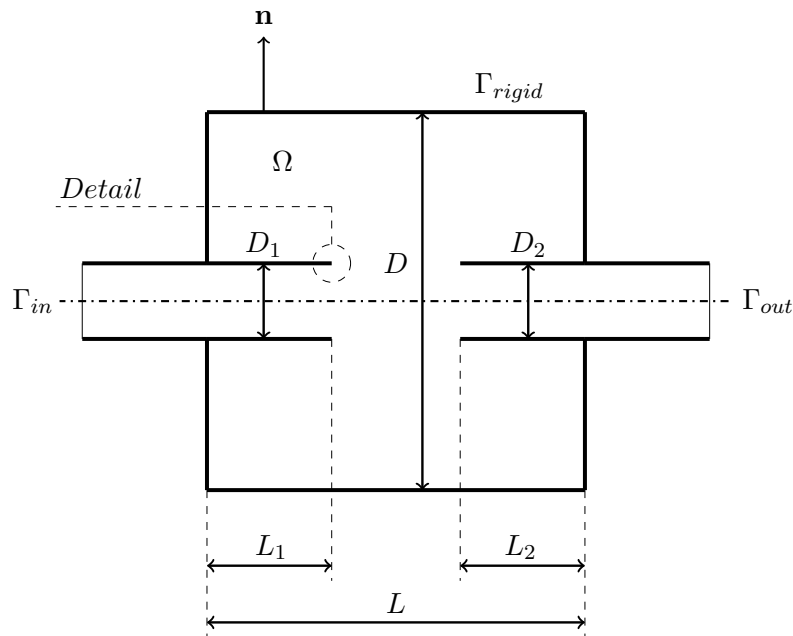
Figure 5.1: Cross section of the muffler with extended inlet/outlet tubes.
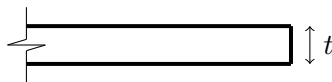
Figure 5.2: Detail for the small thickness of the internal extended tube.

127

which satisfies [51]:

$$\triangle u + k^2 u = 0 \qquad \text{in} \quad \Omega, \tag{5.1}$$

where $\triangle$ denotes the Laplace operator. k is the wavenumber inversely proportional to the wavelength λ according to $\lambda = 2\pi/k$. The Green's function for the 3D Helmholtz equation considering the effect of a boundary point $\mathbf{q}$ on a free space source point $\mathbf{p}$ is written as follows [124]:

$$G(\mathbf{p}, \mathbf{q}) = \frac{e^{ikr}}{4\pi r}, \tag{5.2}$$

where $r = |\mathbf{p} - \mathbf{q}|$ and i is the imaginary unit. The Helmholtz equation is transformed by using the Green's function to the conventional boundary integral equation (CBIE):

$$c(\mathbf{p})u(\mathbf{p}) + \int_\Gamma \frac{\partial G(\mathbf{p}, \mathbf{q})}{\partial \mathbf{n}(\mathbf{q})} u(\mathbf{q}) d\Gamma(\mathbf{q}) = \int_\Gamma G(\mathbf{p}, \mathbf{q}) \frac{\partial u(\mathbf{q})}{\partial \mathbf{n}(\mathbf{q})} d\Gamma(\mathbf{q}), \qquad \mathbf{p}, \mathbf{q} \in \Gamma, \tag{5.3}$$

in which $c(\mathbf{p})$ refers to the jump-term [8].

The Burton-Miller method (BM) consists of combining two boundary integral equations as follows [38]:

$$\mathbf{CBIE} + \beta \mathbf{HBIE} = 0, \tag{5.4}$$

where β indicates the coupling parameter set as $\beta = \frac{i}{k}$ following [124]. HBIE is the hyper-singular boundary integral equation and is derived by the differentiation of CBIE with respect to the normal $\mathbf{n}(\mathbf{p})$ at the source point $\mathbf{p}$ as follows:

$$c(\mathbf{p})\frac{\partial u(\mathbf{p})}{\partial \mathbf{n}(\mathbf{p})} + \int_\Gamma \frac{\partial^2 G(\mathbf{p}, \mathbf{q})}{\partial \mathbf{n}(\mathbf{q})\partial \mathbf{n}(\mathbf{p})} u(\mathbf{q}) d\Gamma(\mathbf{q}) = \int_\Gamma \frac{\partial G(\mathbf{p}, \mathbf{q})}{\partial \mathbf{n}(\mathbf{p})} \frac{\partial u(\mathbf{q})}{\partial \mathbf{n}(\mathbf{q})} d\Gamma(\mathbf{q}), \quad \mathbf{p}, \mathbf{q} \in \Gamma. \tag{5.5}$$

All derivatives mentioned in equations (5.3) and (5.5) are explained in details in section 4.2.

5.3 Isogeometric analysis (IGA) with NURBS, collocation and numerical integration

The description of the isogeometric analysis with the collocation schemes are considered as same as the previous sections 4.3 while the numerical integration schemes are considered similar to section 4.4.

5.4 The Transmission Loss (TL)

The Transmission Loss (TL) can be predicted using different methods: the 4-pole transfer matrix method, the improved 4-pole transfer matrix method and the 3-point method [60]. The two methods utilized in this section are briefly explained as follows:

5.4.1 The 4-pole transfer matrix method

The muffler problem presented in figure 5.1 can be represented by the linear acoustic 4-pole network defined as follows:

$$\begin{bmatrix} u_{in} \\ v_{in} \end{bmatrix} = \begin{bmatrix} A & B \\ C & D \end{bmatrix} \begin{bmatrix} u_{out} \\ -v_{out} \end{bmatrix},$$

(5.6)

where u is the acoustic sound pressure and v is the normal particle velocity. The indices in and out refer to the muffler inlet and outlet (Γ_{in} and Γ_{out}) respectively as shown in figure 5.1 where the mentioned quantities are evaluated. Since the normal direction on the muffler inlet is opposite to that on the muffler outlet, a negative sign is added to v_{out} in eq.(5.6). In order to obtain the 4-pole parameters A, B, C and D, two BEM solutions are used with the following boundary conditions at the muffler inlet/outlet:

1) v_{in}=1 and v_{out}=0 to produce $A = u_{in}/u_{out}$ and $C = v_{in}/u_{out}$,

2) v_{in}=1 and u_{out}=0 to produce $B = u_{in}/(-v_{out})$ and $D = v_{in}/(-v_{out})$.

Finally, the TL in (dB) can be defined as follows:

$$TL = 20 \log_{10} \left[\frac{1}{2} |A + B/(\rho c) + C\rho c + D| \right] + 10 \log_{10} S_{in}/S_{out},$$

(5.7)

in which S_{in}/S_{out} is the ratio between the cross-sectional areas of the muffler inlet and outlet tubes respectively. In this chapter, $S_{in} = S_{out}$, so that, this term is eliminated. The 4-pole parameters are calculated in complex format and kept complex even in their summation in eq.(5.7) while finally the TL computes the absolute value.

The normal derivative of the acoustic pressure in terms of the normal particle velocity (v) is written as follows:

$$\frac{\partial u}{\partial n} = -i\rho\omega v,$$

(5.8)

where the angular frequency is $\omega = kc$ and c is the sound speed. For all mufflers in this chapter, the sound speed c is 346.1 m/s in air medium with density ρ= 1.1839 kg/m^3.

It can be noticed from the two different boundary conditions on the muffler outlet tube that, the same known vector $\mathbf{b}$ is used twice with two different coefficient matrices $\mathbf{A}$ of the linear system of equations in eq.(4.32). This leads to more computational cost due to the integration effort for the coefficient matrices $\mathbf{A}$.

5.4.2 The improved 4-pole transfer matrix method

In order to accelerate the computation of the TL, the improved 4-pole transfer matrix method is introduced in [60]. The linear system of equations in eq.(4.32) is solved in this method twice as well but with two different known vectors $\mathbf{b}$ and the same coefficient matrix $\mathbf{A}$ which allows to reduce the computational cost. This method is formulated by re-arranging the linear acoustic 4-pole network in eq.(5.6) as follows:

$$
\left[\begin{array}{c} u_{in} \\ u_{out} \end{array} \right] = \left[\begin{array}{cc} A^* & B^* \\ C^* & D^* \end{array} \right] \left[\begin{array}{c} v_{in} \\ -v_{out} \end{array} \right],
\tag{5.9}
$$

where the improved 4-pole parameters A^*, B^*, C^* and D^* are evaluated using two BEM solutions with the following boundary conditions:

1) v_{in}=1 and v_{out}=0 to produce $A^* = u_{in}$ and $C^* = u_{out}$,

2) v_{in}=0 and v_{out}=-1 to produce $B^* = u_{in}$ and $D^* = u_{out}$.

Then, the original 4-pole parameters of eq.(5.6) can be obtained as follows:

$$
\begin{aligned}
A &= A^*/C^*, \\
B &= B^* - A^*D^*/C^*, \\
C &= 1/C^*, \\
D &= -D^*/C^*,
\end{aligned}
\tag{5.10}
$$

to yield the TL of eq.(5.7).

In the next validation examples, both the 4-pole and the improved 4-pole transfer matrix methods are implemented and compared against previously published works using the same methods in addition to the 3-point method producing almost the same results. It is mentioned in [60] that the 3-point method is faster than the 4-pole transfer matrix as a single BEM solution is required. However, it is slower than the improved 4-pole

130

transfer matrix since it needs a post-processing calculation for field points.

5.5 Description of the structural shape optimization problem

The coupled structural shape optimization problem with BEM using the Particle Swarm Optimization (PSO) algorithm is considered as same as the previous section 2.6

5.6 Numerical results

Several numerical examples are studied to present the performance of IGA-BM for solving muffler problems. The examples are divided into two parts. In the first part, IGA-BM is verified against the analytical solution using the interior spherical cavity problem. Then, IGA-BM is validated against previously published experimental data and the numerical results obtained from FEM, BEM and IGA models using different mufflers with and without extended inlet/outlet tubes. Subsequently in the second part, the lengths of the extended inlet/outlet tubes are optimized using PSO to enhance the TL and the results are compared against the previously published results obtained from FEM with sensitivity analysis.

5.6.1 Verification examples

Three examples are discussed in this section to verify the proposed IGA-BM algorithm that is used in the next section for optimization problems.

5.6.1.1 The interior spherical cavity problem

An interior spherical cavity with a radius $a = 1.0$ m centered at the origin is considered. The cavity pulsates radially with a unit normal velocity prescribed over its entire surface as shown in figure 5.3 which can be defined with the Neumann boundary condition in BM eq.(5.4) as follows:

$$\frac{\partial u}{\partial n} = 1.$$ (5.11)

The analytical solution of this problem is defined in [51] as follows:

$$u^{ex}(r) = \frac{ka^2}{ka\cos(ka) - \sin(ka)}\frac{\sin(kr)}{kr},$$ (5.12)
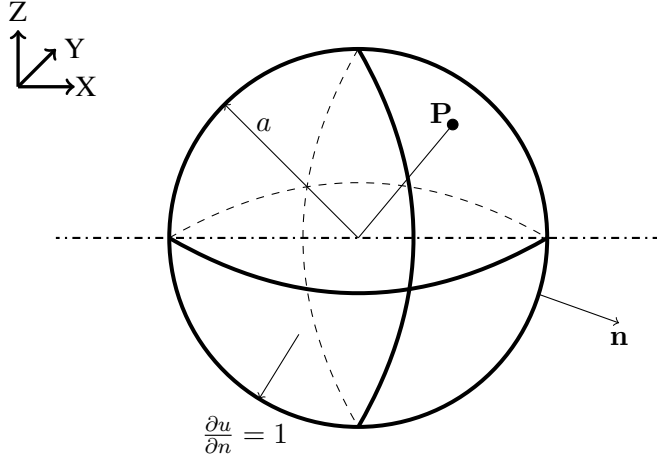
Figure 5.3: The interior spherical cavity problem.

in which r indicates the distance from the origin to the concerned point $\mathbf{P}$. Hence, when the point $\mathbf{P}$ is located in the origin of the cavity ($r = 0$), $\frac{\sin(kr)}{kr} = 1$.

The NURBS polynomial degree 2 is considered for each knot direction where the two knot vectors in the two dimensions are written as follows: $\Xi = \{0, 0, 0, 0.5, 0.5, 1, 1, 1\}$ and $\Upsilon = \{0, 0, 0, 0.25, 0.25, 0.5, 0.5, 0.75, 0.75, 1, 1, 1\}$. Figure 5.4 shows the NURBS model and the corresponding control points. The proposed numerical solution u^{num} of eq.(5.4) is calculated on the surface of the cavity and verified against the analytical solution of eq.(5.12) using the relative L_2 error norm following the formula:

$$e_{L_2} \equiv \frac{||u^{ex} - u^{num}||}{||u^{ex}||} = \sqrt{\frac{\int_\Gamma (u^{num} - u^{ex})^T (u^{num} - u^{ex})d\Gamma}{\int_\Gamma u^{ex T} u^{ex} d\Gamma}}, \tag{5.13}$$

while 6 Gauss quadrature points for each knot span are considered for the integration.

Figure 5.5 presents the variation of e_{L_2} as a function of DOFs per wavelength in each coordinate direction for the frequencies: 100, 500 and 1000 Hz with wavenumbers k= 1.82, 9.08 and 18.15 respectively. The results prove the accuracy of the proposed technique for treating such interior acoustic problem with moderate DOFs. Moreover, figure 5.6 shows the spectrum of the acoustic pressure value at the cavity origin ($r = 0$) for IGA-BM using the coarse mesh of 128 DOFs for all frequencies. The IGA-BM spectrum is plotted against the analytical spectrum. It can be concluded that, IGA-BM is in excellent agreement with the analytical solution even for the frequencies when $\tan(ka) = ka$ producing infinite magnitudes.

132
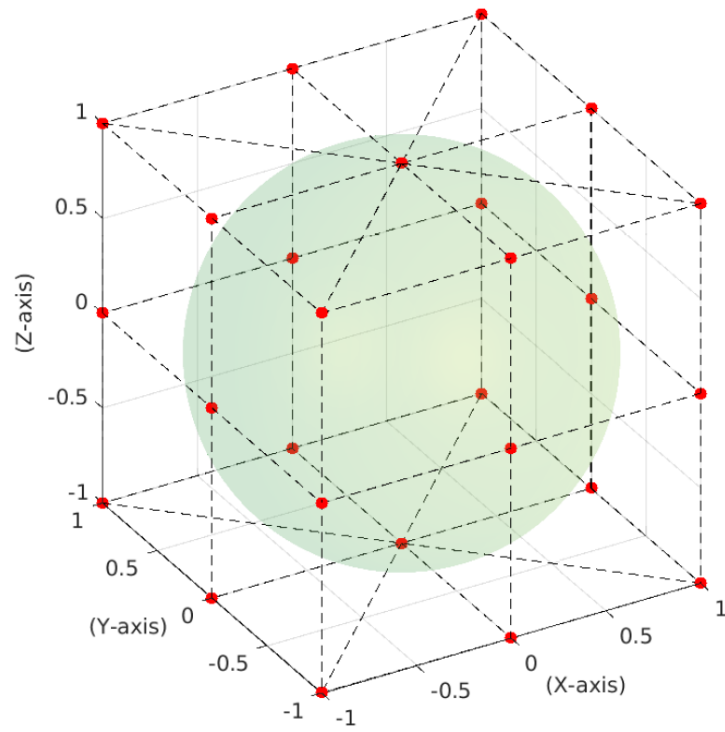
Figure 5.4: NURBS model and the corresponding control points grid for the interior spherical cavity.
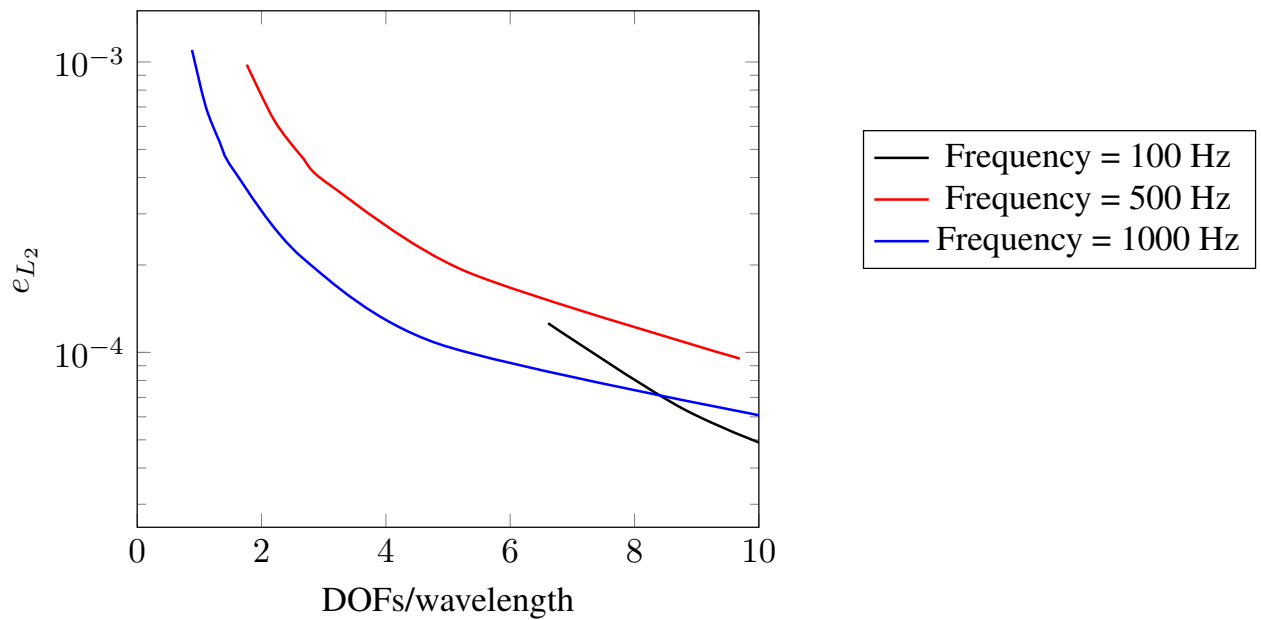
Figure 5.5: L_2 error norm for different frequencies in terms of DOFs per wavelength in each coordinate direction.
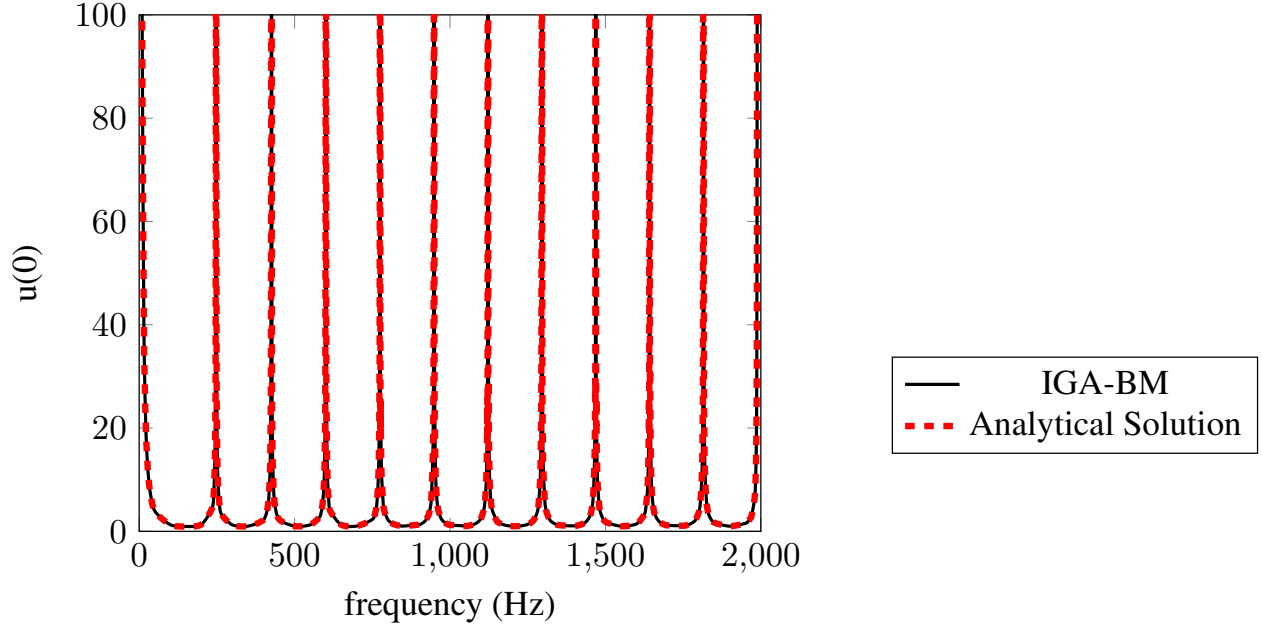
Figure 5.6: Acoustic pressure spectra at the cavity origin u(0).

5.6.1.2 Muffler without extended inlet/outlet tubes

In this section, two examples are studied and verified against previously published results using BEM, FEM and experimental data.

Example 1: A comparison with BEM using the simple form of polynomial shape functions

In this example, the TL of a muffler without extended inlet/outlet tubes ($L_1 = L_2 = 0$ with reference to figure 5.1) using IGA-BM is compared against the TL results published in [51] using BEM with the simple form of polynomial shape functions and the 4-pole transfer matrix. Moreover, the results of the plane-wave solution is included in this comparison. The discussed muffler is shown in figure 5.7 where both of the radius and the length of the inlet/outlet tubes is 2.54 cm ($D_1 = D_2 = 5.08$ cm). Likewise, the length and the radius of the of the main chamber is 15.24 cm ($D = 30.48$ cm and $L = 15.24$ cm). Figure 5.7 contains an internal section of the muffler showing no extended inlet/outlet tubes. The muffler is modelled using NURBS polynomial degree 2 for each knot direction where the two knot vectors are introduced as follows: $\Xi = \{0, 0, 0, 1/7, 1/7, 2/7, 2/7, 3/7, 3/7, 4/7, 4/7, 5/7, 5/7, 6/7, 6/7, 1, 1, 1\}$ and $\Upsilon = \{0, 0, 0, 0.25, 0.25, 0.5, 0.5, 0.75, 0.75, 1, 1, 1\}$. Figure 5.8 illustrates the NURBS model and the corresponding control points.
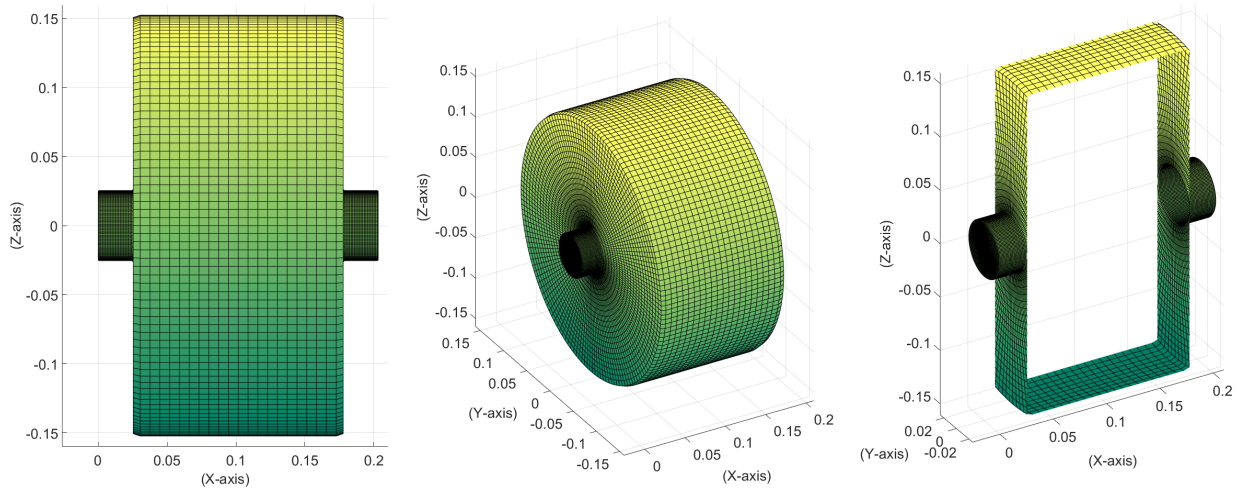
Figure 5.7: Elevation, outer isometric and internal isometric views for a muffler without extended inlet/outlet tubes (Example 1).

Figure 5.8: Elevation and isometric views showing the NURBS model and the corresponding control points grid for a muffler without extended inlet/outlet tubes (Example 1).

Figure 5.9: TL spectra for a muffler without extended inlet/outlet tubes (Example 1). Note that, both 4-pole and improved 4-pole transfer matrix solutions (black and dashed red curves respectively) are quasi identical.

Figure 5.9 includes all the TL spectra of the comparison data. IGA-BM models are plotted for both of the 4-pole transfer matrix and the improved 4-pole transfer matrix. A constant mesh is employed in [51] using 7 DOFs along the chamber length (15.24 cm) for all frequencies while two meshes are implemented for IGA-BM models to obtain high accuracy proportional to the increased frequencies; 6 DOFs for the same length for frequencies less than 600 Hz and 10 DOFs for the rest of frequencies. The plane-wave solution for the TL in (dB) can be approximated analytically for simplest reactive muffler according to the following formula [51]:

$$TL = 10 \log_{10} \left[1 + \frac{1}{4} \left(m - \frac{1}{m} \right)^2 \sin^2 kL \right], \tag{5.14}$$

where m is the expansion ration between the cross-section area of the inlet/outlet tubes and the cross-section area of the main chamber. L indicates the length of the main chamber. It can be seen that, both 4-pole and improved 4-pole transfer matrices result in the same plot, however the 4-pole transfer matrix requires more time to assemble 2 system matrices. Both methods are also in a very good agreement with [51] except for small deviations in the cases of higher frequencies. The reason may be because a constant coarse mesh is used in [51] even for higher frequencies. The plane-wave solution given by eq.(5.14) is accurate only for

136

small frequencies less than 300 Hz. After that, it fails to predict the correct TL due to the large chamber diameter.

Example 2: A comparison with FEM and experimental data

In this example, the TL produced by a bigger muffler (silencer) without extended inlet/outlet tubes is validated against the TL results produced by FEM models with full 3D hexahedron elements presented in [52] using the 3-point method. The experimental data shown in the same reference are included in the comparison as well. The concerned muffler/silencer is shown in figure 5.10 where both the inlet/outlet tubes have the same length 50.0 cm and the same diameter $D_1 = D_2 = 5.25$ cm. The main chamber has a length $L = 45.30$ cm with a diameter $D = 14.93$ cm. Figure 5.11 clarifies the NURBS model and the corresponding control points where the two knot vectors are written similar to Example 1.

Similar to the previous example, the TL spectra for all comparison data are plotted in figure 5.12. The spectra of IGA-BM models using both the 4-pole and improved 4-pole transfer matrices are plotted as well, where it can be seen that, the two plots are identical to each other. The IGA-BM models employed 9 DOFs for the inlet/outlet tube length (50.0 cm) or the chamber length (45.30 cm) for frequencies less than 800 Hz and 12 DOFs for the rest of frequencies while a constant finer mesh is used in [52]. It can be concluded that the IGA-BM solutions are in a very good agreement with the FEM solution of [52] while the small differences with the experimental data are possible due to the measurement error.

5.6.1.3 Muffler with extended inlet/outlet tubes

In this section, the TL of a muffler with extended inlet/outlet tubes using IGA-BM is compared with the TL results obtained from the following:

1) The models implemented in [55] using Galerkin-FEM (GFEM) with quadratic axi-symmetric triangular elements and the improved 4-pole transfer matrix.

2) The 3D IGA models reported in [56] using NURBS with polynomial degree 3 and a mathematical expression for the TL.

3) The models implemented in [57] using BEM with the simple form of quadratic shape functions and the 4-pole transfer matrix.

4) The experimental data obtained in [57].

This comparison is performed for the muffler configuration shown in figure 5.13 where the main chamber

Figure 5.10: Elevation, outer isometric and internal isometric views for a muffler without extended inlet/outlet tubes (Example 2).
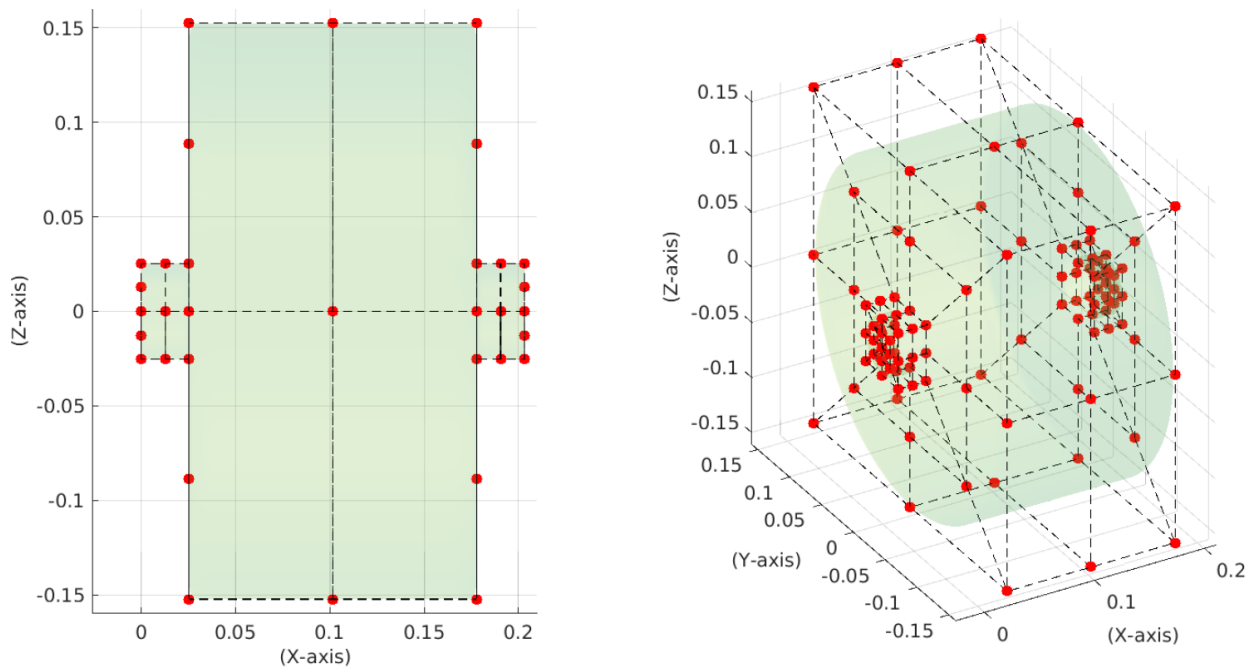
Figure 5.11: Elevation and isometric views showing the NURBS model and the corresponding control points grid for a muffler without extended inlet/outlet tubes (Example 2).
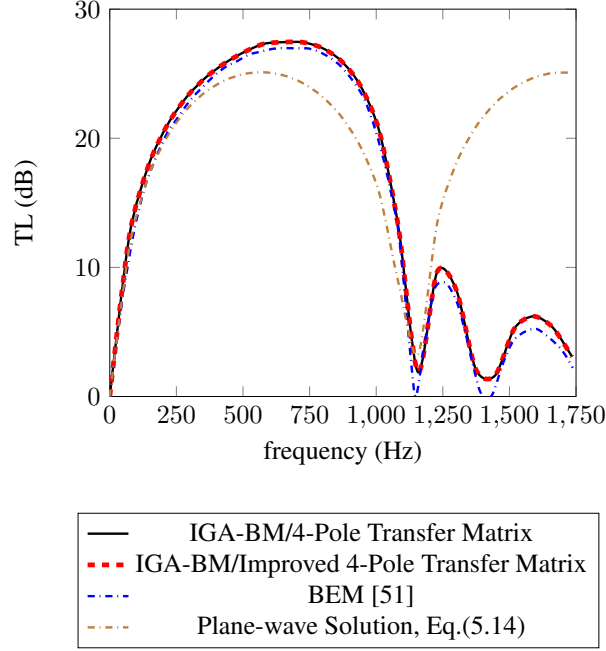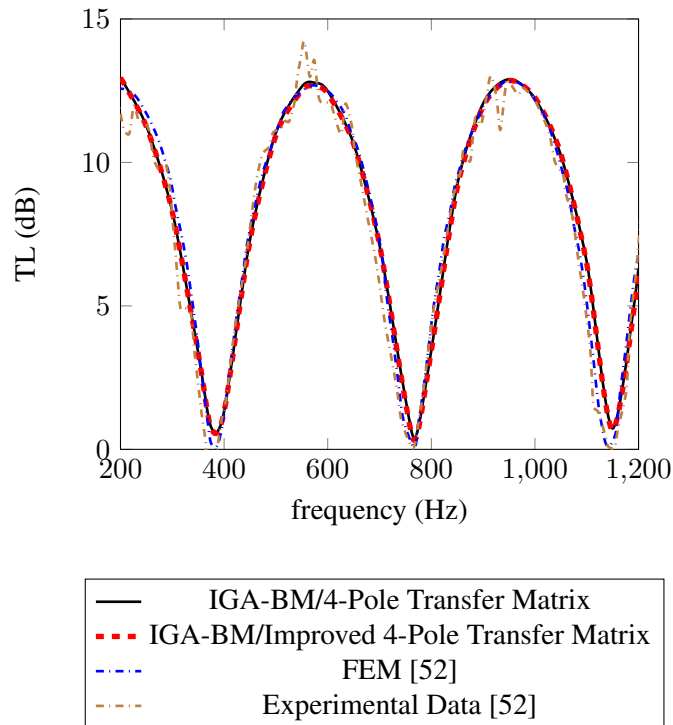

Figure 5.12: TL spectra for a muffler without extended inlet/outlet tubes (Example 2). Note that, both 4-pole and improved 4-pole transfer matrix solutions (black and dashed red curves respectively) are quasi identical.

has a length $L = 28.23$ cm with a diameter $D = 15.32$ cm. Both the inlet/outlet tubes have the same diameter $D_1 = D_2 = 4.86$ cm. With reference to [52], the outside length of the inlet/outlet tubes has no significant effect on the TL. Therefore, this length is taken as 8.0 cm. The most important factor in the TL is the internal extended length of the inlet/outlet tubes. In this comparison, the length of the extended inlet tube L_1 is taken as 13.1 cm while the extended outlet length L_2 is taken as 6.1 cm. As discussed, BM can consider the small thickness of the extended tubes which is taken as $t = 0.2$ cm in this example. Figure 5.13 presents also the extended tubes in an internal section of the muffler. The muffler is modelled with NURBS of polynomial degree 2 for each knot direction where the two knot vectors are written as follows: $\Xi = \{0, 0, 0, 1/13, 1/13, 2/13, 2/13, 3/13, 3/13, 4/13, 4/13, 5/13, 5/13, 6/13, 6/13, 7/13, 7/13, 8/13, 8/13,$
$9/13, 9/13, 10/13, 10/13, 11/13, 11/13, 12/13, 12/13, 1, 1, 1\}$ and $\Upsilon = \{0, 0, 0, 0.25, 0.25, 0.5, 0.5, 0.75,$
$0.75, 1, 1, 1\}$. Figure 5.14 presents the NURBS model with the corresponding control points. Additional detail in figure 5.15 shows the small thickness of the extended tube where the control points are so close to each other.

All compared TL spectra are illustrated in figure 5.16 where IGA-BM models are implemented using both the 4-pole transfer matrix and the improved 4-pole transfer matrix. The maximum element sizes employed for all frequencies for the GFEM mesh in [55], the IGA model in [56] and the proposed IGA-BM models are 0.6, 2.82 and 4.03 cm respectively. It is worth noting that the proposed IGA-BM models are also coarser than the IGA model of [56] even through the polar direction.

Similar to the previous conclusion, both 4-pole and improved 4-pole transfer matrices produce the same plot. Both methods are also in an a very good agreement with GFEM models of [55] in addition to the experimental data except in resonance regions, while they keep the good agreement even in resonance regions with IGA models of [56]. Only small differences with the experimental data appear which can be attributed to the measurement error.The differences between the BEM results of [57] and all other results especially for higher frequencies could be due to neglecting modelling the thickness of the extended tubes in the old BEM models. This demonstrates the advantage of the proposed IGA-BM models.
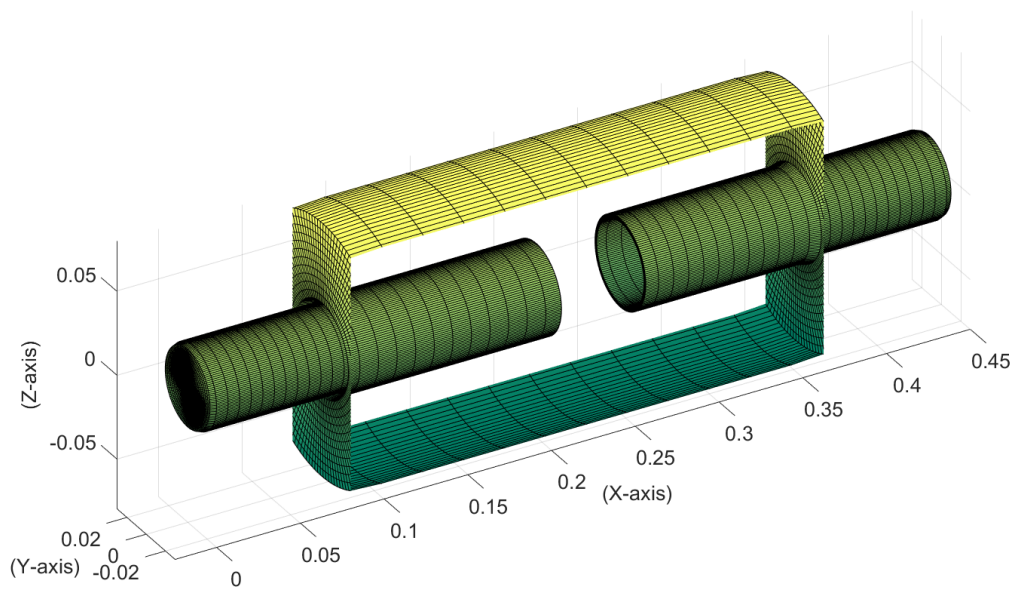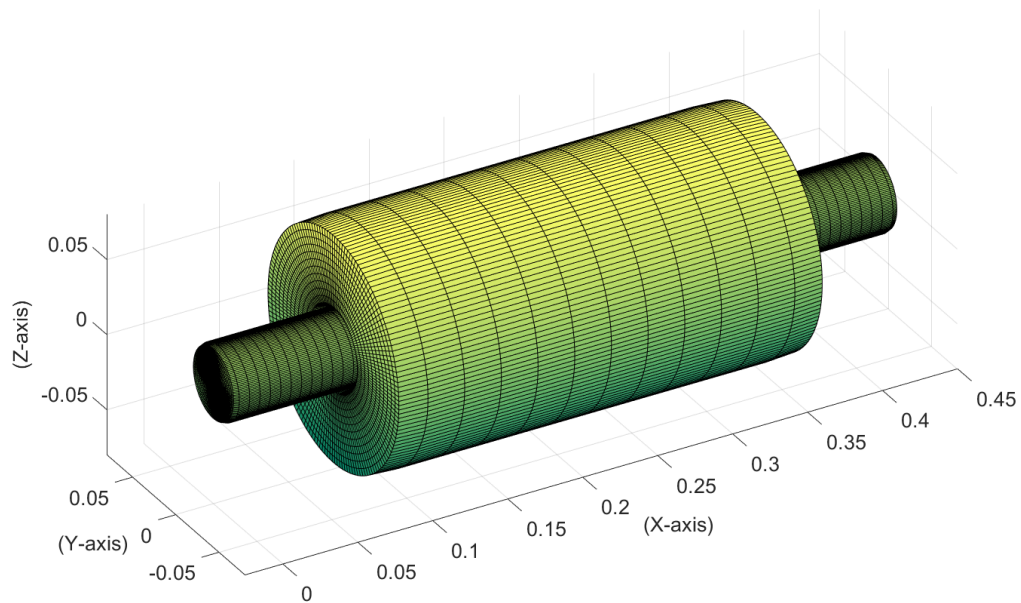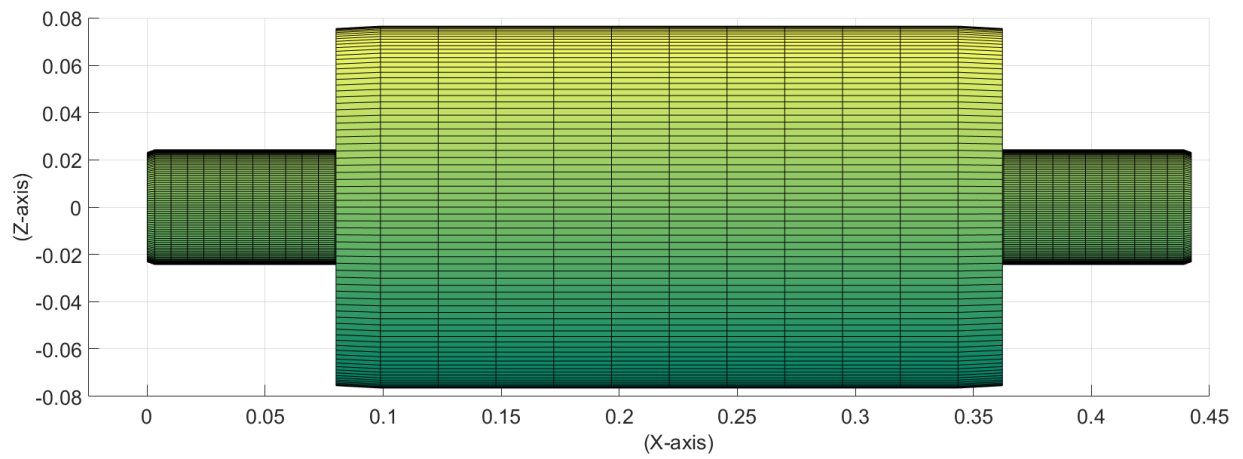
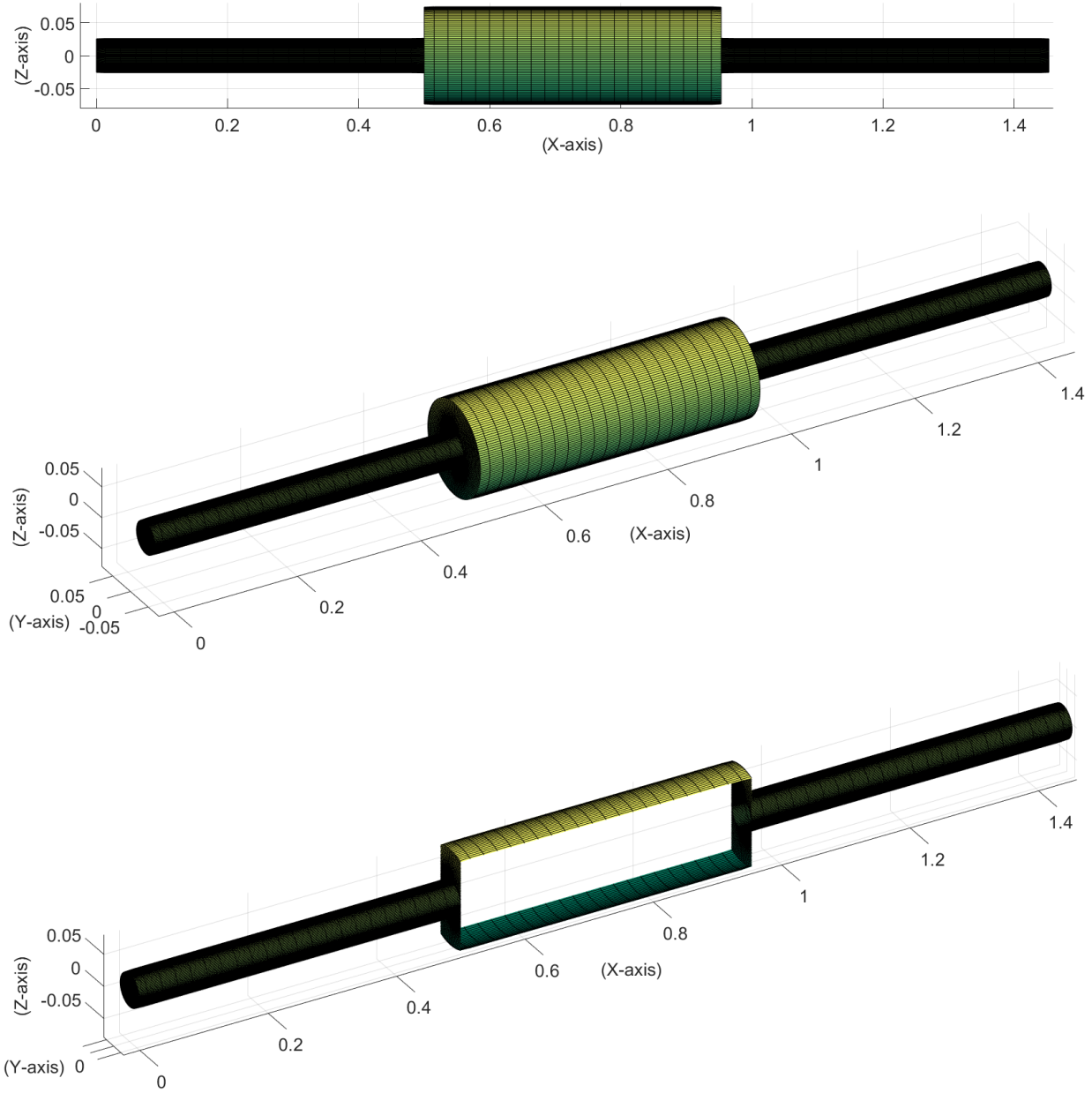**Figure 5.13:** Elevation, outer isometric and internal isometric views for a muffler with extended inlet/outlet tubes.
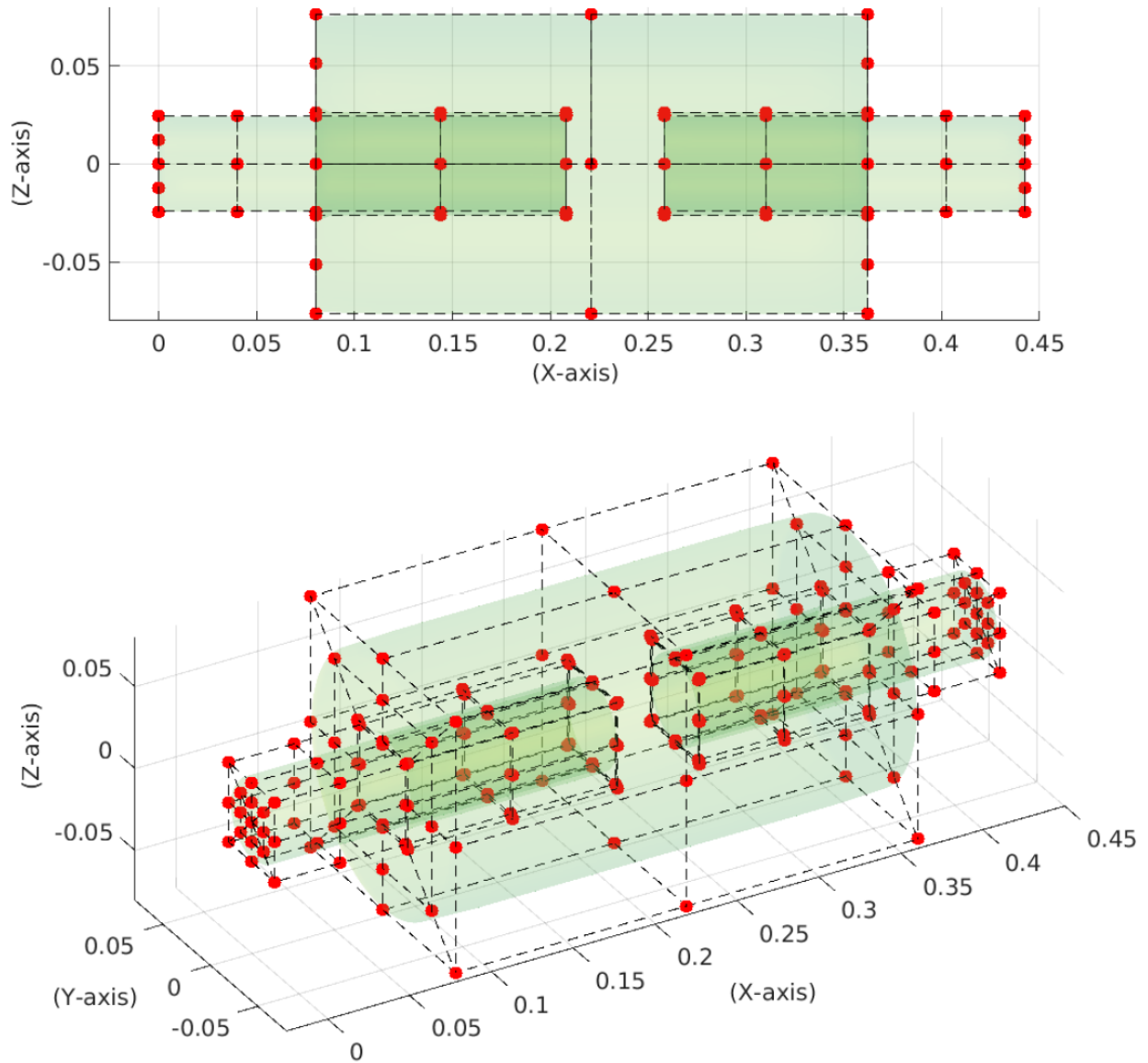
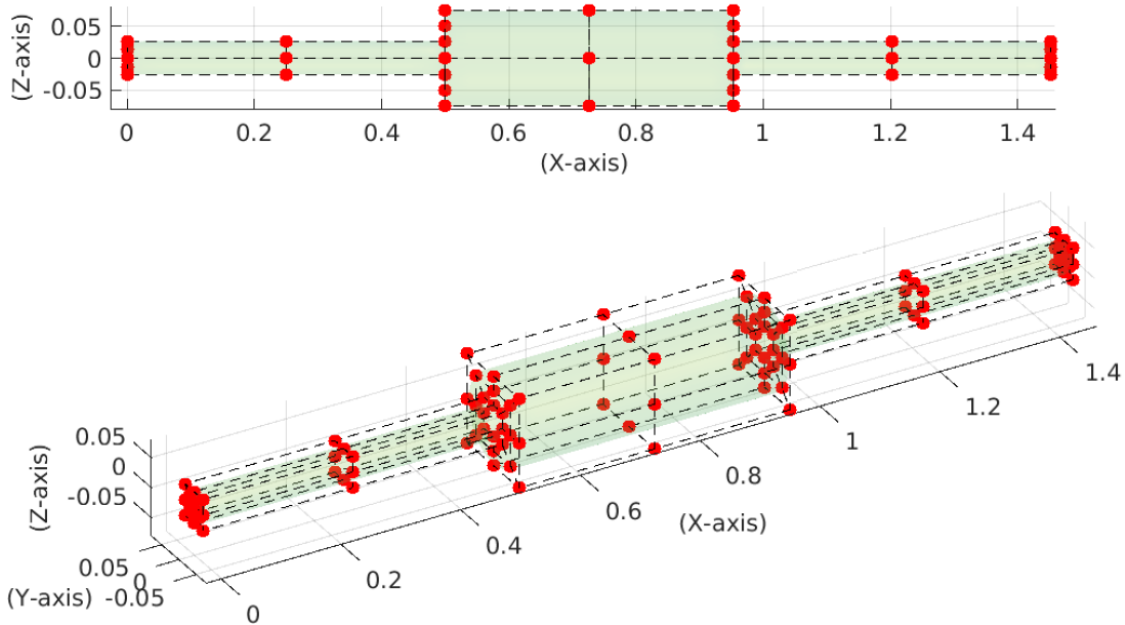**Figure 5.14:** Elevation and isometric views showing the NURBS model and the corresponding control points grid for a muffler with extended inlet/outlet tubes.
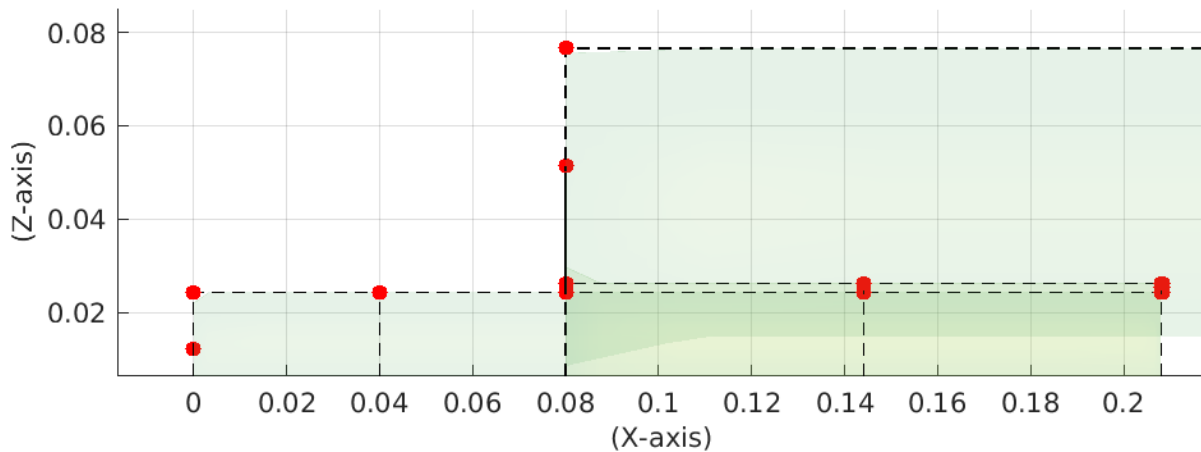
**Figure 5.15:** A detail showing the elevation view for the control points of the extended tube part with small thickness.

5.6.2 Optimization analysis of the TL for mufflers with extended inlet/outlet tubes

The same muffler discussed in section 5.6.1.3 and shown in figure 5.13 is examined in this section as well. Changes are applicable only to the lengths of the internal extended inlet/outlet tubes. The initial inlet/outlet tube lengths (L_1 & L_2) are set as 7.0/8.0 cm which produce the TL spectrum presented in figure 5.17. It can be seen that, two attenuation regions are existing in the frequency band from 600 to 650Hz and from 1200 to 1250 Hz. In order to optimize the TL in these two regions, three optimization cases are discussed in the next sections with the lengths of the two internal extended tubes taken as two design variables. The lengths are allowed to a free change during the optimization process in the range of 1.0 cm to 14.0 cm.

The IGA-BM models using only the improved 4-pole transfer matrix (which builds up one system matrix) are employed to speed up the optimization analysis. The optimization results are implemented using the PSO algorithm and compared against the previously reported results in [126] using quadratic axi-symmetric triangular FEM and sensitivity analysis. The maximum element size of these FEM models is 0.6 cm while the IGA-BM models with maximum element size of 4.03 cm are used in this comparison.

It is worth noting that the first calculated matrix $\mathbf{A}$ and vector $\mathbf{b}$ in eq.(4.32) are stored. Then for each following iteration, they are re-called again while only changes are applicable to the rows corresponding to the collocation points placed on the modified internal extended inlet/outlet tubes and also to the columns containing the integration over the surface of the modified tubes. This helps to accelerate the optimization

143
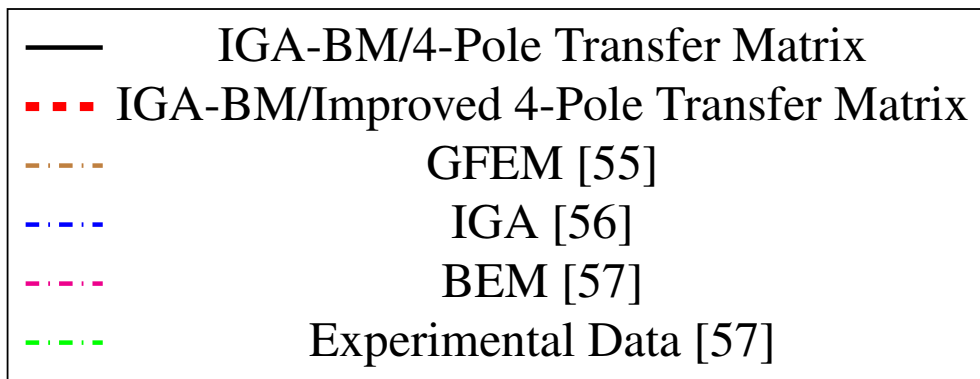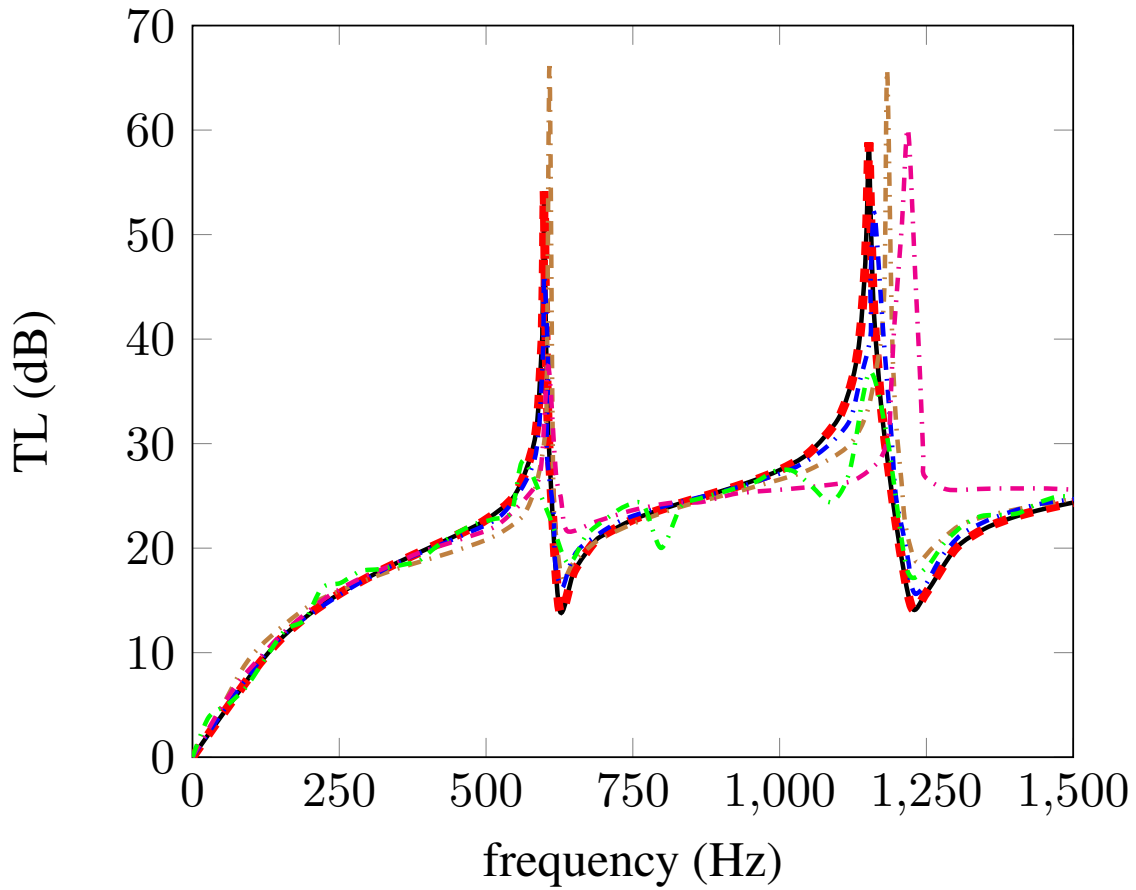
Figure 5.16: TL spectra for a muffler with extended inlet/outlet tubes. Note that, both 4-pole and improved 4-pole transfer matrix solutions (black and dashed red curves respectively) are quasi identical.
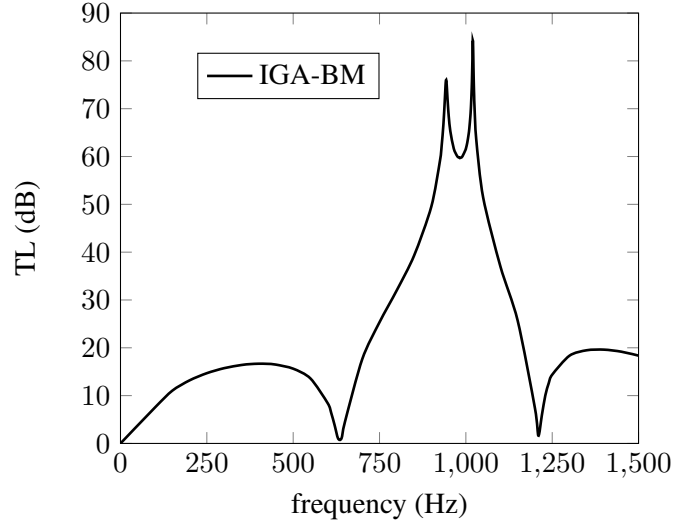
Figure 5.17: TL spectrum for a muffler with initial extended tubes before optimization.

process and prevent any repeated integration.

5.6.2.1 Optimization for frequency band from 600 to 650 Hz without physical constraints

In order to optimize the TL for the frequency band from 600 to 650 Hz, the following objective function is defined:

$$F(x) = \min \frac{\alpha}{\frac{1}{50} \int_{600}^{650} TL(f) \, df}, \tag{5.15}$$

in which f indicates the frequency in interest under the integral and α refers to a scalar factor which is chosen as 10 for all examples in this work. The variable x is the length of the internal extended inlet/outlet tubes (L_1 & L_2). Several tests are implemented using only 4 and 10 Gauss quadrature points for the integration inside the objective function instead of 200 points with Simpson's integration rule in [126] since increasing the number of Gauss points does not improve the solution. This is supported by the study discussed in [21] where the adequacy of using few Gauss quadrature points was proven for such integration to give the same results as produced by using more points or other integration methods. Since there is no constraint defined for this case, the fitness function of eq.(2.28) equals the the objective function in eq.(5.15) where it can be written as follows:

$$\text{Fitness} = F(x) = \min \frac{\alpha}{\frac{1}{50} \int_{600}^{650} TL(f) \, df}. \tag{5.16}$$

145
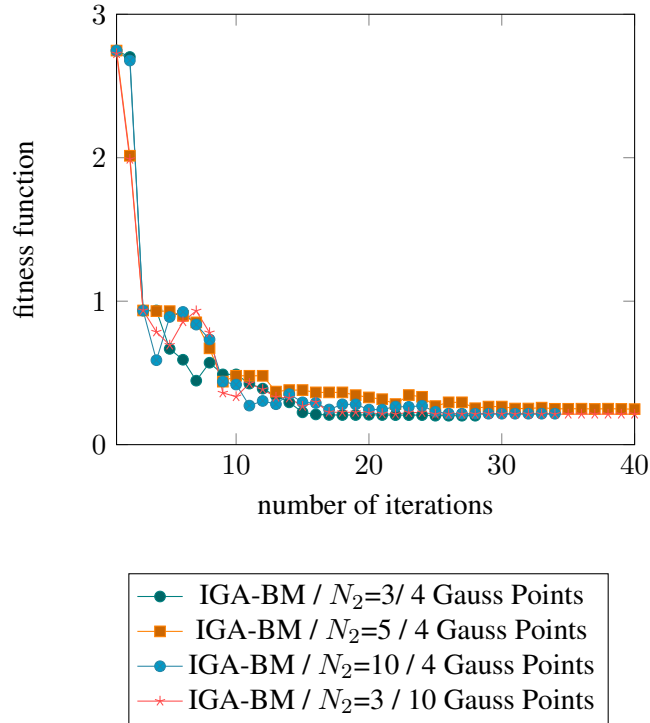
Figure 5.18: Convergence of the fitness function in terms of the number of iterations for the optimization problem of the frequency band from 600 to 650 Hz.

Figure 5.19: TL spectra for the initial and optimized mufflers with extended inlet/outlet tubes for the frequency band from 600 to 650 Hz.

146

Figure 5.18 illustrates the variation of the fitness function during the optimization process for different values of the Number of Consecutive Iterations (N_2) and using 4 and 10 Gauss quadrature points. It can be seen that all configurations lead to close results. Furthermore, it can be observed that, the configuration of $N_2 = 3$ with 4 Gauss points is sufficient to produce accurate results. Figure 5.19 shows the TL spectra for the initial and optimized mufflers. The comparative data are shown in table 5.1. It can be shown that, the results obtained from the IGA-BM model - in terms of the optimized lengths, spectrum and the objective function - are in a very good agreement with those of [126]. As shown in figure 5.19, the TL in the frequency band from 600 to 650 Hz could be enhanced using the fitness function of eq.(5.16). However the attenuation region in the frequency band from 1200 to 1250 Hz still exists.

	FEM [126]	IGA-BM
Objective Function	0.195	0.202
Number of Design Variables	2	2
Number of frequencies inside the the frequency band	200	4
N_2 - Number of Consecutive Iterations for PSO	-	3
Max. Element Size (cm)	0.6	4.03
Optimized lengths L_1 & L_2 (cm)	12.86 & 10.55	12.74 & 10.37

Table 5.1: Comparative data for the optimization problem of frequency band from 600 to 650 Hz.

5.6.2.2 Optimization for two frequency bands from 600 to 650 Hz and from 1200 to 1250 Hz without physical constraints

In order to optimize the TL of the attenuation regions in the two frequency bands from 600 to 650 Hz and from 1200 to 1250 Hz, the objective function is modified to the following formula:

$$F(x) = \min \left[\frac{\alpha}{\frac{1}{50} \int_{600}^{650} TL(f) \, df} + \frac{\alpha}{\frac{1}{50} \int_{1200}^{1250} TL(f) \, df} \right]. \tag{5.17}$$

Consequently, the fitness function of eq.(2.28) with no defined constraint equals the objective function in eq.(5.17) and can be re-written for this case as follows:

$$\text{Fitness} = F(x) = \min \left[\frac{\alpha}{\frac{1}{50} \int_{600}^{650} TL(f) \, df} + \frac{\alpha}{\frac{1}{50} \int_{1200}^{1250} TL(f) \, df} \right]. \tag{5.18}$$

Figure 5.20: Convergence of the fitness function in terms of the number of iterations for the optimization problem of two frequency bands without a constraint function.
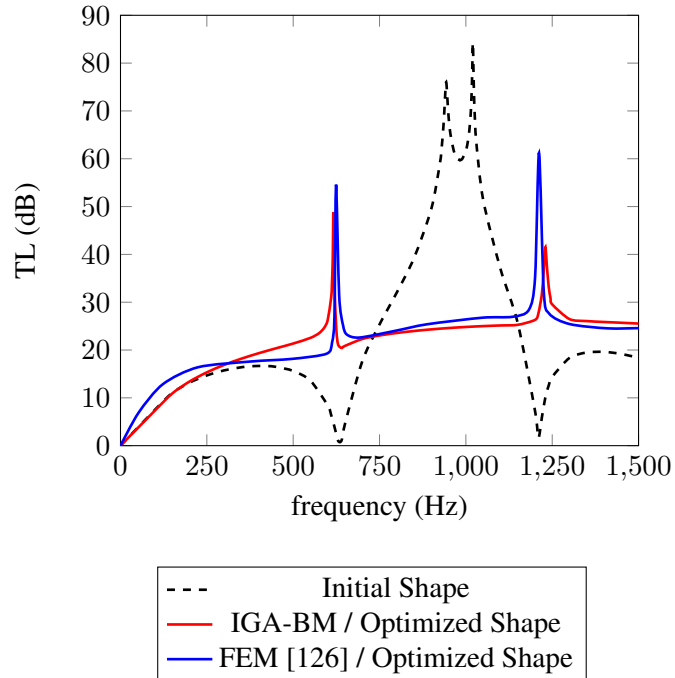
Figure 5.21: TL spectra for the initial and optimized mufflers with extended inlet/outlet tubes for the two frequency bands without a constraint function.

Figure 5.20 shows the variation of the fitness function during the optimization process for different values of N_2 and using 4 and 10 Gauss quadrature points, where it can be seen that all trials converge to close results. Figure 5.21 displays the TL spectra for the initial and optimized mufflers. The comparative data are shown in table 5.2 where the objective function obtained from the proposed model is less than that of [126]. Moreover, there is a study implemented in [126] to find out manually the optimum length of the internal extended inlet tube L_1 while fixing the length of the internal extended outlet tube L_2 to be 12.21 cm and the optimum length was obtained as $L_1 = 5.8$ cm giving an objective function of 0.65. Reaching the optimum results directly with the proposed model verifies its efficiency. Furthermore, figure 5.21 demonstrates the enhancement of the TL in the two concerned frequency bands using the fitness function of eq.(5.18), where it can be seen that the two initial attenuation regions vanish.

	FEM [126]	IGA-BM
Objective Function	1.0	0.624
Number of Design Variables	2	2
Number of frequencies inside the the frequency band	200	4
N_2 - Number of Consecutive Iterations for PSO	-	3
Max. Element Size (cm)	0.6	4.03
Optimized lengths L_1 & L_2 (cm)	5.23 & 12.21	5.67 & 12.70

Table 5.2: Comparative data for the optimization problem of two frequency bands without a constraint function.

5.6.2.3   Optimization for the frequency band from 600 to 650 Hz with a constraint in the frequency band from 1200 to 1250 Hz

Another objective function is defined in this section to optimize the TL of the attenuation region in the frequency band from 600 to 650 Hz as follows:

$$F(x) = \min \frac{\alpha \frac{1}{50} \int_{1200}^{1250} TL(f)\, df}{\frac{1}{50} \int_{600}^{650} TL(f)\, df}, \tag{5.19}$$
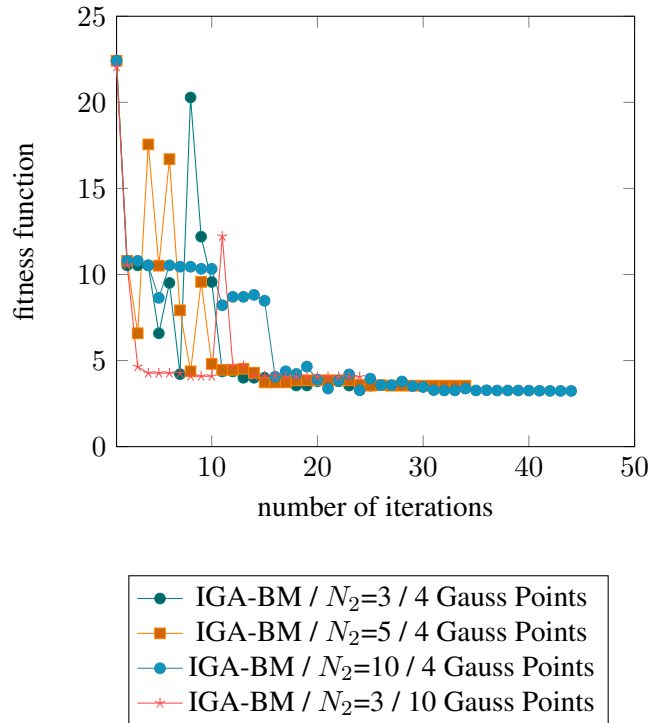
Figure 5.22: Convergence of the fitness function in terms of the number of iterations for the optimization problem of two frequency bands with a constraint function.
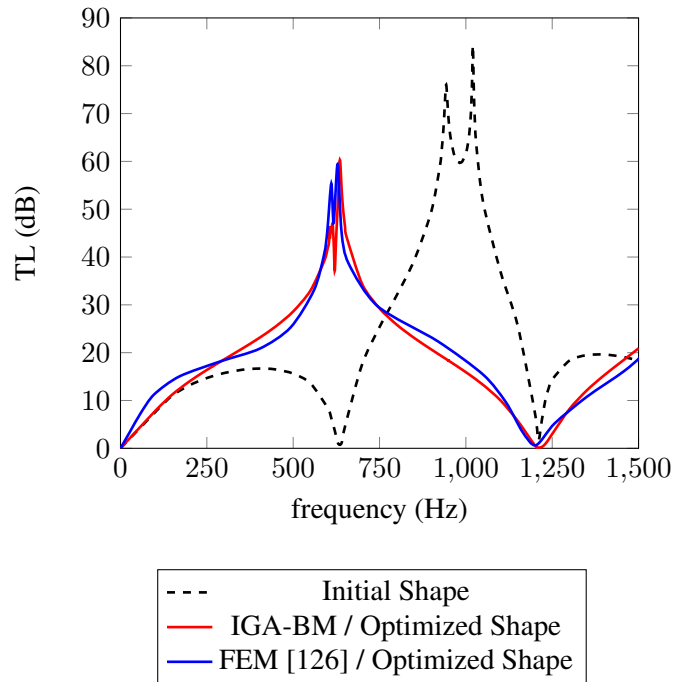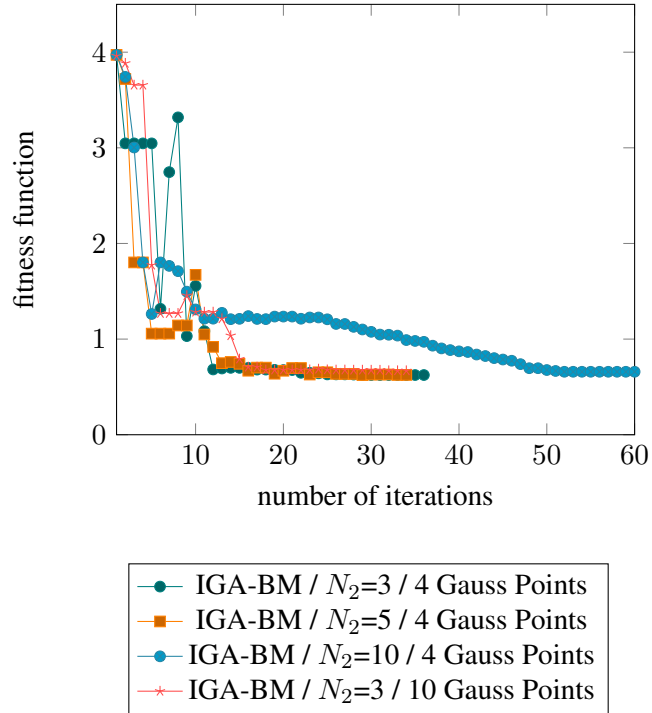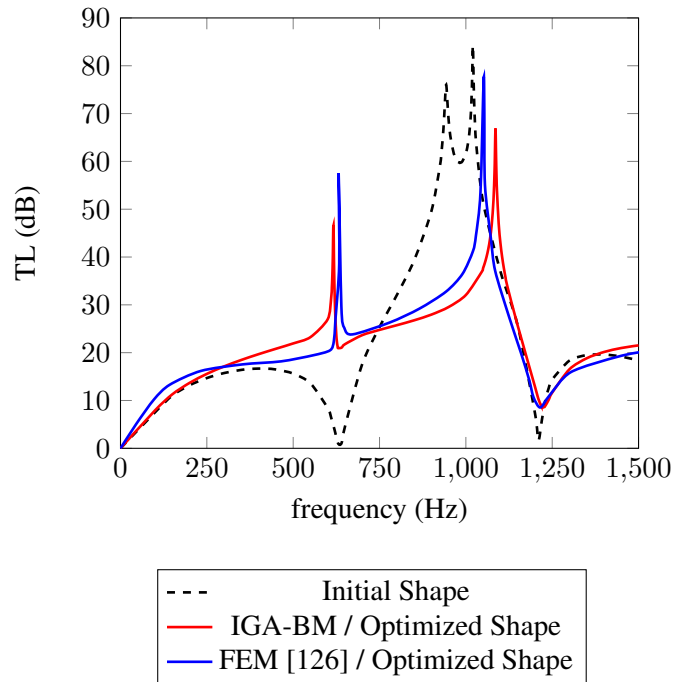

Figure 5.23: TL spectra for the initial and optimized mufflers with extended inlet/outlet tubes for the two frequency bands with a constraint function.

but with another constraint to force the TL in the frequency band from 1200 to 1250 Hz to be at least equal to 10. This constraint can be written mathematically as follows:

$$g_l(x) = \frac{10}{\frac{1}{50} \int_{1200}^{1250} TL(f) \, df} - 1 \leq 0. \tag{5.20}$$

Thus, the fitness function of eq.(2.28) including both the objective and constraint functions can be introduced as follows:

$$\text{Fitness} = \min \left[\alpha \frac{\frac{1}{50} \int_{1200}^{1250} TL(f) \, df}{\frac{1}{50} \int_{600}^{650} TL(f) \, df} \right] + \eta \times \max \left[\left(\frac{10}{\frac{1}{50} \int_{1200}^{1250} TL(f) \, df} - 1 \right), 0 \right]. \tag{5.21}$$

The variation of the fitness function during the optimization process is presented in figure 5.22 for different N_2 values using 4 and 10 Gauss quadrature points converging to close results. Figure 5.23 clarifies the TL spectra for the initial and optimized mufflers. The comparative data are shown in table 5.3. The enhancement of the TL in the two considered frequency bands is clear in figure 5.23 where the two initial attenuation regions vanish. Finally, it can be concluded that the proposed model of IGA-BM with PSO using coarser meshes and extremely few Gauss quadrature points for the integration of the objective function produces comparable results with those obtained from FEM models with sensitivity analysis reported in [126].

	FEM [126]	IGA-BM
Objective Function	3.70	3.26
Number of Design Variables	2	2
Number of frequencies inside the the frequency band	200	4
N_2 - Number of Consecutive Iterations for PSO	-	10
Max. Element Size (cm)	0.6	4.03
Optimized lengths L_1 & L_2 (cm)	6.82 & 12.54	6.51 & 12.70

Table 5.3: Comparative data for the optimization problem of two frequency bands with a constraint function.

5.7 Summary

One of the boundary element methods; Burton-Miller method (BM) is coupled with the isogeometric analysis (IGA) - forming IGA-BM - to study the muffler problem with extended inlet/outlet tubes as an interior Helmholtz acoustic problem. BM can properly model the extended tubes with thin thickness as two surfaces

separated from each other by a small gap since the normal direction at each collocation point over all surfaces can be evaluated. Moreover, BM provides the merit of BEM models of modelling only the surface/boundary of the 3D problem reducing its dimensionality. In addition, IGA is powerful for modelling complex surfaces with accelerated refinement process and higher accuracy by approximating both the CAD geometry and the physical boundary variables with Non-Uniform Rational B-splines basis functions (NURBS).

The main design factor for mufflers, the transmission loss (TL), is calculated using three methods; the 3-point method, the 4-pole transfer matrix method and the improved 4-pole transfer matrix method. All methods give almost the same results while the improved 4-pole transfer matrix is preferred since it requires only one system matrix with two different vectors for different boundary conditions. This speeds up the computation process. In addition, the TL produces the 4-pole parameters entering/exiting the inlet/outlet tubes which is convenient to the nature of BM of predicting the physical variables on the boundary of the problem.

The validity of IGA-BM using coarser meshes is proven in comparison with the analytical solution, experimental data and the previously published numerical results with BEM, FEM and IGA models. The Particle Swarm Optimization (PSO) is shown as a simple gradient-free method which does not require any sensitivity analysis. Pairing it with IGA-BM models for shape optimization problems makes the communication straightforward between the three models: CAD, design and optimization models. As long as few design variables are set for the optimization problem, a lower value for the Number of Consecutive Iterations (N_2) can be chosen converging to excellent results. In addition, minimization of the objective function for optimization problems for maximizing the TL can be achieved by dividing the frequency band only to 4 frequencies and using 4 Gauss quadrature points for integration purposes [127].

Chapter 6

Conclusion

6.1 Summary of the findings

In this thesis, the isogeometric analysis (IGA) is proposed in the framework of the boundary element methods (BEM) forming the so-called (IGABEM) to study the Helmholtz time harmonic equation for acoustic problems. BEM is superior in handling the Helmholtz equation since it models only the inner boundaries and avoids the truncation error for infinite domain problems. NURBS approximate both the CAD geometries and the physical fields. IGABEM accelerates re-meshing and provides higher accuracy compared to the standard BEM.

Furthermore, Particle Swarm Optimization (PSO) - as a simple gradient-free method which does not require any sensitivity analysis - is coupled with IGA for shape optimization problems. This model provides a great advantage in optimization models, since it gets benefit from the IGA feature of representing the three different models: shape design, analysis and optimization models using a single set of control points. This allows a smooth transition between the three models through the optimization iterations.

The proposed model is verified using several numerical examples compared against analytical and previously published numerical methods.

The conclusion of each chapter can be summarized here as follows:

In Chapter 2, an approach is developed for 2D Helmholtz acoustic problem by coupling the particle swarm method (PSO), with the isogeometric analysis (IGA) using two boundary element methods avoiding an interior discretization of the domain; the conventional (IGABEM) and the eXtended (XIBEM). Several numerical examples considering the duct problem and different optimization cases of the noise barrier and horn problems are examined and the obtained results are compared against the analytical solution or the previously published methods. It is demonstrated that, the results of the present approach are generally in good agreement with some computation advantage to XIBEM which allows coarser meshes. PSO is simpler than the gradient-based optimization methods since it does not need any sensitivity analysis, but it has some trade-offs with regard to the convergence speed. Furthermore, as the number of design variables increases, a larger number of consecutive iterations (N_2) is required. Larger N_2 helps also in higher frequency cases. In some cases the solution may not be unique and different optimal geometries can be obtained.

In Chapter 3, a 3D axi-symmetric Helmholtz acoustic problem is solved by coupling the isogeometric analysis (IGA) and the boundary element method (IGABEM). Due to the axial symmetry, surface integration in the boundary integral equation (BIE) can be split into the line integral and reduced integration in the angular direction. This enables us to reduce dimensionality of the BIE to 1D (i.e. only the line BIE is descretised), resulting in significant computational savings and therefore, for the same computational capabilities, the proposed approach can be applied to much higher frequencies in comparison to a fully 3D IGABEM. Three numerical examples with a variety of frequencies are analysed for the spherical problems. The performance of IGABEM for axi-symmetric models is verified with the analytical solutions showing better capabilities for handling extremely high frequencies compared to the already published 3D models. Axi-symmetric IGABEM is subsequently paired with the PSO for shape optimization. Different numerical examples considering several optimization cases of the horn problem with cylindrical symmetry are studied and the obtained results are compared with previously published methods. It is demonstrated that, the results of the present approach using fewer degrees of freedoms were in very good agreement with the previously published results. Minimization of the objective function regarding the frequency band cases using either summation or averaging methods with only 4 frequencies shows superior efficiency.

154

In Chapter 4, two boundary element methods (BEM): the conventional boundary integral equation (CBIE) and Burton-Miller (BM), are employed in the framework of the isogeometric analysis (IGA) to solve three dimensional Helmholtz acoustic scattering problems forming IGABEM. BM is employed to overcome the fictitious eigenfrequencies problem caused by the non-uniqueness of the numerical solution when using CBIE alone. However, in the absence of the eigenfrequencies problem CBIE produces competitive results since it contains only regular integrals. We have applied the NURBS basis functions with an offset to the collocation points wherever C^0 is encountered, so that the normal directions at collocation points required by BM can be defined distinctly and the total DOFs would equal the total number of linear system of equations. The jump-term is defined also easily on smooth surfaces without any need for complex calculations. It can also prevent any singularity of order $\mathcal{O}(1/r)$ and convert it into regular integrals. Singularity subtraction technique (SST) is employed to overcome the hyper-singular integral of order $\mathcal{O}(1/r^3)$ that appears in BM when the collocation point coincides with the integrated element, while an adaptive integration is implemented for neighbor elements to the collocation point. Both CBIE and BM show satisfactory results using only NURBS polynomial of degree 2. Nearly singularity treatment corresponding to collocation on sphere poles when using SST for the hyper-singular integral due to highly distorted elements is avoided using the offset scheme. IGABEM is coupled with the Particle Swarm Optimization (PSO) for structural shape optimization problems. Different numerical examples are discussed to present the validity of the proposed approach with respect to the analytical solution and against already published numerical results showing the agreement between the results.

In Chapter 5, Burton-Miller method (BM) is coupled with the isogeometric analysis (IGA) - forming IGA-BM - to study the muffler problem with extended inlet/outlet tubes as an interior Helmholtz acoustic problem. BM can properly model the extended tubes with thin thickness as two surfaces separated from each other by a small gap since the normal direction at each collocation point over all surfaces can be evaluated. Moreover, BM provides the merit of BEM models of modelling only the surface/boundary of the 3D problem reducing its dimensionality. In addition, IGA is powerful for modelling complex surfaces with accelerated refinement process and higher accuracy by approximating both the CAD geometry and the phys-

ical boundary variables with Non-uniform Rational B-splines basis functions (NURBS). The main design factor for mufflers, the transmission loss (TL), is calculated using three methods; the 3-point method, the 4-pole transfer matrix method and the improved 4-pole transfer matrix method. All methods give almost the same results while the improved 4-pole transfer matrix is preferred since it requires only one system matrix with two different vectors for different boundary conditions. This speeds up the computation process. In addition, the TL produces the 4-pole parameters on the inlet/outlet transparent surfaces which is convenient to the nature of BM of predicting the physical variables on the boundary of the problem. The validity of IGA-BM using coarser meshes is proven in comparison with the analytical solution, measured data and the previously published numerical results with BEM, FEM and IGA models. The Particle Swarm Optimization (PSO) is shown as a simple gradient-free method which does not require any sensitivity analysis. As long as few design variables are set for the optimization problem, a lower value for the Number of Consecutive Iterations (N_2) can be chosen converging to excellent results. In addition, minimization of the objective function for optimization problems regarding maximizing the TL can be achieved by dividing the frequency band only to 4 frequencies (Gauss quadrature points) for integration purposes.

6.2   Scope of future work

The present methods can be further extended in the future to address the following:

- The Artificial Neural Network Methods for acoustic applications with BEM [128].

- The inverse problem detecting the object shape inside the problem domain [129, 130].

- Local refinement schemes based on T-splines [11], LR-B-splines [131], or PHT-splines [89].

- GPU computing to speed up the analysis process [132, 133, 79].

- Other engineering problems based on collocation methods such as frictional problems [134], crack modeling [135], ocean circulation [136] and inelastic materials [137].

Bibliography

[1] G. C. Goel and D. L. Jain. Scattering of plane waves by a penetrable elliptic cylinder. *JASA*, 69(2):371–379, 1981.

[2] J.H. Su, V. V. Varadan, V.K. Varadan, and L. Flax. Acoustic wave scattering by a finite elastic cylinder in water. *JASA*, 68(2):686–691, 1980.

[3] S. Duczek, C. Willberg, D. Schmicker, and U. Gabbert. Development, validation and comparison of higher order finite element approaches to compute the propagation of Lamb waves efficiently. *Key Engineering Materials*, 518:95–105, 2012.

[4] C. Willberg, S. Duczek, J. M. Vivar Perez, and Z. A. B. Ahmad. Simulation methods for guided-wave based structural health monitoring: A review. *Applied Mechanics Reviews*, 67(1):1–20, 2015.

[5] I. Harari and T.J.R. Hughes. Galerkin/least-squares finite element methods for the reduced wave equation with non-reflecting boundary conditions in unbounded domains. *CMAME*, 98(3):411 – 454, 1992.

[6] T. Strouboulis, I. Babuška, and R. Hidajat. The generalized finite element method for helmholtz equation: Theory, computation, and open problems. *CMAME*, 195(37):4711 – 4731, 2006. John H. Argyris Memorial Issue. Part I.

[7] S. Suleau and Ph. Bouillard. One-dimensional dispersion analysis for the element-free galerkin method for the helmholtz equation. *IJNME*, 47(6):1169–1188, 2000.

[8] L.C. Wrobel. The boundary element method: Applications in thermo-fluids and acoustics. *John Wiley & Sons*, 1, 2002.

[9] A.Sommerfeld. Partial differential equations in physics. *Academic Press*, 1949.

[10] T.J.R. Hughes, J.A. Cottrell, and Y. Bazilevs. Isogeometric analysis: CAD, finite elements, NURBS, exact geometry and mesh refinement. *CMAME*, 194(39):4135 – 4195, 2005.

[11] Y. Bazilevs, V.M. Calo, J.A. Cottrell, J.A. Evans, T.J.R. Hughes, S. Lipton, M.A. Scott, and T.W. Sederberg. Isogeometric analysis using T-splines. *CMAME*, 199(5):229 – 263, 2010. Computational Geometry and Analysis.

[12] F. Auricchio, L. Beirao da Veiga, T. J. R. Huges, A. Reali, and G. Sangalli. Isogeometric collocation methods. *Math. Models Methods Appl. Sci.*, 20(11):2075–2107, 2010.

[13] R.N. Simpson, S.P.A. Bordas, J. Trevelyan, and T. Rabczuk. A two-dimensional Isogeometric Boundary Element Method for elastostatic analysis. *CMAME*, 209-212:87 – 100, 2012.

[14] X. Peng, E. Atroshchenko, P. Kerfriden, and S. P. A. Bordas. Linear elastic fracture simulation directly from cad: 2D nurbs-based implementation and role of tip enrichment. *International Journal of Fracture*, 204(1):55–78, Mar 2017.

[15] X. Peng, E. Atroshchenko, P. Kerfriden, and S.P.A. Bordas. Isogeometric boundary element methods for three dimensional static fracture and fatigue crack growth. *Computer Methods in Applied Mechanics and Engineering*, 316:151 – 185, 2017. Special Issue on Isogeometric Analysis: Progress and Challenges.

[16] Gernot Beer, Vincenzo Mallardo, Eugenio Ruocco, Benjamin Marussig, Jürgen Zechner, Christian Dünser, and Thomas-Peter Fries. Isogeometric boundary element analysis with elasto-plastic inclusions. part 2: 3-d problems. *Computer Methods in Applied Mechanics and Engineering*, 315:418 – 433, 2017.

[17] A.I. Ginnis, K.V. Kostas, C.G. Politis, P.D. Kaklis, K.A. Belibassakis, Th.P. Gerostathis, M.A. Scott, and T.J.R. Hughes. Isogeometric boundary-element analysis for the wave-resistance problem using t-splines. *Computer Methods in Applied Mechanics and Engineering*, 279:425 – 439, 2014.

[18] M.J. Peake, J. Trevelyan, and G. Coates. Extended isogeometric boundary element method (xibem) for two-dimensional helmholtz problems. *Computer Methods in Applied Mechanics and Engineering*, 259:93 – 102, 2013.

[19] Yi Sun, Jon Trevelyan, Gabriel Hattori, and Chihua Lu. Discontinuous isogeometric boundary element (igabem) formulations in 3d automotive acoustics. *Engineering Analysis with Boundary Elements*, 105:303–311, 2019.

[20] Ahmed Mostafa Shaaban, Cosmin Anitescu, Elena Atroshchenko, and Timon Rabczuk. Shape optimization by conventional and extended isogeometric boundary element method with pso for two-dimensional helmholtz acoustic problems. *Engineering Analysis with Boundary Elements*, 113:156 – 169, 2020.

[21] Ahmed Mostafa Shaaban, Cosmin Anitescu, Elena Atroshchenko, and Timon Rabczuk. Isogeometric boundary element analysis and shape optimization by pso for 3d axi-symmetric high frequency helmholtz acoustic problems. *Journal of Sound and Vibration*, 486:115598, 2020.

[22] M.J. Peake, J. Trevelyan, and G. Coates. Extended isogeometric boundary element method (xibem) for three-dimensional medium-wave acoustic scattering problems. *Computer Methods in Applied Mechanics and Engineering*, 284:762 – 780, 2015. Isogeometric Analysis Special Issue.

[23] Sören Keuchel, Nils Christian Hagelstein, Olgierd Zaleski, and Otto von Estorff. Evaluation of hypersingular and nearly singular integrals in the isogeometric boundary element method for acoustics. *Computer Methods in Applied Mechanics and Engineering*, 325:488 – 504, 2017.

[24] L.L. Chen, H. Lian, Z. Liu, H.B. Chen, E. Atroshchenko, and S.P.A. Bordas. Structural shape optimization of three dimensional acoustic problems with isogeometric boundary element methods. *Computer Methods in Applied Mechanics and Engineering*, 355:926 – 951, 2019.

[25] Leilei CHEN, Wenchang ZHAO, Cheng LIU, Haibo CHEN, and Steffen MARBURG. Isogeometric fast multipole boundary element method based on burton-miller formulation for 3d acoustic problems. *Archives of Acoustics*, 44(3), 2019.

[26] Jon Vegard Venås and Trond Kvamsdal. Isogeometric boundary element method for acoustic scattering by a submarine. *Computer Methods in Applied Mechanics and Engineering*, 359:112670, 2020.

[27] Leilei Chen, Chuang Lu, Haojie Lian, Zhaowei Liu, Wenchang Zhao, Shengze Li, Haibo Chen, and Stéphane P.A. Bordas. Acoustic topology optimization of sound absorbing materials directly from subdivision surfaces with isogeometric boundary element methods. *Computer Methods in Applied Mechanics and Engineering*, 362:112806, 2020.

[28] Ahmed Mostafa Shaaban, Cosmin Anitescu, Elena Atroshchenko, and Timon Rabczuk. 3d isogeometric boundary element analysis and structural shape optimization for helmholtz acoustic scattering problems. *Computer Methods in Applied Mechanics and Engineering*, 384:113950, 2021.

[29] J.M. Melenk and I. Babuška. The partition of unity finite element method: Basic theory and applications. *Computer Methods in Applied Mechanics and Engineering*, 139(1):289 – 314, 1996.

[30] E. Perrey-Debain, J. Trevelyan, and P. Bettess. Plane wave interpolation in direct collocation boundary element method for radiation and wave scattering: numerical aspects and applications. *Journal of Sound and Vibration*, 261(5):839 – 858, 2003.

[31] A. F. Seybert, B. Soenarko, F. J. Rizzo, and D. J. Shippy. An advanced computational method for radiation and scattering of acoustic waves in three dimensions. *The Journal of the Acoustical Society of America*, 77(2):362–368, 1985.

[32] Louise Wright, Stephen P. Robinson, and Victor F. Humphrey. Prediction of acoustic radiation from axisymmetric surfaces with arbitrary boundary conditions using the boundary element method on a distributed computing system. *The Journal of the Acoustical Society of America*, 125(3):1374–1383, 2009.

[33] Stephanos V. Tsinopoulos, John P. Agnantiaris, and Demosthenes Polyzos. An advanced boundary element/fast fourier transform axisymmetric formulation for acoustic radiation and wave scattering problems. *The Journal of the Acoustical Society of America*, 105(3):1517–1526, 1999.

[34] Weiping Wang, Noureddine Atalla, and Jean Nicolas. A boundary integral approach for acoustic

radiation of axisymmetric bodies with arbitrary boundary conditions valid for all wave numbers. *The Journal of the Acoustical Society of America*, 101(3):1468–1478, 1997.

[35] Sai Sudha Ramesh, K.M. Lim, and B.C. Khoo. An axisymmetric hypersingular boundary integral formulation for simulating acoustic wave propagation in supercavitating flows. *Journal of Sound and Vibration*, 331(19):4313 – 4342, 2012.

[36] Rajitha Udawalpola, Eddie Wadbro, and Martin Berggren. Optimization of a variable mouth acoustic horn. *International Journal for Numerical Methods in Engineering*, 85(5):591–606, 2011.

[37] R.N. Simpson, M.A. Scott, M. Taus, D.C. Thomas, and H. Lian. Acoustic isogeometric boundary element analysis. *Computer Methods in Applied Mechanics and Engineering*, 269:265 – 290, 2014.

[38] A. J. Burton, G. F. Miller, and James Hardy Wilkinson. The application of integral equation methods to the numerical solution of some exterior boundary-value problems. *Proceedings of the Royal Society of London. A. Mathematical and Physical Sciences*, 323(1553):201–210, 1971.

[39] G. Krishnasamy, L. W. Schmerr, T. J. Rudolphi, and F. J. Rizzo. Hypersingular Boundary Integral Equations: Some Applications in Acoustic and Elastic Wave Scattering. *Journal of Applied Mechanics*, 57(2):404–414, 06 1990.

[40] Guiggiani M, Krishnasamy G., Rudolphi T. J., and Rizzo F. J. A general algorithm for the numerical solution of hypersingular boundary integral equations. *Journal of Applied Mechanics, ASME*, 59(3):604 – 614, 1992.

[41] Benjamin Marussig, Jürgen Zechner, Gernot Beer, and Thomas-Peter Fries. Fast isogeometric boundary element method based on independent field approximation. *Computer Methods in Applied Mechanics and Engineering*, 284:458 – 488, 2015. Isogeometric Analysis Special Issue.

[42] Joseph W. Sullivan and Malcolm J. Crocker. Analysis of concentric-tube resonators having unpartitioned cavities. *The Journal of the Acoustical Society of America*, 64(1):207–215, 1978.

[43] Ying-Chun Chang, Long-Jyi Yeh, Min-Chie Chiu, and Gaung-Jer Lai. Computer aided design on

single expansion muffler with extended tube under space constraints. *Journal of Applied Science and Engineering*, 7:171–181, September 2004.

[44] A. Gupta and A. Tiwari. Enhancement on sound transmission loss for various positioning of inlet and outlet duct of the muffler. *International Journal of Engineering and Manufacturing*, 5:1–11, 2015.

[45] Chu Zhigang, Kuang Fang, Kang Runcheng, and Gao Xiaoxin. Effects of airflow on the acoustic attenuation performance of reactive muffler. *Journal of Vibroengineering*, 18(1):637–648, 2016.

[46] Mahesh Vasantrao Kulkarni and Ravindra B Ingle. Effect of extended inlet and outlet placement on transmission loss of double expansion chamber reactive muffler. *International Journal of Research and Analytical Reviews*, 5(4):552–558, 2018.

[47] Anna Snakowska and Jerzy Jurkiewicz. A new approach to the theory of acoustic multi-port networks with multimode wave and its application to muffler analysis. *Journal of Sound and Vibration*, 490:115722, 2021.

[48] A. Selamet and P.M. Radavich. The effect of length on the acoustic attenuation performance of concentric expansion chambers: An analytical, computational and experimental investigation. *Journal of Sound and Vibration*, 201(4):407–426, 1997.

[49] Jeong-Guon Ih and Byung-Ho Lee. Analysis of higher-order mode effects in the circular expansion chamber with mean flow. *The Journal of the Acoustical Society of America*, 77(4):1377–1388, 1985.

[50] F.D. Denia, E.M. Sánchez-Orgaz, L. Baeza, and R. Kirby. Point collocation scheme in silencers with temperature gradient and mean flow. *Journal of Computational and Applied Mathematics*, 291:127–141, 2016. Mathematical Modeling and Computational Methods.

[51] A. F. Seybert and C. Cheng. Application of the boundary element method to acoustic cavity response and muffler analysis. *Journal of Vibration and Acoustics-transactions of The Asme*, 109:15–21, 1987.

[52] S. Bilawchuk and K.R. Fyfe. Comparison and implementation of the various numerical methods used for calculating transmission loss in silencer systems. *Applied Acoustics*, 64(9):903–916, 2003.

[53] S. Kamarkhani and A. Mahmoudi Kohan. Muffler Design with Baffle Effect and Performations on Transmission Loss. *Mechanics and Mechanical Engineering*, 22(4):1337–1344, September 2020.

[54] C. Shen and L. Hou. Comparison of various algorithms for improving acoustic attenuation performance and flow characteristic of reactive mufflers. *Appl. Acoustics*, 116:291 – 296, 2017.

[55] R. Barbieri, N. Barbieri, and K. F. Lima. Application of the galerkin-fem and the improved four-pole parameter method to predict acoustic performance of expansion chambers. *Journal of Sound and Vibration*, 276:1101–1107, 2004.

[56] Yaqiang Xue, Guoyong Jin, Tiangui Ye, Kangkang Shi, Saifeng Zhong, and Chuanmeng Yang. Isogeometric analysis for geometric modelling and acoustic attenuation performances of reactive mufflers. *Computers and Mathematics with Applications*, 79(12):3447–3461, 2020.

[57] A. Selamet and Z.L. Ji. Acoustic attenuation performance of circular expansion chambers with extended inlet/outlet. *Journal of Sound and Vibration*, 223(2):197–212, 1999.

[58] R. Martinez. The thin-shape breakdown (tsb) of the helmholtz integral equation. *The Journal of the Acoustical Society of America*, 90(5):2728–2738, 1991.

[59] T. W. Wu and G. C. Wan. Muffler Performance Studies Using a Direct Mixed-Body Boundary Element Method and a Three-Point Method for Evaluating Transmission Loss. *Journal of Vibration and Acoustics*, 118(3):479–484, 07 1996.

[60] T.W. Wu, P. Zhang, and C.Y.R. Cheng. Boundary element analysis of mufflers with an improved method for deriving the four-pole parameters. *Journal of Sound and Vibration*, 217(4):767–779, 1998.

[61] T. W. Wu and C. Chen. Boundary element analysis of reactive mufflers and packed silencers with catalyst converters. *Electronic Journal of Boundary Elements*, 1(2):218–235, 2003.

[62] J. H. Kane, S. Mao, and G. C. Everstine. A boundary element formulation for acoustic shape sensitivity analysis. *The Journal of the Acoustical Society of America*, 90(1):561–573, 1991.

[63] L. Chen, C. Liu, W. Zhao, and L. Liu. An isogeometric approach of two dimensional acoustic design sensitivity analysis and topology optimization analysis for absorbing material distribution. *CMAME*, 336:507 – 532, 2018.

[64] Erik Bängtsson, Daniel Noreland, and Martin Berggren. Shape optimization of an acoustic horn. *Computer Methods in Applied Mechanics and Engineering*, 192(11):1533 – 1571, 2003.

[65] L. Chen, H. Chen, C. Zheng, and S. Marburg. Structural–acoustic sensitivity analysis of radiated sound power using a finite element/ discontinuous fast multipole boundary element scheme. *IJNMF*, 82(12):858–878, 2016.

[66] J. Kennedy and R. Eberhart. Particle swarm optimization. In *Proceedings of ICNN'95 - International Conference on Neural Networks*, volume 4, pages 1942–1948. IEEE, 1995.

[67] R. Eberhart and J. Kennedy. A new optimizer using particle swarm theory. In *Proceedings of the Sixth International Symposium on Micro Machine and Human Science*, pages 39–42. IEEE, 1995.

[68] Gábor Renner and Anikó Ekárt. Genetic algorithms in computer aided design. *Computer-Aided Design*, 35(8):709 – 726, 2003. Genetic Algorithms.

[69] S.H. Sun, T.T. Yu, T.T. Nguyen, E. Atroshchenko, and T.Q. Bui. Structural shape optimization by IGABEM and particle swarm optimization algorithm. *EABE*, 88:26 – 40, 2018.

[70] R. Barbieri, N. Barbieri, and K. Fonseca de Lima. Some applications of the PSO for optimization of acoustic filters. *Appl. Acoustics*, 89:62 – 70, 2015.

[71] Kang Li and Xiaoping Qian. Isogeometric analysis and shape optimization via boundary integral. *Computer-Aided Design*, 43(11):1427 – 1437, 2011. Solid and Physical Modeling 2011.

[72] Louis Blanchard, Régis Duvigneau, Anh-Vu Vuong, and Bernd Simeon. Shape gradient for isogeometric structural design. *Journal of Optimization Theory and Applications*, 161(2):361–367, May 2014.

[73] C. S. Ding, X. Y. Cui, and G. Y. Li. Accurate analysis and thickness optimization of tailor rolled

blanks based on isogeometric analysis. *Structural and Multidisciplinary Optimization*, 54(4):871–887, Oct 2016.

[74] L. F. R. Espath, R. V. Linn, and A. M. Awruch. Shape optimization of shell structures based on NURBS description using automatic differentiation. *International Journal for Numerical Methods in Engineering*, 88(7):613–636, 2011.

[75] J. Kiendl, R. Schmidt, R. Wüchner, and K.-U. Bletzinger. Isogeometric shape optimization of shells using semi-analytical sensitivity analysis and sensitivity weighting. *Computer Methods in Applied Mechanics and Engineering*, 274:148 – 167, 2014.

[76] K.V. Kostas, M.M. Fyrillas, C.G. Politis, A.I. Ginnis, and P.D. Kaklis. Shape optimization of conductive-media interfaces using an IGA-BEM solver. *Computer Methods in Applied Mechanics and Engineering*, 340:600 – 614, 2018.

[77] Byong-Ug Park, Yu-Deok Seo, Ole Sigmund, and Sung-Kie Youn. Shape optimization of the stokes flow problem based on isogeometric analysis. *Structural and Multidisciplinary Optimization*, 48(5):965–977, Nov 2013.

[78] Peter Nørtoft and Jens Gravesen. Isogeometric shape optimization in fluid mechanics. *Structural and Multidisciplinary Optimization*, 48(5):909–925, Nov 2013.

[79] Q. M. Nguyen, V. Dang, O. Kilic, and E. El-Araby. Parallelizing fast multipole method for large-scale electromagnetic problems using GPU clusters. *IEEE Antennas and Wireless Propagation Letters*, 12:868–871, 2013.

[80] K.V. Kostas, A.I. Ginnis, C.G. Politis, and P.D. Kaklis. Shape-optimization of 2D hydrofoils using an isogeometric BEM solver. *Computer-Aided Design*, 82:79 – 87, 2017. Isogeometric Design and Analysis.

[81] H.J. Kim, Y.D. Seo, and S.K. Youn. Isogeometric analysis for trimmed CAD surfaces. *Computer Methods in Applied Mechanics and Engineering*, 198(37):2982–2995, 2009.

[82] H.J. Kim, Y.D. Seo, and S.K. Youn. Isogeometric analysis with trimming technique for problems of arbitrary complex topology. *Computer Methods in Applied Mechanics and Engineering*, 199(45):2796–2812, 2010.

[83] R. Schmidt, R. Wüchner, and K.U. Bletzinger. Isogeometric analysis of trimmed NURBS geometries. *Computer Methods in Applied Mechanics and Engineering*, 241-244:93–111, 2012.

[84] M.R. Dörfel, B. Jüttler, and B. Simeon. Adaptive isogeometric analysis by local h-refinement with T-splines. *Computer Methods in Applied Mechanics and Engineering*, 199(5):264–275, 2010. Computational Geometry and Analysis.

[85] D. Schillinger, L. Dedè, M.A. Scott, J.A. Evans, M.J. Borden, E. Rank, and T.J.R. Hughes. An isogeometric design-through-analysis methodology based on adaptive hierarchical refinement of NURBS, immersed boundary methods, and T-spline CAD surfaces. *Computer Methods in Applied Mechanics and Engineering*, 249-252:116–150, 2012. Higher Order Finite Element and Isogeometric Methods.

[86] A. Buffa, D. Cho, and G. Sangalli. Linear independence of the T-spline blending functions associated with some particular T-meshes. *Computer Methods in Applied Mechanics and Engineering*, 199(23):1437–1445, 2010.

[87] X. Li, J. Zheng, T.W. Sederberg, T.J.R. Hughes, and M.A. Scott. On linear independence of T-spline blending functions. *Computer Aided Geometric Design*, 29(1):63–76, 2012. Geometric Constraints and Reasoning.

[88] H. Casquero, L. Liu, Y. Zhang, A. Reali, and H. Gomez. Isogeometric collocation using analysis-suitable T-splines of arbitrary degree. *Computer Methods in Applied Mechanics and Engineering*, 301:164–186, 2016.

[89] Jiansong Deng, Falai Chen, Xin Li, Changqi Hu, Weihua Tong, Zhouwang Yang, and Yuyu Feng. Polynomial splines over hierarchical T-meshes. *Graphical Models*, 70(4):76 – 86, 2008.

[90] N. Nguyen-Thanh, H. Nguyen-Xuan, S.P.A. Bordas, and T. Rabczuk. Isogeometric analysis using polynomial splines over hierarchical T-meshes for two-dimensional elastic solids. *Computer Methods in Applied Mechanics and Engineering*, 200(21):1892–1908, 2011.

[91] P. Wang, J. Xu, J. Deng, and F. Chen. Adaptive isogeometric analysis using rational PHT-splines. *Computer-Aided Design*, 43(11):1438–1448, 2011. Solid and Physical Modeling 2011.

[92] N. Nguyen-Thanh, J. Kiendl, H. Nguyen-Xuan, R. Wüchner, K.U. Bletzinger, Y. Bazilevs, and T. Rabczuk. Rotation free isogeometric thin shell analysis using PHT-splines. *Computer Methods in Applied Mechanics and Engineering*, 200(47):3410–3424, 2011.

[93] C.L. Chan, C. Anitescu, and T. Rabczuk. Volumetric parametrization from a level set boundary representation with PHT-splines. *Computer-Aided Design*, 82:29–41, 2017. Isogeometric Design and Analysis.

[94] N. Nguyen-Thanh and K. Zhou. Extended isogeometric analysis based on PHT-splines for crack propagation near inclusions. *International Journal for Numerical Methods in Engineering*, 112(12):1777–1800, 2017.

[95] E. Atroshchenko, S. Tomar, G. Xu, and S.P.A. Bordas. Weakening the tight coupling between geometry and simulation in isogeometric analysis: From sub- and super-geometric analysis to Geometry-Independent Field approximation (GIFT). *International Journal for Numerical Methods in Engineering*, 114(10):1131–1159, 2018.

[96] P. Yu, C. Anitescu, S. Tomar, S.P.A. Bordas, and P. Kerfriden. Adaptive isogeometric analysis for plate vibrations: An efficient approach of local refinement based on hierarchical a posteriori error estimation. *Computer Methods in Applied Mechanics and Engineering*, 342:251–286, 2018.

[97] C. Anitescu, M.N. Hossain, and T. Rabczuk. Recovery-based error estimation and adaptivity using high-order splines over hierarchical T-meshes. *Computer Methods in Applied Mechanics and Engineering*, 328:638–662, 2018.

[98] Javier Videla, Cosmin Anitescu, Tahsin Khajah, Stéphane P.A. Bordas, and Elena Atroshchenko. h- and p-adaptivity driven by recovery and residual-based error estimators for pht-splines applied to time-harmonic acoustics. *Computers & Mathematics with Applications*, 77(9):2369 – 2395, 2019.

[99] J. Videla, F. Contreras, H.X. Nguyen, and E. Atroshchenko. Application of PHT-splines in bending

and vibration analysis of cracked Kirchhoff–Love plates. *Computer Methods in Applied Mechanics and Engineering*, 361:112754, 2020.

[100] N. Nguyen-Thanh, K. Zhou, X. Zhuang, P. Areias, H. Nguyen-Xuan, Y. Bazilevs, and T. Rabczuk. Isogeometric analysis of large-deformation thin shells using RHT-splines for multiple-patch coupling. *Computer Methods in Applied Mechanics and Engineering*, 316:1157–1178, 2017. Special Issue on Isogeometric Analysis: Progress and Challenges.

[101] N. Nguyen-Thanh, J. Muthu, X. Zhuang, and T. Rabczuk. An adaptive three-dimensional RHT-splines formulation in linear elasto-statics and elasto-dynamics. *Computational Mechanics*, 53:369–385, 2014.

[102] C. Giannelli, B. Jüttler, S. K. Kleiss, A. Mantzaflaris, B. Simeon, and J. Špeh. THB-splines: An effective mathematical technology for adaptive refinement in geometric design and isogeometric analysis. *Computer Methods in Applied Mechanics and Engineering*, 299:337–365, 2016.

[103] A. Pawar, Y. Zhang, Y. Jia, X. Wei, T. Rabczuk, C.L. Chan, and C. Anitescu. Adaptive FEM-based nonrigid image registration using truncated hierarchical B-splines. *Computers & Mathematics with Applications*, 72(8):2028–2040, 2016. Finite Elements in Flow Problems 2015.

[104] M.A. Scott, R.N. Simpson, J.A. Evans, S. Lipton, S.P.A. Bordas, T.J.R. Hughes, and T.W. Sederberg. Isogeometric boundary element analysis using unstructured t-splines. *CMAME*, 254:197 – 221, 2013.

[105] H. Lian, P. Kerfriden, and S.P.A. Bordas. Shape optimization directly from CAD: An isogeometric boundary element approach using T-splines. *Computer Methods in Applied Mechanics and Engineering*, 317:1–41, 2017.

[106] R.N. Simpson and Z. Liu. Acceleration of isogeometric boundary element analysis through a black-box fast multipole method. *Engineering Analysis with Boundary Elements*, 66:168–182, 2016.

[107] J. B. Keller and D. Givoli. Exact non-reflecting boundary conditions. *Journal of Computational Physics*, 82(1):172 – 192, 1989.

[108] L. Piegl and W. Tille. The NURBS book. *Springer*, 1995.

[109] J. C. F. Telles. A self-adaptive co-ordinate transformation for efficient numerical evaluation of general boundary element integrals. *International Journal for Numerical Methods in Engineering*, 24(5):959–973, 1987.

[110] T. Huttunen, P. Gamallo, and R. J. Astley. Comparison of two wave element methods for the Helmholtz problem. *Communications in Numerical Methods in Engineering*, 25(1):35–52, 2009.

[111] T. Ishizuka and K. Fujiwara. Performance of noise barriers with various edge shapes and acoustical conditions. *Appl. Acoustics*, 65(2):125 – 141, 2004.

[112] R. Barbieri and N. Barbieri. Acoustic horns optimization using finite elements and genetic algorithm. *Appl. Acoustics*, 74(3):356 – 363, 2013.

[113] Rajitha Udawalpola and Martin Berggren. Optimization of an acoustic horn with respect to efficiency and directivity. *International Journal for Numerical Methods in Engineering*, 73(11):1571–1606, 2008.

[114] A. F. Seybert, B. Soenarko, F. J. Rizzo, and D. J. Shippy. A special integral equation formulation for acoustic radiation and scattering for axisymmetric bodies and boundary conditions. *The Journal of the Acoustical Society of America*, 80(4):1241–1247, 1986.

[115] J.W.Strutt(Lord Rayleigh). Theory of sound. *MacMillan, London*, II, 1896.

[116] P.M. Morse. Vibration and sound. *McGraw-Hill, New York*, 1948.

[117] Oleg Godin. Rayleigh scattering of a spherical sound wave. *The Journal of the Acoustical Society of America*, 133:709–20, 02 2013.

[118] P.M.Morse and H.Feshbach. Methods of theoretical physics: Part II. *McGraw-Hill*, 1953.

[119] Robert Hickling and N. M. Wang. Scattering of sound by a rigid movable sphere. *The Journal of the Acoustical Society of America*, 39(2):276–279, 1966.

[120] E. Wadbro and M. Berggren. Topology optimization of an acoustic horn. *Computer Methods in Applied Mechanics and Engineering*, 196(1-3):420–436, December 2006.

[121] Eddie Wadbro, Rajitha Udawalpola, and Martin Berggren. Shape and topology optimization of an acoustic horn–lens combination. *Journal of Computational and Applied Mathematics*, 234(6):1781 – 1787, 2010. Eighth International Conference on Mathematical and Numerical Aspects of Waves (Waves 2007).

[122] Anders Bernland, Eddie Wadbro, and Martin Berggren. Acoustic shape optimization using cut finite elements. *International Journal for Numerical Methods in Engineering*, 113(3):432–449, 2018.

[123] Stephan Schmidt, Eddie Wadbro, and Martin Berggren. Large-scale three-dimensional acoustic horn optimization. *SIAM Journal on Scientific Computing*, 38(6):B917–B940, 2016.

[124] Chang-Jun Zheng, Hai-Bo Chen, Hai-Feng Gao, and Lei Du. Is the burton–miller formulation really free of fictitious eigenfrequencies? *Engineering Analysis with Boundary Elements*, 59:43 – 51, 2015.

[125] M. Guiggiani and A. Gigante. A General Algorithm for Multidimensional Cauchy Principal Value Integrals in the Boundary Element Method. *Journal of Applied Mechanics*, 57(4):906–915, 12 1990.

[126] Renato Barbieri and Nilson Barbieri. Finite element acoustic simulation based shape optimization of a muffler. *Applied Acoustics*, 67(4):346–357, 2006.

[127] Ahmed Mostafa Shaaban, Cosmin Anitescu, Elena Atroshchenko, and Timon Rabczuk. An isogeometric burton-miller method for the transmission loss optimization with application to mufflers with internal extended tubes. *Applied Acoustics*, 185:108410, 2022.

[128] Cosmin Anitescu, Elena Atroshchenko, Naif Alajlan, and Timon Rabczuk. Artificial neural network methods for the solution of second order boundary value problems. *Computers, Materials & Continua*, 59(1):345–359, 2019.

[129] A. V Goncharsky and S. Y Romanov. Supercomputer technologies in inverse problems of ultrasound tomography. *Inverse Problems*, 29(7):075004, 2013.

[130] E. A. Sisamon, S. C. Beck, S. C. Langer, and A. P. Cisilino. Inverse scattering analysis in acoustics via the bem and the topological-shape sensitivity method. *Comp. Mechanics*, 54(5):1073–1087, Nov 2014.

[131] Kjetil André Johannessen, Trond Kvamsdal, and Tor Dokken. Isogeometric analysis using LR B-splines. *Computer Methods in Applied Mechanics and Engineering*, 269:471 – 514, 2014.

[132] R. Yokota, J. P. Bardhan, M. G. Knepley, L.A. Barba, and T. Hamada. Biomolecular electrostatics using a fast multipole BEM on up to 512 GPUs and a billion unknowns. *Computer Physics Communications*, 182(6):1272 – 1283, 2011.

[133] S. Hamada. GPU-accelerated indirect boundary element method for voxel model analyses with fast multipole method. *Computer Physics Communications*, 182(5):1162 – 1168, 2011.

[134] Ashkan Almasi, Tae-Yeon Kim, Tod A. Laursen, and Jeong-Hoon Song. A strong form meshfree collocation method for frictional contact on a rigid obstacle. *Computer Methods in Applied Mechanics and Engineering*, 357:112597, 2019.

[135] Iman Asareh and Jeong-Hoon Song. Nonnodal extended finite-element method for crack modeling with four-node quadrilateral elements. *Journal of Engineering Mechanics*, 145(10):04019081, 2019.

[136] Andrew Beel, Tae-Yeon Kim, Wen Jiang, and Jeong-Hoon Song. Strong form-based meshfree collocation method for wind-driven ocean circulation. *Computer Methods in Applied Mechanics and Engineering*, 351:404–421, 2019.

[137] Young-Cheol Yoon, Peter Schaefferkoetter, Timon Rabczuk, and Jeong-Hoon Song. New strong formulation for material nonlinear problems based on the particle difference method. *Engineering Analysis with Boundary Elements*, 98:310–327, 2019.

PERSONAL INFORMATION	Ahmed Mostafa Shaaban Mohamed

Brennerstraße 42, Weimar, 99423, Germany

📞 +4915201354115 📱 +201006276285

✉ ahmed.mostafa.shaaban.mohamed@uni-weimar.de
ashaaban_egypt@yahoo.com

Gender Male | Date of Birth 24/05/1985 | Nationality Egyptian

EDUCATION

(October 2017 - October 2021)	Ph.D., Institute of Structural Mechanics, Faculty of Civil Engineering, Bauhaus-Universität Weimar, Germany.
(October 2007 – October 2012)	M.Sc., Department of Civil engineering, Faculty of Engineering, Cairo University, Egypt.
(September 2002 – May 2007)	B.Sc., Department of Civil engineering, Faculty of Engineering, Cairo University, Egypt.

WORK EXPERIENCE

(April 2018 – September 2018)	Research Assistant, Institute of Structural Mechanics, Faculty of Civil Engineering, Bauhaus-Universität Weimar, Germany.
(March 2008 –July 2017)	Structural Engineer, Dar Al-Handasah (Shair and Partners), Egypt.
(July 2007 – March 2008)	Civil Engineer, TICE Consultative Engineering Office, Egypt.